DTIC FILE COPY

DTIC
ELECTE
SEP 1 2 1985

S   D

A

85   8   29   063

ADVANCES
IN
ELECTRICAL CURRENT
COLLECTION

Accession For

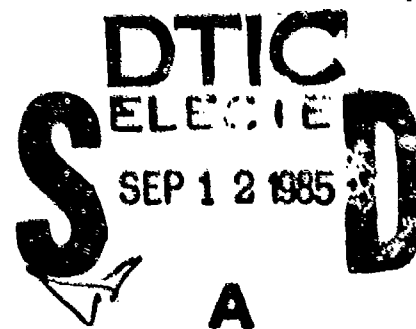| NTIS GRA&I | |
DTIC TAB	
Unannounced	
Justificc	
By	
Distribut /	
Availab 11 Codes	
Dist	or

DTIC
COPY
INSPECTED
3

A1

RE: Right to Reproduce and Sell Book
Because of the royalty free licence for
the U. S. Govt on this book, DTIC and NTIS
have permission to reproduce and sell it.
Per Mr. A. W. Ruff, ONR/Code 431

ADVANCES IN ELECTRICAL CURRENT COLLECTION

Editor: I. R. McNAB

(Pittsburgh, PA, U.S.A.)

1982

ELSEVIER SEQUOIA S.A., LAUSANNE and NEW YORK

Contents

vi

Foreword

Advances in electrical current collection

I. R. MCNAB

Electrotechnology Department, Westinghouse Electric Corporation Research and Development Center, 1310 Beulah Road, Pittsburgh, PA 15235 (U.S.A.)

During the last decade, substantial advances have taken place in several areas of technology concerned with the transfer of electrical current across sliding interfaces. The requirement to transfer current from moving metal surfaces to sliding conductors is essential for many electrical machines, and research in this field goes back to the earliest days of the electrical industry.

In recent years several advanced rotating and linear electrical machine concepts have been developed which depend for their success on the efficient transfer of current across sliding interfaces. For example, the steady state operation of brushes at 8 MA m^{-2} is the goal for advanced land or sea propulsion machinery. Even higher current densities (18 MA m^{-2}) and speeds (300 m s^{-1}) are required for the subsecond operation of inertial storage pulsed power sources. Speeds and current densities more than an order of magnitude higher, although for millisecond pulses, may prove to be necessary for linear electromagnetic projectile accelerators. In all these cases the requirement for the efficient transfer of electrical current complicates the frictional and wear effects that take place at mechanically contacting sliding interfaces.

In the U.S.A. the major research and development efforts during the last few years have been centered on the David Taylor Naval Ship Research and Development Center, Annapolis, MD, and at Westinghouse Research and Development Center, Pittsburgh, PA. The former effort focused on the use of liquid metal techniques while the research of the Westinghouse scientists, and their colleagues in associated universities, has been concentrated on solid or multielement brush techniques. The Westinghouse program was supported by the Materials Science Office of the Advanced Research Projects Agency of the U.S. Department of Defense (DARPA) and monitored by the Office of Naval Research (ONR). Throughout the program regular Workshop meetings were held to enable the contributing researchers to meet and exchange information. However, since attendance at these Workshops was limited and the proceedings were not published, it was decided to hold a full International Conference at which a combination of researchers, manufacturers and

users could interact to discuss the recent advances in this field. This conference, cosponsored by the Office of Naval Research and by Westinghouse Electric Corporation, was held in Chicago on September 23 - 25, 1981. Although relatively small in numbers, with approximately 60 attendees, the Conference brought together active experts in this field from the U.S.A., Canada, France, Gt. Britain and China, and two papers were submitted from the U.S.S.R. In view of the difficulties inherent in this subject it is likely that the combined efforts of these international experts with their spectrum of research and industrial perspectives will be needed to enable further progress in this subject to be made.

Substantial advances in liquid metal current collection techniques have been made during the last decade under the auspices of the U.S. Navy program. The work reported here shows that the use of the "narrow gap" collector geometry, based on the use of surface tension effects in a metallic braid that is virtually in touching contact with the rotor surface, enables the problems associated with liquid metal expulsion as a result of the $J \times B$ forces to be solved, and long term stable operation has been demonstrated. The major problem with liquid metals is the choice of fluids available, most of which have significant disadvantages. Sodium and potassium and their alloys (Na–K) are very reactive chemically while mercury is toxic and Ga–In alloys form contact-disrupting black powder oxides in oxygen-containing atmospheres. Despite the excellent performance observed in carefully controlled laboratory conditions, these considerations are likely to limit the practical use of liquid metals. Some work reported in this meeting was therefore devoted to discovering whether less reactive liquid metals, such as low melting point alloys, can be used for this application.

In most electrical machinery at present in operation, the current transfer function is provided by carbon-based brushes supplied by the brush industry. In most cases the operation of such brushes is limited by a current density–speed–wear loss envelope for which typical current densities and speeds are 0.2 MA m^{-2} and 40 m s^{-1}. Evaluation of the reasons for these limitations shows that the primary cause is the build-up of a complex film, mainly cuprous oxide, on the surface of the slip ring or commutator. In addition, the choice of the carbon-based brush is generally mandated by the requirement to develop a high voltage to force the current to flow into a new circuit, i.e. to commutate. For some of the new machine applications mentioned above, the commutation function may not exist, or may be less arduous, thereby opening the way to other brush concepts or materials.

As reported here, the work under the DARPA–ONR–Westinghouse program has shown that solid or monolithic brushes made from relatively conventional materials can be operated up to much higher current densities and speeds than previously considered possible provided that (i) careful atmosphere control (non-air) is provided, (ii) brush and environment temperatures are controlled, (iii) adequate mechanical control is maintained and (iv) optimal materials are chosen. Under these conditions several remarkable advances have taken place in recent years.

(i) Multiple brush assemblies have been operated continuously in machines at current densities in excess of 1.5 MA m^{-2} at 40 m s^{-1}.

(ii) Individual brushes have been operated in steady state conditions to current densities of 6 MA m^{-2} at 15 m s^{-1}.

(iii) Multiple brush assemblies have been pulsed to more than 3 MA m^{-2} at 40 m s^{-1}.

(iv) Prototypic multiple brush modules have been pulsed at current densities of 18 MA m^{-2} for periods of 0.25 s with simultaneous speeds up to 280 m s^{-1}.

Supporting these practical advances has been a wide range of fundamental studies into materials and surface physics at Westinghouse and in associated universities. These studies have encompassed aspects such as the following.

(i) Advanced diagnostic techniques (scanning electron microscopy, Auger analysis etc.) are used to determine the physical state of the materials.

(ii) Theoretical and practical studies on the electrical and mechanical effects taking place at the sliding interfaces are carried out.

(iii) Evaluations are made of materials compatibility and interactions.

(iv) New wear models are developed.

(v) The mechanical conditions imposed by practical materials and engineering limits and their effects on the sliding contact process are evaluated.

While much has been learned, and is reported in this volume, it is clear that these investigations are far from complete and that more remains to be done if we are to reach the goal of a unified theory to explain sliding contact behavior.

An alternative to the use of liquid metals or monolithic blocks of carbon, or metal–carbon, is the multielement contact which in its most common form may utilize the "fiber" brush. Much of the early work in this area was based on the development of carbon fibers in the 1960s when it was realized by researchers in Gt. Britain that this technology would permit a flexible carbon brush having multiple independent contacts to be made. This has been found to have some application in a modified form as the fringe fiber brush for machines operating in an arduous environment as described in two papers in this volume. However, for applications where low contact voltage drops were required, it was found to be beneficial to provide a coating on each individual fiber, for example by electroplating, to provide a high conductivity sheath on the high strength fiber. Although brushes have been successfully manufactured in this way, studies during the Westinghouse program showed that the optimum performance may not require as many contacts as provided by the standard 8 μm diameter carbon fibers. Consequently, new metal fiber brushes have been developed, with typical fiber diameters of 125 μm. Experiments with these brushes have been very successful showing, for example, continuous operation at very high current densities (greater than 10 MA m^{-2}) with very low losses and wear. An interesting feature of this work has been that independent groups have

followed similar lines, with similar results. This technology has been applied to the pulsed homopolar machine at the Naval Research Laboratory and has shown successful operation at sliding speeds up to 475 m s^{-1}, which is believed to be the highest peripheral speed achieved with sliding contacts in rotational machinery.

This same technology has also been applied to the problems found in switch ring machines, and results obtained with a combined metal–carbon plus metal fiber brush are described in a paper in this meeting. With this technology, current densities of 1.5 MA m^{-2} were achieved on a continuous basis. Although still at an early stage, this technology may represent the next step in commutation technology after the carbon fiber fringe brush.

Probably the ultimate sliding contact operation is represented by the conditions which exist in linear electromagnetic projectile accelerators. In such systems extremely high current densities (of the order of gigaamperes per meter squared) have to be transferred at very high speeds (of the order of kilometers per second or more). The only feature that makes such a contact feasible is its transient nature, usually of the order of a thousandth of a second. Nevertheless, conditions in such contacts are very severe and generally approach melting of the contacts. Research in this field is at a very early stage but some experimental work is reported here, together with factors that influence the successful operation, including electromagnetic transient effects. (See note added in proof.)

In summary, the work reported here provides a cross section of progress in this field which has traditionally shown relatively slow growth but where several important advances have been made in the last decade. Many of these advances have resulted from the DARPA–ONR program and I should like to take this opportunity to thank the Department of Defense program managers for their advice and encouragement .roughout this program, especially A. Bement and M. R. Buckley of DARPA, and R. Seng, R. A. Burton and H. B. Martin of ONR. The financial support offered by the ONR and Westinghouse Electric Corporation that made this conference possible is gratefully acknowledged. In addition, I should like to express my appreciation of the help and advice offered in connection with the organization of this conference by R. E. Armington, Chairman of the Holm Conference.

Finally, I should like to thank all the authors and participants for making this a pleasant and rewarding meeting, and D. J. DiCesare for her secretarial help in organizing the meeting.

Bibliography

Although the individual papers contained in this volume reference many of the prior studies in this field, it was considered helpful to enclose the following more complete list.

C. A. Bronlarek and O. S. Taylor, Mechanical stability of solid brush current collection systems, *IEEE Trans. Power Appar. Syst.*, 99 (6) (1980) 2413.

C. P. Chen and R. A. Burton, Thermoelastic effects in brushes with high current and high sliding speeds, in *Proc. Conf. on Electrical Contacts, September 1978*, Illinois Institute of Technology, Chicago, IL, 1978, p. 571.

R. M. Garrett and G. T. Hummert, Controlled conductance current switching in low voltage, high current DC machines, *Int. Conf. on Electric Machines, Athens, September 1980*.

J. L. Johnson, Monolithic brushes for high current collection applications, in *Extended Abstracts 15th Bienn. Conf. on Carbon, University of Pennsylvania, Philadelphia, PA, June 22 - 23, 1981*, pp. 318 - 319.

J. L. Johnson and O. S. Taylor, High current brushes. Part IV: machine environment tests, *IEEE Trans. Components, Hybrids Manuf. Technol.*, 3 (March 1980) 31.

J. L. Johnson and L. E. Moberly, High current brushes. Part I: effect of brush and ring materials, *IEEE Trans. Components, Hybrids Manuf. Technol.*, 1 (March 1978) 36.

P. K. Lee, High current brush material development. Part II: metal–solid lubricant coated wires, *IEEE Trans. Components, Hybrids Manuf. Technol.*, 4 (March 1981) 114.

P. K. Lee, High current brush material development. Part I: sintered metal coated graphite, *IEEE Trans. Components, Hybrids Manuf. Technol.*, 3 (March 1980) 4.

P. K. Lee and J. L. Johnson, High current brushes. Part II: effects of gases and hydrocarbon vapors, *IEEE Trans. Components, Hybrids Manuf. Technol.*, 1 (March 1978) 40.

R. A. Marshall and R. M. Slepian, Pulsed high power brush research. III: experiments at 15.5 MA/m^2 and 277 m/s, *IEEE Trans. Components, Hybrids Manuf. Technol.*, 2 (March 1979) 100.

R. A. Marshall, P. Reichner and R. M. Slepian, Current collection systems for pulse power homopolar machines, in *Proc. 7th Symp. on Engineering Problems of Fusion Research, Knoxville, TN, October 25 - 28, 1977*, Vol. I, in *IEEE Publ. 77CH1267-4-NPS*, pp. 434 - 438 (Institute of Electrical and Electronic Engineers).

I. R. McNab, Electric current transfer across sliding surfaces. In N. Suh and N. Saka (eds.), *Proc. Int. Conf. on Fundamentals of Tribology*, Science Press, Princeton, NJ, 1980, p. 333.

I. R. McNab, Recent advances in electrical current collection, *Wear*, 59 (1980) 259.

I. R. McNab and J. L. Johnson, Brush wear, in *ASME Centennial Wear Control Handbook*, American Society of Mechanical Engineers, New York, 1980, Chap. 33.

I. R. McNab and W. R. Gass, High current density carbon fiber brush experiments in humidified air and helium, *IEEE Trans. Components, Hybrids Manuf. Technol.*, 3 (March 1980) 26.

I. R. McNab and J. L. Johnson, High current brushes. Part III: performance evaluation for sintered silver-graphite grades, *IEEE Trans. Components, Hybrids Manuf. Technol.*, 2 (March 1979) 84.

I. R. McNab, Pulsed high power brush research, *IEEE Trans. Components, Hybrids Manuf. Technol.*, 1 (March 1978) 30.

I. R. McNab, Pulsed high power brush research. II: interpretation of experimental data. In E. K. Inall (ed.), *High Power High Energy Pulse Production and Application*, Australian National University Press, Canberra, 1978, p. 201.

I. R. McNab, Current conduction experiments with single carbon fibers, in *Proc. 13th Bienn. Conf. on Carbon, Irvine, CA, July 11 - 14, 1977*.

E. Rabinowicz and P. Chan, Wear of silver graphite brushes against various ring materials at high current densities, in *Proc. Conf. Electrical Contacts, 1978*, Illinois Institute of Technology, Chicago, IL, 1979, p. 123.

P. Reichner, Graphite function in composite brush materials, in *Extended Abstracts 15th Bienn. Conf. on Carbon, University of Pennsylvania, Philadelphia, PA, June 22 - 23, 1981*, pp. 320 - 321.

P. Reichner, High current tests of metal fiber brushes, *IEEE Trans. Components, Hybrids Manuf. Technol.*, 4 (March 1981) 2.

6

P. Reichner, Brush contact on eccentric slip rings, *IEEE Trans. Power Appar. Syst.*, *100* (1) (1981) 281.

P. Reichner, Pressure–wear theory for sliding electrical contacts, *IEEE Trans. Components, Hybrids Manuf. Technol., 4* (1981) 45.

P. Reichner, Metallic brushes for extreme high current applications, *IEEE Trans. Components, Hybrids Manuf. Technol., 3* (March 1980) 21.

P. Reichner and O. S. Taylor, Shunts for high current density brushes, *IEEE Trans. Components, Hybrids Manuf. Technol., 2* (March 1979) 89.

J. Schreurs, J. L. Johnson and I. R. McNab, Characterization of thick films formed on slip rings during high current density operation, *IEEE Trans. Components, Hybrids Manuf. Technol., 4* (March 1981) 30.

J. Schreurs, J. L. Johnson and I. R. McNab, High current brushes. Part VI: evaluation of slip ring surface films, *IEEE Trans. Components, Hybrids Manuf. Technol., 3* (March 1980) 83.

B. Singh and R. W. Vook, *In situ* AES characterization of rotating electrical contacts, *IEEE Trans. Components, Hybrids Manuf. Technol., 4* (March 1981) 36.

B. Singh, R. W. Vook and E. A. Knabbe, AES study of sulphur segregation on polycrystalline copper, *J. Vac. Sci. Technol., 17* (1980) 29.

B. Singh and R. W. Vook, Interfacial characterization of copper slip ring wire brush contacts, in *Proc. 8th Int. Vacuum Congr., Cannes, September 1980*, Vol. II, in *Vide, Couches Minces, Suppl., 201* (1980) 441.

R. M. Slepian, High current brushes. V: subdivided monolithic brushes at very high current levels, *IEEE Trans. Components, Hybrids Manuf. Technol., 3* (March 1980) 56.

O. S. Taylor, A solid brush system as a 1.5×10^6 ampere make switch, in *Extended Abstracts 15th Bienn. Conf. on Carbon, University of Pennsylvania, Philadelphia, PA, June 22 - 23, 1981*, pp. 322 - 323.

O. S. Taylor and P. Reichner, Mechanical load aspects of high current brush system design, *IEEE Trans. Components, Hybrids Manuf. Technol., 2* (March 1979) 95.

R. W. Vook *et al.*, Elemental surface composition of slip ring copper as a function of temperature, *IEEE Trans. Components, Hybrids Manuf. Technol., 3* (March 1980) 9.

Note added in proof. A fiber brush projectile has recently been accelerated to over 4 km s^{-1} while it transferred a current of more than 2 MA.

IN SITU AUGER ELECTRON SPECTROSCOPY CHARACTERIZATION OF WET-CO₂-LUBRICATED SLIDING COPPER ELECTRICAL CONTACTS*

B. H. HWANG, B. SINGH, R. W. VOOK and J. G. ZHANG

Department of Chemical Engineering and Materials Science, Syracuse University, Syracuse, NY 13210 (U.S.A.)

Summary

The electrical contact resistance, elemental surface composition and friction of an OFHC copper slip ring rotating in contact with two high purity copper wire brushes on different tracks were investigated *in situ* for heavy and light normal contact forces under a wet CO_2 environment at atmospheric pressure. Scanning electron microscopy was also used to characterize the slip ring and brush surfaces. Previous work in ultrahigh vacuum showed that, as rotation proceeded, interfacial impurities were almost totally removed and the electrical contact resistance decreased until cold welding occurred. In the present work, the slip ring surface was sputter cleaned (more than 95% Cu) before contact rotation and was only slightly contaminated after rotating in wet CO_2. Both the contact resistance and the friction decreased quickly and reached steady state values almost simultaneously in the early stages of rotation. Also, cold welding phenomena did not occur. Scanning electron micrographs taken after each experiment showed that the surfaces of the slip ring tracks and the brush wire ends were much rougher when heavy normal contact forces were used than in the light normal force condition. All these results confirm that wet CO_2 is an effective lubricant for Cu–Cu electrical sliding contacts.

1. Introduction

Most previous studies of electrical contact phenomena have been carried out under normal atmospheric conditions. Recently, however, it has been found that the electrical and mechanical properties of rotating electrical contacts can be strongly influenced by the gaseous environment in which

---

8

they operate [1 - 3]. One particularly auspicious environment is wet CO_2 at atmospheric pressure. Not only does it give rise to low values of friction and wear but it also permits the flow of high currents across the interface [4]. In the present work, this environment was used in a study of the interface between a copper wire brush and a rotating copper slip ring across which a high current flowed. The elemental composition of the surface of the slip ring was measured *in situ* with Auger electron spectroscopy (AES) as a function of exposure and the number of rotations in contact with the brush. Similarly, measurements of electrical contact resistance and friction were made. The surfaces of both the brushes and the slip ring were examined subsequently by scanning electron microscopy (SEM). Both high and low normal contact forces were used in the experiments. The results were different from those carried out earlier under ultrahigh vacuum (UHV) conditions in several significant ways [5].

2. Experimental details

Figure 1 shows a block diagram of the complete experimental system. A stainless steel UHV system was used to investigate the electrical contact phenomena associated with the rotation of a copper slip ring in contact with two copper wire brushes running on different tracks. Residual pressures in the low (10^{-9} Torr) range were obtained in the baked system. The brushes are pressed against the slip ring by means of an electrically insulated stainless
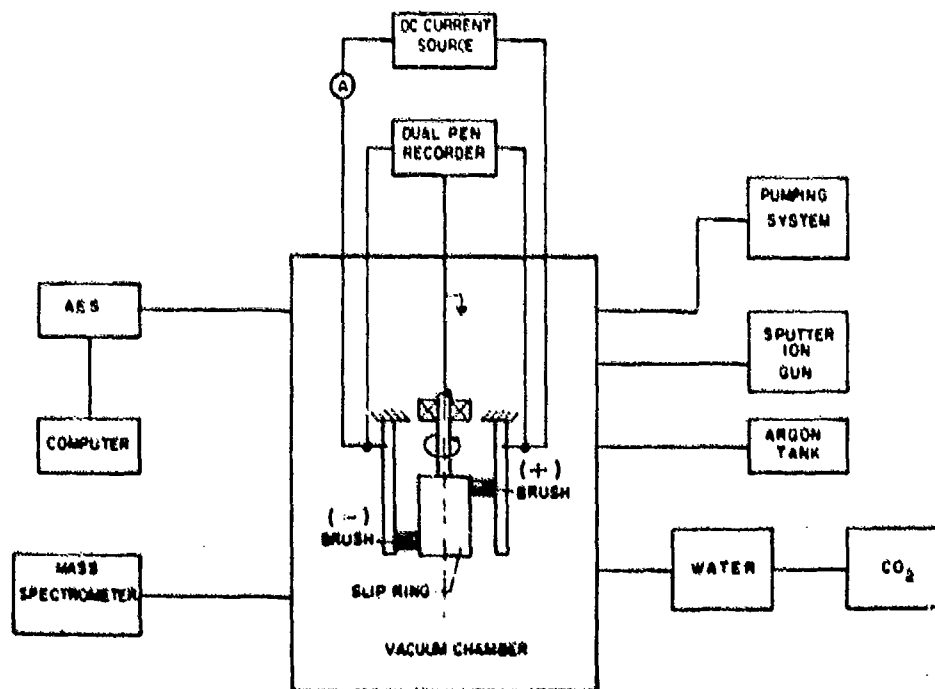
Fig. 1. Block diagram of UHV system and attachments for the electrical sliding contact experiments.

steel spring. They can be removed from contacting the slip ring surface by manipulating two linear–rotary vacuum feedthroughs. The slip ring is axially attached to a magnetically coupled rotary feedthrough which is turned by an a.c. motor coupled to it by a rubber belt. The slip ring is a cylinder (diameter, 1 in) of OFHC (99.98%) copper and the brushes each consist of 362 copper wires (wire diameter, 0.005 in; 99.999% Cu). The whole brush–slip ring assembly is mounted on a specimen manipulator capable of x,y,z displacements. The UHV system also contains an Auger cylindrical mirror analyzer, a 3 keV sputter ion gun and a 90° magnetic sector partial pressure analyzer. The details of the slip ring–brushes assembly, UHV system and AES measurements were given previously [5 - 7].

The surfaces of the slip ring and wire brushes were polished smooth with emery paper (grit 600-A), rinsed in acetone and ethanol, and then cleaned in an ultrasonic bath for 30 min before being put in the vacuum system. After the system was baked and pumped to a 5×10^{-9} Torr pressure, Auger spectra were taken from the contaminated slip ring surface (less than 50% Cu). Argon was then introduced into the vacuum chamber through the leak valve to a pressure of $(1 - 2) \times 10^{-5}$ Torr and the slip ring surface was sputter cleaned for 2.5 h with a primary electron beam setting of 3000 V and 30 mA. Subsequent AES measurements showed that the slip ring surface was almost completely cleaned (more than 99% Cu in the center region of the bombarding ion beam).

Wet CO_2 at atmospheric pressure was obtained by allowing the gas to flow through a distilled-water trap and then into the vacuum chamber via a vacuum leak valve. The detailed procedures will be reported elsewhere [8]. The rotating electrical contact experiment was then performed with a current of 30 A running through the contact interfaces. An angular velocity of about 150 rev min^{-1} was used. During the experiment, the slip ring was electrically grounded by means of thick copper wires sliding on the stainless steel axis, the neutral contact. The contact resistances between (1) the lower brush and slip ring and (2) the upper brush and slip ring were recorded on a dual-pen recorder. The rotational speed of the slip ring was measured with an optical tachometer together with the input power to the motor. The frictional force was determined from the calibrated decrease in rotational speed of the slip ring [9]. Then the ratio of the frictional force to the sum of the measured normal contact forces on both brushes gave the friction coefficient μ.

After 10 min of rotation, the brushes were retracted and the wet CO_2 was pumped out. AES spectra of the contact surfaces were taken when a residual gas pressure in the 10^{-8} Torr range was achieved after at least 30 h of pumping. Subsequent sputtering was carried out and AES spectra were taken alternately at regular intervals to obtain the concentration depth profiles of the elements on the slip ring surface. After the experiment was over, the slip ring and brushes were removed from the vacuum chamber. SEM pictures were taken of both the lower and the upper surface tracks and also of the brush contact surfaces.

3. Results

3.1. Contact resistance and friction measurements

The coefficients of friction and the electrical contact resistances of both the lower and the upper interfaces for two different experiments are shown in Fig. 2. Both experiments were carried out under similar conditions except for different contact forces. During rotation, a direct current of 30 A (approximately 4200 A in^{-2}) ran through the contacts. The subscripts s, w, u, l in Fig. 2 denote strong spring, weak spring, upper interface and lower interface respectively, e.g. R_{wl}(27 gf) denotes the electrical resistance of the lower interface in the weak spring experiment. 27 gf is the corresponding normal contact force. Contrary to the corresponding experiments carried out in UHV [9], the coefficients of friction in the present experiments decreased with increasing number of slip ring revolutions until steady state values were obtained. Although the electrical contact resistances of the lower and upper interfaces in the present experiments decreased with increasing number of slip ring revolutions, as in the UHV experiments, they reached their steady state values more rapidly and remained stable without adhesion in the former case. This stability and lack of cold welding demonstrated the lubricating function of wet CO_2. In addition, the resistance curves were more or less parallel to each other,
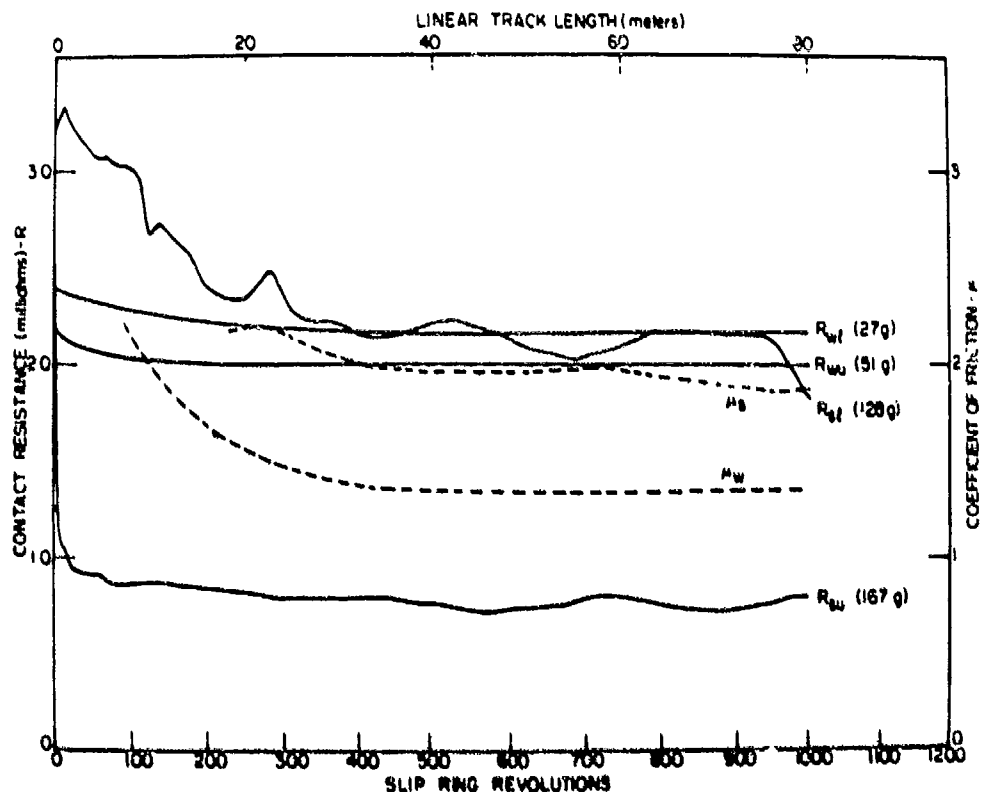
Fig. 2. Electrical contact resistances and coefficients of friction vs. number of slip ring revolutions under 1 atm of wet CO_2 and a 30 A brush current (4.2 kA in^{-2} (654 A cm^{-2})): the notation is discussed in the text.

indicating that the initial conditions determined whether a curve was "low" or "high". These initial conditions include such variables as brush orientation, stiffness and contact force. In the latter case a higher contact force always resulted in a lower contact resistance, as expected.

3.2. Auger electron spectroscopy

The elemental compositions of the lower track (track 1), upper track (track 2) and neutral track (track 0, which is between tracks 1 and 2) of the slip ring surface before sputtering, after sputtering and after running in wet CO_2 for the strong and weak spring experiments are listed in Table 1. The elemental balances in Table 1 mainly consisted of chlorine and nitrogen. The slip ring surfaces for both experiments were initially largely covered by impurities. With the ion sputter gun aimed at the neutral track region, *i.e.* between tracks 1 and 2, very clean surfaces were obtained for all three tracks in the weak spring experiment. In the strong spring experiment similar cleaning effects were observed after sputtering, but somewhat more impurities remained on track 1 and the neutral track regions because the ion gun had been aimed at track 2 instead.

After running in wet CO_2, the slip ring surfaces became contaminated only slightly (Table 1). The major contaminants were carbon and sulfur. It should be noted also that the contamination in the near-surface region is less serious in the strong than in the weak spring experiment. Figures 3 and 4 show the elemental depth profiles of sulfur and carbon on the slip ring after running in 1 atm of wet CO_2. The order of taking AES spectra was track 2, neutral and track 1. The impurities on the neutral track generally were more easily sputtered away because they were only adsorbed on the surface of the slip ring. The impurities on tracks 1 and 2, however, took a longer time to be sputtered away because they were buried in the near-surface region of the copper substrate by the mechanical mixing action of the brushes. For example, in Fig. 4, it took four times as long for the carbon concentration to reach the initial (or "background") level for track 2 than for the neutral track. It should be noted also from Table 1 and Figs. 3 and 4 that the mechanical mixing of impurities in the near-surface region by the brushes is more significant when there are *light* loads on the brushes.

A separate experiment was carried out to examine the high concentration of sulfur on the slip ring surface after rotating in wet CO_2. A very pure flat copper specimen (99.9999% Cu) was cleaned and mounted on the manipulator in the UHV chamber. The system was evacuated and the copper specimen was cleaned by sputter ion etching. It was then exposed to 1 atm of wet CO_2, which was then pumped out. Although all measurements and experimental processes took place at room temperature without any mechanical disturbance of the surface, the sulfur concentration on the flat specimen surface was found to be about the same (about 5 at.%) as that of the slip ring surface after rotating in contact with two brushes in 1 atm of wet CO_2 (Table 1). Clearly, the extra amount of sulfur on the surfaces of both the flat specimen and the slip ring came from an impurity in the

TABLE 1

Elemental compositions of slip ring tracks before sputtering, after sputtering and after rotating in wet CO_2 (and 30 h of pumping) for the strong and weak spring experiments

| | Track | Concentration on slip ring[a] (at.%) | | | | | |
| | | Strong spring | | | Weak spring | | |
		Before sputtering	After sputtering	After rotating in wet CO_2	Before sputtering	After sputtering	After rotating in wet CO_2
Cu	1	48.4	83.6	93.3	39.9	99.4	88.0
	0	29.8	95.8	91.8	45.7	99.1	89.3
	2	16.9	99.0	93.3	49.8	99.7	88.8
S	1	0.0	0.1	4.5	0.0	0.0	4.7
	0	0.0	0.1	3.2	0.0	0.2	5.0
	2	0.0	0.1	4.8	0.0	0.0	5.2
C	1	35.3	12.9	2.2	40.9	0.6	7.3
	0	59.7	3.6	4.7	39.3	0.5	5.5
	2	68.9	0.6	1.6	35.1	0.2	5.6
O	1	15.6	3.3	0.0	14.2	0.0	0.0
	0	10.4	0.3	0.2	12.9	0.0	0.1
	2	14.2	0.2	0.1	11.4	0.1	0.2
Balance	1	0.7	0.1	0.0	5.0	0.0	0.0
	0	0.1	0.2	0.1	2.1	0.2	0.1
	2	0.0	0.1	0.2	3.7	0.0	0.2

[a] Accuracy, ± 0.1 at.%.
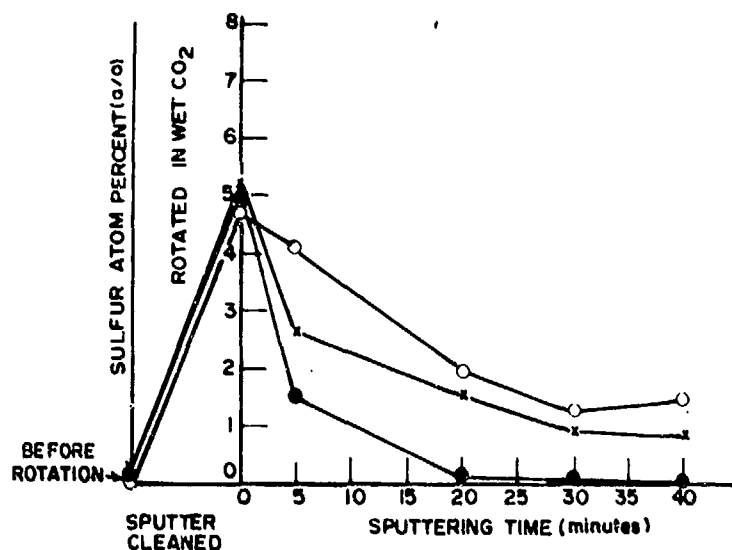
Fig. 3. Sulfur concentration depth profile on slip ring surface after rotating in wet CO_2 (weak spring condition): ○, track 1; ✕, track 2; ●, neutral.
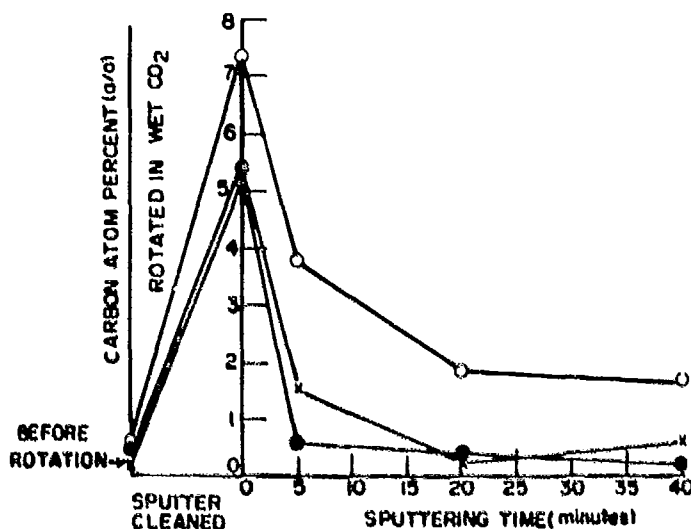
Fig. 4. Carbon concentration depth profile on slip ring surface after rotating in wet CO_2 (weak spring condition): ○, track 1; ✕, track 2; ●, neutral.

CO_2 gas and not as a result of segregation from the bulk of the copper sample [7].

3.3. Scanning electron microscopy

SEM pictures of slip ring tracks and brush wire ends for both the strong and the weak spring experiments were taken after the experiments were over and the manipulator was taken out of the vacuum chamber. Figures 5 and 6 show the brush wire ends after each experiment. Clearly, the contact surface of the brush wire end in the weak spring experiment is much smoother than that in the strong spring experiment. The rough region of the brush wire in Fig. 6 was produced by the initial emery paper polishing
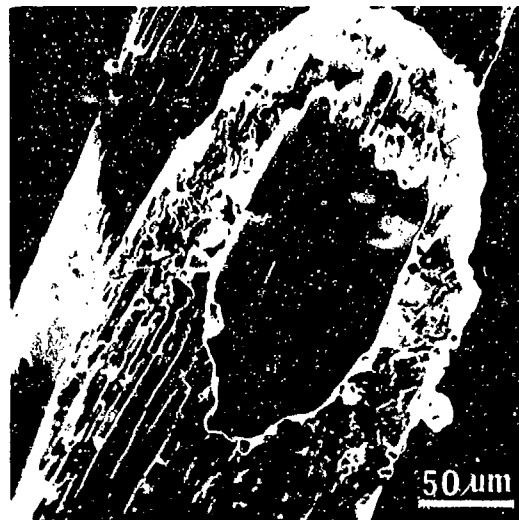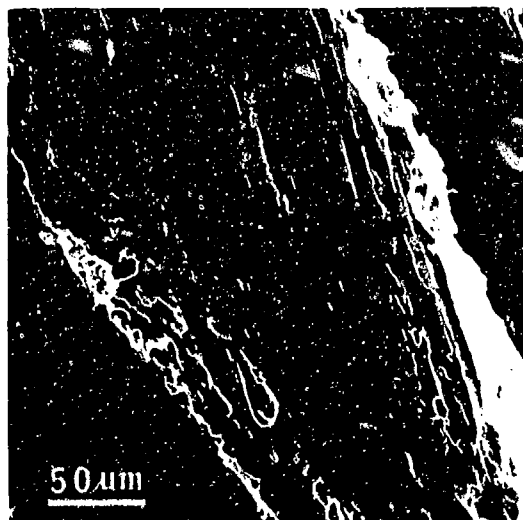
14

Fig. 5. SEM micrograph of a single brush wire end after sliding contact in wet CO_2 (strong spring condition; lower brush negative).

Fig. 6. SEM micrograph of a single brush wire end after sliding contact in wet CO_2 (weak spring condition; upper brush positive).
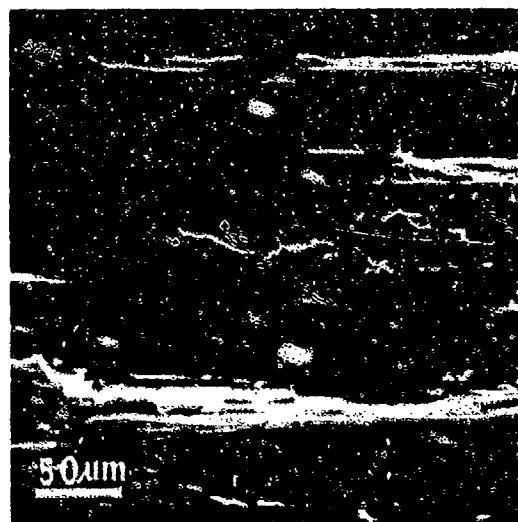
Fig. 7. SEM micrograph of a slip ring track after sliding contact in wet CO_2 (strong spring condition; lower track).

Fig. 8. SEM micrograph of a slip ring track after sliding contact in wet CO_2 (weak spring condition; lower track).

before insertion in the UHV chamber. It apparently did not touch the slip ring during rotation. In contrast, the brush wire end in Fig. 5 shows a smoother surface and longer ridges compared with the rough region in Fig. 6. This surface resulted from frictional contact during rotation. Figures 7 and 8 show SEM pictures of slip ring tracks after the strong and weak spring experiments respectively. Obviously the size of the ridges in the surface of the slip ring track is much smaller in the weak than in the strong spring experiment.

These results dramatically show that the normal contact force plays an important role in determining the properties of a rotating electrical contact: the smaller the normal contact force, the lower the contact frictional force and consequently the smoother the contact interface.

4. Discussion

In these experiments an initially clean copper slip ring rotated in electrical and mechanical contact with two copper wire brushes through which a current of approximately 4200 A in^{-2} flowed. Rotations were made in a UHV system that had been back filled with wet CO_2 at a 1 atm pressure. Both strong and weak normal forces were applied to the brushes in successive experiments. The results show that, except for a slight contamination with sulfur, rotation in wet CO_2 does not contaminate the surface of the slip ring. Since the surface remained essentially clean, the lubricity of the thin film at the interface must be due only to the H_2O and CO_2 molecules that are present.

In previous experiments carried out in UHV [5, 7], it was shown that the interface became much cleaner as the copper brush rotated over the copper slip ring. The present results in wet CO_2 are consistent with the earlier result. In addition, it was found that weak contact forces resulted in greater near-surface–bulk mixing of surface contaminants than stronger springs. This interpretation follows from the Auger depth profile studies. We can conclude that the greater penetration of the brush asperities into the bulk of the slip ring in the case of a stronger normal force is less effective in distributing the contaminants in the near-surface region.

It was also found that during rotation the adsorbates were pumped off in less than 30 h. This result means that they were not very tightly bound to the copper surfaces. We could not examine the surfaces by AES in a much shorter time because of the high residual gas pressure in the vacuum system. These results are consistent with the known desorption energies of water on metal surfaces, which range from 22 to 24 kcal mol^{-1} [10]. Since the adsorption energy of CO_2 is much less than that of H_2O, it is expected that the H_2O molecule aids the adsorption of CO_2 during rotation.

The decreases in electrical contact resistance and friction during rotation presumably arise from an increase in the contact area as the asperities on the contacting faces are smoothened. This effect is most noticeable in the weak spring case where the normal forces were in the neighborhood of 30 - 50 gf. Because cold welding did not occur in the wet CO_2 case, as observed in UHV, the H_2O–CO_2 molecules must form a more or less continuous layer at the slip ring–brush interface. If this layer were broken, localized cold welding would occur. Presumably, the higher friction in the case of higher normal forces arises from the partial fracture of this H_2O–CO_2 layer. It is also expected that, on the basis of this model, the thickness of the H_2O–CO_2 interfacial layer would depend on the contact pressure. The electrical con-

tact resistance measurements support this view. In all cases the higher normal force has the lower contact resistance. It is expected that the interfacial resistance arises from a combination of quantum mechanical tunneling through the CO_2-H_2O layer as well as occasional erratic direct brush–slip ring cold welding, resulting in the fracture of surface regions from the bulk and concomitant wear. It is therefore clear from these studies that the film resistance at a Cu–Cu interface is not due to contamination by carbon, organic impurities etc. but rather arises from the presence of this thin H_2O-CO_2 layer at the interface.

Acknowledgments

References

1 J. L. Johnson and O. S. Taylor, High current brushes. Part IV: machine environment tests, in *Proc. Conf. on Electrical Contacts, 1979*, Illinois Institute of Technology, Chicago, IL, 1979, pp. 129 - 135.

2 P. Reichner, Metallic brushes for extreme high current applications, in *Proc. Conf. on Electrical Contacts, 1979*, Illinois Institute of Technology, Chicago, IL, 1979, pp. 191 - 197.

3 I. R. McNab and W. R. Gass, High current density carbon fiber brush experiments in humidified air and helium, in *Proc. Conf. on Electrical Contacts, 1979*, Illinois Institute of Technology, Chicago, IL, 1979, pp. 159 - 163.

4 J. Schreurs, J. L. Johnson and I. R. McNab, High current brushes. Part VI: evaluation of slip ring surface films, in *Proc. Conf. on Electrical Contacts, 1979*, Illinois Institute of Technology, Chicago, IL, 1979, pp. 145 - 151.

5 B. Singh and R. W. Vook, *In situ* AES characterization of rotating electrical contacts, in *Proc. Conf. on Electrical Contacts, 1980*, Illinois Institute of Technology, Chicago, IL, 1980, pp. 53 - 58.

6 R. W. Vook, B. Singh, E.-A. Knabbe, J. H. Ho and D. K. Bhavsar, in *Proc. Conf. on Electrical Contacts, 1979*, Illinois Institute of Technology, Chicago, IL, 1979, pp. 17 - 21.

7 B. Singh, R. W. Vook and E.-A. Knabbe, AES study of sulfur surface segregation on polycrystalline copper, *J. Vac. Sci. Technol.*, 17 (1) (1980) 29 - 33.

8 B. Singh, B. H. Hwang and R. W. Vook, Characterization of copper slip ring–wire brush electrical contacts, *J. Vac. Technol.*, (1981) in the press.

9 B. Singh and R. W. Vook, Interfacial characterization of copper slip ring–wire brush contacts, in *Proc. 8th Int. Vacuum Congr.*, Vol. II, *Vacuum Technology and Vacuum Metallurgy*, in *Vide, Couches Minces, Suppl.*, 201 (1980) 441.

10 R. Glang, R. A. Holmwood and J. A. Kurtz, in L. I. Maissel and R. Glang (eds.), *Handbook of Thin Film Technology*, McGraw-Hill, New York, 1970, p. 2-44.

MICROSTRUCTURAL CHARACTERIZATION OF ROTATING Cu–Cu ELECTRICAL CONTACTS IN VACUUM AND WET CO_2 ENVIRONMENTS*

B. SINGH, J. G. ZHANG, B. H. HWANG and R. W. VOOK

Department of Chemical Engineering and Materials Science, Syracuse University, Syracuse, NY 13210 (U.S.A.)

(Received November 5, 1981)

Summary

The chemical, electrical and wear properties of the rotating interface between OFHC copper slip rings and two high purity copper wire brushes were investigated *in situ* in ultrahigh vacuum (UHV) and in 1 atm wet CO_2. The chemical composition of the slip ring surface was determined by Auger electron spectroscopy. The contact resistance was measured by a potentiometric four-point probe technique while the wear properties of the interface and the morphology of the debris were studied by frictional force, scanning electron microscopy (SEM), transmission electron diffraction (TED) and X-ray diffraction (XRD) measurements. Rotation in UHV of a conventionally cleaned (CC) slip ring produced a much cleaner surface. The contact resistance of both brush interfaces decreased and the frictional force increased with increasing number of revolutions. After many revolutions the brush and slip ring welded. The decrease in contact resistance with the number of slip ring revolutions more or less paralleled the decrease in total impurities. Rotation in wet CO_2 of a CC slip ring and brushes also produced much cleaner surfaces. In contrast, initially argon ion sputter-cleaned surfaces became slightly contaminated (mainly carbon and sulfur) when rotated. The contact resistance at both interfaces and the coefficient of friction decreased with increasing number of slip ring revolutions, finally reaching steady state values.

After each experiment, SEM examination of vacuum rotated surfaces showed deep ridges and broken pieces of material on the slip ring surface and badly deformed brush wire ends. Wet CO_2 rotated surfaces were relatively smooth and shallow ridges were seen. SEM examination of wear particles collected during rotation indicated that they may have come from both the slip ring and brush wire materials and were rolled in the regions between the brush and slip ring. XRD and TED from individual particles showed a randomly oriented polycrystalline microstructure. The particles collected from the wet CO_2 experiments were much smaller in size than those collected

---

in vacuum experiments. In wet CO_2, the contact resistance was interpreted as being predominantly due to an electron tunneling mechanism through the CO_2–H_2O molecular layer at the interface. As expected, the thickness of the layer appeared to vary with the contact pressure. Friction would then arise largely when the molecular layer was occasionally broken, allowing intimate contact and temporary welding of the brush and slip ring surfaces. Subsequent fracture of these welds during continued rotation would initiate the formation of wear particles.

---

1. Introduction

Over the last 20 years, considerable effort has been made theoretically [1, 2] and experimentally [3 - 5] to reduce friction, wear and contact resistance between dynamic interfaces. Attempts have hitherto been made to devise conditions to yield minimum contact resistance and minimum friction and wear between the brushes and slip ring. The brush and slip ring materials and the contact load and environment are the most influential parameters affecting these properties. There are various techniques and surface tools available for the study of the atomic nature of the wear surfaces [6]. In this paper, Cu–Cu dynamic contact interfaces are characterized in vacuum and in 1 atm of wet CO_2 by measuring contact resistance, frictional force, chemical composition and mechanical wear. A morphological and microstructural study of the debris formed during sliding contact provided important information about their origins and evolution. While there are various techniques [7, 8] available for a morphological analysis of the wear debris, the techniques of scanning electron microscopy (SEM), X-ray diffraction (XRD) and transmission electron diffraction (TED) were used in the present study.

2. Slip ring–brush arrangement and experimental procedure

The brush–slip ring arrangement has already been described in greater detail elsewhere [9, 10]. A stainless steel ultrahigh vacuum (UHV) system of low (10^{-10} Torr) range capability was used to characterize rotating electrical contacts. Figure 1 shows the arrangement of the copper slip ring which rotates in contact with two copper wire brushes. The slip ring is axially attached to a magnetically coupled rotary feedthrough, which is turned by an a.c. motor coupled to it by a rubber belt. The slip ring is of cylindrical shape, 2.5 cm in diameter, composed of OFHC (99.98%) copper. The brushes each consist of 362 99.999% Cu wires, each 0.127 mm in diameter. The brushes are clamped to two rectangularly shaped stainless steel electrodes, each having a smooth hinge in the middle. The brushes are arranged at 180° to each other, making an approximately 40° - 45° angle with the normal to the slip ring surface and axially displaced (1 - 1.5 cm) to make separate tracks on the slip ring. The
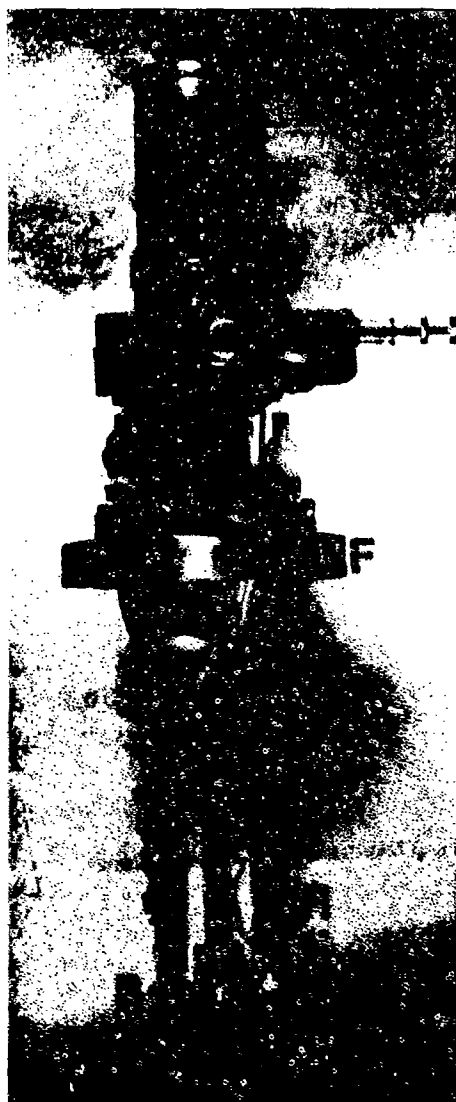
Fig. 1. Photograph of the slip ring–brush assembly: M, magnetically coupled rotary feedthrough; H, brush holder; R, slip ring; B, brush; S, spring; F, vacuum flange.

whole brush–slip ring assembly is mounted on a specimen manipulator capable of X, Y, Z displacements. The UHV system includes an Auger cylindrical mirror analyzer, a 3 keV sputter ion gun and a 90° magnetic sector partial pressure analyzer.

Before each experiment, the surfaces of the slip ring and the brush wire ends were mechanically polished with a series of emery papers ending with grit 600A and then rinsed ultrasonically (brush retracted) in acetone and ethanol. The contact resistances between the two brushes and the slip ring (grounded) were recorded on a dual-pen recorder. Experiments were performed with three brush direct currents: 50 mA, 5 A and 30 A in vacuum and 30 A in wet CO_2. With the brushes retracted, the speed of the rotating slip ring was monitored with an optical tachometer. During the experiment,

the rotational speed of the slip ring was measured at regular time intervals together with the input power to the motor.

The Auger electron spectrometer which was used to examine the surface tracks was fully controlled by a Hewlett Packard 9825A desktop computer and multiprogrammer. Typical Auger traces covering a 50 - 1300 eV range were directly digitalized with an energy increment of 0.65 eV or less. Computerized values of peak-to-peak heights of the Auger electron spectroscopy (AES) signals of various elements were obtained with a precision of 1 in 2000. These Auger spectra were taken using a primary beam energy of 3 keV, a modulation amplitude of 1 V (peak to peak) and a $25 \mu A$ beam current.

A wet CO_2 environment in the vacuum system was obtained by running CO_2 from the cylinders (commercial grade, 99.8%) through a doubly distilled H_2O-CO_2 solution in a stainless steel trap and finally through a UHV leak valve [11]. The pressure of wet CO_2 in the vacuum system during the course of the rotation experiments was approximately atmospheric. Auger spectra from the wet CO_2 rotated slip ring surface were taken only after the wet CO_2 was pumped down to the high 10^{-8} Torr region, a process which took about 2 days. A molybdenum sheet tray was placed inside the vacuum chamber under the brush—slip ring assembly to collect wear particles during contact rotation.

After the experiment was over, the slip ring assembly and wear debris were removed from the chamber. The normal force on each brush was measured. The average frictional force was determined from the decrease in rotational speed of the slip ring by comparing it with a calibration involving known torques applied to the slip ring in a separate experiment in air. SEM pictures were taken of both the slip ring surface tracks, brush contact surfaces and of wear particles. XRD photographs were obtained from relatively large particles (about 0.5 mm) and TED photographs were taken from small particles (about 0.05 mm or less).

3. Results

3.1. Contact resistance and friction measurements

Figure 2 shows the contact resistance for both the upper and the lower interfaces and the average coefficient of friction as a function of the number of slip ring rotations or linear track length covered. The contact resistance decreased with increasing number of slip ring revolutions. The curves are more or less parallel to each other, indicating that the initial conditions determine whether a curve is "high" or "low". These initial conditions include such variables as contact fo ce, lead resistance, brush wire orientation with respect to slip ring, surface impurities etc. The contact resistances in the wet CO_2 experiments are consistently higher than those in the vacuum experiments and result in much smoother curves. This high contact resistance could be due to the lower normal force, smaller contact area and the addi-
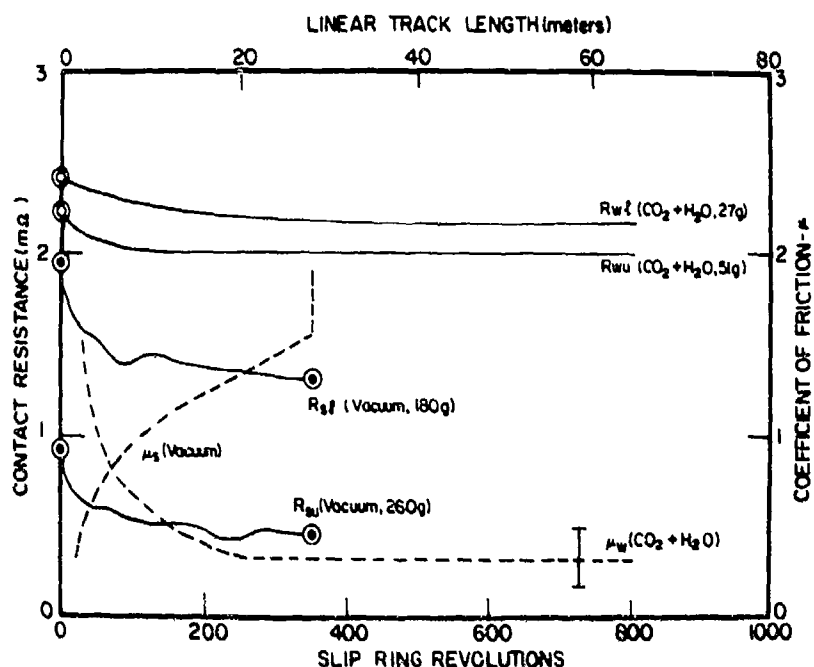
Fig. 2. Contact resistance and average coefficient of friction *vs.* number of slip ring revolutions. Subscripts s, w, u and l denote strong spring, weak spring, upper brush interface and lower brush interface respectively.

tional resistance introduced by the thin wet CO_2 layer at the interface. The circled points indicate the contact resistance before the slip ring started rotating and after it stopped. For wet CO_2, the slip ring rotation did not stop, but the experiment was terminated after about 5 - 10 min of rotation when the resistance attained steady state values. The resistance of the interfaces clearly depended on the magnitude of the contact force. In vacuum experiments, the frictional force increased substantially as the rotation proceeded and finally after many hundreds of revolutions the motor stopped rotating because of excessive friction and ultimate cold welding. The average coefficient μ of friction was calculated from the ratio of the frictional force to the measured normal force and is shown in Fig. 2 for both the vacuum and wet CO_2 experiments. For the vacuum experiment it increased by a factor of more than 4 while for wet CO_2 it decreased to about 0.35 where it remained relatively stable.

3.2. Auger electron spectroscopy measurements

In the vacuum experiments, the elemental surface compositions of both the upper and lower tracks on the slip ring were obtained by AES before and immediately after the contact resistance measurements. However, in the wet CO_2 experiments Auger spectra were taken about 2 days after the contact rotation because the system had to be pumped down to the high 10^{-8} Torr region before operating the Auger spectrometer. The brushes were retracted during the AES measurements and the slip ring was continuously rotated. This procedure gave the average impurity concentrations on the whole track.

TABLE 1

Elemental concentrations (at.%) on slip ring tracks for rotation in vacuum (contact force, 235 gf) and wet CO_2 (contact force, 51 gf)

Elements	Vacuum		Wet CO_2		
	Before rotation	After rotation	Before sputtering	After sputtering	After rotation
Cu	47.5	97.1	39.9	99.4	88.0
S	0.8	0.1	0.0	0.0	4.7
C	42.1	2.0	40.9	0.6	7.3
O	7.1	0.4	14.2	0.0	0.0
Balance (Cl, N, Ar)	2.5	0.4	5.0	0.0	0.0

The peak-to-peak heights of all Auger signals were normalized [12, 13] to atomic per cent concentrations. The elemental surface concentrations on the slip ring for two typical experiments in vacuum and wet CO_2 are given in Table 1. The copper, sulfur, carbon and oxygen concentrations are listed together with the impurity balance. In vacuum rotated experiments the conventionally cleaned (CC) interface became cleaner, while in the wet CO_2 experiments the sputter-cleaned interface became only slightly contaminated. The impurities picked up were sulfur and carbon. Argon ion sputter depth profiles of the slip ring surface showed that these impurities were rapidly removed by small amounts of ion etching.

To understand the cause of the high concentration of sulfur, an additional experiment was performed in which the brush–slip ring assembly was replaced by a flat OFHC copper sample. The sample was first sputtered clean (to 98 at.% Cu, 0.2 at.% S) and then heated to 585 °C for 30 min where 9 at.% of sulfur segregation was detected [14]. Sulfur was removed by argon ion sputter depth profiling techniques and its concentration was monitored as a function of sputtering time. After it was almost completely removed (0.2 at.%), the clean sample was exposed to 1 atm of wet CO_2, resulting in a surface concentration of 7 at.% of sulfur. The sulfur concentration was again removed by sputter depth profiling. The results are shown in Fig. 3. It is clear that the adsorbed sulfur is removed much faster than the bulk segregated sulfur. Thus the high concentration of sulfur on the slip ring surface was due to an impurity in the wet CO_2 supply and not to bulk segregation.

3.3. Scanning electron microscopy

After each experiment, the brush–slip ring assembly and wear particles collected during rotation were removed from the vacuum chamber and examined by SEM. For the same period of rotation, the quantity and size of the debris collected in vacuum experiments were larger than those in the wet CO_2 experiments. The average length of vacuum wear particles was about 0.3 - 0.5 mm while for wet CO_2 the length of the wear particles was about
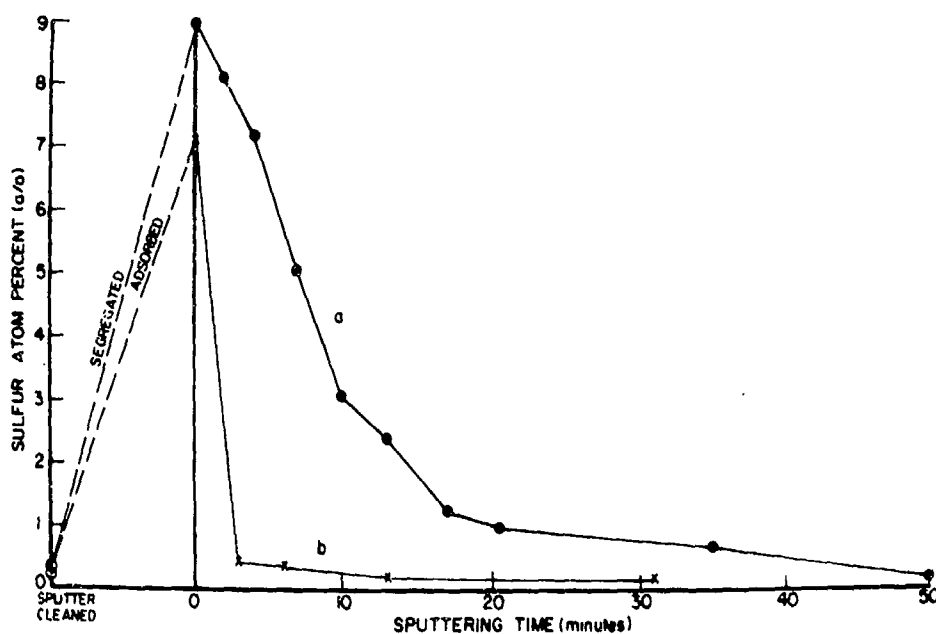
Fig. 3. Sputter depth profile of sulfur on a flat OFHC copper sample: curve a, segregated on heating at 585 °C for 30 min; curve b, adsorbed on exposure to 1 atm wet CO_2 at room temperature for 15 min.

Fig. 4. SEM photograph of copper wear particles collected during slip ring rotation in contact with brushes in wet CO_2.

Fig. 5. SEM photograph of copper wear particles collected during slip ring rotation in contact with brushes in wet CO_2.

0.03 - 0.08 mm. SEM photographs of several particles from the wet CO_2 experiments are shown in Fig. 4. Figure 5 shows details of the structure of two typical wear particles collected in a wet CO_2 experiment. The morphology of these particles suggests that they are rolled layers or rolled particles. Figure 6 shows a particle collected from a vacuum experiment. XRD was carried out on large individual particles by mounting them on a glass fiber and by using a transmission pinhole technique. The very small

24
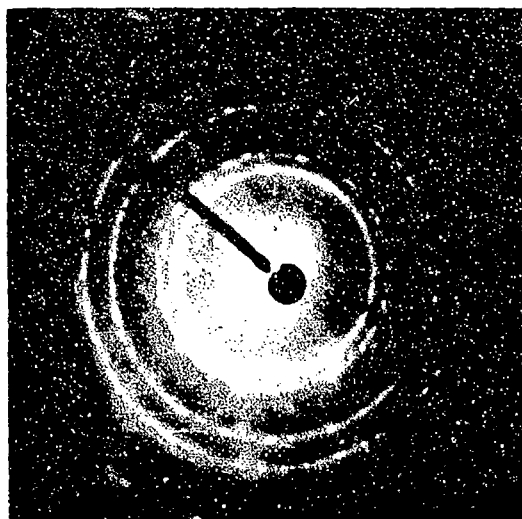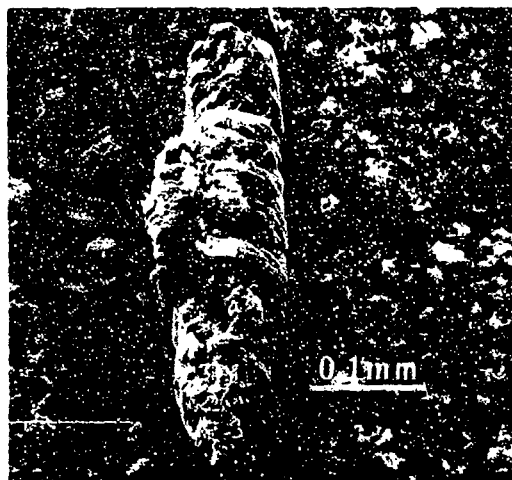
Fig. 6. SEM photograph of copper wear particle collected during slip ring rotation in contact with wire brushes in vacuum. Particles of silver paint on the substrate should be noted.

Fig. 7. TED photograph of a small wear particle collected while the slip ring rotated in contact with a wire brush in wet CO_2.
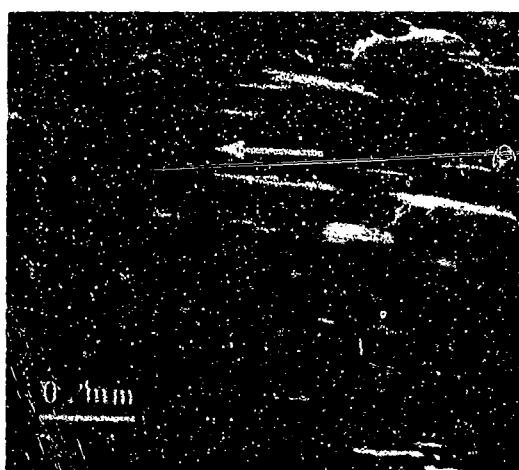
Fig. 8. SEM photograph of OFHC copper slip ring, upper track, showing broken wire pieces (W) and deep ridges. The arrow indicates the direction of relative brush motion (high vacuum).

Fig. 9. SEM photograph of OFHC copper slip ring, upper track, showing shallow ridges. The arrow indicates the direction of relative brush motion (wet CO_2).

particles were difficult to mount in such a way and therefore their individual diffraction patterns were studied by TED. The results from XRD studies of large particles were identical with those obtained by TED from small particles. Figure 7 shows a TED pattern obtained from a small particle. The absence of preferred orientation is apparent.

Figures 8 and 9 show typical SEM pictures of brush tracks on slip rings rotated in vacuum and in wet CO_2 respectively. The surface from the vacuum
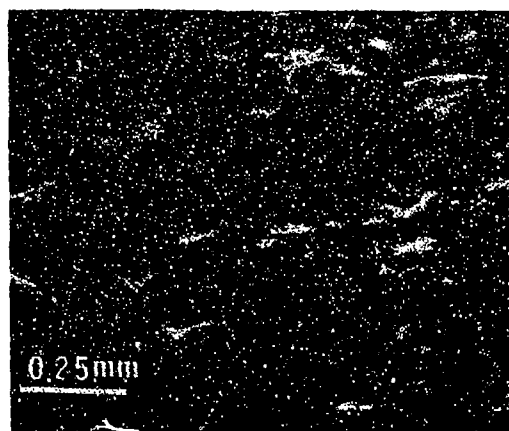
Fig. 10. SEM photograph of wear surfaces on upper brush copper wires (contact force, 235 gf). The arrow indicates the direction of relative motion of the slip ring (high vacuum).
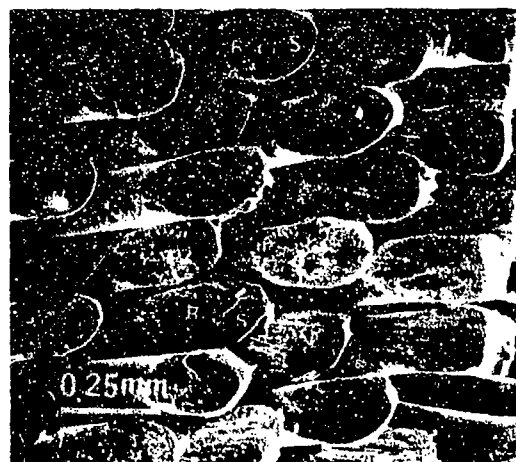
Fig. 11. SEM photograph of wear surfaces on upper brush copper wires (contact force, 51 gf). The arrow indicates the direction of relative motion of the slip ring (wet CO_2).

experiment shows deep grooves and high ridges and several pieces of brush wire wear particles adhering to the surface. The wet CO_2 rotated surface shows shallow grooves and low ridges with a few occasional deep ridges. Also, no wear particles are observable. The ridges shown in these micrographs lie parallel to the directions of travel. SEM pictures of brush ends are shown in Figs. 10 and 11 for vacuum and wet CO_2 experiments. The vacuum contact brush wire ends appear very rough and abruptly broken, while the wet CO_2 contact brush wire ends are much smoother and of round shape. In Fig. 11, two regions S and R are clearly seen on the wire ends. The smooth (S) regions touched the slip ring and the rough (R) and long streaked regions were produced by the initial emery paper polishing before insertion in the UHV chamber. These latter regions apparently did not touch the slip ring during rotation.

4. Discussion

The elemental surface compositions of OFHC copper slip rings that rotate in contact with two high purity copper wire brushes in vacuum and in 1 atm of wet CO_2 are presented. In vacuum, the initial CC surfaces (50 at.% Cu) became almost completely clean (98 at.% Cu) after several hundred rotations. Carbon was the major impurity observed. As the surface became cleaner with continued rotation, adhesion, friction and occasional cold welding started to develop. The occasional and erratic stick-slip resulted in large momentary fluctuations in the contact resistance. Finally the adhesion became so large that the motor rotating the slip ring could not overcome the frictional torque and cold welding occurred.

For rotation in wet CO_2, the surface also became clean except for the development of slight sulfur and carbon contamination. The studies involving a flat OFHC copper sample (see Section 3.2) suggest that the sulfur came from an impurity in the CO_2 gas and not as a result of bulk segregation [14]. The carbon concentration was of the same order as that observed in the vacuum experiments. Thus running in wet CO_2 contributed no additional carbon to the surface. In wet CO_2, the rotational speed of the slip ring increased and became steady after a few hundred rotations. Cold welding did not occur. These results indicated that the wet CO_2 environment provided good lubrication [3, 4]. The AES composition of the wet CO_2 surface was taken only when the wet CO_2 was pumped down to the 10^{-8} Torr region which usually took about 30 h. This result means that the H_2O-CO_2 mixture was not very tightly bound to the surface. It is well known that CO_2 is not chemisorbed on copper and its maximum heat of physical adsorption [15] on metals is about 9 kcal mol^{-1}. Water, in contrast, has a heat of adsorption of about 22 - 24 kcal mol^{-1} and is notoriously difficult to remove at room temperature [16]. Thus CO_2 is pumped out much faster than H_2O, which was also observed by the mass spectroscopy analysis of the residual gas. It is thus expected that the H_2O molecules aid in the adsorption of CO_2.

The thickness of the H_2O-CO_2 interfacial layer would be expected to depend on the contact pressure. This result is in agreement with the contact resistance measurements, where the higher normal forces have lower contact resistances. Thus the interfacial resistance appears to arise from a combination of quantum mechanical tunneling through the CO_2-H_2O layer as well as occasional direct brush–slip ring contact, resulting in adhesion and fracture of plastically deformed surface regions. The net effect is that wear particles are formed. A determination of the approximate layer thickness h can be made from an empirical relation [17] $R_f = \rho_t \xi H/F$, where ρ_t is the tunnel resistivity, $\xi \approx 0.7$ is a pressure factor and H is the contact or penetration hardness, based on a tunneling conduction mechanism together with an experimental relationship between ρ_t and h [18]. The results are approximate but indicate that the H_2O-CO_2 layer is about 6 Å thick for a 2.2 mΩ film resistance R_f and 80 gf normal force F. This result is reasonable since it implies a layer of CO_2-H_2O one to three molecules thick. The thickness of the layer also depends on the orientation of the molecules with respect to the substrate as well as with respect to each other. It is thus concluded that the contact resistance at the Cu–Cu interface in wet CO_2 is not due to contamination by carbon or other impurities, but rather arises from the presence of this H_2O-CO_2 layer at the interface. The low contact resistance in vacuum arises from direct metal–metal contact. It decreases during rotation because the initial surface impurities are buried during rotation or possibly partially removed by the fallen wear particles and also because the surface contact area increases.

Formation of the wear particles and the ridges on the slip ring surface are of much interest. In vacuum, deep ridges arise from brush end ploughing and/or random localized welding of brush wire ends to the slip ring during

rotation, resulting in tensile plastic deformation of the weld and then final fracture of the weld material or wire. Continued rotation may pull out some of these broken wire ends or material from the protruded ridges. These pieces then roll over between the brush–slip ring interface and eventually fall away from the interface. Clearly, the wear particles in the vacuum case would be larger in size than those produced on occasional localized metal–metal contact through the thin CO_2–H_2O layer where the weld area is likely to be smaller. This result is what has been observed experimentally. The average length of the vacuum wear particles is 0.3 - 0.5 mm and their diameter is 0.09 - 0.12 mm. The wet CO_2 wear particles have average lengths of 0.03 - 0.08 mm and diameters of 0.02 - 0.04 mm.

The morphologies of the wear particles are more or less the same. Some are made of thin layers rolled as sheets and some with more compacted but still rolled surfaces. There appears to be some relationship between the size of the wear particles, the ridges and the diameter of the brush wires. The average height of the broken wire pieces shown in Fig. 8 (vacuum) is about 0.09 - 0.13 mm, which is close to the diameter of the wires of the brush. It is thus reasonable to suppose that these pieces are parts of the broken wire which cold welded to the slip ring surface as it became cleaner in vacuum. In Fig. 9 (wet CO_2), the lengths of the well-defined ridges vary from about 0.02 to 0.2 mm. The estimated unfolded length of the layer making up the particle in the upper left corner of Fig. 5 is about 0.09 mm, which is within the range of the length of the ridges in Fig. 9. Therefore, it is possible that this particle originally came from the slip ring surface rather than from the wire of the brush. The variation in the length of the ridges could be due to variations in contact force at individual wire ends of the brush. The ridges may be formed by the ploughing action of the wire ends through the surface material of the slip ring. Continued rotation in the case of wet CO_2 tends to smooth these ridges, resulting in burnishing. The vacuum rotated surface has deep and sharp ridges because erratic cold welding prevented burnishing from occurring.

Acknowledgments

References

1 P. Reichner, Pressure–wear theory for sliding electrical contacts, *Proc. Conf. on Electrical Contacts, 1980*, Illinois Institute of Technology, Chicago, IL, 1980, pp. 25 - 32.

28

2 C. M. Adkins III and D. Kuhlmann-Wilsdorf, Development of high-performance metal fiberbrushes. II: testing and properties, *Proc. Conf. on Electrical Contacts, 1979*, Illinois Institute of Technology, Chicago, IL, 1979, pp. 171 - 186.

3 P. Reichner, Metallic brushes for extreme high current applications, *Proc. Conf. on Electrical Contacts, 1979*, Illinois Institute of Technology, Chicago, IL, 1979, pp. 191 - 197.

4 J. L. Johnson and O. S. Taylor, High current brushes. Part VI: machine environment tests, *Proc. Conf. on Electrical Contacts, 1979*, Illinois Institute of Technology, Chicago, IL, 1979, pp. 129 - 135.

5 E. Rabinowicz and P. Chan, Wear of silver–graphite brushes against various ring materials at high current densities, *Proc. Conf. on Electrical Contacts, 1979*, Illinois Institute of Technology, Chicago, IL, 1979, pp. 123 - 127.

6 D. H. Buckley, The use of analytical surface tools in the fundamental study of wear, *Wear, 46* (1978) 19 - 53.

7 J. K. Beddow, S. T. Fong and A. F. Vetter, Morphological analysis of metallic wear debris, *Wear, 58* (1980) 201 - 211.

8 A. W. Ruff, Characterization of debris particles recovered from wearing systems, *Wear, 42* (1977) 49 - 62.

9 B. Singh and R. W. Vook, *In situ* AES characterization of rotating electrical contacts, *Proc. Conf. on Electrical Contacts, 1980*, Illinois Institute of Technology, Chicago, IL, 1980, pp. 53 - 58.

10 B. Singh and R. W. Vook, Interfacial characterization of copper slip ring–wire brush contacts, *Proc. 8th Int. Vacuum Congr., Cannes*, Vol. II, *Vacuum Technology and Vacuum Metallurgy*, in *Vide, Couches Minces, Suppl., 201* (1980) 441 - 444.

11 B. Singh, B. H. Hwang and R. W. Vook, Characterization of copper slip ring–wire brush electrical contacts, *J. Vac. Technol.*, (1981) in the press.

12 C. C. Chang, Analytical Auger spectrometry. In P. F. Kane and G. B. Larrabee (eds.), *Characterization of Solid Surfaces*, Plenum, New York, 1978, pp. 509 - 561.

13 R. W. Vook, B. Singh, E.-A. Knabbe, J. H. Ho and D. K. Bhavsar, Elemental surface composition of slip ring copper as a function of temperature, *Proc. Conf. on Electrical Contacts, 1979*, Illinois Institute of Technology, Chicago, IL, 1979, pp. 17 - 21.

14 B. Singh, R. W. Vook and E.-A. Knabbe, AES study of sulfur surface segregation on polycrystalline copper, *J. Vac. Sci. Technol., 17* (1) (1980) 29 - 33.

15 G. Wedler, *Chemisorption: An Experimental Approach* (Engl. transl., D. F. Klemperer), Butterworths, Boston, 1976, pp. 198 - 204.

16 R. Glang, R. A. Holmwood and J. A. Kurtz, in L. I. Maissel and R. Glang (eds.), *Handbook of Thin Film Technology*, McGraw-Hill, New York, 1970, p. 2-44.

17 H. N. Wagar, in D. Baker, W. O. Fleckenstein, D. C. Koehler, C. E. Roden and R. Sabice (eds.), *Physical Design of Electronic Systems*, Vol. III, *Integrated Device and Connection Technology*, Prentice-Hall, Princeton, NJ, 1971, p. 465.

18 I. Dietrich, Messung des Widerstandes dünner isolierender Schichten zwischen Goldkontakten im Bereich des Tunneleffektes, *Z. Phys., 132* (1952) 231 - 238.

THE TEMPERATURE RISE AT SLIDING ELECTRICAL CONTACTS*

ERNEST RABINOWICZ

Department of Mechanical Engineering, Massachusetts Institute of Technology, Cambridge, MA 02139 (U.S.A.)

(Received November 5, 1981)

Summary

The equations for the temperature rise due to ohmic heating at stationary electric contacts and to frictional heating at sliding electric contacts are combined to give closed-form equations for the temperature rise of sliding electric contacts. The relationship applicable at high sliding speeds indicates that in many cases increasing the sliding speed can reduce the interfacial temperature. An experimental program has been carried out to test the applicability of the equation, using wear tests carried out on graphite–Cu sliding systems in a high temperature friction apparatus to determine the relationship between wear coefficient and surface temperature. Tests using a graphite brush sliding against a copper disk at speeds of around 10 m s^{-1} show that the wear increases with current density, and application of the temperature equation confirms that the wear coefficient is determined by the interfacial temperature, whether that temperature is produced by bulk heating in a furnace, by interfacial heating as a result of sliding or as a result of ohmic heating of the interface.

1. Introduction

In sliding electric contacts carrying very high currents, one of the obvious limitations to the transmittal of even higher currents results from interfacial heating. If the temperature at the interface becomes too great, the materials may soften or even melt, or else excessive oxidation may occur. Associated with effects such as these there is likely to be excessive wear.

In spite of the obvious importance of interfacial heating in the operation of sliding electric contacts, it does not seem that equations for the interfacial temperature of sliding current-carrying contacts are in regular use, nor

are the way that variables such as velocity or load affect the temperature well known. It is the purpose of this paper to derive such expressions, to illustrate their application to a simple graphite–Cu sliding system and then to test the correctness of the expression experimentally.

2. Theoretical background

The theoretical analysis of the temperature rise at contacting surfaces is generally based on the work of Blok [1] and Jaeger [2], and the relationships obtained by these workers have been discussed and applied to the problem of the temperature rise caused by friction by Archard [3] and Rabinowicz [4]. The temperature rise of electric contacts, especially the static case, has been discussed by Holm [5 - 7], and Shobert [8] has considered also the case of sliding contacts.

Taking first the situation where slow speed sliding occurs and heating is caused by friction, it turns out that if there is a circular region of contact between the sliding surfaces (Fig. 1), the average temperature rise θ is given by the relationship

$$\theta = \frac{fLv}{4Jr(k_1 + k_2)} \tag{1}$$

where J is the mechanical equivalent of heat (a conversion factor from thermal to mechanical units of heat), r is the radius of the junction, f is the friction coefficient, L is the normal load at the junction, k_1 is the thermal conductivity of body 1, k_2 is the thermal conductivity of body 2 and v is the velocity.
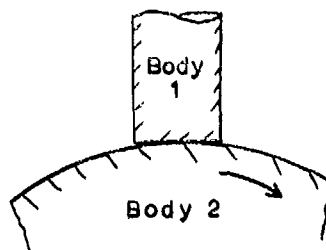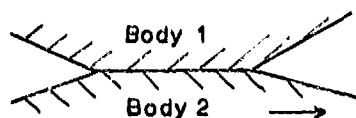
Fig. 1. Schematic illustration of a junction or contact between two solid bodies.

Fig. 2. The system analyzed at high sliding speeds considers a small body 1 always in contact with a large body 2. Points in body 2 only make contact periodically.

This relationship (ref. 9, eqn. (4.14)) assumes that heat originates at the interface and is then conducted into the two adjacent bodies. The reason why the temperature rise is proportional to the velocity is because the rate of heat generation per unit of time is itself proportional to the velocity.

When the sliding speed becomes large this relationship is no longer applicable. Let us consider the simplest case when body 1 is a small specimen while body 2 has an extended surface. In that case the small specimen will be continually in contact and will slide always over fresh areas of the large specimen (Fig. 2). For that case the temperature rise is given by

$$\theta = \frac{fLv^{1/2}}{3.6J(\rho_2 c_2 r^3 k_2)^{1/2}} \tag{2}$$

where f, L, v, r, J and k_2 have the same definitions as above and $\rho_2 c_2$ is the volume specific heat of the extended surface.

This relationship (ref. 9, eqn. (4.16)) differs from the previous one in two ways. First, it is unsymmetrical as regards the top and bottom surfaces because the top surface, being small and continually in contact, soon becomes hot, while the bottom surface, being always fresh, is much cooler, so essentially all the heat travels into it and thus only its thermal properties are significant.

Secondly, it will be noted that velocity to the power one-half comes into eqn. (2). This comes about because as we raise the speed we increase the rate of heating, but we also increase the amount of cool bottom material into which this heat can be dissipated. Thus, it is logical to expect that the temperature rise increases with v but less rapidly than to the first power.

In general, eqn. (1) is applicable when a certain dimensionless parameter $vr\rho_2 c_2/k_2$ is less than 2, while eqn. (2) is applicable when the parameter is greater than 2 [3].

So far we have considered only the frictional heating. As regards electrical heating, Holm (ref. 6, eqn. (11)) states that for a stationary junction the temperature rise (using our terminology) is given by

$$\theta = \frac{i^2 R}{4Jr(k_1 + k_2)} \tag{3}$$

where i is the current carried by the junction and R is the electric resistance of the junction.

This is very similar to the low speed friction temperature rise expression (eqn. (1)) except that $i^2 R$, the electrical heat input per unit of time, has replaced fLv, the mechanical heat input per unit of time. Holm (ref. 7, Section 43) argues that the expression for θ in eqn. (3) should be reduced by a factor of about 2, because the heat input is throughout the constriction (i.e. to some extent away from the interface rather than being localized at the interface). However, there are in practice a large number of uncertainties involved. All sorts of corrections might be applied, and it seems best to keep eqn. (3) as simple as possible.

If we add the mechanical and electrical temperature rise terms we have for the overall temperature increase in the slow speed regime

$$\theta = \frac{fLv + i^2 R}{4Jr(k_1 + k_2)} \tag{4}$$

It is this expression which (although never stated in closed form) is implicitly assumed by Holm and by Shobert.

If we are in the high speed regime then by adding the electrical heating term to eqn. (2) we obtain

$$\theta = \frac{fLv + i^2 R}{3.6J(r^3 k_2 \rho_2 c_2 v)^{1/2}} = \frac{1}{3.6J(r^3 k_2 \rho_2 c_2)^{1/2}}\left(fLv^{1/2} + \frac{i^2 R}{v^{1/2}}\right) \tag{5}$$

In this case the influence of velocity on the temperature is difficult to estimate, since a higher velocity will increase the temperature caused by friction (the first term in parentheses in eqn. (5)) while it will reduce the electrical heating effect (the second term in parentheses in eqn. (5)). Since most tribologists find it hard to believe that raising the sliding speed can lower the interfacial temperature, it seemed appropriate to test eqn. (5) experimentally.

There are some difficulties in measuring the temperature of sliding electric contacts over and above the problems of measuring the interfacial temperature of sliding bodies in general. In particular, the use of the interface as the hot junction of a thermocouple system, often used successfully in friction studies [10], is of course impossible. It was decided to use the fact that in many sliding systems the wear rate increases rapidly when the interfacial temperature reaches a critical point known as the transition temperature, and that this can be used as a measure of the temperature.

3. Experimental testing

3.1. In high temperature friction apparatus

Tests were carried out in the friction apparatus shown in Fig. 3. Three pieces of one material are pressed against a disk of the other material which rotates via the motor and transmission system. The sliding surfaces are inside a metallurgical-type furnace which can be heated up to 1000 °C. The three pieces are loaded by a dead weight and prevented from rotation by a strain ring outside the furnace. The apparatus has been described more completely elsewhere [11].

For these tests, rods of electrographite of 9 mm diameter were slid against a copper disk. The speed of sliding was kept low (0.41 m s^{-1}) so as to keep the temperature rise due to sliding small. The normal load was 1/kgf per rod and the duration of the tests was 0.5 h. Most of the testing was in air, in the spring (i.e. at a reasonably high humidity level). Tests in a wet CO_2 environment gave rather similar wear results. The wear was measured for various ambient temperatures and the plot of wear coefficient as a function
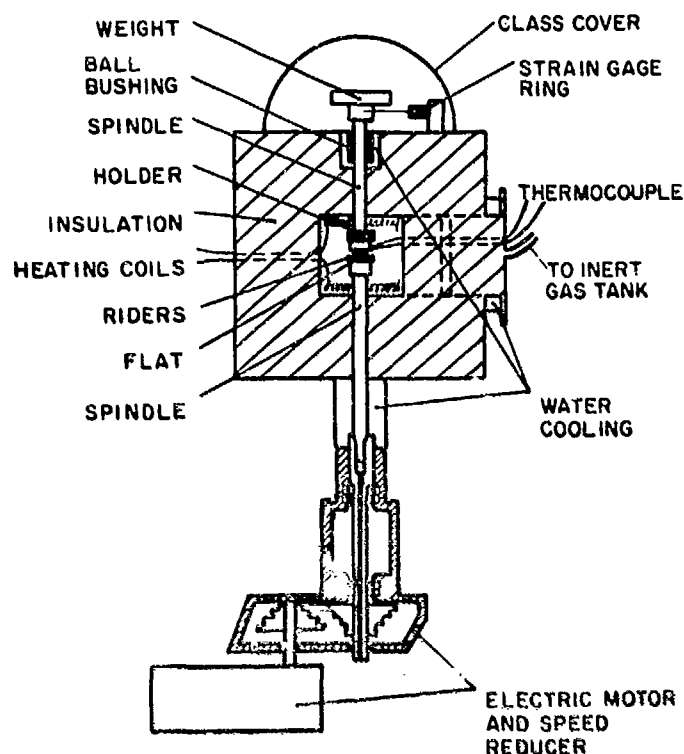
Fig. 3. Schematic illustration of high temperature friction apparatus using the geometry of three pins of graphite sliding against a copper flat.
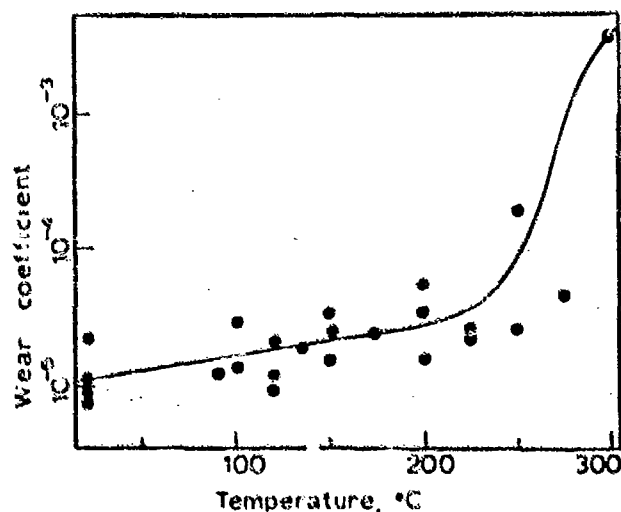
Fig. 4. Plot of the dimensionless wear coefficient for graphite–Cu (the volume of wear multiplied by the hardness and divided by the normal load and the distance of sliding) as a function of the surface temperature in low speed sliding tests carried out using the apparatus shown in Fig. 3. There is a drastic increase in wear as the temperature approaches 300 °C.

of temperature is shown in Fig. 4. The wear coefficient increases drastically when the temperature reaches 300 °C and in general increases monotonically with temperature. Further details of the testing are available [12].
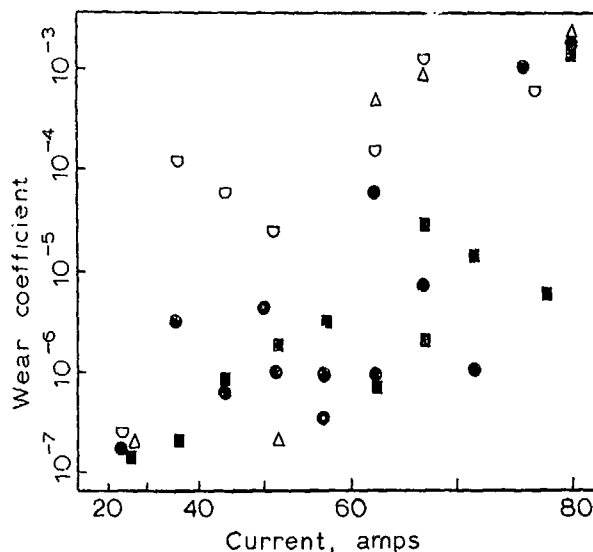
Fig. 5. Plot of wear coefficient as a function of the electric current (on a scale linear in i^2) for various sliding speeds: ○, 1.5 m s^{-1}; △, 5 m s^{-1}; ●, 9 m s^{-1}; ■, 13 m s^{-1}. The low speeds tend to give greater wear for the same current.

3.2. High current sliding tests

These tests were carried out in the high speed friction apparatus described earlier [10], using a pin of graphite on a cylindrical disk of copper. The graphite pin traces out a continuous track on the curved surface of the disk. A high current was passed through the interface, and the wear coefficient was measured after some length of sliding. Both the current and the speed of sliding were varied. The load was 0.7 kgf, the diameter of the electrographite pins was 6 mm, the diameter of the copper disk was 150 mm and the duration of the tests was generally 4 h. Testing was in the ambient air, in the summer (i.e. at a high humidity level).

The plot of wear coefficient as a function of current for various sliding speeds is shown in Fig. 5. In general, wear is higher when the current becomes greater, and for any level of current the wear becomes lower as the sliding speed increases.

The wear data were analyze in terms of eqn. (5), assuming that at the interface there was at any time only one circular contact, whose radius was given by the plastic deformation equation:

$$p\pi r^2 = L \tag{6}$$

where p is the hardness of the softer surface, the graphite.

Figure 6 shows the plot of wear coefficient as a function of temperature computed by the use of eqn. (5). The parameters used in the equation are given in Table 1.

In general, the wear coefficient increases as a function of computed interfacial temperature, slowly at moderate temperatures, but sharply at around 300 °C. The line from Fig. 4 is drawn on Fig. 6 as a broken curve and
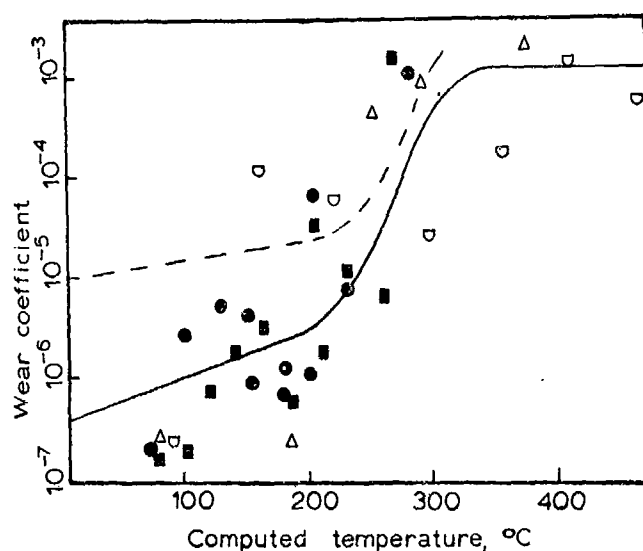
Fig. 6. Plot of wear coefficient as a function of interface temperature computed by the use of eqn. (5) for various sliding speeds: ○, 1.5 m s^{-1}; △, 5 m s^{-1}; ●, 9 m s^{-1}; ■, 13 m s^{-1}. The scatter of wear rates is much lower than in Fig. 5, the low speed and high speed results are well intermingled, and there is a drastic rise in wear at computed temperatures of just under 300 °C.

TABLE 1

Units and values of the parameters used in eqn. (5)

Parameter	Unit or value in the following systems	
	Old engineering units	Metric units
f	0.25	0.25
L	1.54 lbf	0.60 kgf
J	1	4.2 W s cal^{-1}
ρc	254 lb in^{-2} °F^{-1}	8.2×10^5 cal m^{-3} °C^{-1}
k	51 lb s^{-1} °F^{-1}	91 cal m^{-1} s^{-1} °C^{-1}
r	4.8×10^{-3} in	1.2×10^{-4} m
R	—	21×10^{-3} Ω (W A^{-2})
v	in s^{-1}	m s^{-1}
i	—	A

gives a reasonable fit for the experimental data points at high temperatures, since the experimental data points indicate a drastic increase in wear coefficient in the vicinity of 300 °C. Thus, it seems that the temperatures computed by the use of eqn. (5) are realistic ones.

4. Discussion

The reason why wear coefficients from the high temperature tests shown in Fig. 4 do not fit the experimental data shown in Fig. 6 at low

temperatures is as follows. Stephenson [12] found that at moderate temperatures the wear rate was high for the first hour of testing and was then reduced by about an order of magnitude. His tests were all in the high wear regime, while the tests shown in Fig. 6, being at higher speeds for longer periods of time, were mainly in the low wear regime.

While Holm and Shobert have carried out analyses of the temperature rise of sliding electric contacts which are roughly equivalent to the use of eqn. (5), I have been unable to find any indication that the equation itself has been used, and the remarkable fact that increases in sliding speed can reduce the interfacial temperature of current-carrying contacts seems not to have been previously reported.

In our tests, eqn. (5) seems to give rather accurate values for the temperature rise because of a number of compensating factors. The first of these, mentioned above, is that all the electrical heat is assumed to be generated at the interface, whereas it is in fact generated within the constriction and some of it never reaches the interface. The second factor is that the disk is assumed to be at all times at room temperature, whereas it may become quite warm after extensive sliding. A third factor is that it is assumed that all the heat is carried away from the interface by conduction through the disk, whereas some travels through the pin and some is convected away. This is seen most clearly by noting that in initial tests the pin holder was made of copper, and in this case the pins were distinctly cooler because heat could be more easily dissipated through the holder.

For our top current of 80 A, calculations indicate that at a speed of 77 $m\ s^{-1}$ the mechanical and electrical energy inputs are equal. Almost all our tests were done in a regime in which the electrical heating exceeded the mechanical, so that the surface temperature–velocity function was negative.

The assumption that the contact between pin and disk was made at only one junction proved surprisingly accurate, possibly because in many cases a thermal patch as postulated by Burton [13] was formed. It should be noted that our pins were of 6 mm diameter. Presumably when brushes of large area are used there are a sizable number of contacts, perhaps about 10 as assumed by Holm. This fragmentation of the contact area would reduce the temperature at the interface to below the value given by eqn. (5).

5. Conclusion

This study started in an attempt to explain an anomaly, namely that in studying the wear of current-carrying Ag–graphite contacts sliding against copper, experiments at Massachusetts Institute of Technology (MIT) [14] were producing more wear that was being experienced at Westinghouse [15], even though our sliding speeds were much lower (4 $m\ s^{-1}$ at MIT as against 13 $m\ s^{-1}$ at Westinghouse). It is now clear that the experimental results are perfectly logical in that the surface temperature, and hence the wear, is lower at 13 $m\ s^{-1}$ than at 4 $m\ s^{-1}$.

Acknowledgments

References

1 H. Blok, Fundamental mechanical aspects in boundary lubrication, *SAE Trans.*, *46* (1940) 54 - 68.
2 J. C. Jaeger, Moving sources of heat and the temperature at sliding contacts, *J. R. Soc. N.S.W.*, *56* (1942) 203 - 224.
3 J. F. Archard, The temperature of rubbing surfaces, *Wear*, *2* (1959) 438 - 455.
4 E. Rabinowicz, Friction temperatures, *Prod. Eng. (NY)*, (March 30, 1964) 97 - 99.
5 R. Holm, Calculation of the temperature development in a contact heated in the contact surface, and application to the problem of the temperature rise in a sliding contact, *J. Appl. Phys.*, *19* (1948) 361 - 366.
6 R. Holm, Temperature development in a heated contact with application to sliding contacts, *J. Appl. Mech.*, *19* (1952) 369 - 374.
7 R. Holm, *Electric Contacts*, Springer, New York, 4th edn., 1967, Section 21.
8 E. I. Shobert, *Carbon Brushes*, Chemical Publishing Co., New York, 1965, Chap. 7.
9 E. Rabinowicz, *Friction and Wear of Materials*, Wiley, New York, 1965.
10 F. J. Carignan and E. Rabinowicz, Friction and wear at high sliding speeds, *ASLE Trans.*, *24* (1980) 451 - 459.
11 M. Imai and E. Rabinowicz, Lubrication by low-melting-point metals at elevated temperatures, *ASLE Trans.* *6* (1963) 286 - 294.
12 D. Stephenson, Wear of high speed, high current density slip ring materials at elevated temperatures, *S.B. Thesis (Mech. Eng.)*, Massachusetts Institute of Technology, June 1981.
13 R. A. Burton, Thermal deformation in frictionally heated contact, *Wear*, *59* (1980) 1 - 20.
14 E. Rabinowicz and P. Chan, Wear of silver-graphite brushes against various ring materials at high current densities, in *Proc. Conf. on Electrical Contacts, 1979*, Illinois Institute of Technology, Chicago, IL, 1979, pp. 123 - 127.
15 I. R. McNab and J. L. Johnson, High current brushes — III — performance evaluation for sintered silver-graphite grades, in *Proc. Conf. on Electrical Contacts, 1978*, Illinois Institute of Technology, Chicago, IL, 1978, pp. 493 - 499.

THERMAL STABILITY IN GRAPHITE CONTACTS*

J. B. P. WILLIAMSON

Williamson Interface Ltd., Monkfield House, Malvern, Worcs. WR13 5BA (Gt. Britain)

NANCY ALLEN

Westinghouse Research and Development Center, Pittsburgh, PA 15235 (U.S.A.)

Summary

When current flows through a contact spot heat is generated in the constriction resistance and is then dissipated into the bulk of the conductors. The generation depends on the electrical resistivity, and the dissipation on the thermal conductivity; both of these vary with the local temperature. The equilibrium temperature of the spot reflects the balance between these two processes. For the graphite used for sliding brushes, the electrical resistivity, after an initial decrease, is level or rises with temperature: by contrast the thermal conductivity usually falls as the temperature increases. Consequently, as the current is increased and the temperature rises, more heat is generated, but the conductive dissipation does not increase at the same rate.

A theoretical and experimental study of this behavior in graphite-to-graphite and graphite-to-metal contacts is described in this paper. It shows that for any given size of contact there is a maximum current which may be passed safely. For currents greater than this critical value no thermal equilibrium is possible, and the temperature rises indefinitely until it is limited by some other phenomenon, *e.g.* the disintegration of the contact interface due to thermal shock.

Some observations on surface degradation in practical brushes are described, and these are discussed in terms of this thermally unstable behavior.

---

1. Introduction

It is well known that current crosses an interface by flowing through the tiny contact spots where the two conductors come into intimate contact. The constriction as the current funnels through these spots gives rise to a small extra resistance, called the constriction resistance. Heat generated in

---

this resistance by the current raises the temperature in the contact region, and this can damage the interface. This basic picture is true both for static contacts and for sliding current collectors.

The classical method of calculating the maximum temperature rise developed in the constriction (the supertemperature T_m) uses the Kohlrausch relation [1]

$$U^2 = 8 \int_0^{T_m} \lambda \rho \ dT \tag{1}$$

which gives it in terms of the voltage U between the conductors. This is a straightforward relation, requiring as input the values of the electrical resistivity ρ, the thermal conductivity λ and their variations with temperature. It indicates that T_m rises monotonically with U. The problem is that in practice current collectors do not have voltages applied across them: their impedances are insignificant, and consequently they have currents driven through them. The voltages developed across them are, like their supertemperatures, dependent variables. The distinction is important because an equation linking two dependent variables tells us nothing about the stability of the relation.

In this paper we explore the dependence of the temperature on the independent variable, the current I, and show that for graphite collectors T_m does not increase steadily as I rises: often there is a critical value of current above which the temperature rises discontinuously.

2. Thermal balance in contact spots

The heat generated in the constriction region is given by the square of the current times the constriction resistance R. R itself depends on the resistivity. Therefore for a given current the heat generated (HG) will vary with the temperature in the same way that ρ varies with temperature. The exact relation is complicated because the temperature is different from point to point in the constriction, but it is clear that the HG varies with T_m in some manner such as that shown in Fig. 1(a), curve I_1. (This curve gives the heat which would be generated in the contact region by a current I_1 if the maximum temperature in the constriction were T_m.) Higher currents would generate more heat: curves I_2, I_3 etc.

By contrast, the dissipation of heat from the contact region into the bulk conductors depends on the thermal conductivity and on how it varies with temperature. For constant λ, the heat dissipation (HD) will be proportional to T_m, as shown in Fig. 1(b). However, when, as is common in graphite, λ falls with increasing temperature, the HD curve will be as shown by the broken line.

In practice, the current will raise the temperature until the HD equals the HG; the equilibrium temperature will be given by the intersection of the
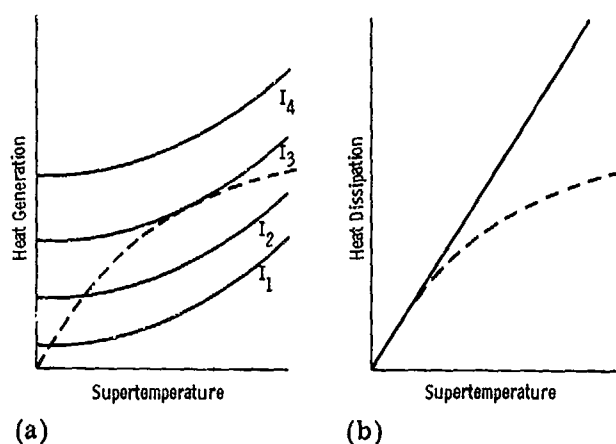
Fig. 1. (a) Representation of the way the supertemperature affects the heat generated by currents flowing through a constriction resistance (the broken line is the heat dissipation, and is superimposed to show the temperature at which there will be a thermal balance); (b) the influence of the supertemperature on the heat dissipation from the contact region (the full line is for a constant λ; the broken line shows the effect when λ falls as T_m increases).

HD–T_m curve with the appropriate HG–T_m curve, as illustrated by the broken line transposed to Fig. 1(a) from Fig. 1(b). This graphical approach shows immediately that, although at low currents the HD and HG curves intersect, there is in general a critical current above which the HG is greater than the HD *at all temperatures*. This marks a discontinuity in the behavior which is not revealed by the voltage–temperature characteristic calculated using the Kohlrausch relation. This current is the maximum which can be passed through the collector in equilibrium; above it there is no thermal balance and the temperature rises indefinitely. The maximum equilibrium temperature is a function of the thermal variation in λ and ρ: it is not associated with any change of state.

3. Theoretical calculation of the supertemperature

The dependence of the supertemperature on the current, which is implied by the points of intersection of the curves in Fig. 1(a), has been treated theoretically by Greenwood and Williamson [2]. Unfortunately their relation

$$IR_{20} = 2\rho_{20} \int_0^{T_m} \left(2 \int_T^{T_m} \lambda\rho \, dT \right)^{-1/2} \lambda \, dT \qquad (2)$$

yields analytical solutions only when λ and ρ vary with T in very simple ways. However, it can be evaluated numerically for any material, using step by step integration, provided that the variations in λ and ρ with temperature are known. Using this approach we have determined the current–

42

temperature characteristics of the contact spots of several grades of graphite. R_{20} is the "cold resistance" of the contact, *i.e.* that measured at an ambient temperature of 20 °C using a current too small to cause any temperature rise in the constriction. This factor can be used to normalize the current; the above relation then describes the behavior of any size of contact spot.

A typical result is shown in Fig. 2. At first the supertemperature rises slowly, but above a few hundred degrees Celsius it becomes extremely sensitive to changes in the current. A 50% increase in the current necessary to produce a supertemperature of 400 °C will raise the temperature to 2000 °C; a further small increase will destroy the thermal balance and cause the temperature to rise indefinitely. The cross marks the critical current and the critical temperature, the most extreme case for which the curves in Fig. 1(a) intersect. The section of the curve at higher temperatures than this, *i.e.* with the negative slope, is unstable. The behavior shown in Fig. 2 was calculated for 875S graphite. Closely similar characteristics have been derived for 890S (3474D), ATJ and Acheson graphites. The λ and ρ values of these graphites all vary with temperature in broadly the same way. (Useful publications on the resistivities and conductivities of graphites are given in ref. 3.)

The exact variations in the conductivities, however, cannot be known accurately. In polycrystalline graphite they are functions of the raw materials, processing procedure, baking temperature and baking time. They differ from one graphite to another, even from one batch to another; indeed the high temperatures developed around the contact spots may themselves cause changes in the conductivity during the life of a brush. Nevertheless, the important aspects of the relation between current and supertemperature, *i.e.* the extreme sensitivity of the supertemperature to small changes in the current and the thermal runaway above a certain maximum current, appear to be independent of the detailed variation.

We have calculated the current–voltage–supertemperature characteristics for many different graphites. They all show a region in which the super-temperature rises extremely rapidly for very small increases in the current, and almost always there is some current level at which the thermal behavior becomes unstable. In a few cases, where the resistivity fell sharply as the temperature increased, the supertemperature rose very rapidly with the current but did not actually become unstable. Figure 3 shows the character-istic calculated for an electrographitic material. The behavior is essentially the same as that shown in Fig. 2.

4. Experimental observation of the critical current

The supertemperature cannot easily be measured experimentally, and so it is more convenient to verify the theoretical predictions by observing the way the current through the constriction depends on the voltage across it. Just as there is a maximum value of the current in the I–T_m relation (as
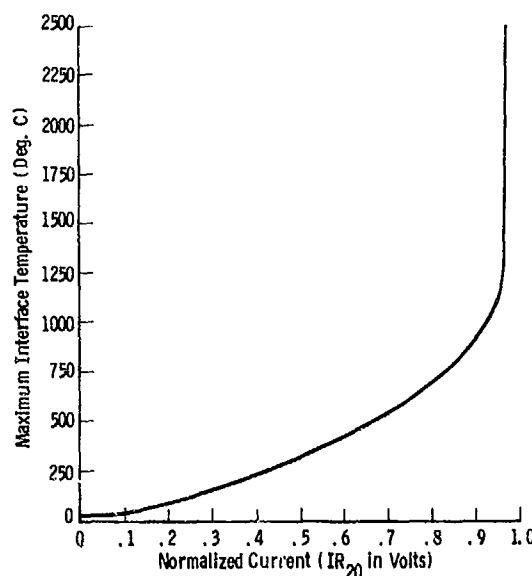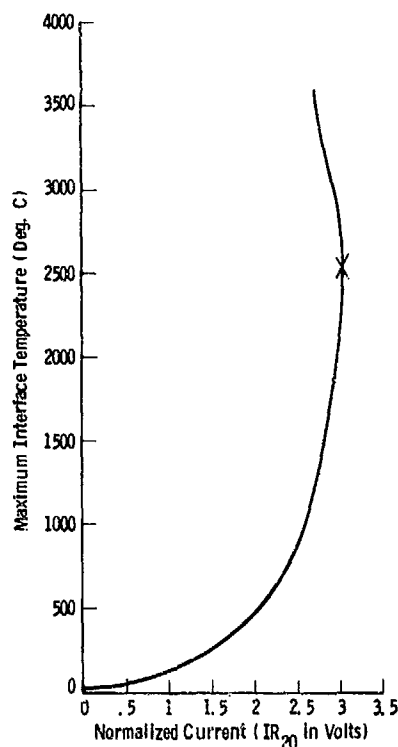
Fig. 2. The influence of the current on the supertemperature at the interface between two 875S graphite blocks. The current has been normalized by being multiplied by R_{20}, and consequently the graph is valid for any size of contact spot.

Fig. 3. The influence of the current on the supertemperature in an electrographitic collector.

shown in Figs. 2 and 3), so there is in the $I-U$ relation [2]. The theory predicts that when an increasing voltage is applied across the interface of a graphite collector the current will rise to a maximum and then *fall* as the voltage continues to increase. Using data for ATJ graphite the voltage corresponding to the current maximum was calculated to be 2.7 V, as shown in Fig. 4.

A simple experiment was carried out in which two pieces of ATJ graphite were brought into contact with a force sufficient to create contact spots between them with a constriction resistance of approximately 0.1 Ω. A voltage was applied across the interface and the resulting current was observed. It was found that as the voltage rose, the current did indeed rise to a maximum and then decrease. The experiment was repeated many times. The voltage at which the current maximum occurred varied slightly from run to run; its average value was 2.9 ± 0.25 V, which agrees well with the theoretical prediction.

5. Practical considerations

The phenomenon illustrated in Figs. 2 and 3 ultimately sets a limit to the working current of a collector, and this may become critical in the
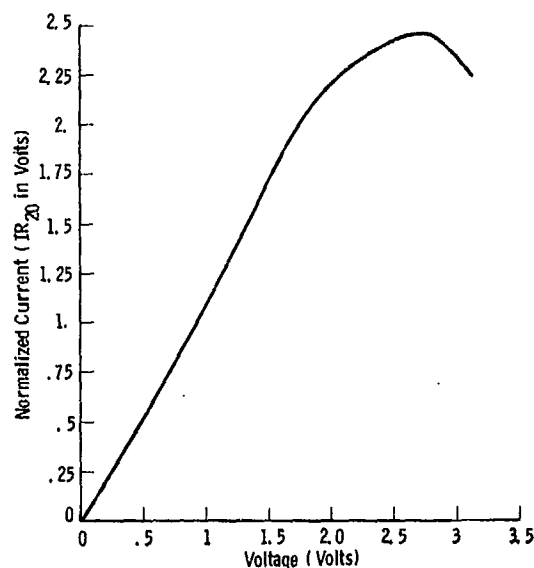
Fig. 4. The relation between current and voltage for the contact between two pieces of ATJ graphite.

development of very high current density brushes. However, its immediate practical significance lies in the influence it has on the effect of current surges. The contact spots at the sliding interface are tiny, and the heat generated in their constrictions is released into a very small mass of material. Their thermal capacity is small, and their temperature can rise and fall rapidly; microsecond thermal response times are common. Contact spots respond to current peaks not to average values. The current flowing through sliding collectors is very far from constant; it fluctuates as a result of switching and commutation and, in addition, it quite commonly suffers interruptions and surges caused by perturbations in the forces and angles with which the brushes bear on the slip ring.

The behavior revealed in Figs. 2 and 3 suggests that the effects of such fluctuations may be more serious than has been suspected. For example, if a collector is passing a current large enough to raise the temperature of the contact spots to 300 °C, then a surge which momentarily increases the current by a factor of 3 (which is by no means an unusual event) will create a temperature well above 2000 °C. The resulting thermal shock can be very harmful.

6. Graphite-to-metal collectors

It is convenient to visualize the constriction region in terms of a set of equipotential surfaces which are orthogonal everywhere to the lines of current flow. In the simple case of contact between conductors of the same material, the interface is a plane of symmetry (regardless of the macroscopic

shape of the conductors), and so the contact spots form one of the equipotentials. (If the contact is a single circular spot, the equipotentials are in fact a set of ellipsoids centered on it, and the current flow lines are the orthogonal set of hyperboloids.)

Surprisingly, the pattern of equipotentials and current flow is not altered when the constriction region lies partly in the graphite and partly in the slip ring. It can be shown (by a simple extension of the analysis given by Greenwood and Williamson [2]) that the pattern is not disturbed when the material is changed to a second conductor inside a constriction as long as the change is made at an equipotential surface of the original homogeneous system. This condition is met by the interface between the collector and the slip ring (the contact spots). The two halves of the constriction can thus be treated independently and then added. In fact the resistance of the metal half is negligible, so the R_{20} of the system is half that of the equivalent graphite-to-graphite contact; thus the current required to create any given temperature in the constriction is doubled. More importantly, the place at which the maximum temperature occurs is altered. It has been shown that, in equilibrium, the isotherms in the constriction region coincide with the equipotentials and also that the maximum temperature occurs at the mid-potential of the constriction [2]. In the symmetrical case this is at the interface, but when the entire potential drop occurs in the graphite the mid-potential is inside the brush, approximately one contact-spot radius below its surface.

This asymmetry enhances the importance of the thermal instability described above. The sudden generation of an extremely high temperature just inside the graphite is likely to produce a thermal crack and to cause the material between the isotherm and the interface to spall leaving a small crater.

7. Metal-loaded graphite collectors

Many graphites are loaded with metal powder. The nature of their sliding interface can vary greatly, and it is not possible to say at any instant whether the contact is graphite-to-slip ring or particle-to-slip ring. Indeed, the deposition of graphite onto the slip ring may result in a graphite-to-graphite interface [4]. It is probable that the nature of the contact is continually changing. However, it is clear from Fig. 3 that if, while the current is very high, the contact is momentarily made through a graphite-to-slip ring spot, then the temperature in the contact regions will immediately rise far above the melting point of the metal powder. Any particles close to the graphite contact spots are likely to be melted and lost. This will reduce the probability of metallic contact spots and, conversely, increase the chance that the next current surge will pass through a graphite constriction and so lead to renewed high temperatures and further loss of metal. Once started,

such a process would continue removing metal powder from the surface of the collector, and the state of the interface would presumably depend on the balance between this thermal removal and the exposure of new particles as the surface wore.

This process may offer an explanation for the behavior illustrated in Fig. 5. This shows a silver-loaded graphite brush which had been used to collect current from a segmented ring. The interesting observation is that almost all the silver has been removed from the trailing end of the brush interface. It seems possible that the following sequence of events may have occurred. As the brush slid from one segment to the next, the force between it and the first segment decreased as the load became transferred to the following segment. Thus the area of contact between the brush and the first segment became smaller. (The segmented slip ring is an unusual case in which the true area of contact does vary with the nominal area of contact.) As the contact area decreased, the cold constriction resistance R_{20} increased. The actual value of R_{20} at any instant would depend on whether the contact was metallic or graphitic. In either case, the product IR_{20} would increase even if the current remained constant. If at any time the contact was graphitic, and its IR_{20} exceeded the critical value, the sequence of melting and metal removal described above would be initiated. The process would repeat every time the brush left a segment and could lead to the situation shown in Fig. 5.

It is interesting to note that if this argument is correct a very sharp demarcation should develop on the brush between the unaffected surface and the metal-depleted surface. The process of metal removal will begin at the trailing edge because that is the part in contact when the force between the brush and the segment is smallest and the constriction resistance is greatest. When the brush overlaps the segment more, the force is greater and R_{20} is smaller. At some overlap the value of R_{20} will have fallen so that even for a graphitic contact IR_{20} will be less than the critical value. The depleted region cannot extend from the trailing edge further than this, and so we should expect it to have a sharp edge. We should also expect the width of the depleted region to be proportional to the current.

Garrett and Hummert [5] have studied this phenomenon and have observed that the depletion width is indeed proportional to I. The brush shown in Fig. 5 is one used in their experiments. The distribution of particles in the surface of this brush is shown in Fig. 6 which was taken by scanning electron microscopy (SEM) using silver X-ray emission. The micrograph was divided into 14 strips, each 61.5 mm $\times$ 6.35 mm, with the edge of the depleted zone between strips 6 and 7. The silver spots were counted, and their densities are given in Table 1. A recount confirmed these figures within 5%. As the edge of the strips probably did not coincide with the edge of the zone, the counts in strips 6 and 7 are not reliable. The sharpness of the edge of the depleted zone is clear. The sudden transition from the unaffected area to the depleted area is not easy to explain by conventional descriptions of brush wear, but is exactly as predicted by the present arguments.
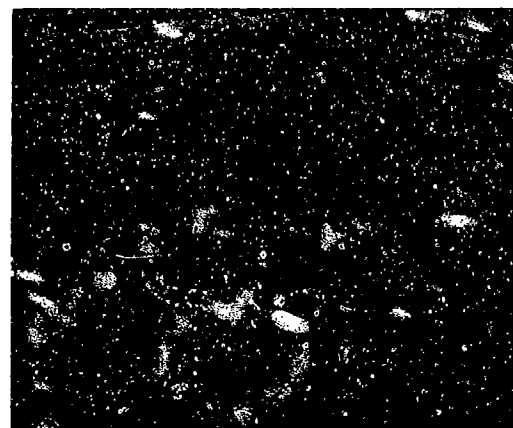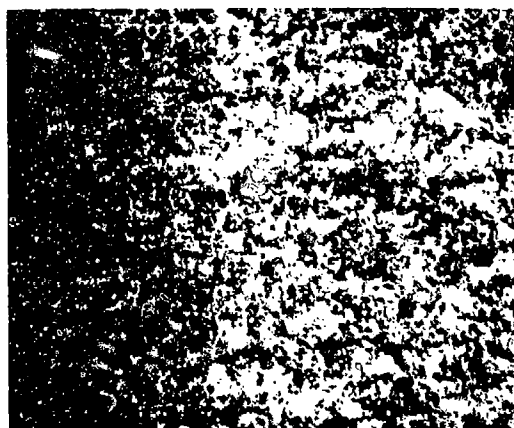
Fig. 5. SEM micrograph of the surface of a worn silver-loaded brush. The silver particles have been removed from the trailing edge. (Magnification, 14×.)

Fig. 6. Silver X-ray emission from the surface of Fig. 5, showing the density of silver particles in the surface. (Magnification, 14×.)

TABLE 1

Density of silver spots in each of 14 equal strips of the SEM silver X-ray micrograph

Strip	Silver spots (mm^{-2})	Strip	Silver spots (mm^{-2})
1	79	7	308
2	116	8	330
3	170	9	305
4	168	10	326
5	160	11	342
6	182	12	318
		13	316
		14	321

8. Discussion

In this exploratory study frictional heating has been neglected. Although it is unlikely to be significant compared with the effects of the large temperature excursions which are the main theme of this paper, it undoubtedly influences the behavior of the contact region in its more normal state. It is hoped that it may be possible to develop a broader theory embracing both frictional and electrical heating.

Small increases in the current can create very high temperatures in the contact region. These thermal transients can seriously damage collectors. They occur more commonly than is generally realized and are particularly significant in circuits which are prone to surges. The performance of a graphite will be strongly influenced by the way its thermal conductivity and electrical resistivity vary with temperature, for this determines its tolerance

48

to large currents. It is unfortunate that so little data are available on these critical parameters at high temperatures. Such information is clearly important and may become a critical input in research aimed to extend the current-carrying limit of collectors.

Acknowledgments

References

1 F. Kohlrausch, *Ann. Phys. (Leipzig)*, *1* (1900) 132.
   See also: R. Holm, *Electric Contacts*, Springer, New York, 1967, pp. 60 *et seq.*
2 J. A. Greenwood and J. B. P. Williamson, *Proc. R. Soc. London, Ser. A*, *246* (1958) 13.
3 R. W. Powell, *Proc. Phys. Soc. London*, *49* (1937) 419.
   R. W. Powell and F. H. Schofield, *Proc. Phys. Soc. London*, *51* (1939) 153.
   S. Mrozowski, *Phys. Rev.*, *85* (1952) 609.
   S. Mrozowski, *J. Am. Ceram. Soc.*, *35* (1952) 282 (discussion).
   S. Mrozowski, J. F. Andrew, N. Juul, J. Okada, J. Repetski, H. E. Strauss, T. Tsuzuku and D. C. Wobschall, *WADC Tech. Rep. 58-360*, Parts II - IV, 1960 - 1961 (Carbon Research Laboratory, University of Buffalo).
   A. R. Ubbelhode and F. A. Lewis, *Graphite and its Crystal Compounds*, Oxford University Press, London, 1960.
   Industrial Graphite Engineering Handbook, Union Carbide Corporation, New York, 1970.
   Modern Materials, Academic Press, New York, 1964, pp. 41 *et seq.*
   E. I. Shobert II, *Carbon and Graphite*, Academic Press, New York, 1964, pp. 34 - 42.
   P. L. Walker, *Chemistry and Physics of Carbon*, Dekker, New York, 1969, p. 99.
   L. E. Moberly and J. L. Johnson, in *Proc. Conf. on Electric Contact Phenomena*, Illinois Institute of Technology, Chicago, 1967, p. 27.
   Thermophysical Properties of High Temperature Solid Materials, Vol. I, Macmillan, New York 1967.
   C. Y. Ho, R. W. Powell and P. E. Liley, *J. Phys. Chem. Ref. Data*, *3* (Suppl. 1) (1974); *J. Phys. Chem. Ref. Data*, *1* (2) (1972).
4 J. F. Thompson and M. J. B. Turner, *Wear*, *6* (1963) 30.
5 G. T. Hummert and R. M. Garrett, in *Proc. Advanced Current Collection Conf.*, *Chicago, IL, September 23 - 25, 1981*, in *Wear*, *78* (1982) 109.

FRICTIONAL AND ELECTRICAL INTERACTIONS IN CURRENT COLLECTORS*

M. D. BRYANT and R. A. BURTON

Mechanical and Aerospace Engineering Department, North Carolina State University, Raleigh, NC 27650 (U.S.A.)

Summary

Numerical results are given for electric current flow through a sliding contact that involves a graphite brush and a copper slip ring. The contact of length $2l$ and unit depth moves with velocity c along the brush face. It is found that for a given fixed set of operating conditions (current I, sliding velocity V, contact force F_N etc.) many values of c and l may exist; it is also found that c is linear in sliding velocity V.

1. Introduction

In this paper, electric currents flowing from a stationary carbon graphite brush to a rotating copper slip ring through a friction-bearing sliding contact are considered. When current and/or frictional heating are sufficient, the contact geometry between the collector (brush) and the slip ring changes from smoothly distributed asperity contact to a configuration where a single thermal asperity forms, supporting the interface loading and holding the surfaces apart except at the asperity tip. This resulting thermal asperity is orders-of-magnitude higher than the initial roughness asperities resident on the initial undeformed surface.

Dow [1] has reported experiments designed to display the transition described above. In those experiments the thermal asperity is brought to incandescence by the electrical and frictional heating.

Earlier, Kilaparti and Burton [2] carried out an analysis of such contact conditions in the absence of electrical heating. Their analysis showed that earlier work with a simplified uniform temperature contact was qualitatively correct as a first approximation.

In a companion paper [3], a problem of electric current collector behavior was presented, and the surface displacements generated by elec-

---

trical heating were calculated. In the present paper these displacements, together with those for wear and frictional heating, are combined to give a prediction of overall contact behavior. The approximation of an isothermal contact patch is made, and it is assumed that the brush and the slip ring share this common temperature at the zone of actual contact. With such approximations a heat balance is possible; once the amount of heat going into the brush is estimated, surface displacements are calculated for the zone of contact as if all surface loadings were removed. To reintroduce the loading, it is assumed that the brush and the slip ring must be in full contact over the specified contact zone. Noting that the slip ring material is much stiffer than typical carbon graphite brush material, only the displacements of the brush must be considered. These can be divided into two components: a secular rise from the leading edge to the trailing edge; a bulge of the center of the contact area relative to its edges. The latter displacement is pressed flat by the contact loading in a nearly hertzian manner. Careful consideration will lead to the conclusion that the secular rise cannot exist under the other assumptions (*e.g.* full contact over the contact zone). Thus the contributions from frictional heating, electrical heating and wearing of material must exactly balance one another. Application of this condition leads to the prediction that the contact patch is slowly traversing the surface of the brush at a speed c. The contact width $2l$ and the speed c can be calculated simultaneously by applying the aforementioned heat and material balances. The derivations which follow outline these operations and show typical results.

2. Formulations

Figure 1 schematically shows a brush–slip ring system in contact at $y = 0$, $|x| \leq l$. The slip ring surface moves with velocity V perpendicular to the brush face, and the contact patch moves with velocity c from left to right along the brush face. The outer periphery of the brush is maintained at the ambient temperature and the entire brush face, except the contact patch, is thermally insulated. All electric currents and heat flowing from the brush to the slip ring pass through the contact patch. Finally, the normal force F_N per unit depth, pressing the brush against the slip ring, causes a frictional force $\mu_f F_N$, where μ_f is the dynamic coefficient of friction.

At the junction (the contact patch) between the brush and the slip ring, frictional heat $q_f = \mu_f V F_N /2l$ and thermoelectric heat $q_{te} = (A + B T_J)(I/2l)$ are produced. Here, I is the total current per unit depth flowing from the brush to the slip ring, T_J is the junction temperature due to the frictional and thermoelectric heating and A and B are constants giving the thermo-electric potential between the brush material (graphite) and the slip ring material (copper).

If a heat balance is applied at the contact patch, then the total heat $q_f + q_{te}$ produced at the junction must be equal to the sum of the heat q_b conducted to the brush and the heat q_{sl} conducted to the slip ring:

$$q_b + q_{s1} = q_f + q_{te} \tag{1}$$

q_b and q_{s1} can be written [4] as

$$q_b = K_C \left(\frac{c}{k_C l \pi} \right)^{1/2} T_b \tag{2a}$$

$$q_{s1} = K_{Cu} \left(\frac{c}{k_{Cu} l \pi} \right)^{1/2} T_{s1} \tag{2b}$$

where K and k are thermal conductivity and thermal diffusivity, C and Cu refer to carbon graphite and electrolytic copper and T_b and T_{s1} refer to the brush and the slip ring contact patch temperatures. The slip ring contact temperature $T_{s1} = T_J$, while the brush contact temperature $T_b = T_J + T_{elec}$. Here T_{elec}, the electric heating component of the brush temperature at the contact patch, can be determined using methods described in ref. 3. (For later expediency of calculation, the heat flow q_{elec} through the contact patch due to electric heating was taken as zero.)

If we define

$$\hat{c} = \frac{cl}{k_C} \tag{3}$$

then, after rearrangement, eqns. (2) become
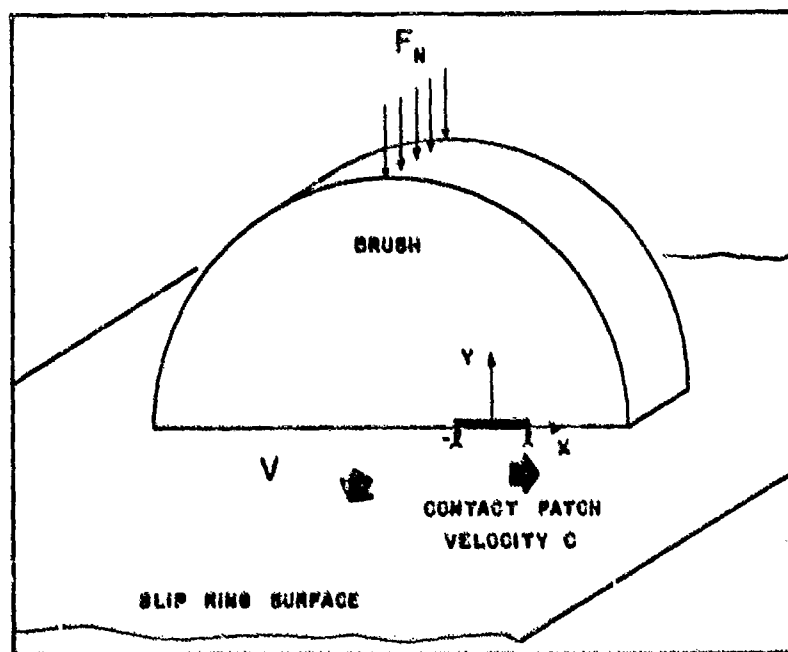
Fig. 1. Geometry and loading of a brush–slip ring system that makes contact at $y = 0$, $|x| < l$. The slip ring surface moves at velocity V perpendicular to the brush face, and the contact patch moves from left to right with velocity c.

$$q_b = \frac{K_C}{l}\left(\frac{\hat{c}}{\pi}\right)^{1/2}(T_J + T_{elec}) \tag{4a}$$

$$q_{sl} = \frac{K_{Cu}}{l}\left(\frac{k_C}{k_{Cu}}\right)^{1/2}\left(\frac{\hat{c}}{\pi}\right)^{1/2}T_J \tag{4b}$$

With the aid of eqn. (4) and of values given earlier for q_f and q_{te}, eqn. (1) becomes

$$\frac{\mu_f VF_N}{2l} + \frac{(A + BT_J)I}{2l} = \frac{K_C}{l}\left(\frac{\hat{c}}{\pi}\right)^{1/2}(T_J + T_{elec}) + \frac{K_{Cu}}{l}\left(\frac{k_C}{k_{Cu}}\right)^{1/2}\left(\frac{\hat{c}}{\pi}\right)^{1/2}T_J \tag{5}$$

from which T_J may be obtained as

$$T_J = \frac{AI + \mu_f VF_N - 2K_C(\hat{c}/\pi)^{1/2}T_{elec}}{2(\hat{c}/\pi)^{1/2}\{K_C + K_{Cu}(k_C/k_{Cu})^{1/2}\} - BI} \tag{6}$$

Equations (4a) and (6) together give the heat flow per unit area into the brush in terms of known material parameters, measurable operating parameters and the unknown variable $\hat{c}$. Thus heat flow q_b gives rise to normal displacements v_{th}, in the brush at the contact patch, which may be computed using results taken from ref. 2:

$$v_{th}(x) = -\int_x^{\hat{c}} \frac{2\alpha_C k_C}{K_C}\, q_b(t)\, dt - \int_{-\infty}^x \frac{2}{\pi}\left(\frac{k_C}{c}\right)^{3/2}\frac{\alpha_C}{K_C}\frac{q_b(t)\, dt}{x - t} \tag{7}$$

where α_C is the coefficient of thermal expansion. (To simplify calculation, average values of T_{elec} over the contact patch will be used.) Thus if the constant q_b given by eqn. (2a) is substituted into eqn. (7), then eqn. (7) becomes

$$v_{th}(x) = -\frac{2\alpha_C k_C}{cK_C}\, q_b\left\{l - x + 2\left(\frac{k_C}{\pi c}\right)^{1/2}(x + l)^{1/2}\right\}$$

$$= -\frac{2l\alpha_C}{\hat{c}K_C}\, q_b\left\{l - x + 2\left(\frac{l}{\pi\hat{c}}\right)^{1/2}(x + l)^{1/2}\right\} \tag{8}$$

The total normal displacement $v(x)$ in the brush at the contact patch is the sum of the normal displacements due to electric heating and to thermal conduction:

$$v(x) = v_{th}(x) + v_{elec}(x) \tag{9}$$

If values for

$$v_{elec} = -\frac{\alpha_C}{\pi^2}\frac{\rho_C I^2 l}{K_C}\hat{v}_{elec}$$

and

$$T_{elec} = \frac{\rho_C I^2 l}{\pi^2 K_C}\hat{T}_{elec}$$

obtained from ref. 3 are substituted into eqns. (4a), (6) and (9), and if eqns. (4a), (6) and (8) are substituted into eqn. (9), then eqn. (9) may be written as

$$v(x) = -\frac{2\alpha_C}{(\hat{c}\pi)^{1/2}}\left[\frac{AI + \mu_f VF_N - 2\rho_C I^2 (\hat{c}/\pi^5)^{1/2}\hat{T}_{elec}}{2(\hat{c}/\pi)^{1/2}\{K_C + K_{Cu}(k_C/k_{Cu})^{1/2}\} - BI} + \frac{\rho_C I^2}{\pi^2 K_C}\hat{T}_{elec}\right] \times$$

$$\times \left\{l - x + 2\left(\frac{l}{\pi\hat{c}}\right)^{1/2}(x + l)^{1/2}\right\} - \frac{\alpha_C \rho_C I^2 l}{\pi^2 K_C}\hat{v}_{elec} \tag{10}$$

where ρ_C is electrical resistivity and $\hat{T}_{elec}$ and $\hat{v}_{elec}$ are dimensionless quantities, defined in ref. 3, that will be determined later as functions of $\hat{c}$.

Equation (10) gives the displacements into the brush (or, with minus signs, the displacements out of the brush) for combined frictional, electrical and thermoelectrical heating. In order that contact be maintained along the entire length of the contact patch, the toe-to-heel rise

$$v_1 = v(-l) - v(l) \tag{11}$$

during the time period $2l/c$ must equal the thickness of the material lost from the surface by wear, *i.e.*

$$v_1 + \hat{W}_C\left(\frac{F_N}{2l}\right)V\left(\frac{2l}{c}\right) = 0 \tag{12}$$

(Equation (12) uses Archard's wear law involving the average contact pressure $F_N/2l$ and the graphite wear coefficient $\hat{W}_C$.) In addition, the center displacement relative to the edges

$$v_C = v(0) - \frac{v(-l) + v(l)}{2} \tag{13}$$

must be pressed flat by the applied load

$$F_N = 1.72E_C(-v_C) \tag{14}$$

Equation (14), taken from ref. 5, is a result of hertzian contact theory; E_C is Young's modulus for graphite.

If eqn. (10) is substituted into eqn. (11) and the result is substituted into eqn. (12), then after rearrangement eqn. (12) becomes

$$\left\{\frac{A^* + V^* - 2/\pi^{5/2}\hat{c}\hat{T}_{elec}}{1 + k^* - B^*/(\hat{c})^{1/2}} + \frac{2}{\pi^{5/2}}\hat{c}\hat{T}_{elec}\right\}\left\{1 - \left(\frac{2}{\pi\hat{c}}\right)^{1/2}\right\} +$$

$$+ \frac{\hat{c}(\hat{v}_{elec})_1}{2\pi^2} - V^*\frac{\hat{W}_C}{W^*}$$

$$= 0 \tag{15}$$

where

$$V^* = \frac{\mu_f F_N V}{\rho_C I^2} \qquad W^* = \frac{2\alpha_C k_C \mu_f}{K_C} \qquad A^* = \frac{A}{\rho_C I}$$

$$B^* = \frac{BI(\pi)^{1/2}}{2K_C} \qquad K^* = \frac{K_{Cu}}{K_C}\left(\frac{k_C}{k_{Cu}}\right)^{1/2} \qquad (\hat{v}_{elec})_l = (\hat{v}_{elec})_{-1} - (\hat{v}_{elec})_1$$

The unknown variable $\hat{c}$ can be determined as the roots of eqn. (15). It should be mentioned that eqn. (15) can possess many real positive roots, the maximum number of which depends on the functional forms of $\hat{T}_{elec}(\hat{c})$ and $(\hat{v}_{elec})_l(\hat{c})$. If the results (determined later)

$$\hat{T}_{elec}(\hat{c}) \approx \frac{1}{\hat{c}^{0.7}}$$

$$(\hat{v}_{elec})_l(\hat{c}) \approx \frac{7}{\hat{c}^{0.7}}$$

are substituted into eqn. (15), then after a lengthy rearrangement eqn. (15) becomes

$$\left\{\frac{7}{2\pi^2} + \left(\frac{7}{2\pi^2} + \frac{2}{\pi^{5/2}}\right)k^*\right\}\hat{c} + \left[A^* + V^*\left\{1 - \frac{\hat{W}_C}{W^*}(1 + k^*)\right\}\right]\hat{c}^{0.7} -$$

$$- \left\{\frac{(2)^{3/2}}{\pi^3}k^* + \left(\frac{2}{\pi^{5/2}} + \frac{7}{2\pi^2}\right)B^*\right\}\hat{c}^{0.5} -$$

$$- \left[\left(\frac{2}{\pi}\right)^{1/2}A^* + V^*\left\{\left(\frac{2}{\pi}\right)^{1/2} - B^*\frac{\hat{W}_C}{W^*}\right\}\right]\hat{c}^{0.2} + \frac{2^{3/2}}{\pi^3}B^*$$

$$= 0 \tag{16}$$

Under the transformation $\hat{c}^* = \hat{c}^{0.1}$, eqn. (16) becomes a tenth-order polynomial that can have as many as ten real positive roots.

Substitution of eqns. (10) and (13) into eqn. (14) yields (after some rearrangement)

$$F_N = 1.72 \, E_C \, \frac{\alpha_C \rho_C}{K_C} \, I^2 l \left[\frac{(\hat{v}_{elec})_C}{\pi^2} + \right.$$

$$\left. + \left\{\frac{2 - 2^{1/2}}{\hat{c}^{3/2}\pi^{1/2}}\right\}\left\{\frac{A^* + V^* - 2/\pi^{5/2}\hat{c}^{1/2}\hat{T}_{elec}}{1 + k^* - B^*/\hat{c}^{1/2}} + \frac{2}{\pi^{5/2}}\hat{c}^{1/2}\hat{T}_{elec}\right\}\right] \tag{17}$$

From this, l can be determined as

$$l = \frac{F_N}{1.72 E_C} \frac{K_C}{\alpha_C \rho_C I^2}\left[\frac{(\hat{v}_{elec})_C}{\pi^2} + \frac{2 - 2^{1/2}}{\hat{c}^{3/2}\pi^{1/2}} \times\right.$$

$$\left. \times \left\{\frac{A^* + V^* - 2/\pi^{5/2}\hat{c}^{1/2}\hat{T}_{elec}}{1 + k^* - B^*/\hat{c}^{1/2}} + \frac{2}{\pi^{5/2}}\hat{c}^{1/2}\hat{T}_{elec}\right\}\right]^{-1} \tag{18}$$

and c as

$$c = \hat{c}K_C/l \tag{19}$$

Finally, once $\hat{T}_{elec}$, $(\hat{v}_{elec})_l$ and $(\hat{v}_{elec})_C$ have been determined, the solution proceeds as follows: determine the roots $\hat{c}$ of eqn. (15); substitute these roots into eqn. (18) to determine the corresponding l; substitute $\hat{c}$ and l into eqn. (19) to determine c. Note that equations such as eqn. (16) may be used in place of eqn. (15).

3. Results and discussion

In Table 1, steady state results with respect to $\hat{c}$ are presented for electric heating of the brush. These data were calculated by assuming an insulated brush face (including contact patch) and a cooled outer boundary. For this problem, heat flow through the contact patch was blocked in order to simplify the heat balance of eqn. (1): otherwise, q_b would possess a term corresponding to electric heat flow. The values presented for $\hat{T}_{elec}$ are average values of $\hat{T}_{elec}$ taken over the entire contact patch.

TABLE 1

Presentation of steady state results *versus* $\hat{c}$ for electric heating of the brush

$\hat{c}$	$(\hat{v}_{elec})_l$	$(\hat{v}_{elec})_C$	$\hat{T}_{elec}$ [a]
1	6.92	4.09	1.024
2	4.37	2.76	0.616
4	2.65	1.81	0.376
8	1.64	1.24	0.237

[a] Average values.

If power law curve fits are applied to the data of Table 1, then $(\hat{v}_{elec})_l \approx 7/\hat{c}^{0.7}$. If these values, and the values for material parameters given in Table 2, are substituted into eqns. (15), (18) and (19), then l and c values may be determined as functions of the operating parameters V, I and F_N.

TABLE 2

Values of material parameters

Material parameter	Values of the parameters for the following materials	
	Graphite	Cu
K (N s^{-1} °C^{-1})	13.5	393
k (cm^2 s^{-1})	7.9×10^{-2}	1.123
ρ (Ω cm)	800×10^{-6}	—
α (°C^{-1})	4.7×10^{-6}	—
W (Pa^{-1})	3.98×10^{-13}	—
A (V)	11.056×10^{-6}	2.705×10^{-6}
B (V °C^{-1})	3.578×10^{-6}	0.7866×10^{-6}
E (MPa)	0.68×10^3	—

Table 3 contains a list of seven values of l and c *versus* V, I, F_N and μ_f determined by numerical iteration of eqn. (16). From Table 3, it can be seen that some of the computed values of l and c are either unreasonably large or unreasonably small; however, in most cases there still appear to exist many values of l and c that appear reasonable ($l \approx 10^{-1}$ mm, $c \approx 10^0$ cm s^{-1}). Furthermore, in many cases these many reasonable values are quite close in value.

TABLE 3

Values of l and c *versus* V, I, F_N and μ_f determined by numerical iteration of eqn. (16)

Case	I (A cm^{-1})	V (m s^{-1})	F_N (N cm^{-1})	μ_f
A	100	60	5	0.2
B	40	100	1	0.4
C	190	80	3	0.4

Case A		Case B		Case C	
l (mm)	c (cm s^{-1})	l (mm)	c (cm s^{-1})	l (mm)	c (cm s^{-1})
3.1×10^{-7}	62.9	1.6×10^{-7}	123	6.4×10^{-8}	302
0.11	0.70	4.7×10^{-2}	1.70	2.6×10^{-2}	3.00
0.29	0.54	0.13	1.24	6.6×10^{-2}	2.39
0.49	0.48	0.23	1.04	0.11	2.17
0.71	0.44	0.34	0.93	0.15	2.07
0.93	0.43	0.46	0.85	0.20	2.02
1.15	0.41	0.59	0.80	0.24	2.00

This suggests that as the contact patch moves across the brush face, its velocity and length may change independently of the operating parameters and material constants cited in the earlier formulations. Furthermore, some stability criteria, favoring one pair of l and c over another, appear to be necessary.

Figures 2(a) and 2(b) are plots of l *versus* I and l *versus* V respectively, for $F_N = 1$, 3 and 5 N cm^{-1}. Hereafter, in all figures presented, full lines represent situations in which $\mu_f = 0.4$ and broken lines represent situations in which $\mu_f = 0.2$. For Fig. 2(a), $V = 60$ m s^{-1} and for Fig. 2(b), $I = 100$ A cm^{-1}.

Examination of Fig. 2 reveals a monotonic decrease in l with I, V and μ_f, and a monotonic increase in l with F_N. The monotonic decrease in l with respect to I may have significance in the fact that as I increases, the contact length l, and hence the contact area, decreases. This increase in current and corresponding decrease in area will provide an accentuated increase in the current density at the contact patch. This may result in increased localized electrical heating of the brush at the contact patch, perhaps resulting in accelerated brush wear.
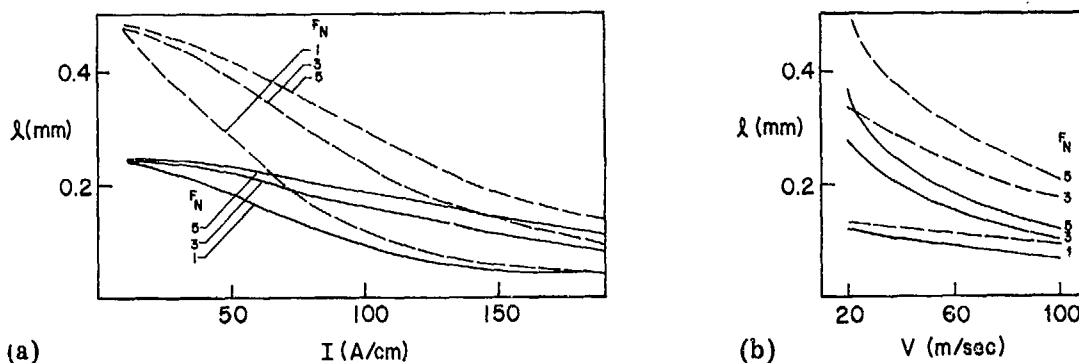
Fig. 2. Plots of (a) l vs. I for $V = 60$ m s^{-1} and (b) l vs. V for $I = 100$ A cm^{-1} ($F_N = 1, 3$ and 5 N cm^{-1}; $---$, $\mu_f = 0.2$; $---$, $\mu_f = 0.4$).
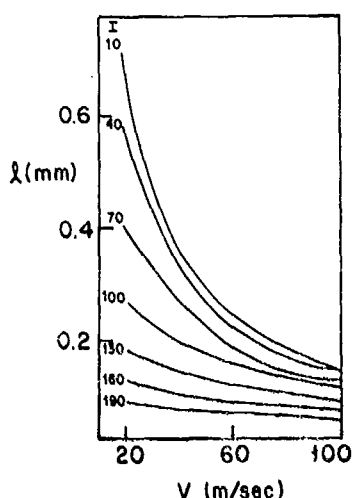
Fig. 3. Plots of l vs. V for $F_N = 3$ N cm^{-1}, $\mu_f = 0.4$ and various values of I.

Figure 3, a plot of l versus V for various values of I, shows that for large I, large increases in V appear to have little effect on l, while for small I, small increases in V can have a marked effect on l.

Figures 4(a) and 4(b) are plots of c versus I and V; these plots give the corresponding c for the values of l found in Figs. 2(a) and 2(b). From Fig. 2, it can be seen that c increases monotonically with I, V and μ_f, and decreases monotonically with F_N. Note also from Fig. 4(b) that c appears to be linear in V.

Figure 5, plots of c versus V for various values of I, corresponds to Fig. 3 in the same manner in which Figs. 4(a) and 4(b) correspond to Figs. 2(a) and 2(b). Examination of Fig. 5 also reveals the linearity of c with respect to V. Since the slope of the c versus V curve only varies with μ_f, this linearity may be expressed as

$$c = m(\mu_f)V + b(I, F_N, \mu_f)$$

where $m = m(\mu_f)$ is the slope and $b = b(I, F_N, \mu_f)$ is the c intercept.

58

(a) I (A/cm) (b) V (m/sec)
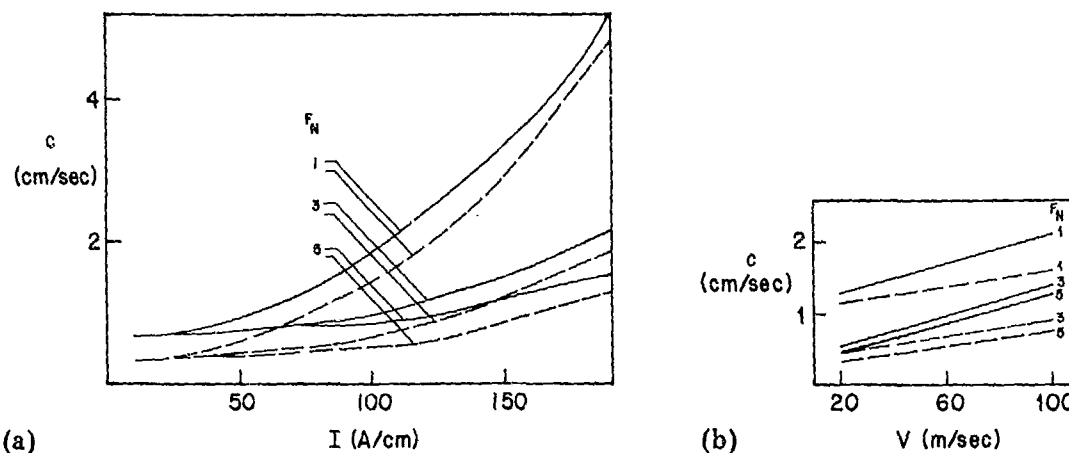
Fig. 4. Plots of (a) c vs. I for $V = 60$ m s^{-1} and (b) c vs. V for $I = 100$ A cm^{-1} ($F_N = 1$, 3 and 5 N cm^{-1}; - - -, $\mu_t = 0.2$; ——, $\mu_t = 0.4$).

V (m/sec)

Fig. 5. Plots of c vs. V for $F_N = 3$ N cm^{-1}, $\mu_t = 0.4$ and various values of I.

4. Conclusions

The following conclusions have been reached from the study.

(1) Many values of c and l may exist for given operation parameters I, V and F_N. Changes from one pair of c and l to another pair may occur during operation, independently of operating parameters. This change may be influenced by some unknown stability criterion.

(2) A moderate increase in I may cause a large increase in current density. This may result in greatly enhanced brush wear.

(3) The contact patch velocity c appears to be linear in V.

References

1 T. A. Dow and J. W. Kannel, Thermomechanical effects in high current density electrical slip rings, Wear, 79 (1982) 93.
2 R. S. Kilaparti and R. A. Burton, The thermoelastic patch contact problem for large Peclet number, J. Lubr. Technol., 100 (1978) 65 - 69.
3 M. D. Bryant and R. A. Burton, Thermal deformation in brushes for current passage through a steadily moving patch, Wear, 79 (1982) 83.
4 R. A. Burton and S. R. Heckmann, The thermoelastic transition from line to point contact, Wear, 59 (1980) 79 - 87.
5 C. P. Chen and R. A. Burton, Thermoelastic effects in brushes with high current and high sliding speeds, Wear, 59 (1980) 277 - 288.

LOW WEAR METALLIC FIBRE BRUSHES*

L. BOYER, J. P. CHABRERIE and J. SAINT-MICHEL

Laboratoire de Génie Electrique de Paris, Equipe de Recherche associée au CNRS 127, Universités Paris VI et XI, Ecole Supérieure d'Electricité, Plateau du Moulon, 91190 Gif-sur-Yvette (France)

Summary

Metal fibre brushes were tested against stationary surfaces over a wide range of relative speed (up to 100 m s^{-1}) for various mean (spatial) current densities J in dry argon or nitrogen. The experimental results presented are valid for several thousands of hours of test duration under "natural cooling" conditions. The various test facilities are described and results on voltage drop, friction coefficient, electrical and mechanical power losses and wear rate are given. For a pair of anodic and cathodic brushes under the working conditions described above, a total loss of 74 W cm^{-2} was obtained for $J =$ 50 A cm^{-2} at a relative speed of 100 m s^{-1} and for a packing density of 11.8%. The wear rate was 10^{-11}. Some experimental results obtained with a recently built apparatus which are described here indicate that the brushes are superior to the best commercially available brushes for a wide range of applications. Ongoing studies at the Laboratoire de Génie Electrique de Paris are briefly reported.

1. Introduction

The stability problem encountered with liquid metal slip rings has led the Laboratoire de Génie Electrique de Paris (LGEP) to undertake a study on multifilamentary brushes for about four years. In view of the results obtained at the International Research and Development Co. with metal-coated carbon fibres in an ambient atmosphere [1, 2], we surmised that the operation of very thin metallic filaments in a neutral or non-oxidizing atmosphere could be rather advantageous [3, 4]. The most difficult problem was to obtain a wire presenting a satisfactory compromise between its mechanical and electrical behaviour. A work-hardening copper alloy appears to offer the less expensive solution. However, when cold drawn to a sufficiently

---

small diameter (30 - 70 μm) the wire is usually inadequate for brush construction and a mechanical treatment is necessary to straighten it. A good compromise between a reasonable lifetime and overall (mechanical and electrical) performance was found by choosing a diameter of about 40 μm for the Cu-1.3%Cd-0.2%Sn wire first used. Considering the difficulties encountered by a research laboratory, at least in France, to get a small quantity of a new given material, we decided to build the machine to ensure the mechanical straightening of the fibres and thus to optimize the procedure required to get satisfactory brushes. Figure 1 shows an elementary test brush which consists of two fibre bundles presenting an overall area of contact of 1 cm^2. Each bundle is composed of 3000 Cu-1.2%Cd filaments 50 μm in diameter. The latter may be seen in Fig. 1 at the right of the copper block in which they are embedded and soldered. These Cu-1.2%Cd filaments allowed a better straightening treatment and therefore an improved packing factor than the 40 μm diameter Cu-1.3%Cd-0.2%Sn fibres shown on the left-hand side of the block. The bundle presenting the same apparent contact area of 1 cm^2 contains only 2500 fibres. Figure 2 shows an annular brush which was successfully tested under permanent working conditions with a current of 2500 A and a slip speed of 100 m s^{-1}. During the last two

Fig. 1. A two-bundle elementary brush made with 3000 Cu-1.2%Cd filaments (50 μm in diameter) lying to the right of the copper block in which they are tin soldered (scale in centimetres).

Fig. 2. An annular brush made with 2500 Cu-1.3%Cd-0.2%Sn filaments (40 μm in diameter) per centimetre squared of apparent contact area. Such a brush admitted a current of 2500 A at a velocity of 100 m s^{-1} on a bare Cu-Cr slip ring in permanent working condition (scale in centimetres).

or three years many similar interesting studies have been carried out [4 - 9]. The main applications are for d.c. and homopolar machines for land or sea propulsion units and inertial storage pulsed power sources. Results obtained in pulsed current applications will be published in a further paper. At present, a 250 kW homopolar torque converter is being built at LGEP as a heteropolar d.c. motor involving a fibre brush commutator unit.

2. Electrical and wear performances

2.1. Experimental apparatus

The electrical and wear performances of the fibre brushes were experimentally investigated using the specially designed apparatus shown in Fig. 3. The rotating disk can be driven up to 16 000 rev min^{-1} by means of a variable speed motor; the peripheral velocity of the disk is then about 120 m s^{-1}. The brushes can be positioned either on the two lateral flat faces of the disk or on its circumference. Most of the experiments have been carried out, however, with the filaments sliding at the periphery of the two parallel flat faces. An auxiliary metal fibre brush sliding on the circumference allows the voltage drop measurements for both polarities to be made. The disk is enclosed in a box, so that the operating atmosphere can be controlled in spite of some leakage at the rotating seal. The copper blocks to which the fibres are soldered can be positioned at a given distance from the faces of the disk, so that no force application system is required. This distance is adjustable from outside the box. The surface temperatures of the disk and of the fibre bundle are measured by an IR thermometer. The brushes are carefully cleaned and weighed before and after operation, so that fiber wear can be estimated using a high precision balance (resolution, 10 μg). In this apparatus, unlike that described below, no friction coefficient measurements can be made. Only a rough estimation of the mechanical losses is possible by the well-known separated power loss measurement technique.
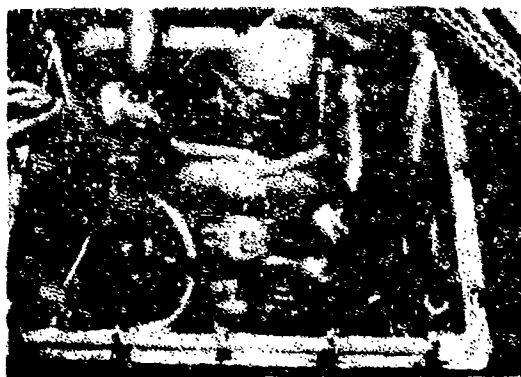
Fig. 3. A top view of the experimental apparatus used for electrical and wear measurements.

2.2. Electrical performance

The main interest has been in high speed applications (*e.g.* d.c. homopolar machines) and permanent working conditions. The previously described brushes are designed to be operated at sliding velocities of up to 100 m s^{-1} and for long test durations (up to 1000 h). At a slip speed of 100 m s^{-1}, two pairs of brushes (each pair presenting an overall contact surface with the disk of 1 cm^2) have been operated at an apparent current density J of 50 A cm^{-2} (mean space value) in permanent working conditions and without any cooling other than the "natural" radiation and accelerated convection due to the vortices induced in the box by the disk rotation. Under these conditions, the total voltage drop ΔV taking into account both polarities (including conduction in the filaments and in the bulk of the disk, constriction and film resistance effects) is not larger than 300 mV. This value is obtained for a very low wear coefficient of 10^{-11} and a mechanical power loss density of 74 W cm^{-2}. (The wear coefficient is defined in Section 2.3.) At zero or low speed operation, the admissible current density can be much higher. These performances are obtained in a neutral or non-oxidizing atmosphere such as dry argon or nitrogen. Electrical performance may be highly affected by hydrocarbon vapours and care has to be taken to avoid pollution of the cover gas by various degassing polymer products.

The voltage drops are found to be highly speed dependent, particularly at low speed (Fig. 4). This tendency seems to be much more important than for classical brushes. At zero-speed operation, the very low voltage drop encountered (10 mV for $J = 50$ A cm^{-2}) allows current densities up to 300 A cm^{-2} in permanent working conditions, depending mainly on the packing factor f. This behaviour may be of interest for some further applications in the intermittent contact field for example. No significant difference
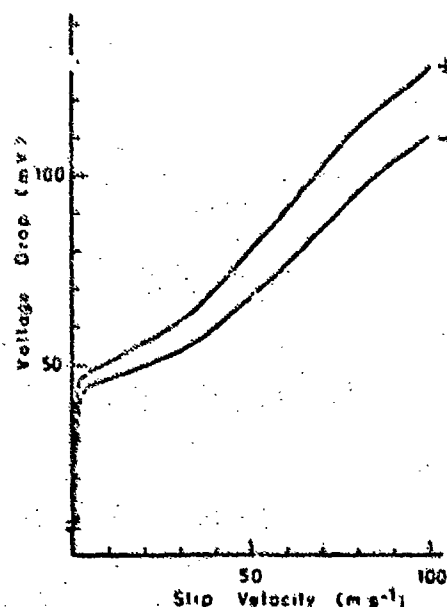
Fig. 4. Total voltage drop *vs.* slip velocity for both polarities.

has been noticed between the anodic and cathodic brush. Obviously, electrical performances are highly dependent on contact pressure, *i.e.* on the distance between the track and the copper blocks for a given fibre free length. The results presented above were for a compromise between good electrical performance and low wear. It should be emphasized that electrical performance, as opposed to wear, is not significantly dependent on the surface processing of the track (bare metal such as Cu–Cr or electroplated track).

2.3. Wear performance

To define the wear performance of this type of "non-solid" brush, a dimensionless wear coefficient $\tau = h/d$ defined as the ratio of the linear wear h of the fibre length (perpendicular to the contact area) over the sliding distance $d = vt$ is used. Such a definition is sufficient to relate wear to electrical performances. For reasonable accuracy, the distances covered by brushes are never less than 20 000 km, and they are sometimes more than 100 000 km. Figure 5 shows the various results obtained in nitrogen. When the electrical performance is as described in Section 2.2, wear rates range between 9×10^{-12} and 7×10^{-11}. If better electrical performances are to be obtained, wear rates will increase considerably. The wear rate is neither significantly velocity dependent nor fibre diameter dependent for the 40 and 50 μm diameters tested. The best results were obtained with Ni–Au electroplated tracks. Using such a plating, the wear rate τ is less than 1×10^{-11} for the nominal operating conditions ($J = 50$ A cm^{-2}; $\Delta V = 300$ mV; 20 m s$^{-1} < v \leqslant 100$ m s^{-1}).
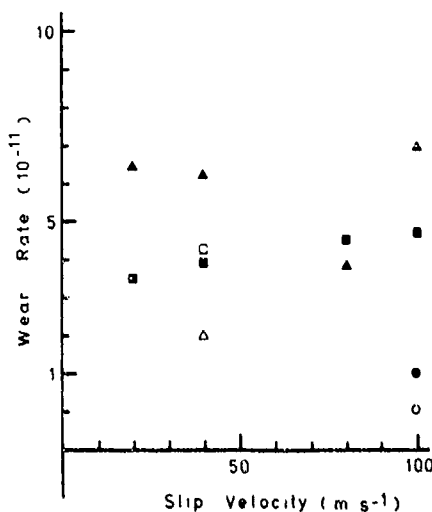
Fig. 5. Wear rate *vs.* slip velocity: ■, 40 μm diameter Cu–1.3%Cd–0.2%Sn fibre, + polarity, gold-plated track, $f = 6.3\%$; ▲, 40 μm diameter Cu–1.3%Cd–0.2%Sn fibre, – polarity, gold-plated track, $f = 6.3\%$; ●, 40 μm diameter Cu–1.3%Cd–0.2%Sn fibre, + polarity, Ni–Au-plated track, $f = 6.3\%$; ○, 40 μm diameter Cu–1.3%Cd–0.2%Sn fibre, – polarity, Ni–Au-plated track, $f = 6.3\%$; △, 50 μm diameter Cu–1.3%Cd–0.2%Sn fibre, – polarity, gold-plated track, $f = 11.8\%$; □, 50 μm diameter Cu–1.3%Cd fibre, + polarity, gold-plated track, $f = 11.8\%$.

3. Friction measurements

3.1. *Experimental apparatus*

In order to determine the mechanical losses of the sliding contacts with a greater accuracy, and to study the correlation between the collective friction coefficient (CFC) and the voltage drop, the experimental set-up shown in Figs. 6 and 7 was developed. The main features of this apparatus are as follows.

Fig. 6. The experimental apparatus used for the friction measurements.
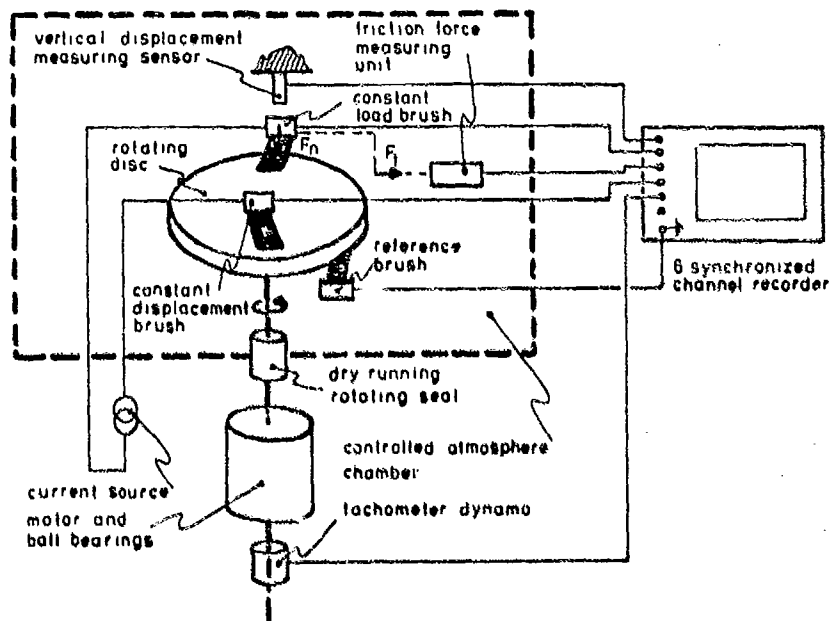
Fig. 7. Schematic representation of the experimental set-up shown in Fig. 6.

(1) The current flows across the disk thickness via two brushes: one brush is loaded by means of a dead weight and the copper block of the other is firmly maintained at a constant distance from the track.

(2) The copper block of the constant load brush is connected to one pole of the current source via a mercury force-free contact system.

A film of secondary pump oil covers the liquid metal in order to avoid the effects of mercury vapour. One of the voltage leads is plunged into the same mercury bath.

(3) The collective friction force (CFF) is measured by means of a system in which a crossed slab balance is supported by two elastic beams.

(4) The vertical displacements of the constant load brush, due mainly to changes in the CFF, are measured by an appropriate sensor.

(5) The two voltage drops, the CFF, the vertical displacement of the constant load brush, as well as the rotation speed, are plotted *versus* time on a six-channel recorder.

(6) The chamber containing the measuring system may be subjected to various atmospheres.

3.2. Results

Before each run, the disk as well as the brushes are carefully cleaned with trichlorethylene and alcohol. The chamber is filled with the chosen atmosphere. Since the measured quantities may vary intrinsically, all external parameters are carefully kept constant during a run. The value of the dead weight is determined in order to obtain a satisfactory compression of the non fixed brush: a rough estimation of the convenient load is given by the following formula:

$$F_N \lesssim N F_b \tag{1}$$

where

$$F_b = \frac{\pi^3 E D^4}{256 L^2} \tag{2}$$

is the buckling load of one filament and N is the number of filaments.

In eqn. (2), E represents the Young's modulus of the material, D is the fibre diameter and L is the fibre free length. Equation (2), with $E \approx 10^{11}$ N m^{-2}, $D = 5 \times 10^{-6}$ m, $L = 2 \times 10^{-2}$ m and $N = 3000$, gives $F_N \leq 0.56$ N.

As shown experimentally below (see Fig. 11) and theoretically in a future paper, the value of the CFC is of great importance for the determination of the brush compression. Consequently, several runs were performed with a dead load of 20 gf (0.196 N) in order to avoid excessive compression.

A typical record is shown in Fig. 8 which exhibits two time regions. At the beginning of the run the voltage drops of both polarities decrease while the CFC and the vertical displacement increase. At the end of the run the phenomena are inverted.

These experimental results can be interpreted as follows. Before a run, there are impurities on the sliding extremity of the filaments as well as on the disk and the shapes of the filament tips are not optimized. During the "running-in" period two processes occur: (a) some of the impurities present on the track as well as on the filaments are removed and (b) the filament tips are worn (mainly in the first run) in such a way that their real contact

66

area with the track increases. Hence two conditions, leading to a low contact resistance, are met: the surface film thickness is small and the real contact area is large.

It is considered that the phenomena occurring towards the end of a run are due to pollution of the atmosphere by a component (probably the base oil) of the ball bearing grease which seems to exhibit important bleeding.

An important conclusion drawn from the results shown in Fig. 8 is that the behaviour of the constant displacement brush is more satisfactory than that of the constant load brush. This is confirmed by Figs. 9 and 10 in which the voltage drops are plotted, for many runs, against the CFC for the two following systems: fibres on a gold track and fibres on CRM 16. Although exhibiting some dispersion, these results show clearly that the voltage drops decrease when the CFC increases and that the behaviour of the constant displacement brush is less sensitive to the friction process than that of the constant load brush.

The maximum CFC values found (about 0.52 for the gold-plated disk and about 0.83 for the CRM 16 disk) should not be definitely retained, because they correspond to a relatively dirty (see above) atmosphere. Further
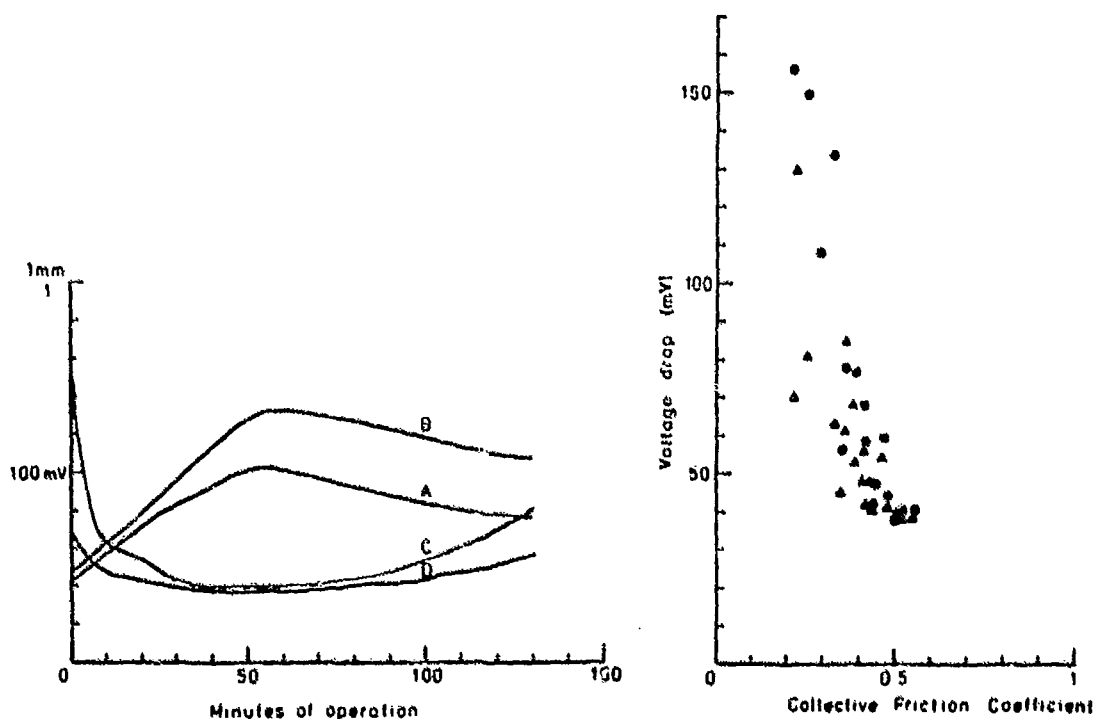
Fig. 8. Various records corresponding to a certain set of conditions (3000 filaments of Cu–1.2%Cd (diameter, 50 µm; free length, 20 mm) rubbing on a gold-electroplated CRM 16 disk; load, 20 gf; intensity, 10 A; slip velocity, 27.2 m s^{-1}): curve A, CFC; curve B, vertical displacement of the copper block (constant load brush); curve C, voltage drop of the constant load brush; curve D, voltage drop of the constant displacement brush.

Fig. 9. Correlation between the voltage drop and the CFC (experimental conditions as for Fig. 8): ●, constant load brush; ▲, constant displacement brush.

experiments with a suitable grease should be performed in order to clarify this point.

Figure 11, which shows the vertical displacements of the constant load brush against the CFC, demonstrates that the collective behaviour of the fibres is somewhat hysteretic. This may be due to the relative motion of the individual fibres composing the brush.

Nevertheless, this first experiment confirmed the values of mechanical power loss found with the apparatus described in Section 2.1.
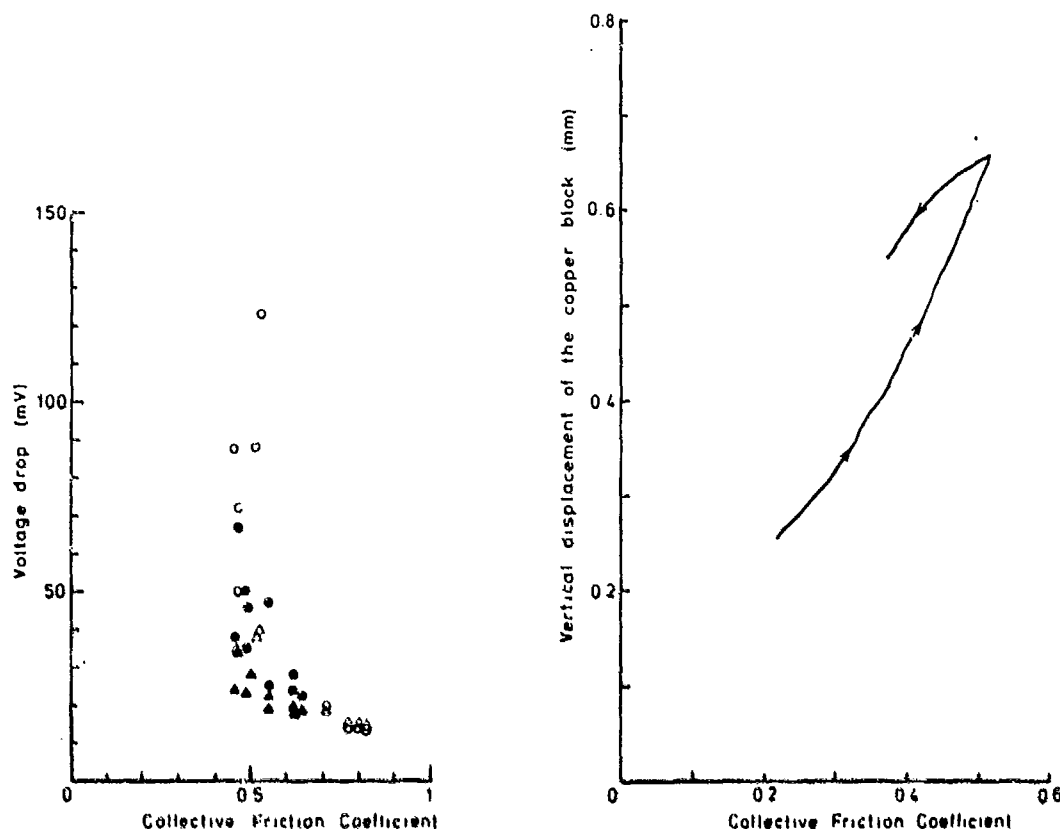
Fig. 10. Correlation between the voltage drop and the CFC (the brushes, load and intensity are the same as those in Figs. 8 and 9; disk, bare CRM 16): O, constant load brush, $v = 13.6$ m s^{-1}; ●, constant load brush, $v = 27.2$ m s^{-1}; ∧, constant displacement brush, $v = 13.6$ m s^{-1}; ▲, constant displacement brush, $v = 27.2$ m s^{-1}.

Fig. 11. Vertical displacement of the copper block (constant load brush) vs. the CFC.

4. Conclusions

The main conclusions drawn from the results presented are as follows.

(1) If appropriate techniques are used, straight fibres of cold-hardening copper alloys of diameter down to 40 μm can be readily obtained.

(2) These fibres can be assembled in order to form bundles which can be used as current brushes in various applications involving d.c. homopolar or heteropolar systems.

68

(3) When sliding on conveniently coated metallic tracks, these brushes exhibit low wear rates as well as low electrical and low mechanical losses, provided that they operate in a non-oxidizing atmosphere.

(4) The improvement in electrical behaviour during the running-in time is well correlated with an increase in the CCF.

(5) From the mechanical point of view, each brush exhibits a hysteretic behaviour which is probably due to an internal friction phenomenon.

Acknowledgments

References

1 A. D. Appleton, Developments with superconducting d.c. machines, *Proc. 4th Int. Cryogenics Conf., Eindhoven University of Technology, May 24 - 26, 1972*, IPC, Guildford, Surrey.

2 I. R. McNab and G. A. Wilkin, Carbon fiber brushes for superconducting machines, *IEE J. Electron. Power*, (January 1972) 8.

3 J. P. Chabrerie (ANVAR–DRET), *Fr. Patent 29,716*, September 1977.

4 M. Amiet, J. Barthélémy and J. P. Chabrerie (DRET), *Fr. Patent 27,526*, 1979.

5 I. R. McNab, Recent advances in electrical current collection, *Wear, 59* (1980) 259 - 276.

6 C. M. Adkins III and D. Kuhlmann-Wilsdorf, Development of high-performance metal fiber brushes, *Proc. 25th Annu. Holm Conf. on Electrical Contacts, 1979*, pp. 67 - 72.

7 P. Reichner, High current tests of metal brushes, *Proc. 26th Annu. Holm Conf. on Electrical Contacts, Chicago, IL, 1980*, in *IEEE Trans. Components, Hybrids Manuf. Technol., 4* (March 1981) 2 - 4.

8 O. S. Taylor and P. Reichner, Mechanical load aspects of high current brush system design, *IEEE Trans. Components, Hybrids Manuf. Technol., 2* (1) (1979) 95 - 99.

9 B. Singh and R. W. Vook, *In situ* AES characterization of rotating electrical contacts, *Holm Semin. on Electric Contact Phenomena, Chicago, IL, September 1980*, Illinois Institute of Technology, Chicago, IL, 1980, pp. 53 - 58.

A HOMOPOLAR MOTOR FOR THE DEMONSTRATION OF NEW HIGH CURRENT BRUSHES*

P. REICHNER and V. B. DOSHI

Westinghouse Electric Corporation Research and Development Center, 1310 Beulah Road, Pittsburgh, PA 15235 (U.S.A.)

(Received November 20, 1981)

Summary

Recent research has demonstrated that very high currents can be transferred efficiently across sliding electrical contacts under laboratory conditions. Further effort is required to apply these research concepts to practical machine designs and to determine their impact on such important machine parameters as power density, efficiency and operating life. Toward this objective, a high technology 50 h.p. homopolar motor was designed and built. It incorporates novel high current metal fiber brushes and water-cooled components in a configuration that has been optimized for maximum power density.

The machine provides a wide range of possible speeds and current levels for brush testing in a controlled environment and may operate as either a motor or a generator. Initial testing will be performed with copper fiber brushes, although other brush materials and configurations may also be evaluated.

---

1. Introduction

Under proper conditions, extremely high currents can be transferred across sliding electrical contacts. This has been demonstrated in recent research experiments with solid and fiber brushes [1 - 5] as well as with liquid metal current collection systems [6]. The ultimate objective of this research is the development of practical electrical machines of high power density and high efficiency. Liquid metal current transfer systems have the advantage of essentially 100% area coverage of the slip ring but they introduce problems of liquid containment, particularly for motors where inertial confinement techniques cannot be applied throughout the full operating

---

70

speed range. Commonly used liquid metals also have problems of chemical stability and compatibility, more stringent insulation requirements and even safety hazards. The recent experimental results with solid and fiber brushes promise efficient collector operation with good brush life.

In low voltage high current machines such as the homopolar (or unipolar) motor or generator, the current collector at conventional current densities is a major factor in machine size, weight and power loss. This is seen in the relative size of the spirally grooved collectors and the active length in the early machine shown in Fig. 1 [7]. Here, the active length is less than 10% of the rotor length.

Translation of experimental high current brush concepts into practical machine applications requires consideration of and control of a number of factors, primarily those associated with temperature and atmosphere. For example, three potential effects of increased slip ring coverage are as follows.

(1) There is a concentration of power dissipation, which will result in excessive temperatures unless adequate cooling techniques are employed.

(a)

(b)
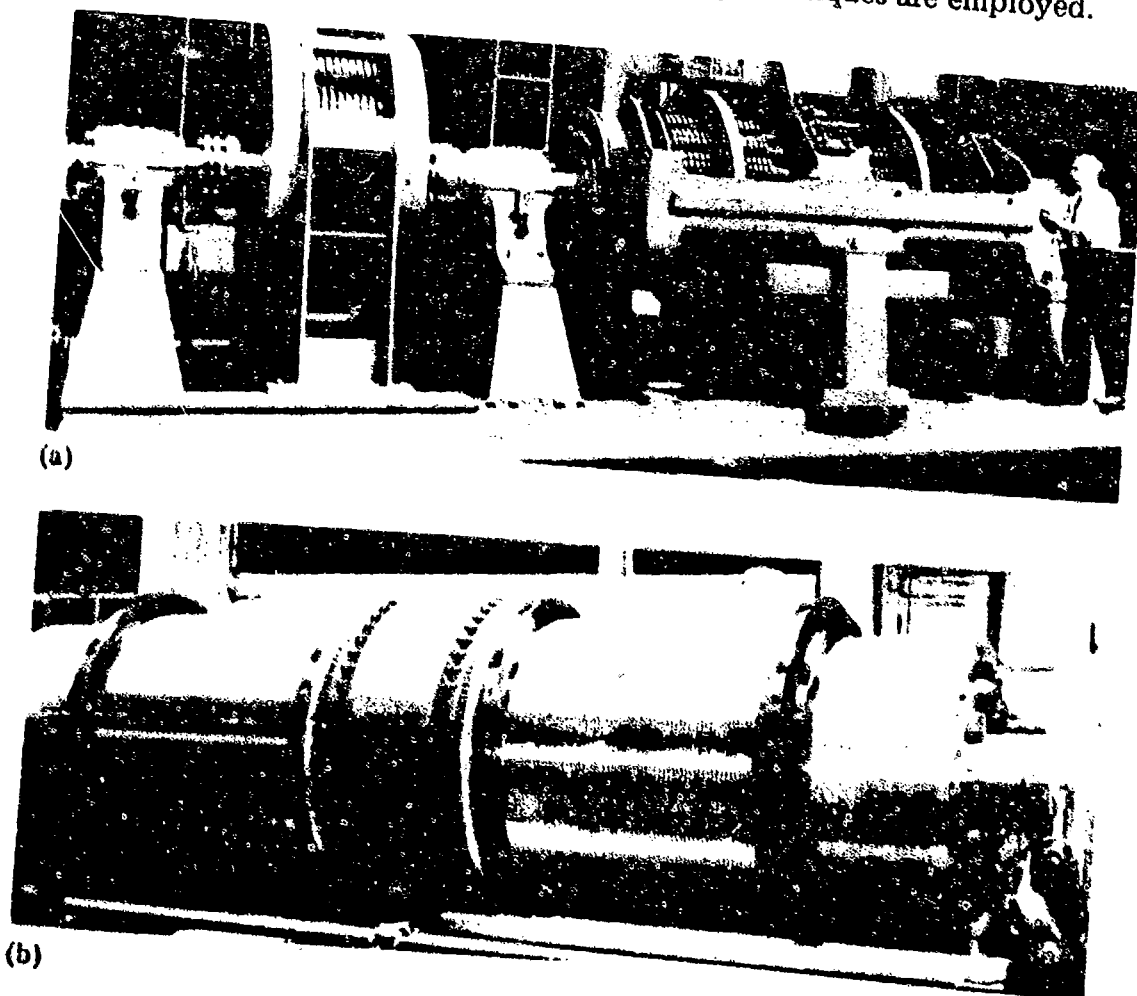
Fig. 1. Westinghouse 150000 A, 7.5 V, homopolar generator (1934): (a) machine assembly; (b) rotor. (From ref. 7.)

(2) The reduced access time of the track surface to the surrounding atmosphere may influence the effectiveness of lubricating films in the form of adsorbed or chemisorbed surface layers and could result in higher friction and wear.

(3) The increased concentration of wear debris, with reduced area for removal, could interfere with the intimacy of brush contact and possibly with the freedom of brush motion.

In addition, when the brush current density is greatly increased, the sectional area of the shunt lead wire, between the brush and the stator conductor, must increase. The shunt length may also be increased to maintain flexibility. The shunt and brush holder become major factors in the current collection system design. Inertial effects must also be considered in some applications, such as vehicular drives.

There is generally a trade-off between high power density and high efficiency, since higher current densities result in higher electrical loss and a higher magnetic flux density results in greater excitation losses and increased flux leakage. Flux leakage may also cause voltage gradients across the slip ring. Brushes which are designed to pass high currents efficiently will have a low contact resistance and therefore are more susceptible to circulating currents due to these voltage gradients. In general, high machine power density is achieved by minimizing magnetic path lengths, maximizing iron flux density and using high current density in conductors with effective cooling to remove the resulting power dissipation.

The objective of the present effort is to identify and evaluate important factors, introduced by a real machine application, through the design, fabrication and testing of a high technology 50 h.p. motor with metal fiber brushes. The motor is intended to be scalable to 400 and 1500 h.p. machine sizes for vehicle applications.

Significant design objectives include a power density of 1.83 kg kW^{-1} (3 lb h.p.$^{-1}$), a brush life at full speed of 120 h and reverse rotation capability.

2. Parametric evaluation

A simplified drum-type homopolar configuration similar to that shown in Fig. 2 was selected for analysis. The influence of a number of parameters on the power density and efficiency was evaluated, with the following values held constant for the study: back-iron flux density, 1.60 T; gap flux density (both radial and axial), 1.35 T; conductor current density, 7.75 MA m^{-2} (5000 A in^{-2}). Bearing, seal and windage losses were neglected. The assumption of equal radial and axial gap flux areas, in a simplified machine geometry, establishes the rotor radius as equal to the total active length. The shape of the excitation coil–collector cross-sectional area was chosen to minimize approximately the flux path length in the iron.

As shown in Fig. 3, there is an optimum machine voltage (per turn) for maximum power density at given values of the collector sliding velocity and
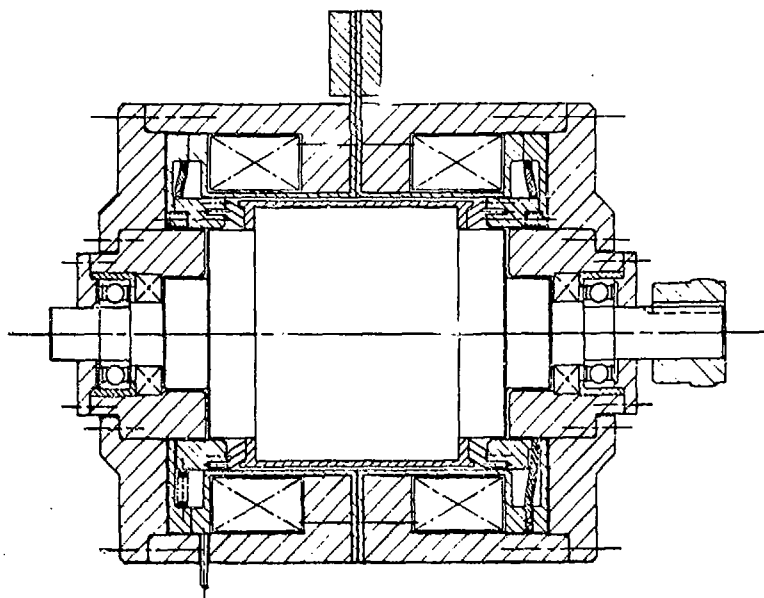
Fig. 2. Homopolar machine for high current brush demonstration.
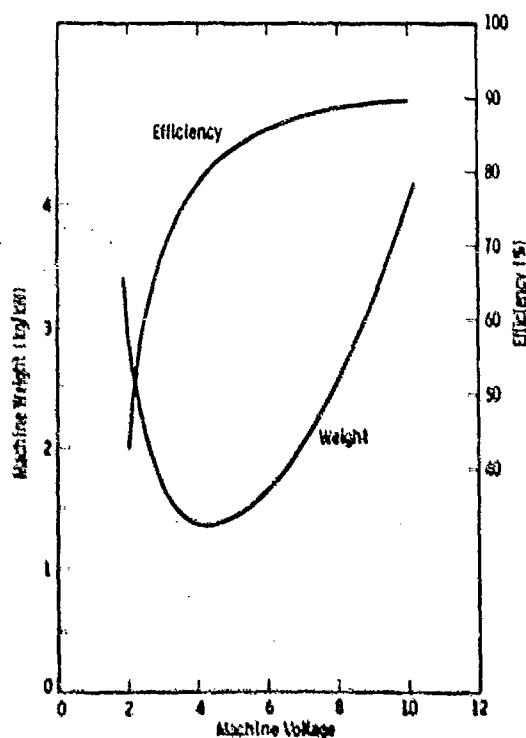
Fig. 3. Machine voltage optimization (50 h.p.; 75 m s^{-1}).

current density in the excitation coil and drum conductors. At the higher voltages, with fixed values of collector tip speed and gap flux density, a reduced voltage means a shorter active length and rotor diameter and therefore a lower weight. However, as the voltage becomes very small, the current must be increased accordingly. This eventually increases the conductor cross section, and thus the magnetic gap and excitation coil size, as well as the col-

lector length to the extent that the total machine size again increases. Figure 3 is based on a collector speed of 75 m s^{-1}, an average slip ring current density of 2.71 MA m^{-2} (1750 A in^{-2}) and an average excitation coil current density of 7.75 MA m^{-2}. For the slip ring, this is equivalent to a brush current density of 7.75 MA m^{-2} with a 35% area coverage. For efficiency calculations, a 60% area packing factor was assumed in the excitation coil to account for water channels and insulation. Based on previous experiments [3], a single-contact voltage drop of 0.1 V and a friction coefficient of 0.33 were assumed.

Although a single-turn machine was assumed, multiturn machines formed by concentric drum conductors would have similar characteristics with multiples of voltage, segmented (parallel) collector rings, and a correspondingly reduced machine current.

The parametric analysis showed an improved optimum power density for machines of higher power rating and also for increased collector sliding velocity. Furthermore, this reduced relative weight was less sensitive to voltage deviation from optimum at higher values of the power and the collector speed. The optimum machine voltage increased with power rating. Figure 4 clarifies the trade-off between power density and efficiency. It shows that a small increase in machine weight can give a significantly improved efficiency if the voltage is increased slightly above the optimum value.

Figure 5 shows the influence of brush current density. For the selected assumptions, it is seen that the power density is very sensitive to this parameter for values below about 3 MA m^{-2} (2000 A in^{-2}). The improvement is small beyond brush current densities of about 8 MA m^{-2}. Similarly, a significant reduction in machine weight can be achieved with average excitation
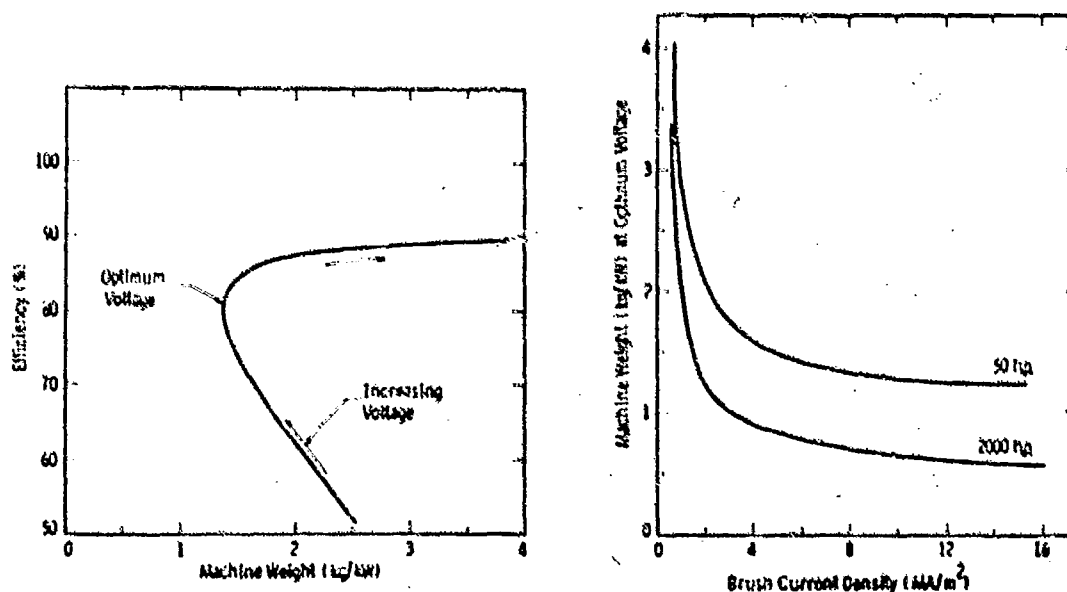
Fig. 4. Efficiency-power density trade-off (50 h.p.; 75 m s^{-1}).

Fig. 5. Brush current density effect on machine power density (single-turn; brush coverage, 35%; 75 m s^{-1}).

current densities up to about 8 MA m^{-2}, but the coil power loss increases and this has a significant effect on efficiency.

As a result of the parametric study, a 5 V single-turn machine was selected. The corresponding current is 7460 A and the rotor speed is 13 650 rev min^{-1}. A collector sliding speed of 75 m s^{-1} was selected as a reasonable objective based on the earlier fiber brush experiments.

3. Machine design

The 50 h.p. motor shown in Fig. 6 was designed and built as a high power density machine. It utilizes advanced technology approaches, such as multielement brushes at a high tip speed and high current density, as a possible forerunner for electric vehicle drive applications, and it satisfies the 1.83 kg kW^{-1} (3 lb h.p.$^{-1}$) weight objective. The reversible fiber brush current collection system is a key feature of the motor, which also includes a high current density excitation coil necessary for the high power density.

The magnetic and the electrical configuration of the demonstration motor is that of a basic drum-type homopolar machine. The motor is approximately 21.6 cm in diameter and 23.8 cm long (excluding the shaft extensions). The major components, shown in Fig. 2, are the rotor, the
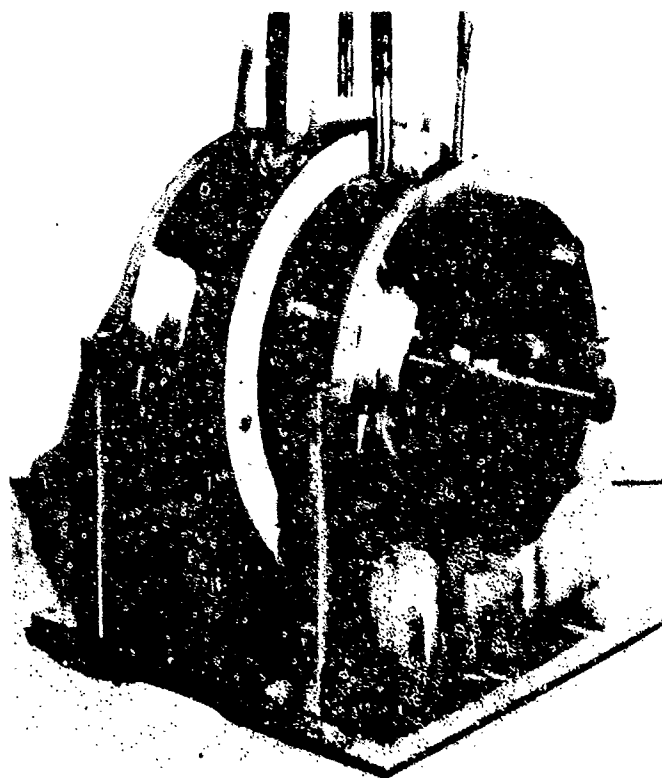
Fig. 6. Brush demonstration motor (50 h.p.).

stator, the current collectors and the end-housing assemblies. The stator halves are symmetrical about the axial center-line and each half consists of an inner copper return conductor, a cylindrical magnetic iron housing and an excitation coil. The return conductor sections are joined with low temperature solder and are insulated with polyimide sheet and tape. The iron housing serves as the flux return path as well as a structural support member. The magnetic end housings also perform the dual function of supporting the rotor through ball bearings and providing a flux return path between the stator and the rotor.

The rotor consists of a 2.54 mm thick cylindrical Zr–Cu armature which surrounds the water-cooled magnetic iron rotor core. These are separated by a 0.254 mm thick electrically insulating layer of aluminum oxide which transmits the armature shrink pressure and torque. The two drums which form the armature are soldered at a central joint location well away from the current collection area where the generated heat is at a maximum because of friction and electrical power losses and where bending stresses may arise from discontinuities in the drum thickness. Cooling water enters the rotor shaft through a rotating union, proceeds to each circumferential annulus adjacent to the slip ring through two diametrically opposite radial holes, and returns through two other radial holes located 90° away. The water passages are plated for corrosion protection. The integral rotor shaft is supported by conventional grease-lubricated ball bearings with nylon cages for high speed operation. To prevent circulating currents, the bearing is housed in an insulated sleeve of non-magnetic stainless steel. Because of its inherent high stiffness and small bearing span, the rotor critical speed is well above the operating speed. Dimensional tolerances of the two axial air gaps were designed to control the direction of any net magnetic force. The axial thrust is small and will be taken by one of the bearings.

The load current flows from a terminal flange at the axial center of the machine through the stator conductor, the current collection system, the rotor armature, and back to the other terminal via the second collector and stator conductor. The maximum conductor current density in the rotor and the stator is 7.75 MA m^{-2}. To avoid an additional magnetic gap and to minimize the magnetic forces on the output current leads, these are taken out radially at the center of the machine, where they do not cross the flux path. The leads are water cooled.

The circumferential current flows in the two helically wound excitation coils are in opposite directions so that the magnetic field enters the rotor in the same radial direction along the full active length. The water-cooled coils are wound from a hollow copper conductor, which is 0.58 cm square. The conductor current density is 11.6 MA m^{-2} and the average coil current density is 5.58 MA m^{-2}.

Initial magnetic analysis showed significant axial voltage gradients in peripheral slip rings which were located at the ends of the cylindrical rotor. Because of their low resistance, metal fiber brushes are susceptible to slip ring gradients which induce circulating currents at the interface. In subse-

quent design modifications, it was found that, if the rotor diameter was increased along its active length, the reluctance of the magnetic gap was reduced and the excitation coil became smaller. The resulting configuration was found to be quite adaptable to an axial brush configuration. The slip ring voltage across the brush width was calculated to be approximately 0.01 V for the selected axial slip ring configuration.

Any discontinuity in the magnetic iron that results in a non-uniform field at the air gap induces eddy current and hysteresis losses. A field analysis indicated that if the edge of a transverse hole is placed at least two diameters from the magnetic gap, the gap field distortion and losses are negligible. The radial holes leading to the annulus for slip ring cooling, and the bolts which clamp the two stator halves, were located on the basis of this criterion.

Non-uniformity in the return conductor current distribution also causes the rotor to see a time-varying magnetic field and generates eddy currents in the rotor conductor. For the demonstration machine, a departure from uniform axisymmetric lead connections to the cylindrical return conductor would result in a non-uniform stator current. Hence the output leads were designed as circular discs. Multiple equal-length flexible leads will be connected from the outer periphery of these discs to the bus bars from the main power supply.

A flux plot of the selected design indicated an armature voltage of 5.54 V for the collector tip speed of 75 m s^{-1} (13645 rev min^{-1}) and a maximum air gap flux density of only 1.1 T. This provided some margin over the nominal 5 V machine rating at the full load current of 7460 A. Transient and steady state thermal analysis indicated a temperature difference of only 8 °C between the copper drum and the iron, which is not sufficient to influence the shrink pressure required for torque transmission. The estimated collector temperature was 74 °C at maximum current.

To insure good performance of the metal fiber brushes, an environment of humidified carbon dioxide, at a slight positive pressure, will be maintained in the machine. A graphite seal at each end prevents the entrance of any contaminant into the collector region. No silicone bearing materials are used in the machine construction in order to avoid their possible adverse effects on brush operation.

4. Current collector

The selected fiber brush configuration draws on experience obtained recently with small metal fiber bundles and groupings of these bundles [3, 4]. With adequate cooling, these bundles of 168 copper fibers, each 125 μm (5 × 10^{-3} in) in diameter, have carried metal current densities as high as 100 MA m^{-2} (65 kA in^{-2}). Although a 50 m s^{-1} sliding speed was reached, most of these tests were run at 12 - 16 m s^{-1} and at current density levels of 12.4 MA m^{-2}. These high current densities have been handled with excellent brush life (dimensionless wear, 10^{-11} - 10^{-10}) and with low power
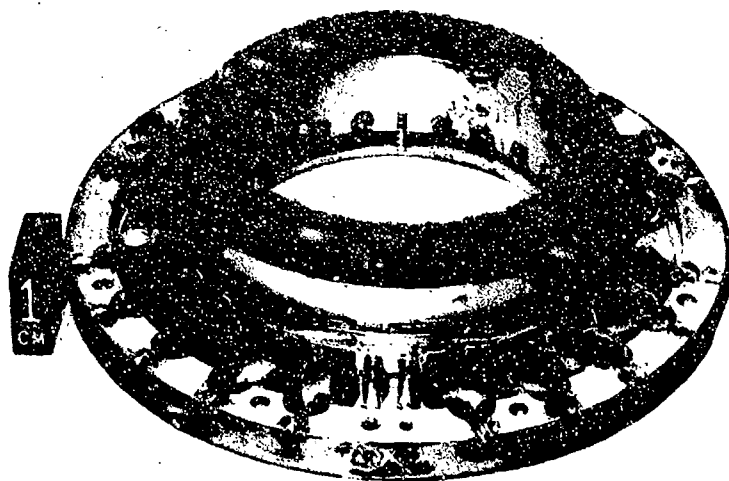
Fig. 7. Metal fiber brush assembly.

loss. The present brush design (Fig. 7) incorporates 150 of these bundles in each collector ring, and these will operate at 23.2 MA m^{-2} (15 kA in^{-2}) at the maximum machine current.

For the small homopolar machine, an axially applied brush appears to have advantages over conventional radial brush application to a peripheral slip ring. This relates to initial contour matching, cooling line flexibility and fiber packing density. Radially applied brushes must be segmented to allow for radial movement due to brush wear. To achieve good conformity of each brush to the slip ring periphery it would be necessary to "run in" these brushes prior to operation. A plane surface axial-face brush should be easier to produce, even for the full annular ring shown in Fig. 7. For a radial application, if direct water cooling of each brush segment is desired then flexible water lines must be connected to each segment. In contrast, each demonstration machine brush ring has only two pairs of flexible cooling lines. The brush rings are guided in their axial travel by two linear antifriction bearings, and the complete annulus is available for fiber bundles. Conventional radial brush holders would reduce the area available to brushes. The complete ring design also permits fewer brush loading springs to be used. (Only four are used in the present design.)

The most important factor in high current brush design appears to be temperature control at the sliding interface, in the brush body and in the flexible shunt leads. This is best accomplished through water cooling of the slip ring and of the brush body directly (rather than through the air gap to a brush holder). Metallic fibers, especially of copper, effectively remove heat from the sliding interface. In the demonstration machine, the brush water-

cooling system has been designed to remove all the predicted brush interface power loss.

Because of the complexity of the water-cooling lines, the flexible shunts and the spring loading system, the brush ring has been made separable to simplify brush replacement. This is accomplished by shrinking the brush ring onto the holder assembly which provides all the above-mentioned functions. This joint adds some small resistance to electrical and thermal transfer. For the selected shrink contact pressure, the additional voltage drop is estimated to be less than 5 mV at maximum current.

It is expected that at high slip ring speeds, the fiber flexibility will permit the brush to follow the slip ring irregularities effectively and the heavy copper fiber support ring will move only slowly, to accommodate brush wear. The copper fibers are applied at an angle to the slip ring (30° to the normal) to increase their flexibility. In a unidirectional machine, this angle would be oriented to place the fibers in a stable, trailing position. However, for machine rotation reversal this would cause a "stubbing" action. Therefore the brush fiber angle is placed in a plane that is normal to the direction of rotation and is thus symmetrical for rotation reversals.

The four brush loading springs provide a total contact force of 37 N (8.3 lbf) per ring. Based on single-bundle performance, the collector contact voltage drop is expected to be less than 0.1 V at the rated machine current.

5. Conclusions

A 50 h.p. motor was designed and fabricated for the evaluation of advanced high current brushes and high power density machine technology. High power density was achieved through the use of water cooling in high current components, high current brushes, and the selection of an optimum machine voltage. Since this sets the machine rotational speed, it will be necessary to consider gear box requirements when a specific application is defined. Although the machine was designed as a motor, which required brushes capable of reverse rotation operation, it is also directly applicable as a generator.

The machine provides a wide range of possible speeds and current levels for brush testing in a controlled atmosphere. For development or experimental purposes, alternative designs of the complete brush holder, or of the brush ring alone, may be substituted easily. Although it is presently limited to axially applied brushes, the collector design could possibly be modified to accommodate a radial brush configuration.

The optimum (single-turn) machine voltage increases with the greater machine power levels foreseen for vehicle and shipboard applications. The parametric analysis also indicates that power density and efficiency will be further improved for the machines of higher power rating.

Acknowledgments

References

1 J. L. Johnson and O. S. Taylor, High-current brushes. Part IV: machine environment tests, *IEEE Trans. Compon., Hybrids Manuf. Technol., 3* (1) (1980) 31 - 36.
2 I. R. McNab and W. R. Gass, High-current density carbon fiber brush experiments in humidified air and helium, *IEEE Trans. Compon., Hybrids Manuf. Technol., 3* (1) (1980) 26 - 30.
3 P. Reichner, High current tests of metal fiber brushes, *IEEE Trans. Compon., Hybrids Manuf. Technol., 4* (1) (1981) 2 - 4.
4 P. Reichner, Metallic brushes for extreme high current applications. In *Proc. 25th Anniversary Meet., Holm Conf. on Electrical Contacts, 1979*, pp. 191 - 197.
5 C. M. Adkins III and D. Kuhlmann-Wilsdorf, Development of high-performance metal fiber brushes: I, Background and manufacture; II, testing and properties. In *Proc. 25th Anniversary Meet., Holm Conf. on Electrical Contacts, 1979*, pp. 165 - 184.
6 J. L. Johnson, G. T. Hummert and A. R. Keeton, Liquid metal current collectors for homopolar machines, *IEEE Trans. Power Appar. Syst., 95* (4) (1976) 1 234 - 1 243.
7 E. H. Myers, The unipolar generator, *Westinghouse Eng., 16* (2) (1956) 59 - 61.

CARBON FIBRE FRINGE BRUSH*

B. R. G. SWINNERTON

Morganite Electrical Carbon Limited, Swansea SA6 8PP (Gt. Britain)

(Received November 5, 1981)

Summary

The fringe brush is now being manufactured commercially primarily for use on those undirectional machines which even with the best grade of conventional brush have considerable commutation difficulties at the leaving edge.

The work carried out by Morganite Electrical Carbon in developing the carbon fibre brush from the original all-fibre design to the present-day fringe brush is described in this paper. The latter combines in one brush the characteristics of conventional brush materials with the additional commutating advantages provided by having carbon fibres at the leaving edge of the brush. Brief details are given of the early laboratory experiments and the expansion of this work onto constructor test bed and field trials over a wide range of machines and applications.

1. Introduction

Early work was carried out with a brush which consisted of a bundle of carbon fibres prepared from carbon and graphite cloth laminates and then from high modulus polyacrylonitrile [1] as shown in Figs. 1(a) and 2. The fibres were held in a metal box and they were stiff enough to withstand light end-on pressure and in theory the brush seemed to offer considerable advantages over conventional brushes for commutating machines because of the very large number of contact points, the relatively high resistance across the brush and the inherent strength and flexibility of the fibres, which would enable them to follow surface irregularities of the collector without loss of contact. Thus the all-fibre brush was expected to give good current collection, good commutation and good brush life.

---

*Paper presented at the Advanced Current Collection Conference, Chicago, IL, U.S.A., September 23 - 25, 1981.
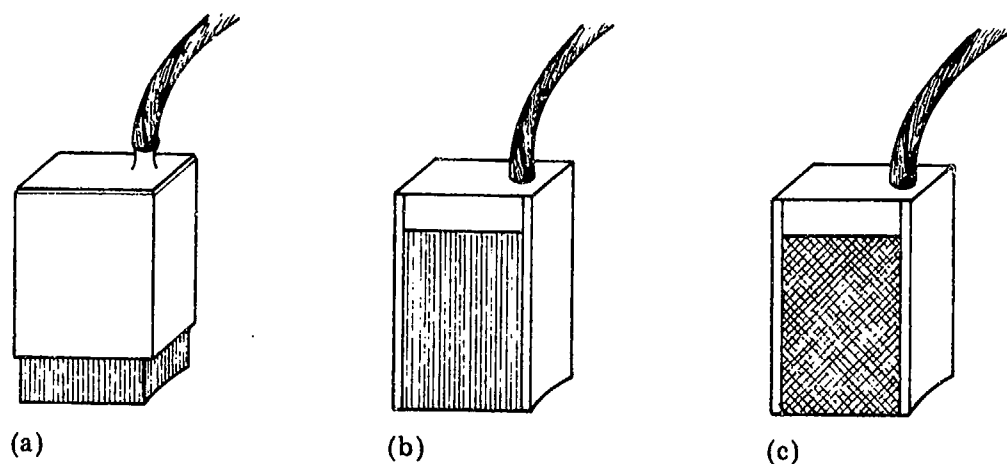
Fig. 1. Types of carbon fibre brush: (a) all-fibre brush held in metal box; (b) solid brush with carbon fibre fringe; (c) solid brush with carbon fibre tape fringe.
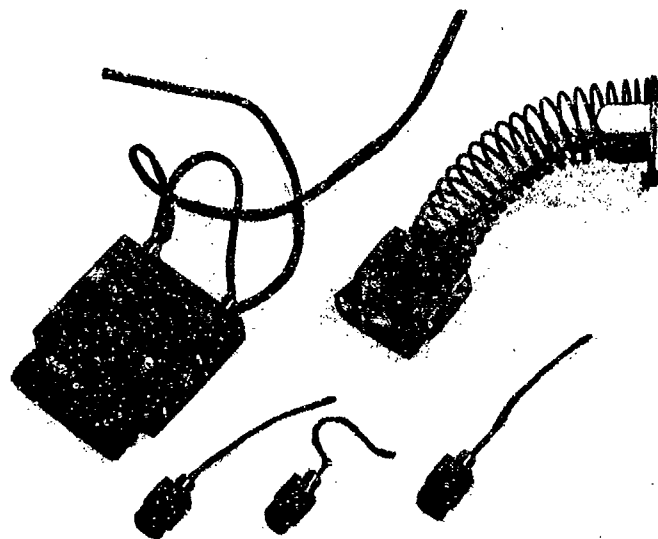
Fig. 2. Typical all-fibre brushes in metal holders.

2. Commutation testing with the all-fibre brush

A number of laboratory experiments were carried out to investigate these ideas further.

On a dummy commutator rig, the characteristics of the brush–segment voltage and of the brush–segment current were studied at the entering and leaving boundaries of each commutator segment passing under the brush for a range of intersegmental voltages. The segment–segment voltage was chosen as a variable parameter because it plays an important role in determining the sparkless commutation zone.

The brush to commutator segment contact resistance was measured for a solid conventional brush and an all-fibre brush for two intersegmental voltages as shown in Fig. 3. The resistance of the fibre brush–segment
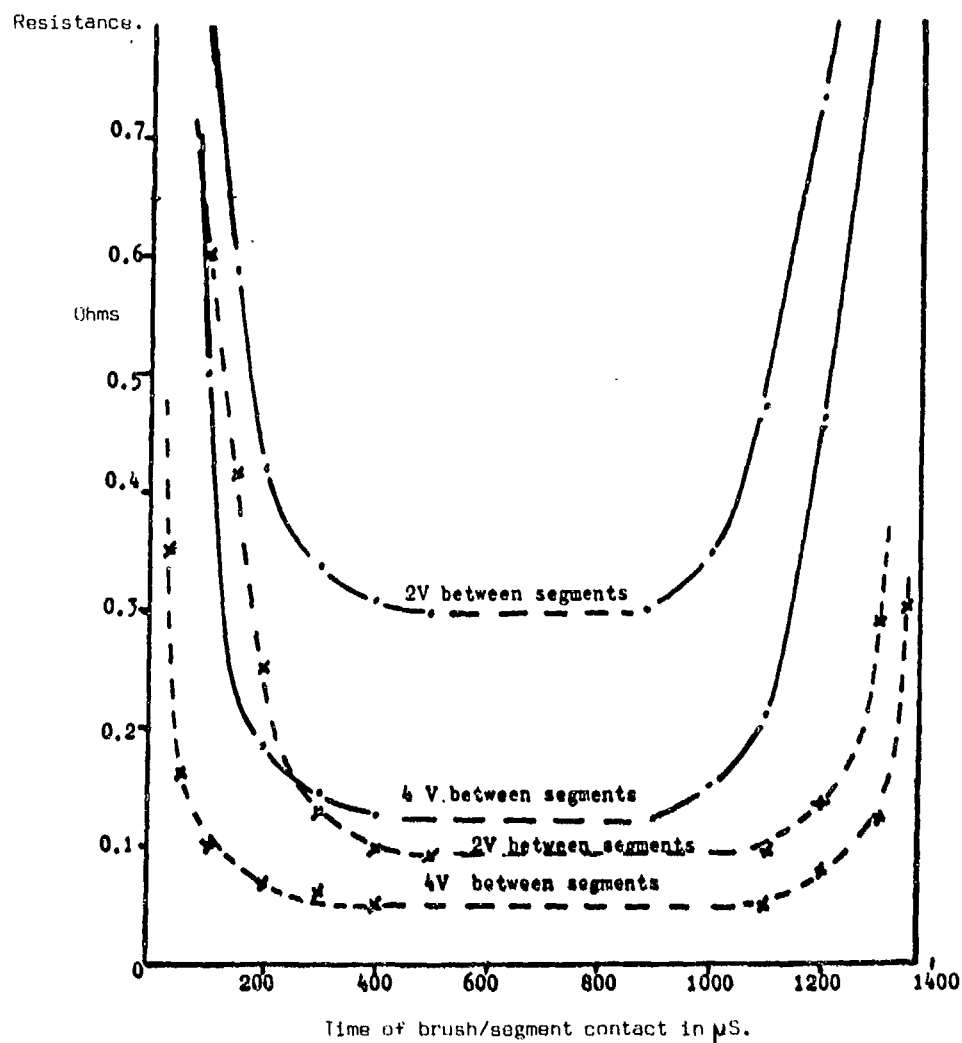
Fig. 3. Comparison of transfer resistance between segment and brush: —·—, carbon fibre brush; —×—, conventional EG-type brush.

contact was found to vary mo_a nearly in inverse proportion to the area of brush covered by the segment than that of the solid brush. Such conditions assist better commutation in that the rise and decay of current in the short-circuited coil itself occur within a shorter time. The higher interface resistance of all-fibre brushes was sufficient to produce resistance commutation and current was transferred without arcing when the brush–segment contact was broken. This occurred even at the higher intersegment voltages when conventional brushes were sparking, as shown in Fig. 4(b). Thus the all-fibre brush would run without sparking under more difficult conditions than the best grades of conventional carbon brush. Black band measurements on a 26 kW laboratory MG set confirmed these results, giving a large increase in band width of about twice that of a conventional grade EG14 brush. Fibre brushes ran satisfactorily at 31 A cm^{-2}, well above the limit for the EG14 brush on this machine.

84
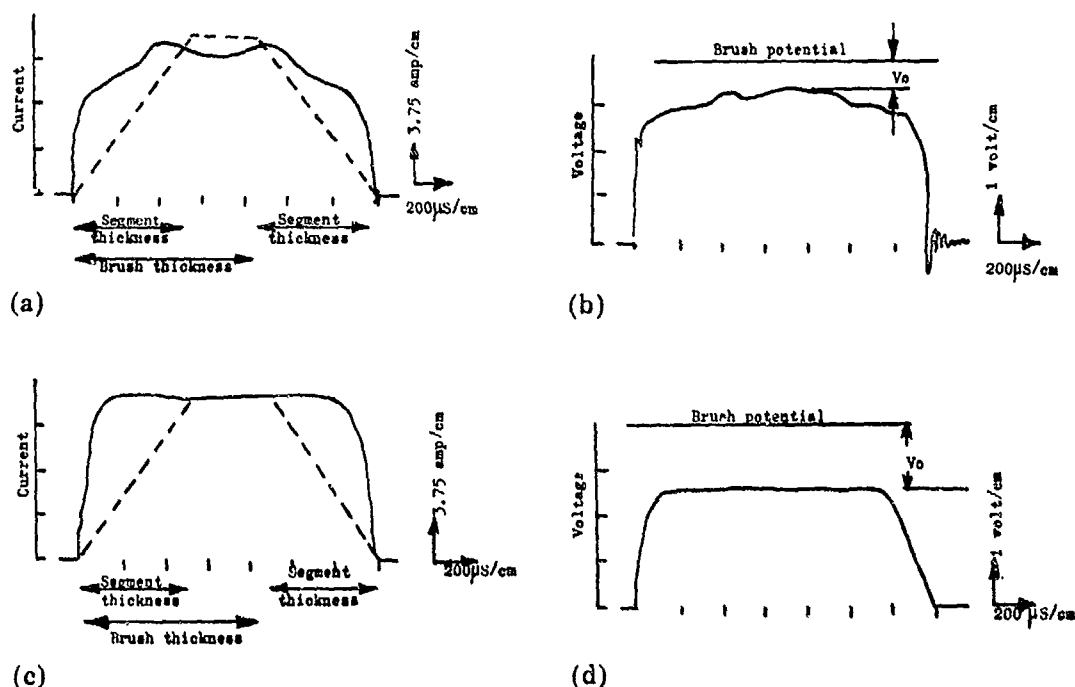
Fig. 4. Variation in brush–segment current and voltage: (a) segment current waveform for EG brush (- - -, theoretical current waveform); (b) brush–segment voltage waveform for EG brush (V_0, interface voltage); (c) segment current waveform for carbon fibre brush (- - -, theoretical current waveform); (d) brush–segment voltage waveform for carbon fibre brush (V_0, interface voltage).

Unfortunately, during the course of all these tests a major disadvantage of the all-fibre brush in the form described was seen to be a very high coefficient of friction, even at low spring pressures. This produced unacceptable track or commutator wear. Compared with conventional brushes, the contact voltage was also high owing to the deposition of a very dark matt film of mainly cuprous oxide.

To overcome these difficulties it was thought that the spillover combination [2] or connection of fibre and solid brushes in parallel would combine the contact characteristic of all-fibre brushes with the commutator filming and brush wear characteristics of conventional brushes and thereby offer a solution. However, some disadvantages were still apparent with this arrangement and the black band was not much better than for conventional brushes. Even when chisel-edged fibre brushes were made up and mounted in a metal fitting such that they could be placed in a brush box with the fibres making contact with the commutator in line with the leaving edge of other solid brushes on the same arm, the black band, whilst slightly better, was insufficient to warrant further investigation. This type of arrangement was aimed at utilizing the fibres only where they were needed at the leaving edge of the brush, as shown in Fig. 5(b).

(a)   (b)   (c)
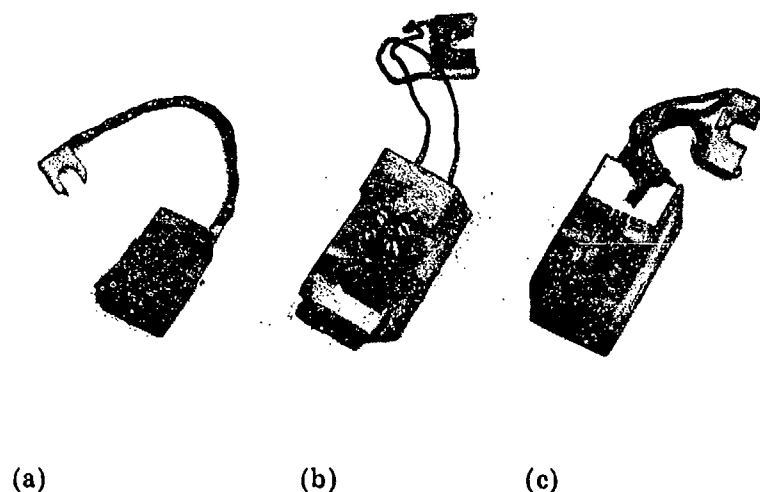
Fig. 5. Modmor fringe fibre brush and spillover design.

3. Fringe fibre brush

A further extension of the chisel brush idea resulted in a patent application being filed in 1971 for the fringe fibre brush [3, 4]. This design incorporated a fringe of carbon fibres attached to the leaving edge of a conventional brush and whilst initially the fringe consisted of a layer of rigid fibres glued at the top (Figs. 1(b) and 5(c)), better results were obtained with a woven carbon fibre tape, as shown in Figs. 1(c) and 6. The carbon fibres are only required to carry current when conditions are most difficult for the conventional brush, and so the fringe brush provides an excellent way of combining the good characteristics of both solid brushes and carbon fibres in one composite brush.

A major advantage of the fringe brush is that there is no need for the low spring pressure necessary for the all-fibre brush in order to reduce the frictional heat loss: therefore no modifications to the existing brush holders are required. Commutator wear is reduced to more normal levels because the comparatively thin layer of fibres has little effect on the skin formation of the base brush grade. Another advantage is that the full wearing length of the brush can be used and also, should sparking develop, the solid part of the brush will remain to prevent catastrophic wear of the brush and failure of the machine. Commutation test results on the 26 kW laboratory machine again gave a band width of about twice normal and, although it was not quite as wide as that measured with the all-fibre brush, the problem of high commutator wear rates had been overcome.

The fringe brush would thus seem to offer considerable advantages for machines where commutation is difficult or indeed for any machine design that can make full use of its superior commutating ability. There can be a number of reasons for poor commutation such as high output over a wide

speed range, rapid current and speed changes, high momentary overloads, operation from supply voltages with harmonic content and operation at high peripheral speeds or under conditions which may produce brush instability and a poor arc of contact.

In order to investigate further its use, Morganite initiated a world-wide programme of trials which were offered for both constructor test bed machines and user machines in the field. The objective was to fit the fringe brush to as wide a range of machines and applications as possible, and whilst initially the majority were with machine constructors for black band measurements, the number in the field on difficult commutating machines has increased. In fact this design of brush has now become a standard commercial product and is manufactured on the production line just like any other brush.

Another feature of interest with the introduction of the fibre fringe is brush design. Conventional brushes may be solid or, in an attempt to increase the real arc of contact, they may be split into two to four parts. If now the fringe gives excellent contact at the leaving edge then it may not be necessary to split the brush, provided that there are no collection problems under the brush. A number of tests have confirmed this and have shown that a solid fringed brush can give a black band equal to or better than a conventional solid or split assembly. A European Research Institute amongst others is investigating this on 41 kW development machines with single- and double-lap-wound armatures.

Other areas of interest which are being investigated on the test bed are operation with and without interpoles, at higher than normal current densities, on commutators presenting stability problems and on uprated machines. In the field the fringe brush has now been in use for some years on
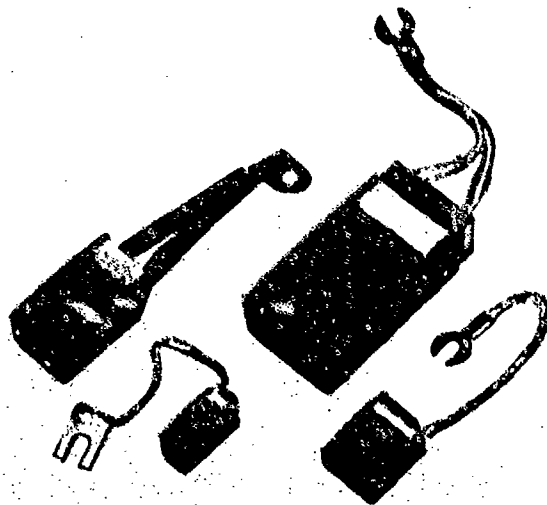
Fig. 6. Typical fringe fibre brushes using woven carbon fibre tape.

a variety of different machines and some of the more interesting applications and results are summarized in the next section.

3.1. Industrial d.c. machine applications

The machines on which results are available range from a 1.5 kW fan motor to a 3700 kW steel mill generator and a 3000 kW strip mill motor.

Black band measurements have been very encouraging and have confirmed the earlier laboratory results. Measurements taken by the General Electric Company for a 1280 kW generator are shown in Fig. 7 [5]. Similar results have been obtained by a number of other constructors in Gt. Britain and overseas and in some instances longer running showed up the additional benefits of reduced sparking, *i.e.* longer brush life and a reduction in commutator burning and damage. However, if commutation with conventional brushes is adequate, then there is not likely to be any further advantage with the fringe brush.
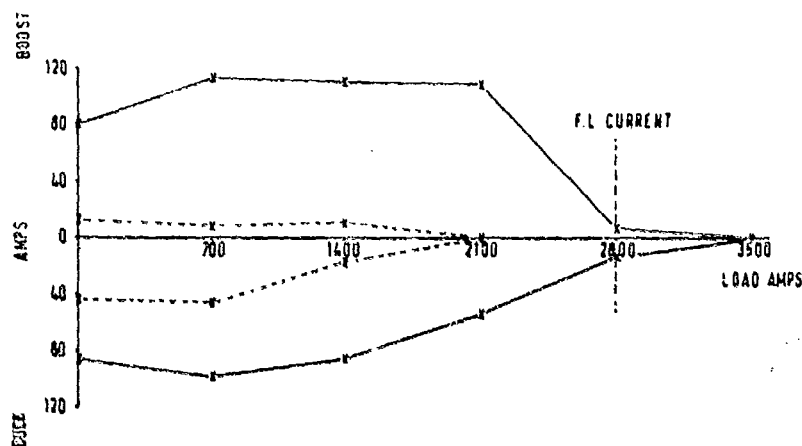
Fig. 7. Black band curves (1280 kW generator): - - -, electrographitic brush; ——, similar brush with fringe fibre.

Figure 8 shows another black band taken on the 3700 kW steel mill generator, enabling a comparison between the bands of a conventional brush and those of a grade EG236S brush fitted with fringe fibre. This machine was very highly rated, having to withstand peaks a factor of 3.2 times greater than the full load (19 500 A). Whilst saturation seemed to be occurring at the higher currents, the fringe brush produced a very marked improvement in the black band width and an extension to the sparkless zone.

The black band results on the test bed have demonstrated the ability of the fringe brush to improve commutation performance on all types of machine and on difficult machines in particular to reduce the amount of spark damage to the brush and commutator.

Commutator and brush erosion due to sparking [6] can be a major cause of excessive brush wear and commutator damage in the field, which may then further deteriorate to produce commutator flatting or the possibility of a flashover [7]. Longer running field trials were therefore fitted to

88
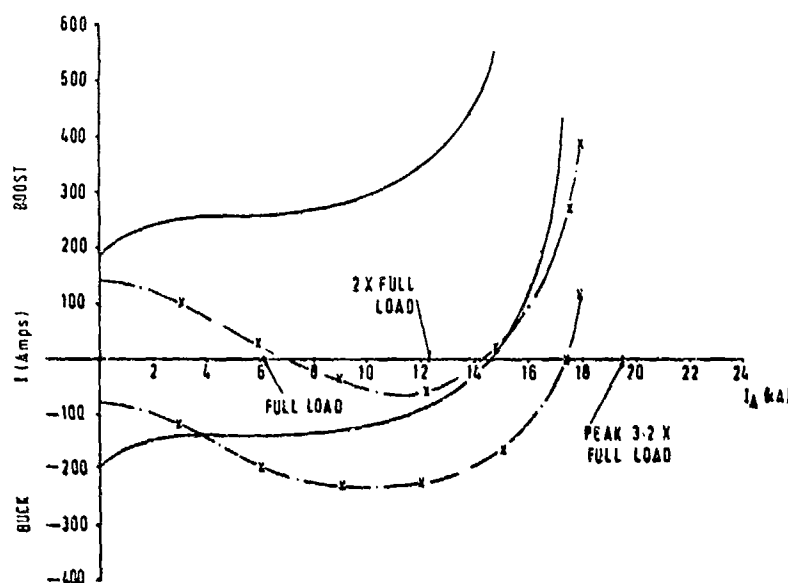
Fig. 8. Black bands for conventional (— · —) and fringe fibre (——) brushes.

see whether the improvement in commutation occurred in practice with the fringe brush without the appearance of any harmful side effects.

3.1.1. Tube mill motors

A long running field trial was held for 9593 h over a 2.5 year period on a 2015 kW d.c. piercer motor in a tube production plant. Peak currents of about 11.6 A cm^{-2} were reached in practice four times a minute and the commutator peripheral speed ranged up to 36 m s^{-1}.

Originally, a conventional four-part brush was fitted to ensure good current collection and commutation at the peak design load of 19.2 A cm^{-2}, but poor commutator condition and excessive brush wear occurred.

Fringe fibres were fitted to the four-part brush and an excellent brush wear rate was achieved (3.1 mm (1000 h)$^{-1}$ or 320 h mm^{-1}). Brush wear with conventional brushes was much worse: 12.7 mm (1000 h)$^{-1}$ or 80 h mm^{-1}.

The fringed brush design was then changed to a two-part brush and again brush life was considerably better than with the conventional four-part design. The commutator exhibited some wavy axial wear but this did not appear to have been caused by the fibres.

3.1.2. Paper mill motors

Fringed brushes were fitted to a 41 kW thyristor-fed paper mill motor because of very poor commutation which produced commutator bar burning and eventually led to flashover. The supply was full wave but the motor had solid interpoles and a peaky waveform, although the current density (4.7 A cm^{-2}) and peripheral speed (12 m s^{-1}) were both low.

Normally, the commutator had to be refurbished every 3 - 6 months and total maintenance costs, together with loss of production, were

estimated at about £6000 year $^{-1}$. Fringe brushes have now run for a number of years without any significant commutator wear that can be attributed to the fibres and without flashovers.

A 340 kW paper mill motor with a six-pulse supply and large ripple content similarly suffered from poor commutation which produced slot pitch marking, and the subsequent bar damage meant that the commutator had to be reskimmed fairly frequently. The fringe brush ran virtually black with just faint sparking at the outer ribs where there was no fibre fitted.

3.1.3. Wire and rod mill rotors

A 22 kW thyristor-fed wire-drawing motor had similar problems to the paper mill machines. With conventional brushes, it was normally operated at reduced speed in an attempt to contain the sparking and streamering from the leaving edge of the brushes. However, even at reduced speeds this still produced the occasional flashover. With the fringe brush, commutation was considerably improved, enabling the motor to run satisfactorily even at the maximum speed of 31 m s^{-1}. The full-load current density was 9 A cm^{-2}. Fringe brushes have been used for over 2 years, during which time maintenance and sudden breakdowns have been considerably reduced.

A 600 kW thyristor-fed rod mill motor had difficulties with commutation which were probably exacerbated by the mechanical shock of the billet as it entered the mill. With conventional brushes, a regular sequence of slot pitch marking was observed which quickly deteriorated and the segment burning produced had to be removed by reskimming the commutator after a fairly short period of operation. With the fringe brush, the motor ran black across the fibre width with slight sparking at the outer ribs. After operation for almost 1 year, the performance appeared to have improved with reduced commutator damage although the commutator skin developed a fairly dark dull lined appearance.

This type of tarnish skin can be typical of fringed brushes and is due to the carbon fibre tows in the tape producing alternating light and dark lines or bands of different skin thickness. Whilst it may not look as good as a nice uniform conventional brush skin, experience so far has not shown any obvious differences in commutator wear.

3.1.4. Steel mill machines

Sparking can occur underneath the brush contact face because of circulating currents or difficulties with current collection, and under these conditions the fringe brush does not offer any advantage. An example of this was on a large 3000 kW strip mill motor where considerable under-brush and leaving-edge sparking was occurring.

The fringe brush reduced the intensity of sparking at the leaving edge at peak loads of up to 14.3 A cm^{-2} but the under-brush sparking still produced burning of the commutator bars such that the presence of an overall improvement was difficult to ascertain, although this might have shown up over a long period if the commutator had been refurbished at the start.

A very difficult application in a cold mill involved some 360 kW coiler generators. These suffered from excessive sparking, particularly at peak loads, which resulted in bar burning and eventually led to the necessity of reskimming the commutators. The fringe fibre has succeeded in reducing the intensity of sparking and commutator damage.

3.2. D.c. traction

An area of considerable interest for the fringe fibre brush is its performance on traction machine application and, in particular, its use on reversing traction motors, where of course it is necessary to fit the fringe on both outer faces of each brush. Results on the test bed have been very good and for a 385 kW traction motor and a 368 kW high speed train traction motor, black band widths at least twice as wide as with conventional brushes were again obtained with both visual and sparkmeter recordings of sparking.

The increase in band width was in fact the greatest under the more difficult commutation condition of high speed at light load under weak field.

In addition, some other interesting features were observed. Normally, conventional brushes undergo a lengthy bedding-in and adjustment period to attain the ideal commutation position, whereas it was found that the fringe brush did not require this settling-in time but would commutate satisfactorily on full load almost immediately. Once again, good contact at the leaving edge was achieved through some of the marginally longer fibres. This point was also demonstrated when the direction of rotation was reversed. With conventional brushes this would initially result in double bedding with contact at the entering edge and a reduction in the time available for commutation. With the fringe brush it was apparent that contact was also being made at the leaving edge fringe because very faint sparking was observed here, whereas the outer ribs of the brush were black and obviously completely out of contact.

The field tests with this brush design, however, did produce a side effect. On certain traction motors it was observed that there was slight entering-edge marking and wear on the commutator segments, which must have been caused by the impact between the fibres on the entering brush face and the commutator segments at the high peripheral speeds of up to 50 m s^{-1} encountered on these motors. Whilst some motors ran for more than 1 year without any further deterioration, more work is necessary to investigate this wear in more detail. The fringe fibre brush has thus been expanded primarily on unidirectional machines where this damage does not occur.

3.3. A.c. machines

Not many results for a.c. commutator motors are available and more work is being carried out.

An excellent performance has been achieved on the NS-type motor where the fringe brush enabled an increase in the normally accepted maximum current density to be made without any increase in sparking.

In addition, it appears that the excellent contact via the fringe fibres not only improves commutation and collection performance but also handles circulating currents more effectively. On a 300 kW frequency converter on the test bed a considerable improvement in performance was achieved compared with conventional brushes.

3.4. Fractional horse-power machines

At the smaller end of the scale, on motors of less power than 1 kW, improvements in commutation performance with the fringe brush have not been readily observed, and it could be that on this type of machine the fringe fibre is unable to handle the high level of spark energy dissipated at the leaving edge. However, on motors slightly larger (about 1.5 - 3 kW) than this, where high rotational speeds of greater than $10\,000$ rev min^{-1} are encountered (such as on fan motors), or where inherent vibration is experienced on machine tool applications, the fringe brush has been very successful and is fitted by constructors to original equipment.

A particularly arduous duty with a peaky supply and high rotational speed (up to $11\,000$ rev min^{-1}) on a 1.5 kW motor resulted in a poor brush life of 420 h and bad commutator bar marking. With the fringe brush commutator marking was reduced and brush life more than doubled. It was considered that modifications to the supply system could also have improved commutation on this motor, but the fringe brush offered a much simpler alternative.

4. Conclusion

Whilst the test bed black band tests have shown the possible electrical advantages of using carbon fibre fringed brushes, the field results so far on industrial machines have highlighted the benefits in practice without any apparent side effects.

The improved commutation performance has given a reduction in commutator bar marking and erosion, fewer flashovers and an increase in brush life. These improvements overall have often produced considerable maintenance savings and less machine and production down-time.

Acknowledgments

References

1 N. L. Parr and E. R. W. May, *Br. Patent 1,105,826*, 1968.
2 J. J. Bates, J. Stanway and R. F. Sansum, Contact problems in machines using thyristor-assisted commutation, *Proc. Inst. Electr. Eng.*, *117* (2) (1970) 387 - 397.
3 J. Cunningham, *Br. Patent 1,369,835*, 1974.
4 R. J. Cooke and M. J. Tomaszewski, Carbon fibres in brushes for large electrical machines, *Proc. 4th Int. Carbon and Graphite Conf., London, 1974*, Society of Chemical Industry, London, pp. 716 - 726.
5 B. Skenfield, Assessment and improvement of commutation performance of d.c. machines on time-varying supplies, *Int. Machine Conf., London, 1974*.
6 B. R. G. Swinnerton and M. J. B. Turner, Sparking and arcing in electrical machines, *Proc. Inst. Electr. Eng.*, *113* (8) (1966) 1376 - 1386.
7 B. R. G. Swinnerton and M. J. B. Turner, Flashover in electrical machines, *Proc. Inst. Electr. Eng.*, *115* (7) (1968) 980 - 986.

OPERATING EXPERIENCE WITH THE FRINGE FIBER BRUSH*

ALFRED MARCUS

Safety Electrical Equipment Corporation, Division of Stone–Platt Industries, Limited, Wallingford, CT 06492 (U.S.A.)

(Received November 5, 1981)

Summary

A new technology emerged in the late 1950s when the carbon fiber was transformed from a laboratory curiosity into a practical product. The fringe fiber brush is an extension of the original all-fiber brush, in which a fringe of carbon fibers is fitted to an otherwise standard brush. The fibers, which are positioned at the trailing brush edge, provide a "paint brush" effect to maintain contact with the rotating surface. This surface contact is provided under all conditions of surface irregularity and vibration. The fibers prevent brush bounce sparking and serve to conduct current at the trailing edge with a resistance-effect type of commutation.

The development and the initial commercial tests have demonstrated the remarkable degree of improvement in commutation and brush performance when compared with the conventional brush. The brush is presently in widespread use throughout Gt. Britain and Europe.

This paper details the supportive data and test experience of the first large-scale application of the brush in the U.S.A.

1. Introduction

From the very beginning in the understanding of the principles underlying the design of d.c. machines, the designers realized that the problems associated with the collection and transfer of current would be a major factor in limiting machine output. In his classic paper, Lamme [1] noted that "Probably the most serious limitation in direct current machinery is

---

that of commutation." He goes on to list "the apparently distinct limitations, such as sparking at the brushes, flashing at the commutator, burning and blackening of the commutator face, picking up of copper, etc., which in reality are very intimately related to each other".

Throughout the years, there have been many significant advances made in the associated areas of commutation and current collection from the time of Van Depeole's introduction of the carbon brush for traction motors in 1889 [2] and the use of interpoles in 1900 to, most recently, the use of "adjuvants during WW II" [3]. It has also been said [4] that "During the past few years, a new type of brush has been developed which uses carbon fibers for electric current transfer across sliding surfaces. A method of construction is used which enables each fibre to flex individually so as to conform to the slip ring or commutator surface. The basic advantage of the construction is that, unlike a solid (or monolithic) brush, a large number of electrically parallel, but mechanically independent contacts, are available for current transfer." In the relatively short time that the carbon fiber was transformed from a laboratory curiosity to a practical product [5, 6], those of us who are involved in the design and manufacture of d.c. machines have seen the beginnings of the most significant advance in brush technology since the introduction of the carbon brush. It can, indeed, now be stated that the limitation in machine output due to the problems inherent in the current transfer and in restrictive commutation have finally been overcome with this unique brush. The brush is now in widespread use throughout Gt. Britain and Europe. However, up to the present time, other than for the special tests conducted for the high current test programs, there has been no significant use made of the carbon fiber or fringe fiber brush in the U.S.A.

The test results involved in the first major application of the fringe fiber brush here in the U.S.A. are described and detailed in this paper. The test experience of its use on small d.c. motors in use on the San Francisco Municipal Railroad (MUNI) and on the Metropolitan Boston Rapid Transit District (MBTA) is discussed and tabulated together with the results of the supportive laboratory tests which preceded the introduction of the brush into the field.

2. Elements of good performance

A d.c. machine which leaves the manufacturer's test floor should be able to meet the general criteria for good brush performance. In the literature, the criteria for acceptable brush performance have been listed in many ways [2, 3, 6, 7]. A typical listing, as in ref. 7, is as follows: (1) freedom from injurious sparking; (2) negligible commutator wear; (3) uniform filming over the commutator surface; (4) minimum electrical and mechanical losses; (5) good brush life.

McNab and Johnson [2] include operating stability and current-carrying capability as key items.

3. The mechanism of wear

It is generally accepted that brush wear cannot be attributed to any single mechanism [2]. The factors which do influence brush wear include (1) friction (including the effects of adhesion, particle transfer and fatigue), (2) pressure, (3) surface speed, (4) current transfer (and the related degree of sparking), (5) surface condition, (6) atmospheric condition and (7) the nature of the materials used.

Hessler [8, 9] surveyed the literature in the mid-1930s and found "very little qualitative information concerning brush wear". He ran a series of tests and deduced that the rate of wear was intimately related to the conduction of current across the contact surface and, further, noted that "wear at zero current shows that ordinary abrasion does not account for more than a small portion of the total wear". After an extensive series of tests, he concluded that "combustion (arcing–sparking) might account for a major portion of the wear".

In later years, Shobert [3] elaborated on the mechanism of wear, detailing Holm's original work in which the concept of "fritting" was first put forth. Holm et al. [10] "compares the influence on brush wear exerted to arcs with that of transient high voltages called flashes" and found that "flashes" cause more wear than arcs.

It is a fact known to all users of d.c. machines, as well as a fact confirmed in the laboratory, that the very existence of sparking in any significant degree will almost always result in a high rate of brush wear. In many instances, sparking will deteriorate the commutator surface, which in itself leads to even more sparking and to a more accelerated brush wear.

It is in this area of brush sparking, either due to an improper commutation adjustment or to a poor surface condition, that the fringe fiber brush has made its most important contribution. In the many cases investigated [11 - 13], conditions which would normally result in abnormally high wear with a conventional brush have been basically contained by use of the carbon fiber or fringe fiber brush. Bates [14] noted in his investigation of specially commutated d.c. machines that "no solid carbon brush has been found to be capable of coping with the rapid current changes" and he found that the carbon fiber brush, either by itself or in parallel with a solid brush, could make his specially designed machines function. The amazing capability of the fringe fiber brush is shown in Figs. 1 and 2. The figures illustrate the difference in wear which occurred when both the conventional brush and the fringe fiber brush were operated on a burned bar commutator.

4. Brush contact stability

Machine designers will generally agree that the maintenance of a good brush-to-contact surface interface is a key factor in providing acceptable brush performance. Hellmund [15], in his paper on brush jumping,
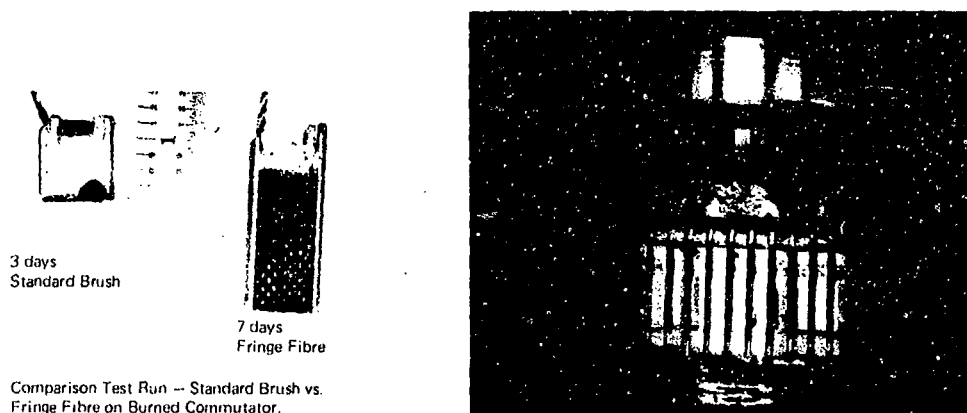
Fig. 1. Comparison of the wear of a fringe fiber brush and a conventional brush when they were operated on a burned bar commutator. The conventional brush is shown after 3 days wear, and the fringe fiber brush after 7 days of wear. The brushes were the same length at the start of the test.

Fig. 2. Burned bar commutator on which the comparison wear test was made. Note the areas of bar etching.

concluded that flashing will occur at high speeds when the brushes jump. He stated that increased spring pressure, many brushes per arm, good design practice and a good stable contact would minimize the problem. Hunter-Brown and Hews [16] found that preferred brush angles and brush box design improved the brush stability and minimized the effects of surface irregularities. Schobert [17], McNab and Johnson [2] and Belt [18] also investigated the problem of maintaining good surface contact and discussed several methods of providing acceptable brush and surface contact interfaces. Belt [18] suggested that improved contact efficiency may be obtained in a practical manner with existing design methods, which include the use of circumferential stagger, tandem brushes and split brushes. He further stated, "these are methods which should be considered for all important or high speed machines".

Finally, available to the d.c. machine user and designer is a new practical and simple means of achieving that all-elusive and very important brush contact stability. As an added bonus, the fringe fiber brush also provides the advantage of a high resistance contact at the trailing edge.

5. The first major American application

The first major American use of the brush was in 1980 on small trolley coach blower motors rated at 2.45 h.p., 3900 rev min^{-1} and 575 V. The motors provide cooling for the traction motors and the associated electronic systems on the Boeing Vertol standard light rail vehicles (SLRVs) which are in service on the MBTA Green Line. In January 1981, a test to determine the principle life was started on similar SLRV cars in service on the MUNI. A

formal approval for fleet-wide use of the brush in San Francisco was given in July 1981.

The SLRV was developed by Boeing Vertol under the sponsorship of the Urban Mass Transportation Administration as a universal replacement for the original Presidents Commission Cars. The intent had been to use the SLRV on all major streetcar systems in the U.S.A. The cars are powered from overhead trolley lines and are propelled by two separately excited field d.c. motors rated at 210 h.p. The motors are controlled by a solid state chopper [19]. For maximum system output, the motors and the associated electronics are individually forced-air cooled by high speed d.c. blower motors. The rating characteristics of the motors are shown in Table 1.

TABLE 1

Performance characteristics of an SLRV blower motor[a]

Motor parameters
    Power, 2.45 h.p.; voltage, 575 V nominal (range 450 - 750 V); current, 4.3 A; series wound with 10 Ω buffer; enclosure, TENV; poles, 2 main, 2 commutating; design, 87 bar commutator with one brush–stud (size, 0.25 in $\times$ 0.5 in); commutator diameter, 4 in

Speed–load characteristics

Rated	Actual
450 V, 3.6 A, 3500 rev min^{-1}	450 V, 4000 rev min^{-1}
575 V, 4.3 A, 3800 rev min^{-1}	575 V, 4600 rev min^{-1}
700 V, 5.0 A, 4400 rev min^{-1}	700 V, 5200 rev min^{-1}

---

[a] Data for an actual run with car 3422 from the A end of the MBTA Green Line.

Soon after the introduction of the cars in.. service, it was found that the blower motors were subject to rapid brush wear and severe bar burning. Typical modes of failure are shown in Figs. 3 and 4. The relevant factors in the design were checked and found to be within the limits of good design practice. It was apparent that the conditions of operation, including higher than rated speeds, excessive blower wheel vibration due to a build-up of debris and occasional line spikes, created a condition of poor commutation and improper current transfer. To improve on the performance, it was decided to embark upon a modification program which included the following changes.

(1) The original radial coil spring trigger brush box was changed to a 10° trailing constant-tension box assembly.

(2) The plain graphite type of brush was changed to a resin-bonded slotted-face type.

(3) A mechanical antiswirl air device was added to improve the air flow and to bring the speed down to the rated 3900 rev min^{-1}. (The original speed was high because of lighter than expected loading.)

(4) A wheel clean-out port was added to allow easier cleaning on a regular maintenance basis.
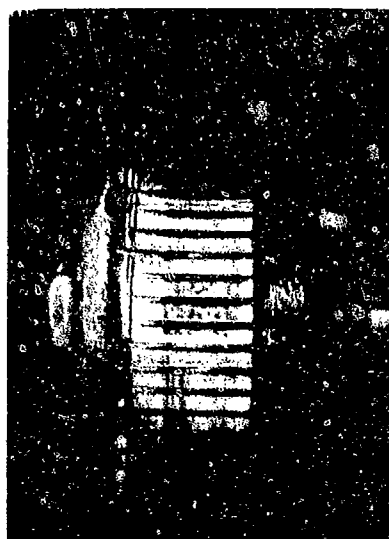
(a)   (b)

Fig. 3. Typical commutator appearance on failed units: (a) burned bar; (b) short brush operation.

Fig. 4. Left side, start of burning; right side, advanced stage of burning.

(5) The brush boxes were repositioned for easier access. This change was only made on the Boston cars. The improved access allowed for simplified brush change-out. One of the problems identified had been an improper insertion of the brush in the radial box where the top angle was put in the wrong position relative to the trigger.

(6) The new box and brush were keyed to allow for only the correct position insertion of the brush.

The original and new-style box assembly and brushes are shown in Figs. 5 and 6.

In all, 800 motors will have been modified in this manner. It was during the time of the laboratory tests with the new box design that a program was also started to test the fringe fiber brush. A series of life tests was conducted with the new slotted-face resin-bonded graphite and the fringe fiber brush. It was soon apparent that the fringe fiber brush was outperforming the conven-
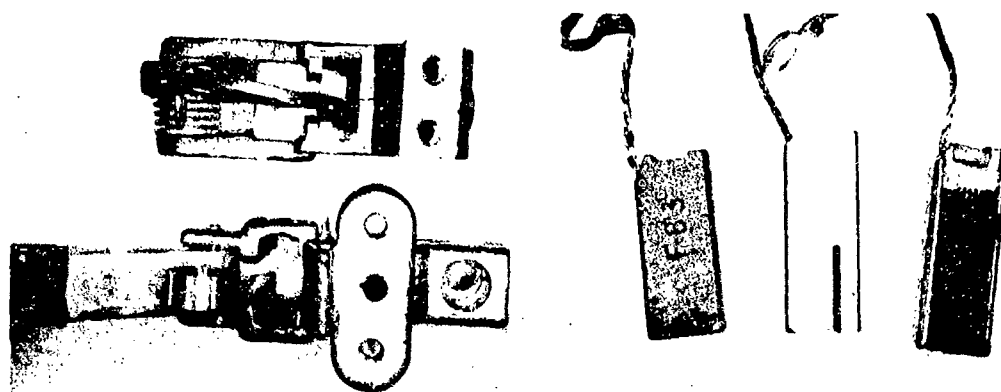
Fig. 5. Original trigger-style radial box and the new-style constant tension trailing angle box.

Fig. 6. The three styles of brush used: left side, original radial brush; center, resin bonded graphite with slotted face; right side, final fringe fiber brush.

tional brush. As the fringe fiber brush was relatively unknown in the U.S.A., and there was customer concern about its wide-scale use, it was decided to use the conventional brush for the initial retrofit program. The conventional resin-bonded graphite brush did have the capability of providing the specified 2500 - 3000 h brush life, and it had been proven to be successful in other similar applications.

The performance and life tests with the fringe fiber brush were continued. In the summer of 1980, a 1500 piece brush order was placed in the anticipation of the eventual phase-in of the fringe fiber brush after the completion of the demonstration and limited field tests.

6. The original laboratory tests

A sequence of tests was conducted with the fringe fiber brush to demonstrate fully its unique capability and suitability for use on the SLRV blower motor application. The description of the several tests and the results are given below.

6.1. The burned bar running test

This is the test which initially demonstrated the unique operating capability of the brush and which led to the placement of the initial 1500 piece order.

The modification program included a 2 - 4 h acceptance test run. On occasion, a unit will show as faulty because of an eccentric or rough commutator. In these cases, the conventional brush will spark and, if continued in service, will in time cause a burning of the commutator. A rejected unit was kept in test for several days to observe the rate of wear and the long-term effect of a condition of this nature. In 3 days of operation, the brush wore its full wear length and burned the commutator. A pair of fringe

100

fiber brushes was installed on the machine without seating or cleaning the surface. Commutation immediately showed black and, as time progressed, it appeared that the surface was starting to clean up. As shown in Fig. 1, after 7 days of operation there was minimal wear on the fringe fiber brush. It was then apparent that the fringe fiber brush could operate under the worst of surface conditions and could provide acceptable performance.

In another case, an improperly wound armature was put into test; the conventional brush wore out in a matter of hours. After 3 days of operation, the fringe fiber brush showed considerable wear but not to the extent of the conventional brush. A photograph of the brushes which were used is shown in Fig. 7. In both cases, the "cathodic brush" exhibited wear, whereas the "anodic", or positive, brush did not wear to any significant degree.
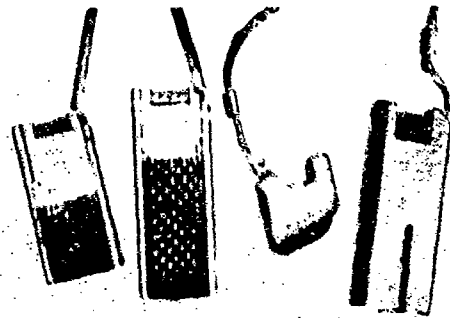
Fig. 7. Comparison of conventional and fringe fiber brushes after operation on a mis-wound armature. Time: conventional brush, 3 hours, fringe fiber brush, 3 days. Note the difference in wear due to the effect of polarity.

6.2. The life test

The objective of the change to the fringe fiber brush was to achieve an increase in the brush life. The projected and actual test life of the conventional brush was 3000 h. The projected life of a fiber brush was 7000 h. It finally exceeded this projected life at the conclusion of the test. The test data are given in Table 2.

Black band tests were taken to compare the commutation capability of the original brush with that of the fringe fiber brush, with the following results: original resin-bonded graphite, 0.1 A; fringe fiber brush (without fiber), 0.29 A; fringe fiber brush (with fiber), 0.52 A. The normal current of the motor is 4.3 A.

As shown by the data, the fringe practically doubled the black band width. The improvement in performance cannot be attributed to the change in grade.

TABLE 2

Test started	June 18, 1980, at 575 V and 3900 rev min^{-1}
Test completed	June 12, 1981. Actual running time, 7800 h
Brush length	Start: 1.3 in Finish: positive 0.8 in; negative 0.7 in Allowable wear: 0.6 in
Conditions	The commutator surface was excellent with a good film. There was no grooving or wear on the commutator, and there were no indications of smutting or burning. A photograph of the commutator at the conclusion of the test is shown in Fig. 8
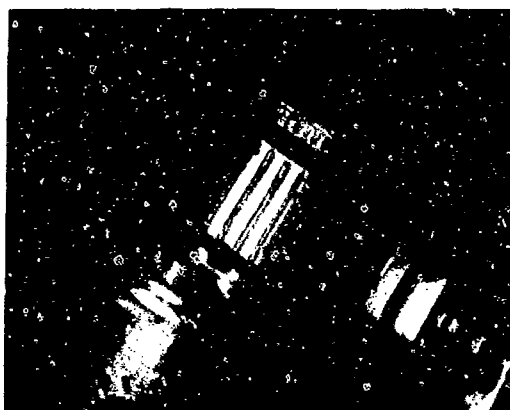
Fig. 8. Commutator appearance at the conclusion of the 7800 h fringe fiber brush life test.

6.3. Test for the mixing of grades

On occasion, especially in a change-out program of this nature, a mix of brush grades and types could occur. The fiber brush was operated with the conventional brush in each polarity position. No adverse results were noted. It was concluded that an inadvertent mix during the change-out program would not create any operational problems.

6.4. Test for the effect of varnish in the slot

The modification program included an armature clean-up with a varnish dip and bake. On occasion, some varnish could remain in the slots. A unit was operated with partially filled slots to observe the effect on the fringe fiber brush operation. The commutation was not affected and the unit showed good surface appearance after 6 months of operation. A photograph of the commutator surface at the conclusion of the test is shown in Fig. 9.

The implications of this capability are far reaching for the industry. It may be possible to use subflush mica commutators and to avoid the necessity of cleaning out the slots when a suitable varnish is used. The slots could also be purposely left full. This would keep debris out of the slots, reduce
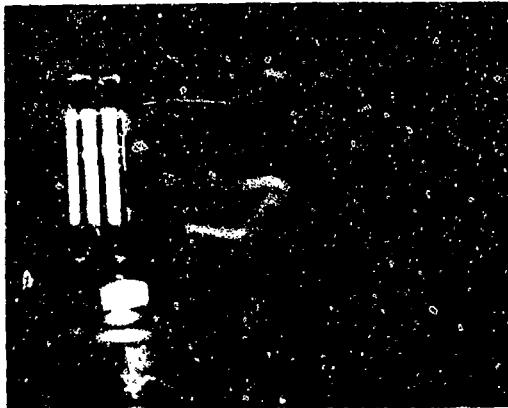
Fig. 9. Commutator appearance of a varnish-filled slot after 6 months of operation with a fringe fiber brush. Note the filled slot at the upper end of the slot.

the likelihood of copper drag-over and prevent bar-to-bar shorting due to such conditions.

For this test a solventless polyester varnish was used. The conventional brush did not provide acceptable performance when operated under the same slot-filled conditions.

6.5. Operation with long fibers

On occasion, it was observed that the fibers would not wear at the same rate as the main carbon body. When this occurred, the fibers could extend as much as 0.25 in beyond the brush edge. Operation under these conditions did not show any adverse effects. In time, the fibers did wear or burn away. It was also noted that the rotational windage tended to lift the fibers away from the surface. Additional investigation will be required to determine why, on occasion, the fibers do not wear at the same rate as the brush body. For maintenance purposes, the maintainers have been instructed to snip away the excess fiber when this condition is observed during a routine brush inspection.

6.6. Operation with the fibers at the leading edge

One of the problems encountered during the original operation of the motors was that of incorrect brush insertion. If the top angle was reversed, this could lead to a radial face instability. The modified boxes and brushes were keyed to accept the brush in the correct position. In applications in which a keyed box is not used, the effect of operation with the fibers at the leading edge is of much importance. A test was set up with the fibers in the leading position. After several months of operating, no adverse results were noted on either the brush face or the commutator. The fibers appeared to wear at the same rate as the brush and were not swept under the brush face. It should be noted that tests conducted on traction machines were discontinued after it was found that the fibers could be swept under the brush face with adverse effects. Additional work in this area is indicated for both the manufacturer and traction brush users.

6.7. *Operation without fibers*

The question was raised as to whether the performance improvement was due to the grade used in the main brush body. The grade (IM-26) is also of resin-bonded graphite. It does have a higher commutating capability than the conventional brush. This was demonstrated by the early black band tests. Although no long-term life tests were conducted with the fringe removed, the early indications were that the fiber is necessary to achieve all the indicated results. The brush operated without the fiber on a faulty surface commutator did exhibit the same rapid wear as the conventional brush. It was concluded, on the basis of the few tests taken, that the fiber is necessary for the long-term improvement of performance.

7. The field tests

The proximity of the Boston cars to the Safety Electrical Equipment Corporation plant allowed for an early start of field testing of the brushes. Several cars were chosen at random. An informal field test was started in conjunction with the laboratory tests. Although exact brush measurements were not taken, the field test results after 3 months of operation confirmed the laboratory test findings of improved life and performance. The engineers at the Boston Transit Authority agreed to a phase-in of the fringe fiber brush on the basis of the initial field and laboratory tests.

In the case of the San Francisco cars, the operation was still under the control of Boeing Vertol. (At the time this paper was written, a formal approval by Boeing Vertol for the change to fringe fiber brushes in San Francisco was in preparation. As noted previously, the Boston operating group had initiated the change at the start of the year.) Before approval for the change could be granted, it was necessary to demonstrate formally the brush capability in a controlled 6 month field demonstration test. This test was initiated in January 1981. The test program included a total of ten cars chosen at random. Five cars were fitted with fringe fiber brushes and five were set up with new conventional brushes. In all, 30 motors, 3 per car, were to be involved in the test program.

The test preparations included the following: (1) inspection and observation of the commutator condition; (2) a running smoothness test; (3) the measurement of the brush length; (4) motor identification and tagging.

Brush measurements and observations were to be made on a monthly basis. Also to be recorded was the actual time in service and miles of operation at the time of brush measurement. The initial observations and conditions are shown in Table 3. The test data after 3 months of service are shown in Table 4.

7.1. *Comments applicable to the test*

After the initial 4 months of operation, the fringe fiber brush test demonstrated conclusively that the brush would be able to provide more

TABLE 3

Starting conditions for the MUNI brush life test (special inspection and test program San Francisco MUNI SLRV blower motors) (units in test and inspection from January 12, 1981 to January 15, 1981)

Car	A traction unit	ECU[a]	B traction unit	Distance (miles)	Comments
Fringe fiber test[b]					
1253[c]	353481	352285	351442	21915	Stone-clean B traction unit
1264	349760	353550	352256	18882	All in order
1266	350518	366105	350293	19870	Horizontal ECU boxes
1268	349787	350591	352254	16242	Confirm serial number A traction unit
1283[d]	353584	350277	353518	9208	—
BG-530 present brush: control test[e]					
1214	352351 (1.34)	353502 (1.32)	352322 (1.31)	9245	Bar burn in A traction unit
1235[f]	350586 (1.34)	352357 (1.34)	352388 (1.31)	22545	Box burn in ECU
1263	353497 (1.23)	351449 (1.10)	353489 (1.21)	21886	All in order
1272	352211 (1.29)	350515 (1.25)	350600 (1.27)	13626	All in order
1278	352343 (1.33)	352308 (1.33)	352349 (1.33)	6973	All in order

[a] ECU, electronic cooling unit (blower for all chopper controls).
[b] Units were identified with a white paint spot on the end bell; all brushes were new (length, 1.34 in) with no seating.
[c] The B traction unit had six to seven groups of burned bars and was stone cleaned in place.
[d] The A traction unit had a bad edge burn and once a failed brush; the ECU had a failed brush and a burned box; the B traction unit had a new motor (unit 352334 had been removed).
[e] The brush length (bottom brush measurement) (in) is given in parentheses.
[f] The ECU box had burned during previous operation.

than twice the life of the conventional brush. The wear data were taken as a worst-case condition, *i.e.* the fastest wearing brush was used as the basis of brush life for each specific car. In two cases, the conventional brush unit required replacement due to a surface problem or malfunction. Under similar conditions of operation, units with fringe fiber brushes would have continued to provide good life and acceptable performance.

8. Other applications

The performance results obtained with the SLRV brushes were so exceptional that the use of the fringe fiber brush was extended to other units. Pertinent data and results obtained to date are as follows.

TABLE 4

Life projections after 4 months in service[a] (special inspection and test program San Francisco MUNI SLRV blower motors units in test and inspection from April 21, 1981, to April 30, 1981)

Car	Date	Life to date (miles (days))	Wear (in)			Projected life (miles (days))
			A traction unit	B traction unit	ECU	
Fringe fiber brush: projected average life, 748 days (5 cars)						
1253	4/21	5717 (98)	0.114	0.126	0.168	20417 (340)
1264	4/21	5593 (98)	0.074	0.047	0.050	45348 (755)
1266	4/29	7856 (106)	0.067	0.073	0.085	55454 (924)
1268	4/29	7433 (105)	0.091	0.087	0.095	46945 (782)
1283	4/29	7915 (106)	0.064	0.049	0.084	56535 (942)
BG-530 brush: projected average life, 307 days (4 cars)						
1214	4/30	6879 (105)	0.208	0.143	0.040[b]	19843 (330)
1235	4/30	6990 (105)	Fiber brushes installed			
1263	4/30	7644 (105)	0.169	0.153	0.366	12530 (208)
1272	4/28	7833 (103)	0.087	0.068	0.441[b]	10657 (177)
1278	4/29	5221 (104)	0.0190	0.052	0.101	31015 (516)

[a] The highest brush wear on each car was used for life projection; the projected life (miles) was given by (miles to date) × (allowable wear)/(wear to date); the projected life (days) was given by (projected life (miles))/60; the Safety unit in the laboratory test had a projected life of 7500 h; the originally specified requirement was 2500 - 3000 h (125 - 150 days); the allowable wear was 0.6 in.

[b] Brushes replaced or about to be replaced with a fringe fiber brush.

8.1. Motor alternator: Toronto Transit Commission (unit on H-5 cars in the Toronto subway)

Rating	45 kV A; powered by a motor rated at 50 h.p., 600 V and 1800 rev min^{-1}
	68 A; operating range 500 - 720 V
Brushes	Four, with a total cross section of 0.5 in × 1.25 in giving 54 A in^{-2}
Style	Radial, with a constant tension spring
Original problems	Occasional bar marking, threading and short brush life
Tests	Several electrographitic grades tested, also slotted-face type

The results with fringe fiber grade included excellent operation, with a good film and appearance, when operated on a burned bar unit: sparking was eliminated. The expected increase in brush life on a normal commutator surface was 20% - 50%. The major objection to the fringe fibre brush is its relatively high cost. At this time, the brush will be used when a conventional

brush unit goes bad and it is necessary to keep the motor alternator in service. There are approximately ten units now fitted with the brush.

8.2. Motor alternator: Southeastern Pennsylvania Transit Authority (new Kawasaki LRV cars)

Rating	40 kV A; powered by a motor rated at 48.5 h.p., 630 V and 1800 rev min^{-1}
	64.5 A; operating range 450 - 750 V.
Brushes	Four, with a total cross section of 0.5 in $\times$ 1.25 in giving 51 A in^{-2}
Style	10° trailing angle, with constant tension spring
Requirements	Long-term operation at light loads, except during the air-conditioning season; the ability to withstand occasional 1000 V transient spikes is also required.

Black band test results are given in Table 5.

TABLE 5

	Boost	*Buck*	*Band*	*Band* (%)
Conventional brush	0.4	1.9	2.3	3.5
EG-259 (fringe type)	0.4	3.5	3.9	6.1
EG-225 (fringe type)	0.8	1.7	2.5	3.9

The units are just starting to go into service. Grade EG-225 was chosen to accommodate light loading conditions. No wear data have been accumulated to date. Fiber brushes will be installed as original equipment.

9. Conclusion

A major breakthrough in brush technology has been accomplished with the development of the fringe fiber brush. The brush is finding increased use in d.c. machines for applications in which an otherwise standard brush would have difficulty in meeting acceptable performance criteria. Considerable improvement in brush life and performance under the most adverse of conditions has been demonstrated.

The very special and difficult application of brushes for low humidity environments appears to be another area of potential use, as was reported by McNab and Gass [4].

In the U.S.A., it is expected that by the mid-1980s thousands of d.c. machines will have been fitted with this unique brush.

With a decrease in the cost of the brush and an increased awareness of its capability, it can be expected that the fringe fiber brush will, in time, replace most existing conventional brush designs.

Acknowledgments

I wish to thank Hal Lewis of Garrett Airesearch for his help in setting up the MUNI test and in collecting the data.

To Bob Thornton and the crew at the MBTA, a special thanks for their support in getting the program going at Boston.

Appreciation is due to all the people at Morganite Electrical Carbon Company, especially to the research group, who had the vision and foresight to transform the carbon fiber into this unique brush.

Thank you to Ian McNab for the material that he provided, and, finally, to the management at Safety Electrical Equipment Corporation, who were willing to invest both time and funds within days of our early test results.

References

1 B. G. Lamme, Physical limitations in d.c. commutating machinery, *AIEE Trans.*, *34* (1915) 1739 - 1800.
2 I. R. McNab and J. L. Johnson, *Brush Wear, Wear Control Handbook*, pp. 1053 - 1100.
3 E. I. Shobert II, *Carbon Brushes*, Chemical Publishing Company, New York, 1965.
4 I. R. McNab and W. R. Gass, High current density carbon fiber brush experiments in humidified air and helium, *IEEE Trans. Components, Hybrids Manuf. Technol.*, *3* (1) (1980) 26.
5 L. H. Matthews, Japan, Taking the initiative in carbon fiber growth, *Bus. Week*, (May 25, 1981) (letter to the Editor).
6 *Carbon Brushes and Electrical Machines*, Morganite Electrical Carbon Limited, Swansea, 1978.
7 W. C. Kalb (ed.), *Carbon, Graphite and Metal–Graphite Brushes*, National Carbon Co., 1946.
8 V. P. Hessler, Electrical brush wear, *Electr. Eng.*, (October 1935) 1050.
9 V. P. Hessler, Abrasion — a factor in electrical brush wear, *Electr. Eng.*, (January 1937) 8 - 12.
10 R. Holm, R. M. Bauer, D. F. Emmet and W. E. Yohe, Brush wear during commutation, *IEEE Trans. Power Appar. Syst.*, *85* (1) (1966) 84 - 88.
11 B. R. G. Swinnerton, Carbon fibre fringe brush, *Wear*, *78* (1982) 81 - 92.
12 Listing of test trials (Morganite Electrical Carbon Company).
13 Morganite fringe fibre brushes, *Sales Brochure* (Morganite Electrical Carbon Limited).
14 J. J. Bates, Using thyristors and diodes to improve commutation, *IEEE Spectrum*, (January 1971) 38 - 47.
15 R. E. Hellmund, Flashing of railway motors caused by brush jumping, *Electr. Eng.*, (November 1935) 1178 - 1185.
16 P. Hunter-Brown and C. J. Hews, A practical investigation into the design of brushes and brush holders, *J. Inst. Electr. Eng.*, *71* (431) (1932).
17 E. I. Shobert II, Carbon brush friction and chatter, *Trans. AIEE*, (February 1957) Paper 57-124.
18 W. B. Belt, Practical aspects of brush contact stability, *Trans. AIEE*, (December 1953) Paper 54-89.
19 Light rail vehicle, *Descriptive Bull.*, November 1975 (Boeing Vertol Co.).

CONTROLLED CONDUCTANCE CURRENT SWITCHING IN LOW VOLTAGE HIGH CURRENT D.C. MACHINES*

G T. HUMMERT

Westinghouse Electric Corporation, Research and Development Center, 1310 Beulah Road, Pittsburgh, PA 15235 (U.S.A.)

R. M. GARRETT

Brown Boveri Control Systems, Inc., 564 Alpha Drive, Pittsburgh, PA 15238 (U.S.A.)

(Received November 5, 1981)

Summary

In a new class of high power density d.c. machines, the effect of rotor leakage inductance creates high current density in the trailing edge of the brush zones. Sintered metal graphite brushes, which are suitable for slip ring applications, are unsatisfactory due to metal "depletion" when used in these machines, even at currents as low as 40 A. Brushes constructed from insulated metal fibers, however, permit controlled conductance switching of currents up to 600 A. An analysis using a simplified equivalent circuit accurately predicts current and voltage waveforms during the switching interval.

1. Introduction

In this paper we describe a recently developed controlled conductance brush used to aid current switching in an experimental class of water-cooled high power density d.c. machines [1]. Differing significantly from conventional designs, these low voltage high current machines employ single-turn parallel axial air-gap conductors banded to a smooth unslotted rotor surface. Since each conductor carries current only during the interval of contact defined by brush zones (beneath the poles), the rotor winding does not undergo commutation in the usual sense but rather an on–off current-switching sequence as it enters and leaves the brush zone. This is illustrated schematically in the diagram of Fig. 1, where linear motion depicts machine rotation and each rotor bar winding is represented by an active L–C branch moving through the brush zone.

---

*Paper presented at the Advanced Current Collection Conference, Chicago, IL, U.S.A., September 23 - 25, 1981.
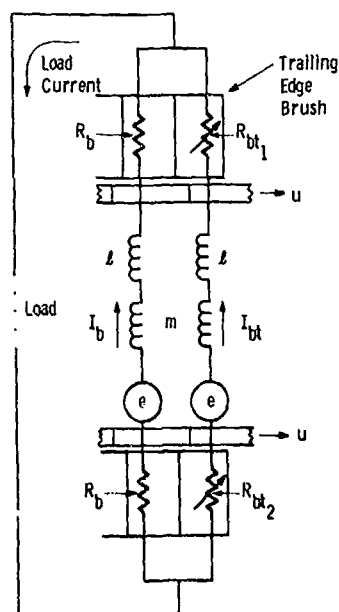
Fig. 1. Simplified machine schematic diagram.

Operating at current densities of about 155 A cm^{-2}, well above the capabilities of conventional graphite materials, the brushes in these machines must exhibit low contact resistance and reasonable frictional losses at high speeds. Our experience with sintered metal–graphite brushes used for pulsed-power systems indicated that sustained current densities of this magnitude could easily be achieved, and a subsequent development program yielded an optimum Ag–graphite brush composition of 75 wt.% Ag [2]. Operating in humidified CO_2, these brushes exhibit a contact resistance of the order of 0.2 mΩ and a coefficient of friction of about 0.2. Such low resistance, however, in conjunction with rotor bar leakage inductance, creates a region of excessive current density at the trailing edges of the brush zones where rotor bars break contact with the load circuit. Hence, the requirement exists for controlled conductance brushes that effectively aid switching by forcing a rapid rate of change in current and by absorbing switching energy contained in the (uncoupled) leakage inductances.

2. Apparatus

Switching studies were performed using a low impedance d.c. generator fashioned from a conventional six-pole open-frame d.c. machine on which the original series-wound slotted rotor was modified, first by machining to a smooth surface, and then by substituting a single-turn air-gap winding. The winding consists of 50 rotor bars connected in pairs through 180° end connections. The end connections of the test generator were wound to approximate the leakage inductance (about 1 μH) expected on larger (3000 h.p.) machines being designed for a demonstration torque converter. Two of

the 25 single-turn windings are instrumented with toroidal coils and switch ring potential taps. Brought out through low noise slip rings, these signals enable us to record rotor bar current and contact potential at any rotational position. At 1200 rev min^{-1} (our nominal operating speed) and full excitation the test generator develops a 4 V open circuit at a slip ring speed of 21 m s^{-1}. Limited chiefly by brush and connection resistance, short-circuit currents range up to 3 kA. The machine can be sealed for controlled-atmosphere testing.

3. Analysis and results

With the aid of the simplified schematic shown in Fig. 1, current in the rotor circuit of our experimental d.c. generator may be described by the following matrix equation:

$$\begin{bmatrix} l+m & m \\ l+m & m \end{bmatrix} \begin{bmatrix} \dot{I}_b \\ \dot{I}_{bt} \end{bmatrix} = \begin{bmatrix} e - V_L \\ e - V_L \end{bmatrix} - \begin{bmatrix} R_0 & 0 \\ 0 & R_t \end{bmatrix} \begin{bmatrix} I_b \\ I_{bt} \end{bmatrix} \tag{1}$$

where the dot denotes the time derivative. Assuming constant load current $\dot{I}_b = -\dot{I}_{bt}$ and letting $e - V_L = R_0 I_0$, we can simplify eqn. (1) to

$$\dot{I}_{bt} = (R_0 I_0 - I_{bt} R_t)/l \tag{2}$$

Finally, this may be normalized to a more familiar form containing the Arnold coefficient A [3].

$$\dot{I}' = dI'/dt' = A(1 - I'R') \tag{3}$$

In deriving this expression we have implicitly assumed that the generated e.m.f. e remains fixed during the switching interval. In conventional interpole machines, of course, this is not true and a varying e.m.f. in fact assists commutation. Here, though, the single-turn air-gap rotor winding experiences a nearly uniform e.m.f. during the switching interval. Equation (3) clearly illustrates the importance of brush resistance during the switching interval: the product $I'R'$ must exceed unity in order to force a negative $\dot{I}'$, and so as I' diminishes, R' must increase at a faster rate to maintain a negative $\dot{I}'$.

A numerical solution of eqn. (3) with an "ideal" contact conductance proportional to brush contact area yields the waveforms shown in Fig. 2. Note the close agreement between these waveforms and those of Fig. 3, which shows experimental results obtained at low current using Ag–graphite brushes with a clean unused contact surface. The experimental brush-to-rotor conductance waveform is derived from the recorded current and voltage waveforms. As indicated by these results, current is not necessarily zero as the rotor conductor breaks contact with the brush zone, and in fact arcing will occur at currents greater than 50 A.

Prior to the onset of arcing, however, the contact voltage easily exceeds the softening-melting levels of silver (0.1 - 0.5 V), and metal near the
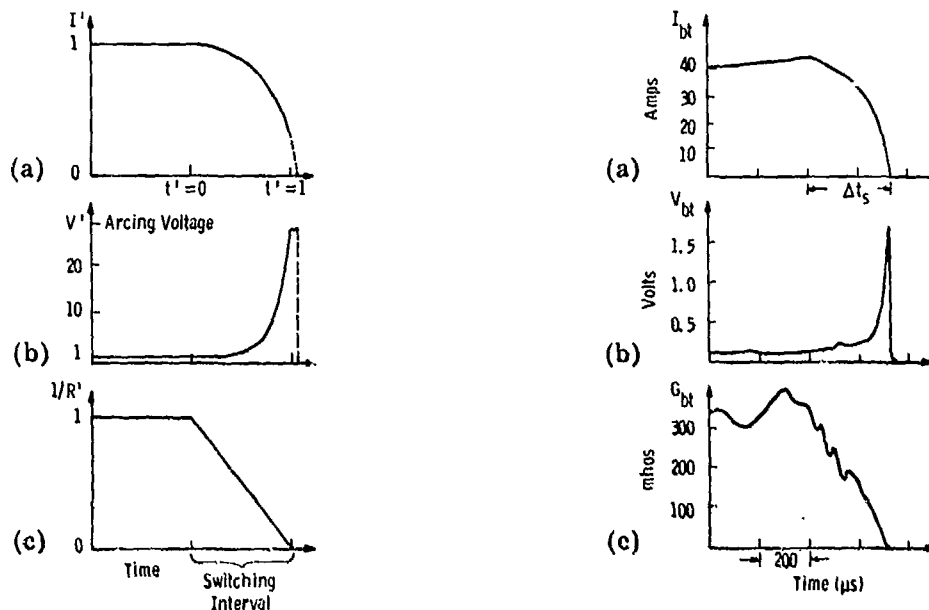
Fig. 2. Calculated (a) current and (b) voltage using (c) conductance proportional to contact area.

Fig. 3. Experimental values of (a) current, (b) voltage and (c) conductance obtained with undepleted Ag–graphite brush.

contact surface softens, liquifies and deposits on the switch ring surface [4].
Metal "depletion" leads to several undesirable conditions, namely increased contact resistance, unpredictable and variable brush performance and shorting across the insulation between adjacent rotor conductors.

Figure 4 shows the resultant waveforms for a depleted Ag–graphite brush (the same brush as in Fig. 3) after about 45 min of operation at about 40 A load current. In general, we found the severity of depletion (i.e. depletion width) increased roughly in proportion to current. Loss of metal at the trailing edge of a visibly discolored Ag–graphite brush surface was verified through scanning electron microscopy (SEM) photomicrographs and X-ray analysis.

Numerical solutions of eqn. (1) indicate that a non-linear conductance versus time characteristic as shown in Fig. 5(c) effectively controls current turn-off in a rotor circuit leaving the brush zone (Fig. 5(a)). The voltages involved, however, exceed the softening–melting limitations (Fig. 5(b)), and so contouring of the brush conductance through the use of varying metal content of the brush, or circumferential brush shaping, is not a satisfactory solution.

These observations and calculations, together with recent fiber brush experiments, led to the concept of controlled brush conductance wherein the desired characteristics are achieved by grouping insulated metal fibers in circumferential segments that are connected to series resistors as shown in Fig. 6 [5]. Insulation on the fibers constrains current flow to the radial direction, i.e. up through the fibers, thereby limiting current at the contact
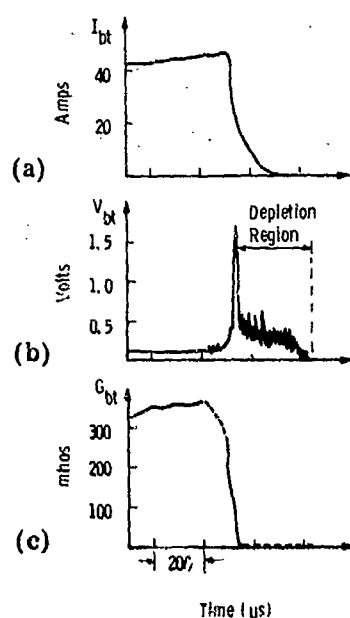
Fig. 4. Experimental values of (a) current, (b) voltage and (c) conductance obtained with depleted Ag–graphite brush.
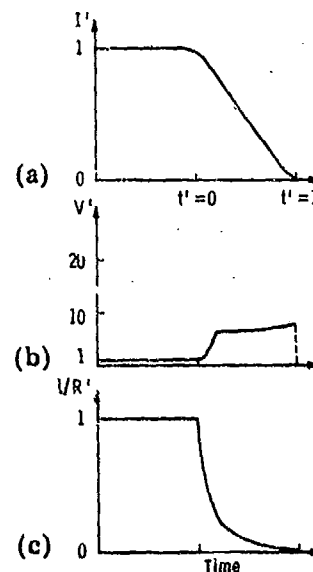
Fig. 5. Calculated values of (a) current and (b) voltage using non-linear (c) conductance.

surface through self-resistance of each fiber. This in turn limits power density at the contact interface, and fiber resistance rather than contact resistance becomes a major factor in determining the overall brush conductance. Series resistors provide controlled conductance during a switching interval; the desired conductance waveform (Fig. 5(c)) can be closely approximated by choosing appropriate values of resistance that not only force current changes, but also absorb switching energy in a region physically removed from the sliding interface. This, together with the energy dissipated by individual fibers as each segment breaks contact, tends to limit contact potentials and to maintain a cool interface. Due to the high intrinsic conductance of parallel fibers, overall brush conductance, including segment resistors, is comparable with that of metal–graphite monolithics.

3.1. Experimental insulated fiber brush

A brush was constructed from polymer-insulated copper wires (0.127 mm in diameter) grouped into four segments of about 700 wires per segment and soldered together as depicted in Fig. 6. Lengths of Nichrome wire were added in series with each of the four segments to yield the desired conductance characteristics. The test waveforms of Fig. 7 were obtained using values of 0 mΩ, 3 mΩ, 16 mΩ and 25 mΩ for series resistors R_1 - R_4 respectively. Note the current magnitude and waveform: in contrast to the Ag–graphite brush performance discussed previously, the insulated fiber brush switches nearly 300 A at a relatively uniform rate. Since the voltage measured here includes a potential drop across the segment resistors and

114
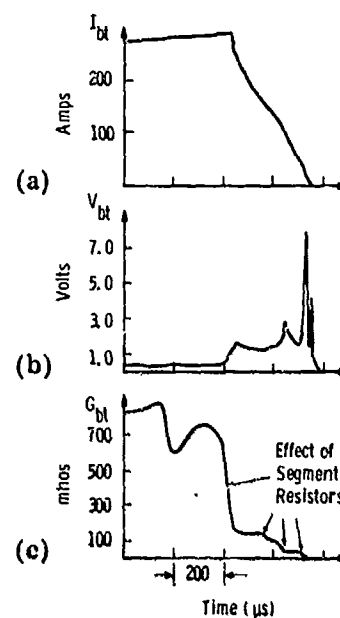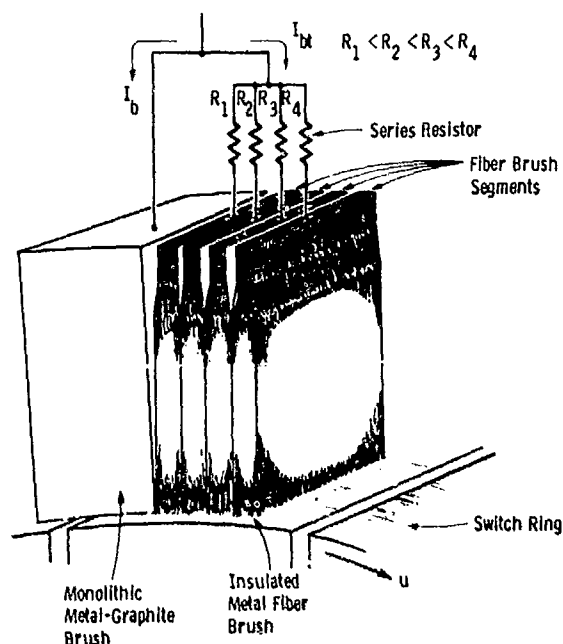
Fig. 6. Schematic diagram of four-segment insulated metal fiber brush.
Fig. 7. Experimental values (a) current, (b) voltage and (c) conductance obtained with segmented fiber brush.

brush fibers, it is not indicative of true "contact" voltage and therefore does not lead to softening or damage near the fiber tips. It is not surprising, then, that these waveforms were stable and the brushes exhibited no noticeable wear after test runs of $4 - 8$ h in a humidified CO_2 atmosphere. Furthermore, the switching surface remained clean and smooth with no obvious damage even after many such tests. (Separate wear tests on a slotted copper slip ring (using a steady current with no switching) indicated wear rates of 8.5 μm h^{-1} at 310 A cm^{-2} and a sliding speed of 51 m s^{-1}. The current density is based on the overall cross-sectional area of a brush. For switching tests this was 3.34 cm^2; for slip ring tests this was 5.0 cm^2.)

4. Conclusions

Insulated fiber brushes provide an effective means for controlling conductance between sliding electrical contacts. Conductance variations, in turn, actively control current during the switching interval that occurs as each rotor circuit breaks contact with the brush zone. Individual fibers and segment resistors, rather than contact resistance, absorb leakage inductance energy. Application of these brushes to conventional machines looks promising, but further investigations of wear and performance in various machine atmospheres are necessary.

Acknowledgments

Nomenclature

A	$R_0 \Delta t_s / l$
e	generated e.m.f.
I_b	rotor current
I_{bt}	switching current
I_0	nominal current prior to switching
I'	I_{bt}/I_0
l	leakage inductance
m	mutual inductance
R_b	nominal brush resistance
R_{bt_1}, R_{bt_2}	variable resistance of trailing edge brushes
R_0	$2R_b$, nominal steady state brush resistance per rotor winding
R_t	$R_{bt_1} + R_{bt_2}$
R'	R_t/R_0
t'	$t/\Delta t_s$
Δt_s	switching time interval
u	speed of switch ring surface
V_L	load voltage
V'	$I'R'$

References

1 D. L. Greene, C. J. Mole, W. P. Welch and W. R. Seng, Analysis of a high-power water-cooled electric propulsion system, *Soc. Nav. Archit. Mar. Eng., Trans.*, 86 (1978) 140 - 162.
2 I. R. McNab and J. L. Johnson, High current brushes. III — Performance evaluation for sintered silver graphite grades, in *Proc. 24th Holm Conf. on Electrical Contacts, September 11 - 15, 1978*, Illinois Institute of Technology, Chicago, IL, p. 493.
3 H. P. Kreuth, On the relationship between shut-down power and contact temperature at the trailing brush-edge, *Elektrotech. Maschinenbau*, 89 (1972) 283 - 287.
4 R. Holm, *Electric Contacts*, Springer, New York, 1967.
5 P. Reichner, Metallic brushes for extreme high current applications, in *Proc. 25th Holm Conf. on Electric Contacts, September 10 - 12, 1979*, Illinois Institute of Technology, Chicago, IL, p. 191.

HIGH CURRENT LIQUID METAL COLLECTORS*

R. A. MARSHALL, B. D. HATCH and R. C. KUMPITSCH

General Electric Co., Schenectady, NY 12301 (U.S.A.)

(Received November 5, 1981)

Summary

Acyclic machines require the transfer of very high d.c. currents from stationary to rotating contacts at low (5 - 300 V) voltages. A development program was undertaken to study new collector concepts for high current collector applications.

A new "narrow-gap" liquid metal collector was developed, analyzed and tested in the laboratory. Several test series were completed that demonstrated a collector design capable of operating at more than 30.9 MA m^{-2} at rotor velocities from 0 to 28 m s^{-1} for acyclic motor applications. A two-collector test fixture was operated for over 9000 h without any significant change in current collector characteristics. A narrow-gap collector design was also tested at speeds up to 100 m s^{-1} for acyclic generator applications.

An analytical model of the collector concept was developed to allow predictions of collector performance for various machine designs.

---

1. Introduction

Developments in the last decade have highlighted the need for advanced electrical machines that are more efficient and have higher power densities. As one major element in accomplishing these objectives, there has been considerable effort applied to the development of high current brushes for electrical machines [1 - 7]. During this recent period, there has also been considerable development effort in liquid metal current collectors for application in acyclic machines. In this paper we address our work in liquid metal current collectors for acyclic machines or for machines with slip rings requiring very high current transfer capabilities. Historically, the development of acyclic machines has been limited primarily by the lack of suitable current collectors. In the late 1960s, the U.S. government initiated technology programs that were focused on improving the performance of liquid metal current collectors [8 - 11]. During these research and development programs,

---

liquid metal current collectors studies were generally confined to the "tongue and groove" collector design with separation between the stationary and moving elements of approximately 0.050 in (1.27 mm). In acyclic motor applications, it is found that at lower speeds the electromagnetic expulsion forces in such tongue and groove collectors exceed the centrifugal forces on the liquid metal and, as a result, the liquid metal is expelled from the collector site and the contact will interrupt or become intermittent. The "narrow-gap" current collector concept [12] has overcome the contact interruption problems because the electromagnetic and mechanical centrifugal effects always dominate and the viscous restrictions on expulsion in the narrow gap are able to permit replenishment of the liquid by actions of the other forces on the liquid metal present during machine operation.

2. Collector evaluation equipment

In order to evaluate properly the liquid metal current collector in machine-like conditions, it was necessary to build a special test rig that is capable of operating at motor speeds, carrying high d.c. currents, in the presence of strong magnetic fields. In this program it was decided to model superconductive motor conditions as closely as possible in a collector test rig. The equipment shown in Fig. 1 shows a cross section of the test rig and a photograph of the equipment during operation as shown in Fig. 2. This collector test rig, which is composed of two collectors shorted together at the rotor, is capable of operating at collector surface speeds up to 28 m s^{-1}. A bank of large lead–acid storage batteries is capable of providing 60000 A through the test rig. A superconducting field coil is provided that produced up to 0.9 T at the current collector locations, which is about as high a magnetic field as would be present in collector sites in a motor. The collector test rig is water cooled through copper channels on the stationary portion of the collector. The rotor collector tips with an area of about 3.4 in^2 (22 cm^2) are conductively cooled through the liquid metal and through the shaft.

Batteries were connected in parallel to the test rig and current was applied in nominal 6000 A increments, which was the current capacity of each battery under these load conditions.

The narrow-gap liquid metal current collector concept uses a compliant member as the stationary portion of the collector. For these experiments, a plated copper braid material was used as the compliant member, which was assembled to a position where it just contacted the rotor surface. A cross section of the narrow-gap current collector is shown in Fig. 3(a). For comparison purposes, this is shown next to the more conventional "wide-gap" collector in Fig. 3(b). The test fixture used for these collector evaluations had a rotor diameter of 12 in (0.3 m). The current path through the equipment is shown in Fig. 1.

In previous work, various conductive liquids have been evaluated for current collector applications such as gallium, mercury and NaK (Na–K eutectic).
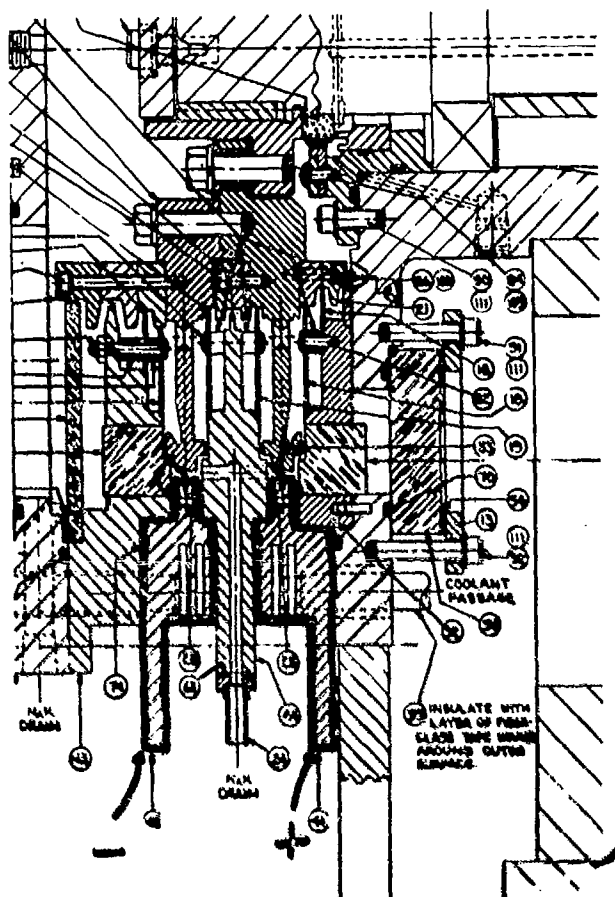
Fig. 1. Cross section of collector test rig.

NaK has very desirable properties for use in liquid metal collectors as it has relatively low density, it is liquid at room temperature, it has good heat transfer and low electrical resistance, and it has relatively low cost. As compared with mercury (toxic and high density), gallium (high cost and materials compatibility), and other low melting point alloys (usually high density), NaK with its materials properties and compatibility was selected as the liquid metal to be used for evaluating the narrow-gap collector concept. Various test series were performed; however, most of the evaluations were based on operation of the collector under motor-like conditions. These test series involved operation of the collector at speeds up to 42 m s^{-1} and slow or quick reduction in the speed so that the collector came to a stop and then reversed direction. These conditions would be common in variable speed motor applications, particularly for ship propulsion applications. It had been observed that the low speed high current regime and the reversing regime are the most difficult operating conditions in which to maintain good contact between rotating and stationary collector surfaces.

120

(a)   (b)
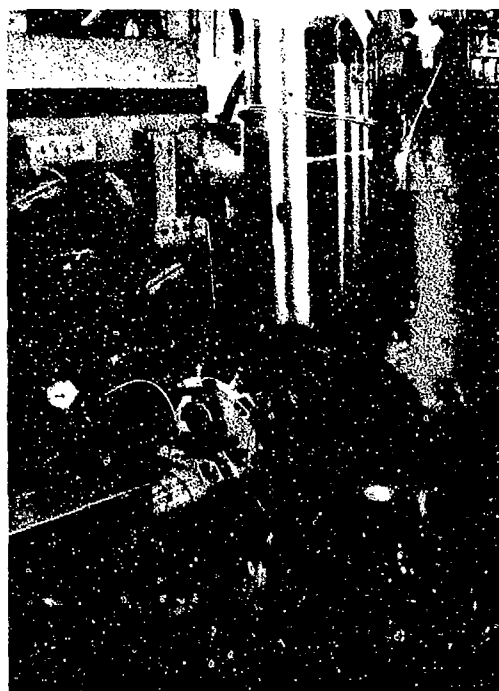
Fig. 2. Photograph of collector test rig superconducting magnet which provides magnetic fields at collector sites.
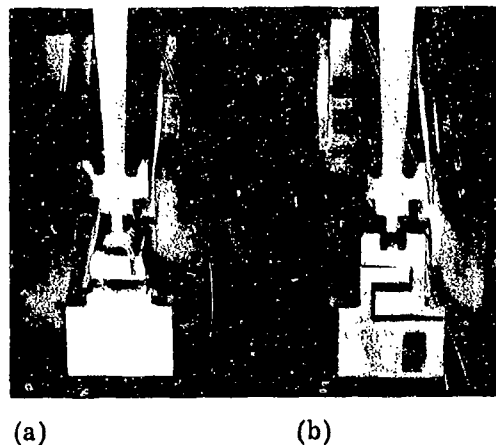
Fig. 3. (a) Narrow-gap collector; (b) wide-gap collector.

3. Test results

After the addition of liquid metal to the test rig, data were taken to measure many parameters. The most important were the viscous drag and the collector drop (voltage drop across the test rig terminals).

Initially, the test rig was operated to achieve braid "wear-in". Figure 4 shows the torque change during the braid wear-in period. Once the collector has been operated sufficiently long (about 50 h) so that the braid is worn to the narrow-gap condition, no further wear occurs. No corrosion or erosion effects were noted on either the braid or the rotor surface after extended operation for 9200 h.

The drag effects of liquid metal on the rotor tips were verified by measuring the torque and viscous drag when the amount of NaK in each collector site was varied. This collector concept has low mechanical losses as the NaK is in laminar flow adjacent to the rotor when the NaK is at the proper level.

The test rig was next evaluated under various current-carrying conditions but in the absence of magnetic field. From the previous experience with wide-gap collectors and analysis, it was expected that the collector could be partially or fully voided given sufficient current and no magnetic field. These predictions were confirmed with tests showing partial voiding taking place at
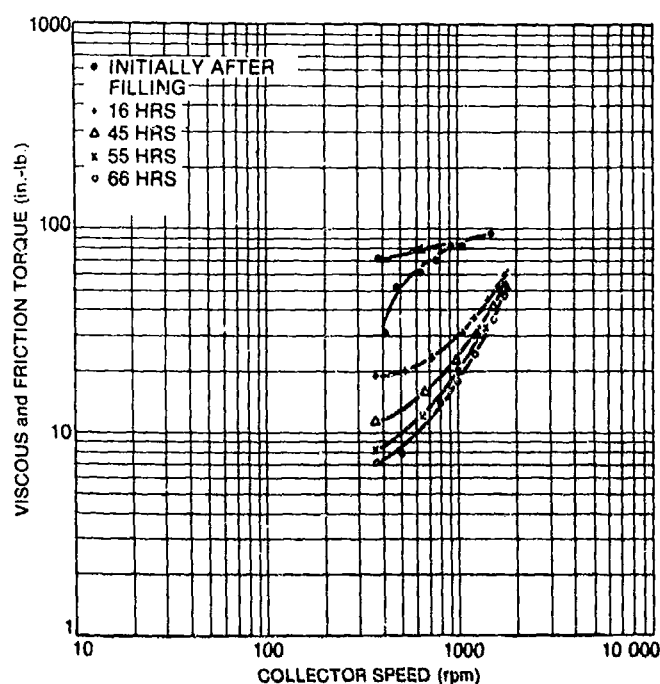
Fig. 4. Narrow-gap collector torque during braid wear-in period ($I = 0$ A; $\beta = 0$ T).
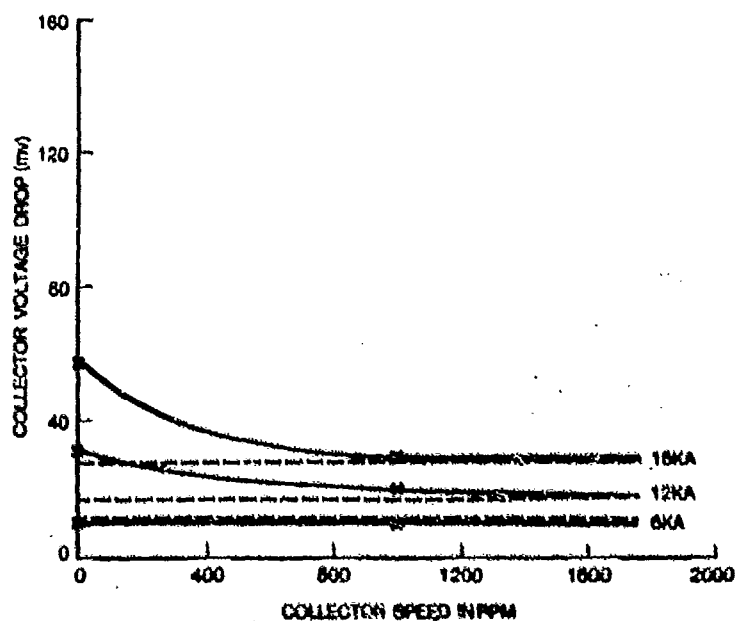
Fig. 5. Change in narrow-gap collector voltage drop with speed in the absence of magnetic fields ($\beta = 0$ T): – – –, before wear-in; –×–, after wear-in.

about 800 rev min^{-1} or less by observing the rising voltage drop across the test rig (Fig. 5). To date, no operating current level has been observed where full voiding or an open circuit developed, even on a transient basis.

The final performance test series involved tests with a combination of speeds from 0 to 28 m s^{-1} in magnetic fields ranging from 0.1 to 0.9 T and

122
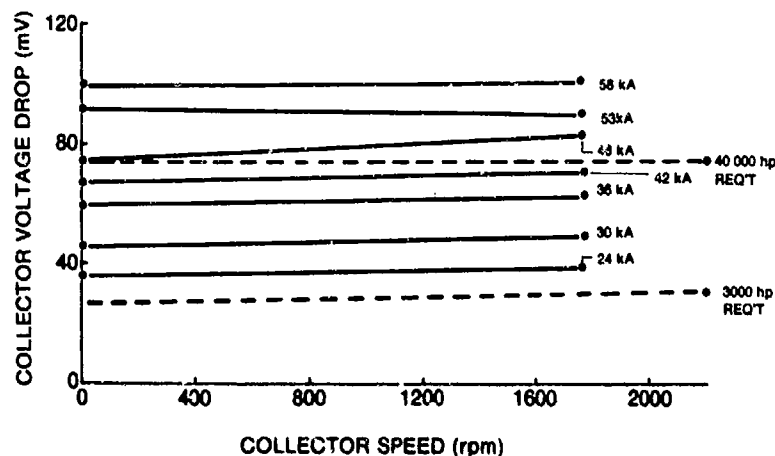
Fig. 6. Narrow-gap collector performance as measured by voltage drop across two collectors in series with a 0.1 T magnetic field at the collector sites.
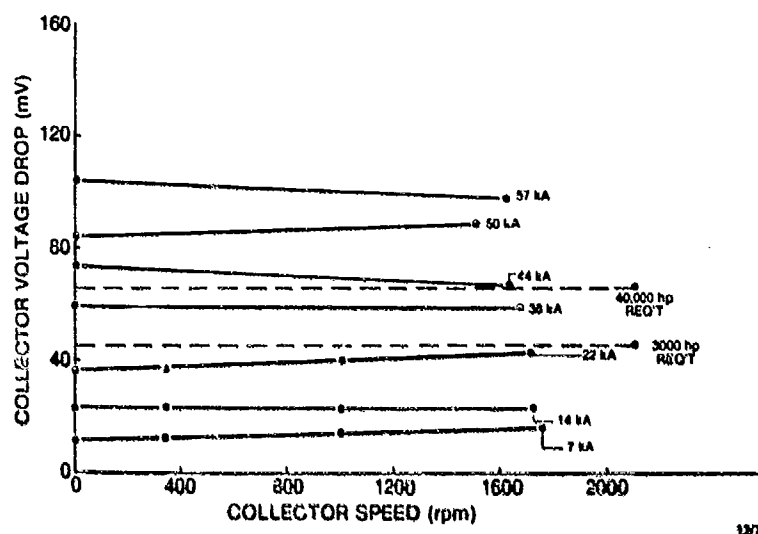
Fig. 7. Narrow-gap collector performance across two collectors in series with a 0.8 T magnetic field at the collector sites.

currents from 0 to 60000 A. Representative data are shown in Figs. 6 and 7 of the performance at 0.1 T and at 0.8 T respectively. The flat lines of data at each current level indicate uniform contact area throughout the entire speed range. These figures were prepared from strip-chart records.

Following this performance testing, the test rig was operated for 9200 h without current or magnetic field. Periodic performance tests were made during the 9200 h run to verify collector performance under various current and magnetic field conditions. No significant changes were noted during this period of operation. Following the 9200 h run, the collector test rig was drained of NaK liquid metal and was disassembled in a nitrogen glove box to examine visually for NaK migration, NaK wetting or other unusual conditions with the NaK material. It should be noted that, at 5400 h in the 9200 h run, an NaK composition adjustment was made by the withdrawal of some NaK

123

from the machine and the addition of Na–56wt.%K to correct for the preferential oxidation of the Na–78wt.%K. This adjustment, which required no disassembly and was performed in a few minutes, was fully successful, and a simple test was derived to monitor the NaK composition for future applications. This replenishment concept should be capable of extending the life of the collector to twenty or thirty thousands of hours.

4. Discussion

In 1977, the narrow-gap liquid metal collector concept was developed and demonstrated in the laboratory, first in static test fixtures and later in rotating test fixtures. Earlier work on wide-gap collectors [9, 10] established analytical techniques for liquid metal collectors which needed to be modified to apply to narrow-gap concepts. Much of the initial experimental work on narrow-gap collectors was completed before the new collector models were established. For example, in a variable-gap static test fixture it was established that a "narrow-gap" collector was one with a gap of about 0.010 - 0.015 in (0.25 - 0.38 mm) or less between the contacts. Our preliminary analysis indicates that a "narrow-gap" should be constrained to 0.009 in (0.22 mm) or less.

The major technical problem with liquid metal collectors in rotating machines is that of maintaining low resistance contacts at locked rotor or low speed operation (below the speeds where the rotor drag or electromagnetic forces on the NaK fluid distributes it around the circumference of the rotor–stator gap). In acyclic machines when current flows through most liquid metal collectors, the NaK fluid will be expelled from the gap in the collector by the reaction force of the magnetic field crossed with the current. A classical electromagnetic pump propels NaK in the same fashion, *except* that, for the acyclic motor, the NaK must *stay* in the gap and not be expelled. With the narrow-gap collector, the NaK wets both surfaces, and the NaK will tend to stay in the gap because of circumferential pumping forces and capillary attraction.

In ref. 10, Appendix 2, there is a good description of the various forces exerted on the NaK liquid metal in a current collector in acyclic machines and the kinds of problems associated with NaK liquid metal confinement. It is apparent from our new data from narrow-gap collectors that the NaK confinement problems are minimal and that a batch fill collector can be designed and operated with confidence at motor and generator speeds. A 400 h.p. acyclic motor and acyclic generator have been designed to use batch-filled narrow-gap collectors at the David W. Taylor Naval Research and Development Center at Annapolis, MD [13]. Both machines have operated at rated load conditions for extended periods without any current collector arcs or faults, and without any signs of NaK liquid metal expulsion. The losses in the collectors are very low, confirming good contact and laminar flow in the narrow gap.

The narrow-gap collector design has been demonstrated without arcing or NaK voiding at current densities of up to 20000 A in^{-2} (3100 A cm^{-2}) on a continuous operation basis. This is a very high current density for a slip ring or collector, particularly when measured against solid brushes, whether carbon or metal–graphite, that operate in the range 50 - 1000 A in^{-2} (8 - 155 A cm^{-2}). The operating electrical and mechanical losses of the narrow-gap collector in a well-designed acyclic machine will be low and, as it is a "non-contacting" collector, there should not be any wear-out phenomena other than infrequent NaK quality maintenance.

5. Summarizing remarks and conclusions

The narrow-gap collector has been developed for operation in high current slip-ring-type applications, such as in acyclic motors and generators. It has demonstrated features that are summarized as follows: (1) very high current density; (2) long life (no wear); (3) simple geometry; (4) it adjusts to machine tolerances; (5) low loss; (6) it operates in external magnetic fields.

The narrow-gap collector concept has overcome the known limitations of the previously used wide-gap collector designs for both low speed and high speed applications. The success of the narrow-gap concept should allow new studies in current transfer at power densities far above those utilized in electrical machines today.

Acknowledgment

References

1 J. L. Johnson and L. E. Moberly, High current brushes, part I: effect of brush and ring materials, *IEEE Trans. Components, Hybrids Manuf.*, *1* (1) (1978) 36 - 40.
2 R. M. Slepian, High current brushes — V — sub-divided monolithic brushes at very high current levels. In *Proc. 25th Annu. Meet., Holm Conf. on Electrical Contacts, September 10 - 12, 1979*, Illinois Institute of Technology, Chicago, IL, pp. 137 - 144.
3 I. R. McNab and J. L. Johnson, High current brushes, part III: performance evaluation for sintered silver graphite grades, *IEEE Trans. Components, Hybrids Manuf.*, *1* (1) (1979) 84 - 89.
4 P. Reichner, Metallic brushes for extreme high current applications. In *Proc. 25th Annu. Meet., Holm Conf. on Electrical Contacts, September 10 - 12, 1979*, Illinois Institute of Technology, Chicago, IL, pp. 191 - 197.
5 P. Reichner, High current tests of metal fiber brushes. In *Proc. 26th Annu. Meet., Holm Conf. on Electrical Contacts, September 29 - October 1, 1980*, Illinois Institute of Technology, Chicago, IL, pp. 73 - 76.

6 R. A. Marshall, High current and high current density pulse tests of brushes and collectors for homopolar energy stores. In *Proc. 26th Annu. Meet., Holm Conf. on Electrical Contacts, September 29 - October 1, 1980*, Illinois Institute of Technology, Chicago, IL, pp. 151 - 155.

7 C. M. Adkins and D. Kuhlmann-Wilsdorf, Development of high performance metal fiber brushes — II — testing and properties. In *Proc. 25th Annu. Meet., Holm Conf. on Electrical Contacts, September 10 - 12, 1979*, Illinois Institute of Technology, Chicago, IL.

8 R. L. Rhodenizer, Development of solid and/or liquid metal collectors for acyclic machines, *Final Rep. Tasks 1 - 3*, February 27, 1970 (U.S. Navy Department) (Contract N00024-68-C-5415).

9 R. L. Rhodenizer, Development of solid and/or liquid metal collectors for acyclic machines, *Final Rep. Tasks 4, 5*, September 30, 1971 (U.S. Navy Department) (Contract N00024-68-C-5415).

10 C. J. Mole, Electrical propulsion machinery study, *Final Rep.*, March 1973 (U.S. Navy Department) (Contract N00014-72-C-0393).

11 B. D. Hatch, Cryogenic systems and superconductive power, *Semiannu. Tech. Rep.*, October 1973 (U.S. Department of Defense Advanced Research Projects Agency) (Contract DAHC-15-72-C-0235).

12 B. D. Hatch, Narrow gap flooded high conductivity filament collector, *U.S. Patent 4,168,446*, September 18, 1979.

13 H. O. Stevens, personal communication, 1980.

LOW MELTING SOLDER FOR SLIP RING CURRENT COLLECTORS*

J. T. MCLANE

*David Taylor Naval Ship Research and Development Center, Annapolis, MD 21402
(U.S.A.)*

(Received November 5, 1981)

Summary

Experiments conducted to measure the effectiveness of liquid solder as
a replacement for liquid Na–K in homopolar machinery are described. Initial
tests are reported together with details of the current collector used in a
model test rig having a twin rotor–stator configuration 10.16 cm in diameter.
Promising test results using a eutectic alloy containing 47 wt.% Bi, 18 wt.%
Pb, 12 wt.% Sn and 21 wt.% In are discussed.

---

1. Introduction

The experimental approach and testing to measure the effectiveness of
liquid solder as a replacement for Na–K in homopolar machinery with liquid
metal collectors are described. The results of an initial performance test,
halted after 2016 h of testing because of a bearing failure in a supporting
equipment system, are discussed together with the results of a follow-on test
lasting 500 h.

2. Experiments and tests

Several approaches were initially considered in planning an experiment
that would demonstrate the usefulness of liquid solder as a current collector
medium. One involved an elaborate series of experiments to measure the
range of physicochemical properties under varying conditions that could be
encountered in full-scale machine operation. Others involved studying the
effects that various shaped rotor–stator configurations may have on solder
performance. The approach taken, and reported herein, was to design a
model test rig having Na–K-proven design features, to insert liquid solder in

---

the test rig and to collect performance data by operating the test rig for several thousand hours. This direct and somewhat simple approach was taken on the premise that if the liquid solder "worked" under typical operational conditions then it could simply replace Na–K in existing machines with little or no modification of those machines. Studies on solder properties and machine design parameters have not been discarded but the potential productivity of the experimental approach was deemed to be most effective.

A half-section view of the model test rig designed and fabricated for the liquid solder experiment is shown in Fig. 1. This model has dual disk-type rotors connected by a common shaft; each rotor measures 11.1 cm in diameter and has a tip width of 0.873 cm. The rotor–stator–current collector configuration is shown in Fig. 2. The multilam strip which is shown between the stator and the braid holder is used to ensure an optimum electrical contact between the test rig components. A detailed description of the contact properties of this material is given in ref. 1. The braid shown in Fig. 2 is a product common in the electronics field and is woven tinned copper strands of wire. The braid porosity aids not only in keeping the liquid metal in the stator groove but also in maintaining a film of liquid metal between the braid and the rotor surface. It is an important key to good electrical contact between stator and rotor. It is the collective voltage drop across this configuration, shown in Fig. 2 (*i.e.* stator to multilam, multilam to braid holder, braid holder to solder and solder to rotor), that was measured in this experimental testing. A sketch of the experimental set-up, test rig and supporting equipment is given in Fig. 3.
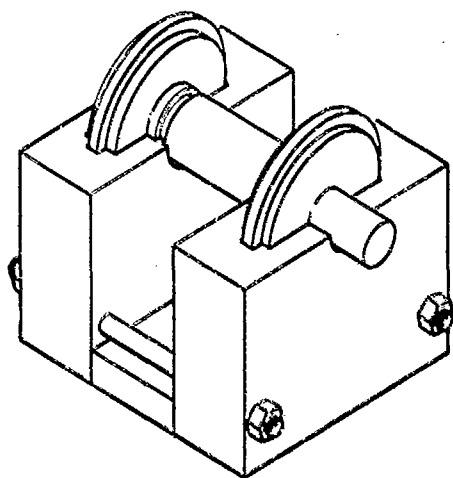
Fig. 1. View of rotor in bottom half of test rig.
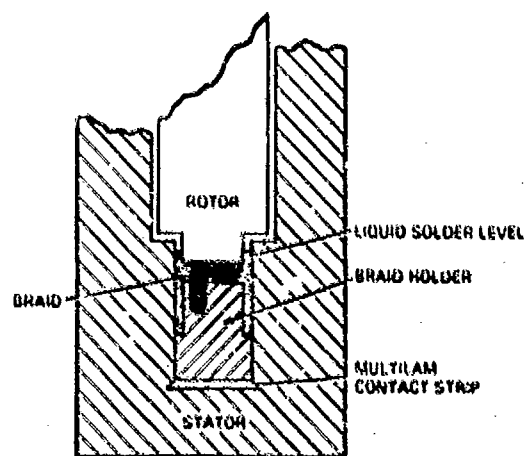
Fig. 2. Rotor–stator details.

3. Test procedures

The following test procedures were carried out prior to the collection of performance data: (1) assembly and preparation of test rig; (2) connection of supporting equipment; (3) definition of operating parameters.
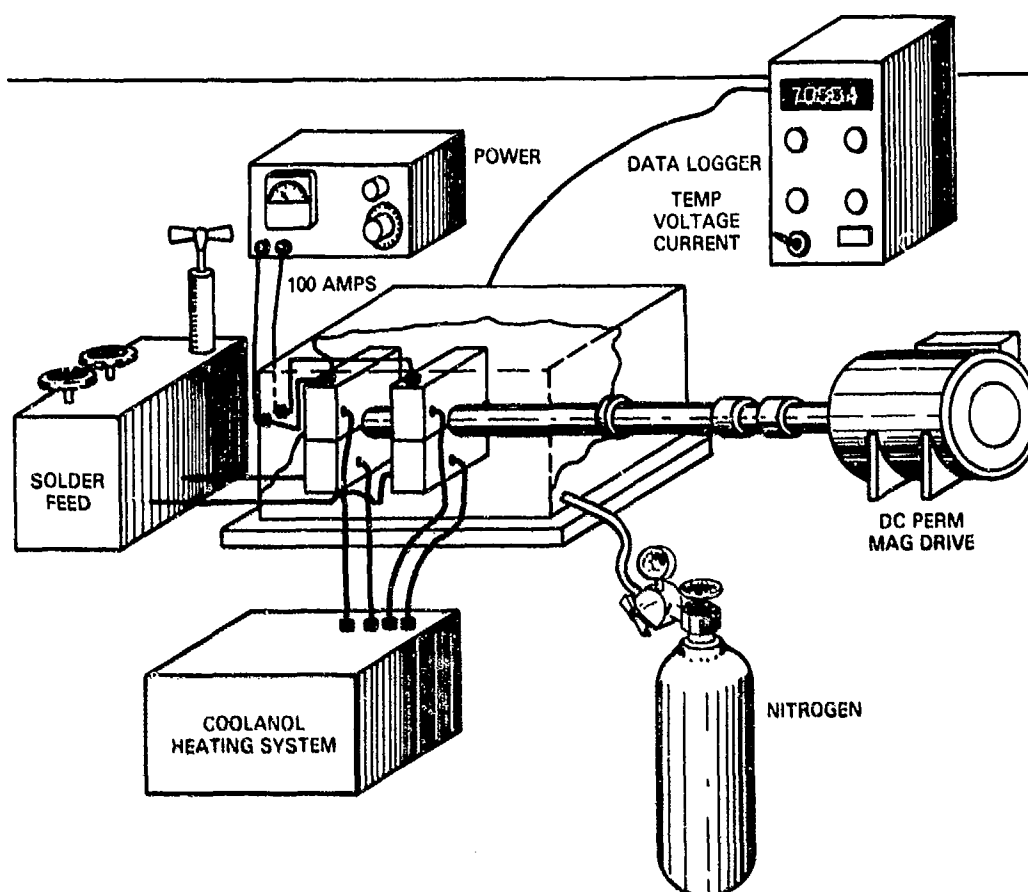
Fig. 3. Experimental set-up.

Liquid solder alloy 136 manufactured by the Pesses Company was used. It has a melting point of 57.8 °C (136 °F) and consists of 47 wt.% Bi, 18 wt.% Pb, 21 wt.% In and 12 wt.% Sn. Prior to assembling the test rig, the braid assemblies were oven heated to 65 °C and the braid was tinned with the 136 solder. After the braid assemblies had cooled to room temperature they were placed in the stator halves which had been assembled with buna-N rubber O-ring seals. The stator halves and the rotor were then oven heated to 65 °C and quickly assembled by carefully pressing the stator halves together around the rotor. This approach resulted in zero clearance between the rotor and the braid. This interface would wear to a minimum clearance during the initial hours of rig operation. The assembled test rig was then allowed to cool to room temperature before it was bolted to the bottom of the test chamber. A heating system using circulating fluid was then connected to the rig.

After these heating connections were completed, the temperature and voltage drop monitoring connections were made. Finally, the clear Lexan cover, sealed by an O-ring, was fastened to the test chamber. The test chamber was then evacuated to a pressure of 35 μmHg and backfilled with N_2 gas. The purity of the N_2 was checked and it contained 20 ppm of O_2

and 6.2 ppm of water vapor (H_2O). The motor drive for the test rig, a 1.5 h.p. permanent-magnet d.c. motor, was then directly coupled to the rotor. This was a calibrated motor in the sense that its torque under various loads had been previously measured in the laboratory as a function of motor voltage and current. Motor voltage and current, therefore, could be used to monitor indirectly the torque produced.

The following operating parameters were measured during the test: time of day and date; rotor speed (rev s^{-1}); drive motor voltage and current; voltage drop across each rotor–stator; current through the collectors; temperatures of the test box atmosphere, the heating–cooling fluid (initial and final temperatures) and each rotor–stator portion of the test rig. All of these parameters were recorded using a digital-type recording system.

In operation, liquid solder at 65.6 °C was injected into the bottom of each collector site so that the tip of each rotor and its braid collector were immersed in a pool of solder. In each site this volume was previously determined to be 5 cm^3 by experimentation using mineral oil. However, due to the needs of the plumbing feed system, 30 cm^3 of solder were actually required. Prior to starting the performance test, the complete system (the test rig and all supporting equipment) was operated for several hours to ensure that all components were functioning properly. Performance testing was carried out with a test rig shaft rotational speed of 16.7 rev s^{-1}. Since the diameter of each rotor was 11.1 cm, the tangential velocity of each rotor tip was calculated to be 5.8 m s^{-1}.

Performance testing was halted after 2016 h of test rig operation due to the catastrophic failure of feed-through bearings in the test box. During the testing period the test rig was stopped at various times due to lesser failures in other components of the supporting equipment, i.e. the data recorder, drive motor controller etc. Because some of the more significant of these failures may possibly have had an impact upon the test results, they have been incorporated into the plots of test performance data. In Fig. 4, the torque of the test rig drive motor is plotted over the duration of the test; in Fig. 5 the test rig voltage drop is plotted over the same time period. It can be seen that there may be some correlation between these failures and the changes, or non-linearities, in performance data. There will be a more detailed discussion about this correlation in Section 4. Throughout this performance test all temperatures monitored varied so little that no correlation could be made with the data already shown; therefore a temperature data plot is not given.

When the performance test was halted and the test rig had reached room temperature, all supporting systems were disconnected. The test rig was removed from the test chamber and disassembled for visual inspection. Samples of solder were then taken from the rig and chemically analyzed. The analytical results are given in Table 1 which also compares those results with the solder prior to its use in the performance test. There are minor differences in the bismuth, indium and lead contents compared with the known alloy. There is however, an approximate 1 wt.% loss in tin content together
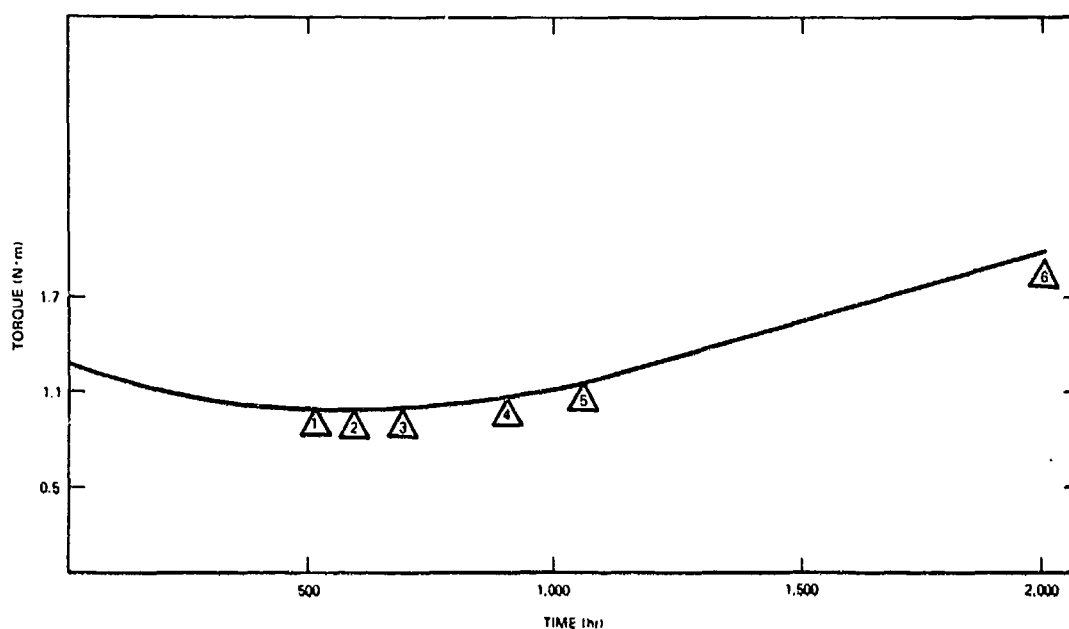
Fig. 4. Test rig torque *vs.* time showing failures ($\triangle$) (16.7 rev s^{-1}): 1, motor controls; 2, nitrogen leak; 3, heater circuit breaker; 4, test chamber seals; 5, heater circuit breaker; 6, testing bearings.
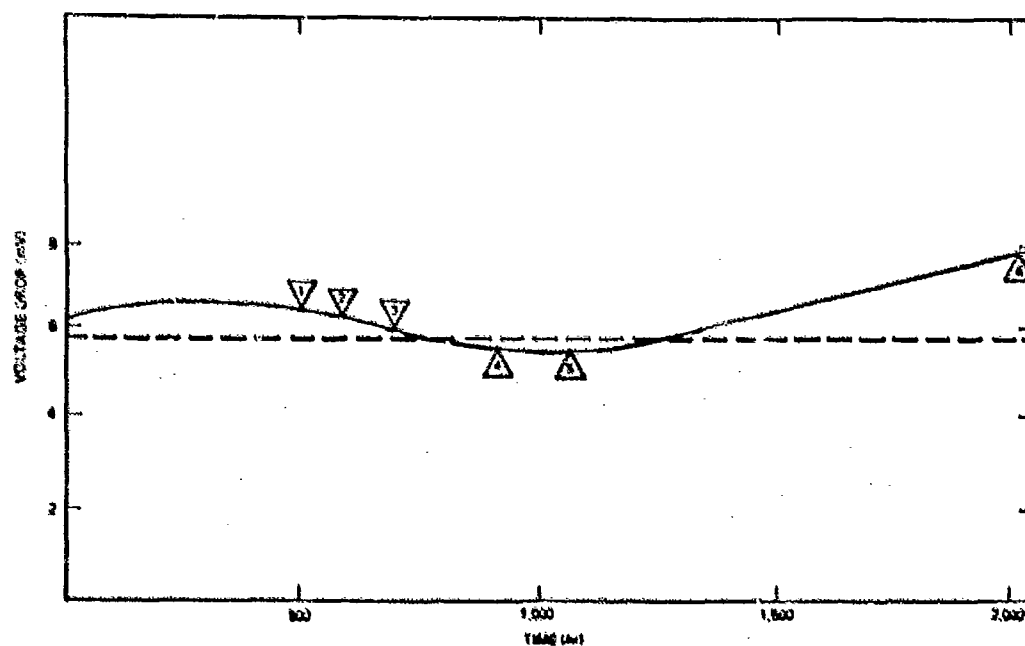
Fig. 5. Test rig voltage drop *vs.* time showing failures ($\triangle$) (16.7 rev s^{-1}): 1, motor controls; 2, nitrogen leak; 3, heater circuit breaker; 4, test chamber seals; 5, heater circuit breaker; 6, test bearings.

with a minor addition of copper to the solder content. Since there was initially no copper in the solder, it may be assumed that its presence was caused by wear or erosion of the rotor. The loss of tin, however, is unexplainable at this time. The bismuth content was only reported to two significant figures

132

TABLE 1

Analytical composition of liquid solder test 1 specimens

Sample	Bi (wt.%)	In (wt.%)	Pb (wt.%)	Sn (wt.%)	Cu (wt.%)
Known alloy 136	49.0	21.0	18.0	12.0	0
Bottom of driven end	49.0	21.7	17.8	10.4	0.75
Top of driven end	50.0	21.4	17.9	10.7	0.17
Bottom of drive end	49.0	22.5	17.3	10.5	0.38
Top of drive end	52.0	20.0	17.7	10.3	0.32

because the test samples were found to be not homogeneous in nature; the implication of this is also not clear at this time.

4. Discussion of failures

The test results presented in the form of simple plots of measurable data recorded over the life of the performance test tend to indicate that the test was successful in that solder satisfactorily performed as a current collector for a 2000 h period of time. However, during the test several failures occurred. These failures are test rig oriented, not current collector oriented. The failures, although not indicative of possible failures in full-scale machines, are discussed as an aid to better understanding of the complexity of the performance tests. Some of the failures were noted in the torque and voltage drop data presented in Figs. 4 and 5, as they tended to explain some of the non-linearities in that data. Because of this indication of a potential impact of failures on the performance test, all failures noted in the test log were then examined using probability statistics criteria as a means of assessment. This examination was undertaken to understand better the relative frequency with which the failures occurred and to estimate the probability of failures that might occur during follow-on tests.

Using this approach a failure was considered to have occurred any time the test was halted for any reason whatsoever. The resulting lengthy list of failures was then narrowed down to six relevant failures using the following refined criteria.

(1) The criterion of relevance was that the failure did, or would, have a direct impact upon the test, e.g. loss of nitrogen cover gas.

(2) The criterion of non-relevance was that the failure did not directly impact the test, e.g. inoperability of the data recorder.

Test stoppages due to such events as holidays, administrative delays, waiting for ordered parts or power outages were not addressed as failures even though, in the strict sense of the word, they impacted the test. As a matter of record, the collective down-time in this special category amounted to approximately 576 h.

As a result of this failure examination the following six failures were identified as being relevant: (1) motor controller; (2) nitrogen leak; (3) heater circuit breaker; (4) test chamber seals; (5) heater circuit breaker; (6) test rig bearings. These failures (which occurred in the same sequence as listed, *i.e.* 1, ..., 6) were plotted on special Weibull probability graph paper in Fig. 6 where the failures are shown to "fit" a straight line plot. This Weibull approach was taken because it is a proven method of interpreting failure rates and the probabilities of their distribution over time. The slope of the straight line plot is much less than 1.0 which means that the failure rate is decreasing with time. The plot also shows that the failures are randomly distributed regarding age of failures since age did not determine the sequence of the failures. The characteristic life of the test is determined to be 250 h; it is the time at which the failure probability is 63%. The median life is 110 h; it is the time at which the failure probability is 50%. The mean life is 652 h; it is the same as the mean time between failures used in reliability analyses. Since most of the failures occurred prior to this time it indicates that time prior to 650 h can be thought of as a "burn-in" time after which the reliability of the performance test will increase because of a decreasing failure rate. For example, let us determine the probability of a failure occurring during a 1000 h period beginning at 1000 h in the test life. From the plot the probability of failure at 2000 h is 92%, at 1000 h it is 83%, *i.e.* $P_{2000} - P_{1000} = 92\% - 83\% = 9\%$, which is the probability of a failure occurring in this case (the reliability here is 91%). In this example, and in any others the reader may make on his own, it must be assumed that the time interval follows a failure which was properly corrected.
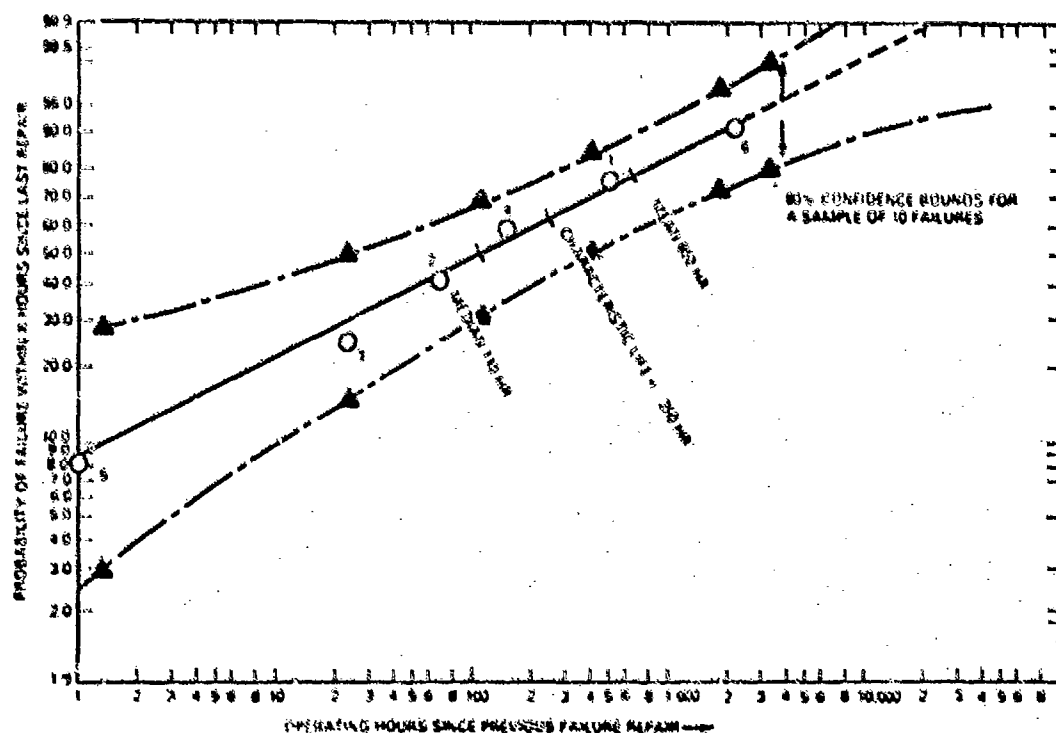
Fig. 6. Failure probability plot.

If this plot of decreasing failure rate is applied to follow-on tests it is especially important that any and all failures receive the following attentions because inadequate handling of failures will invalidate this failure rate prediction: good repair procedures; a complete past repair checkout; a check to ensure repairs have not caused other problems.

5. Second performance test

Prior to starting this test, the key test rig components (*i.e.* braid, braid holders and rotors) were cleaned by heating in an oven, brushing and/or wiping the melted solder 136 from each piece. As a result, these components had tinned copper surfaces. The braid, however, being difficult to tin by this method, was tinned with fresh solder 136. New test rig bearings which had been examined for freedom and ease of movement were then assembled in the rig. All supporting systems were checked, including a recalibration of the torque of the drive system, and all were connected in place. This performance test was started at 16.7 rev s^{-1} ; all test parameters recorded were the same as those in the initial performance test, *i.e.* temperatures, voltage drops etc. At 5 h into this test it was noticed that the interior of the test rig box and all components therein (cables and test rig) were becoming coated with what appeared to be a black sooty deposit. The box was flushed with nitrogen gas and over-night this sooty growth appeared to stop; there were no changes in monitored data during this period. After 276 h into the test the monitored data showed little or no variation in value. At this point in the test it was decided to operate the test rig at 41.7 rev s^{-1}, and thereby to produce a tip speed of 15 m s^{-1}.

A plot of test rig torque *versus* time at this new speed is given in Fig. 7. This plot illustrates the rather erratic behavior of this second test. The torque gradually decreased to zero during the first 180 h of 41.7 rev s^{-1} operation. During that period of time the test rig had also been visually monitored, and
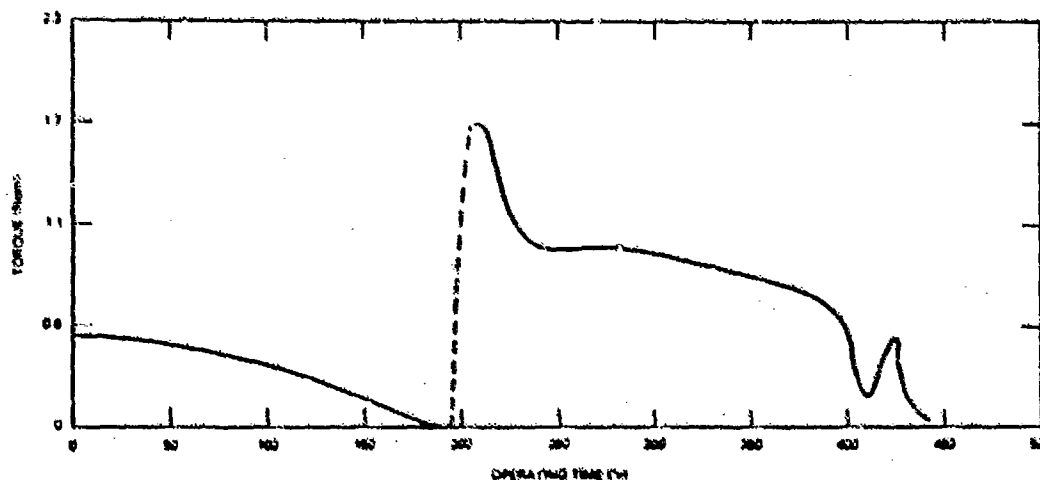
Fig. 7. Test rig torque *vs.* time (41.7 rev s^{-1}).

the formation of a pool of solder on the floor of the test chamber was noticed at 100 h. This pool was located in the vicinity of the test rig bearings and had evidently migrated out of the collector and past the seals. At the time of zero torque, the solder pool was considerably larger in size than when first noticed, and droplets of solder were observed around the bearing on the driven end of the test rig. The voltage drop across the test rig had, at this time, increased from 50 mV to 7.0 V, indicating an open-circuit collector. The test was then interrupted in that all power was disconnected and the rig motion stopped; the heating system was not disconnected. A supply of fresh solder 136 was then added to the test rig and the test was started again. As shown in Fig. 7, the starting torque was 17 N m and it gradually decreased again, becoming erratic as it approached zero at approximately 450 h, when the test was finally discontinued.

On removing the cover of the test chamber it was discovered that a slight leak had occurred in the heating system, and therefore the interior of the chamber and all of its components were found to be coated with a black oily substance. The test rig was again disassembled and solder samples taken from various areas of the rotors and stators and from the pool of solder on the test chamber floor. These samples, together with a sample of the oily black soot, were analyzed. The analyses are given in Table 2. Table 2 shows a comparison between not only test sample deviations from the known solder but also variations between test samples. While not ignoring these latter variations, it is believed that an examination of deviations from the known solder content are more significant in this experimental work. On that basis, all test samples show definite losses in bismuth and tin. The lead content of samples varied, *i.e.* most samples lost lead while one sample showed an increase in lead content. The bismuth and lead losses are reflected in the qualitative results obtained from analyses of the black deposits from within the chamber. The gain in lead content found in one sample is unexplainable as is the higher content of indium in all test samples. The consistent losses in tin are also unexplainable.

Because of this ejection of solder from the rig, the clearance between each rotor and its respective GE braid stator was measured. Each clearance

TABLE 2

Analytical composition of liqu¹ ' solder test 2 specimens

Samples	Bi (wt.%)	In (wt.%)	Pb (wt.%)	Sn (wt.%)	Cu (wt.%)
Known alloy 136	51.67	17.92	18.25	12.06	0.01
Top of driven end	50.95	18.52	17.89	9.39	3.10
Top of drive end	48.27	18.71	18.68	10.00	4.21
External area of driven end bearing	50.42	18.15	17.58	11.35	2.35
Black sooty deposits	Qualitative analyses indicated the presence of Pb, Bi and Cu				

was 0.25 cm on average. This large clearance is a result of rotor and braid wear or erosion and possible deflection of the soft braid material by the hydrodynamic pressure of the heavy metal.

6. Conclusions

Based on the results of the first performance test, solder is a promising replacement for Na–K in advanced electrical machinery. It is not clear why the black soot formed inside the test box during the second test. Following the first performance test, the rotor tips were visually inspected and found to show negligible wear patterns. As a result of this inspection, and because those solder test samples showed what were considered to be only minor copper additions, the rotor–stator clearances of the test rig were not measured until the end of the second test, run at 15 m s^{-1}, when the rotors exhibited pronounced wear patterns and test sample analyses showed heavy deposits of copper in the solder. All data, both clearance and chemical, indicated that the rotors became eroded in the second test. The stability of the rotor–stator interface deteriorated to the point of no return and the solder was literally thrown from its groove-shaped passage. The failures in the second test were, in a way, predicted by the failure analyses which showed a high failure rate occurring before 650 h. The presence of copper in the test samples is attributed primarily to wear of the rotor tips. The resulting "free" copper is fully soluble in bismuth and lead but not when combined with indium and tin. Therefore, the addition of this copper to the solder 136 probably results in the formation of dross-like compounds with indium and tin. These waste products could be abrasive in nature; if so, they could cause a cascading wear effect on the rotor tips such as was seen after the second test. Test sample analyses from both performance tests show a common loss of tin and an increase in indium and copper. The significance, if any, of this has not been determined. Since the black deposits noticed in the second test were found to contain lead, it is therefore presumed that the lead combined with the nitrogen gas to form lead nitride which is black in appearance. All these conjectures about the solder only confirm the need for further study of the physicochemical properties of these materials over a broad range of parameters. The role of rotor speed in these tests is not totally understood with regard to its relation to the hydrodynamic forces which lead to depletion of the liquid solder in the collector sites. The question of clearances that may be required for solder operation has not been addressed prior to, or during, this test. During pre-test assembly of the test rig the braid was pried upward from the braid holder to ensure that when the rotor is positioned in the rig and the rig is assembled, the clearance is zero. It is then assumed that during the early hours of rig operation this configuration will "wear" to a working clearance. However, the braid is rather limp since it became annealed due to the welding required to fasten it to the braid holder. Because of this it may be susceptible to rotational and hydrodynamic forces, which

increased when shaft speeds changed from 16.7 to 41.7 rev s^{-1}, resulting in large rotor–stator braid clearances. The Center is continuing its research in this area and answers to these problems should be forthcoming in the near future.

Reference

1 D. B. Steen, Development of a 30 000-ampere reversing contactor, *Rep. PAs-79/40*, May 1980 (David Taylor Naval Ship Research and Development Center, Annapolis MD).

ULTRAHIGH SPEED FIBER BRUSH DESIGN AND TESTS*

W. H. LUPTON

U.S. Naval Research Laboratory, Washington, DC 20375 (U.S.A.)

P. REICHNER

Westinghouse Research and Development Center, Pittsburgh, PA 15235 (U.S.A.)

(Received December 1, 1981)

Summary

The low inertia of individual fibers in all-metal fiber brushes makes them attractive as current collectors for very high speed slip rings. A set of these brushes was designed and used for rim collectors on a pulse-discharging homopolar generator flywheel. The fiber diameter and length were selected by considering the mechanical stress on individual fibers resulting from interference between the brush and the speed-dependent wheel diameter and from electromagnetic forces. At a slip ring speed of 380 m s^{-1} and a machine current of 40 kA the brushes operated for 19 pulses without adjustment or refurbishing. At 470 m s^{-1} and a machine current of 60 kA a single pulse resulted in surface fusion of about 30% of the brush face. This merging of the fiber tips increases brush stiffness and may eventually limit the practical brush operating life.

1. Introduction

Pulse generators for applications requiring a very large energy are more compact and economical when they exploit the high energy density associated with inertial and inductive energy storage [1]. In a pulse generator built at the Naval Research Laboratory (NRL) [2], the energy storage inductor is energized by a self-excited homopolar generator from energy stored in the inertia of its rotors. This generator uses a pair of contrarotating Be-Cu flywheels with sliding current collectors at rim and axle. The need for high speed rim collectors carrying single unidirectional current pulses provides the motivation for this work.

Because of the relatively rapid energy dissipation (with a characteristic e-fold time of $L/2R$) of an inductor, efficient transfer of energy from the

inertial system to the storage inductor requires that the homopolar generator has enough power to energize the inductor within a time which is of the order of this characteristic time (0.75 s for the NRL inductor). The power output of the homopolar generator is proportional to voltage and this, in turn, is proportional to the rim speed. Thus the flywheels should be operated with the highest possible rim speed. Ultimately, this speed is limited by the strength of the wheel material subjected to speed-dependent internal stresses. At present, the maximum speed is much lower than this and is determined by the need to operate sliding current collectors on its periphery.

Solid metal–graphite brushes are customarily designed for operation at sliding speeds much less than 300 m s^{-1} [3, 4]. This speed limitation is due to their mass and rigidity, which prevent them from being accelerated quickly enough to follow slight irregularities in the moving rotor surface. An alternative to the solid brush is one composed of many low mass fibers, each of which can better follow the wheel irregularities. In fact, brushes made from very fine metalized graphite fibers were used on the NRL pulse generator at rubbing speeds of 360 m s^{-1} [5].

The successful steady state operation of all-metal fiber brushes where sparking and high wear rate were eliminated by proper atmospheric control [6] suggested a possibility of high speed pulsed application of such brushes. This paper relates the functional requirements of the rim brushes and in it a design approach applicable to large diameter fibers is presented. Descriptions are given of the construction of some experimental brushes and their operation at sliding speeds of 320 - 470 m s^{-1} and at pulse currents of 30 - 60 kA.

2. Brush design

The inertial pulse generator presents a very severe environment for the peripheral brushes. The pneumatically actuated brush contacts the rapidly spinning rotor and completes the electrical circuit to initiate the discharge cycle. The brush holder is advanced to an adjustable stop, and the brush must then follow the significant radial contraction of the rotor as its speed is reduced during the discharge. As the rotor moves away from the brush, the current and the resulting magnetic force on the brush are rapidly increasing. A trailing fiber brush utilizes a component of the magnetic loading to increase the contact force with increased current flow. The ultimate speed objective is greater than 500 m s^{-1} with a corresponding radial rotor growth of almost 1 mm. A lowered ambient pressure, for reduction in the windage power loss, restricts the selection of a favorable atmosphere in the machine. The high magnetic field and its pulse nature tend to produce slip ring voltage gradients which induce circulating currents in the brush. The rotor slip ring surface is slightly coned to reduce this effect.

Earlier fiber brushes for this application used small diameter (10 μm) carbon fibers and, because they were extremely flexible, it was necessary to provide mechanical constraint of the fibers through dense packing and by
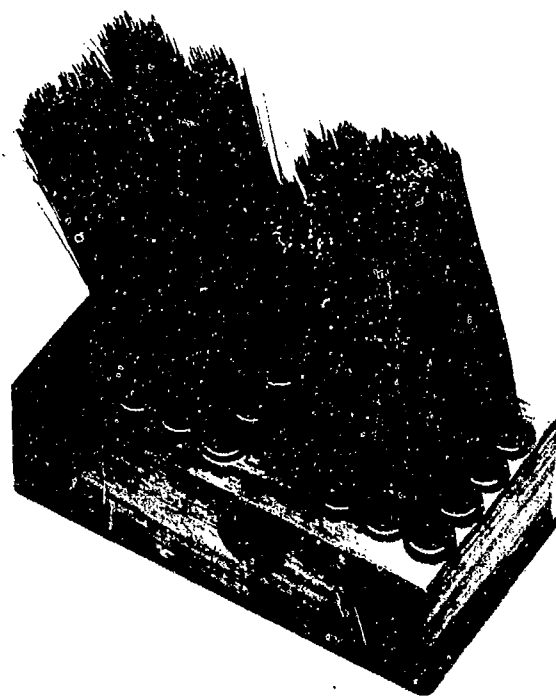
Fig. 1. Multibundle copper fiber brush (fiber diameter, 125 μm).

use of a peripheral support shield. This resulted in a more rigid brush than desired, and one that was difficult to model analytically. The copper fiber brush shown in Fig. 1 was an extension of recent developments in metal fiber brush research, in which a very high steady current capacity was experimentally demonstrated under a controlled atmosphere of humidified inert gases [6, 7]. The brush is composed of 24 bundles, each of which contains 168 hard-drawn copper fibers 125 μm in diameter and about 19 mm long, which are joined at their base with soft solder. The bundles have an approximate 30° trailing angle from a normal to the slip ring surface. The copper base into which the bundles are inserted fits the brush holder as a direct replacement of the earlier carbon fiber brush.

The selected fiber length and diameter are based on the objective that each fiber carry its share of the magnetic force as well as the applied contact force. The fiber interaction is thus minimized and a reasonable mechanical analysis may be performed. The mechanical model of an individual fiber is shown in Fig. 2. The fiber axis is positioned at a trailing angle θ from the normal to the slip ring surface to increase the brush flexibility and to produce a controlled increase in the normal contact force with increased current flow. Contact force control is important to minimize the frictional power loss while also limiting the electrical contact loss by reducing contact resistance when a higher current is being carried.

The fiber is considered to be a simple cantilever beam with a uniformly distributed magnetic force w, normal to the fiber axis, due to the interaction of the electrical current and the axial magnetic field. A small deflection is

142

assumed. The contact force N, normal to the slip ring surface, is the sum of two components. These are the force due to imposed interference δ between the brush and the wheel surface and the force due to the magnetic loading. A frictional force μN results, in the direction of slip ring surface motion. The force normal to the fiber axis is found to be

$$W = 3\left(\frac{EI\delta}{L^3 \cos\theta} + \frac{Lw}{8}\right) \tag{1}$$

where E is the elastic modulus, I the area moment of inertia, δ the wheel–brush interference, L the fiber length and w the magnetic force per unit length. The contact force normal to the slip ring surface is

$$N = \frac{W}{\cos\theta + \mu\sin\theta} \tag{2}$$

where μ is the friction coefficient.

The magnitude and location of the maximum fiber bending stress depend on the relative importance of the magnetic and the interference preload components. When the brush is first applied to the wheel, the interference is maximum and the magnetic force is zero. At this time, the peak bending stress, which occurs at the end of the fiber which is built into the brush base, is

$$\sigma = \frac{3E\delta d}{2L^2 \cos\theta} \tag{3}$$

where d is the diameter of the circular fiber cross section and δ is the initial maximum interference.

When, during the discharge pulse, the magnetic force becomes large $(W/w < L)$, the maximum bending stress along the fiber length is

$$\sigma = \frac{16W^2}{\pi d^3 w} \tag{4}$$
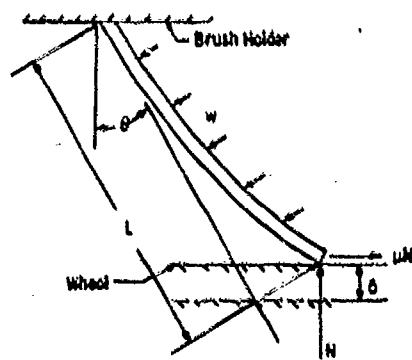
Fig. 2. Single-fiber mechanical model.
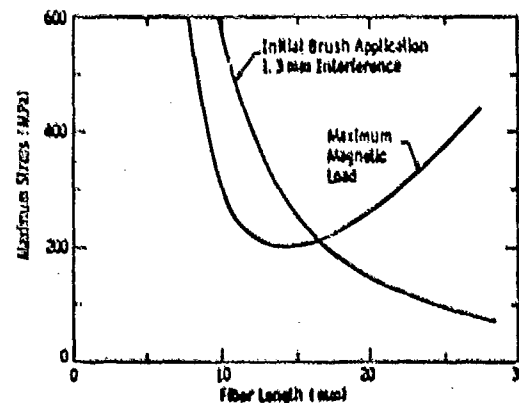
Fig. 3. Stress variation with fiber length (35 brushes per ring; 18000 rev min^{-1}).

If the preload effect is negligible in comparison with that of the magnetic load, eqn. (4) is reduced to

$$\sigma = \frac{9L^2w}{4\pi d^3} \tag{5}$$

and the point of maximum bending stress occurs at a distance $3L/8$ from the sliding end of the fiber. The magnetic force per unit of fiber length depends on the axial magnetic flux density at the flywheel rim. This flux density (T) is $B = 3.82 \times 10^{-5}I$. If this machine current I (A) is collected equally by all the n fibers in contact with a single flywheel, the magnetic force w (N m^{-1}) per unit length on each fiber is

$$w = \frac{3.82 \times 10^{-5}I^2}{n} \tag{6}$$

The maximum interference is determined primarily by the rotor growth which is fixed by its initial speed, and thus the energy storage level. For a given diameter of the copper fiber, and for a selected contact angle, eqn. (3) shows that the initial bending stress is dependent on the fiber length alone. Similarly, once the number of fibers, and therefore the current per fiber, is established, the stress at maximum current, from eqn. (4) or (5), is also a function of length. Figure 3 illustrates this variation in the maximum fiber stress with length at these two points in the cycle. Curves of this type permit the selection of an optimum fiber length for each energy level, although consideration should be given to the fiber length reduction due to wear.

For the experiments described below, three types of copper fiber brushes were used. Preliminary tests used braided conductors with significant mechanical interaction of the fibers. This brush was very inexpensive and simple to fabricate but did not lend itself to mechanical analysis and was found to be excessively stiff. The second brush utilized the same conductor braid but the length extending from the holder was combed out to permit parallel motion of the fibers with reduced interaction (Fig. 4). The third brush configuration was that shown in Fig. 1, in which the fibers were considerably more independent and conformed well to the mechanical model described above.

3. Preliminary tests

Prior to completion of the analysis which led to the design shown in Fig. 1, a preliminary trial was made of metal fiber brushes in the homopolar generator. The brushes for the trial were fashioned from flat braided conductor woven with 384 tinned-copper wires 150 μm in diameter. To make each brush, several short lengths of the braid were cut from the roll, placed parallel and inserted in the holder as shown in Fig. 4. The holders were attached to the existing pneumatic actuators and current shunts and were designed to clamp the braid pieces together and to hold them at a 30° trailing

144
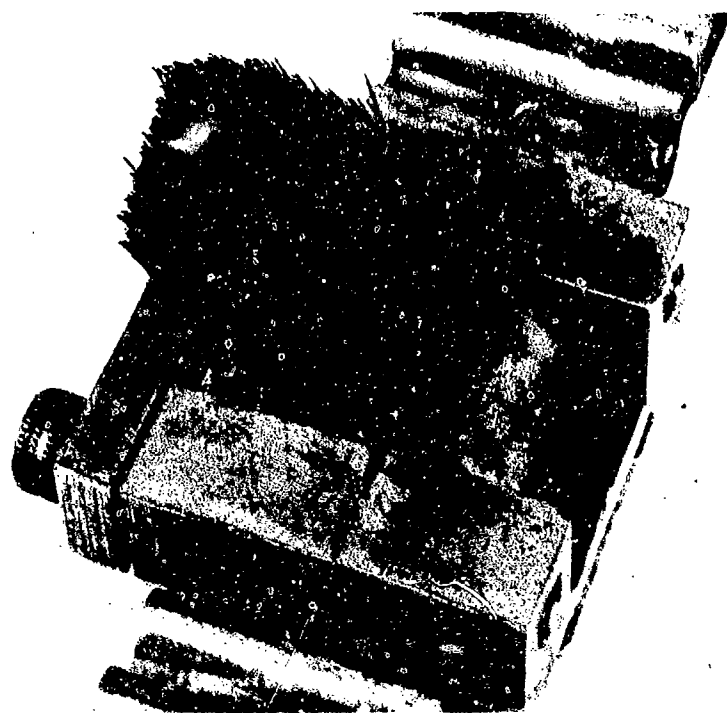
Fig. 4. Clamping holder for assembly of brushes from braid conductor. The brush shown has straightened 150 μm diameter fibers as used in recent tests.

angle from a normal to the contact surface. Each of the resulting brushes contained 4224 wires spread over a 17 mm square contact area and extended 13 mm from the clamp. After assembly, the 18 brushes used with each flywheel were sanded with 150 grit garnet paper so that the contact area conformed to the angle and curvature of the wheel rim.

In the light of subsequent analysis, these woven braid brushes are seen to be too stiff to follow the growth and shrinkage of the flywheel radius during high speed shots. This was of little concern for the preliminary trial at 10 600 rev min^{-1} where the radius variation was only 180 μm between initial and final speeds. These brushes were operated with an atmosphere of low pressure (2 - 3 kPa) humidified nitrogen. Many shots were made at this low speed, where the sliding velocity was 320 m s^{-1}, with no noticeable brush deterioration. When the flywheel speed was increased to 12 000 rev min^{-1} (contact speed, 360 m s^{-1}; machine current, 34 kA), these brushes deteriorated to a point where contact was unsatisfactory after eight shots. From inspection of the brushes it appeared that the contact surface had melted and welded the tips of the wires together. As a result, the brushes acted more like solid brushes which are unable to maintain continuous contact with surface irregularities.

4. High current tests

At higher currents, satisfactory brush performance is limited by the ability of each fiber to withstand the magnetic force. To explore the brush operation in this regime the current per brush was increased by installing only half of the normal complement of brushes for each flywheel. For the left flywheel 18 brushes like that shown in Fig. 4 were used. These were made from braided conductor inserted in the clamping holders and were combed so that the individual fibers were straightened and parallel to conform more nearly to the geometry assumed in the analytical model. Each brush contained 4224 wires with a diameter of 150 μm and length of 13 mm.

The 18 brushes used with the right flywheel were constructed from hard-drawn copper wires inserted in copper blocks as shown in Fig. 1. Each of these brushes contained 4032 wires with a diameter of 125 μm and approximate length of 19 mm. The fibers in both sets of brushes were set at a 30° trailing angle and sanded to conform to the angle and curvature of the wheel rim.

With these brushes the machine was operated for one shot at 12000 rev min^{-1} (contact speed, 360 m s^{-1}; machine current, 34 kA) and for two shots at 13300 rev min^{-1} (contact speed, 400 m s^{-1}; machine current, 45 kA). At the end of the sequence, many wires in the right wheel brushes were bent toward the leading edge in a direction opposite to their normal trailing position as shown in Fig. 5. The stiffer brushes used for the left wheel were not as badly bent.

5. Tests with full brush coverage

Recent operation of the homopolar generator was performed with full sets of 34 rim brushes on each flywheel. The brushes were made of the combed-braid conductor but a lower fiber packing factor was used to provide increased flexibility. Each brush contained 3840 of the stiffer (150 μm in diameter) wires. The brushes were examined and photographed after a sequence of 19 shots. All but two of these shots were made at 12600 rev min^{-1} (rim speed, 380 m s^{-1}; machine current, 40 kA). Two shots in the midst of the sequence were made at 14000 rev min^{-1} (rim speed, 420 m s^{-1}; machine current, 50 kA). No adjustments were made to the brushes between shots. After the sequence the brushes were refurbished by a light sanding with 150 grit garnet paper attached to the flywheel. This removed the accumulated wear debris and returned the brush surfaces to their original condition.

Figure 6 shows the appearance of contact surfaces of typical brushes after this sequence of 19 shots. In these photomicrographs, copper particles worn from the wire tips are seen still adhering to them, predominantly near the trailing edge of each wire. Viewed as a whole, the brushes seem to have

146
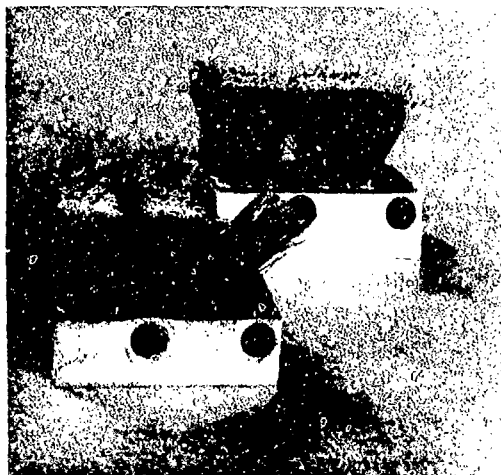
Fig. 5. Pair of brushes after high current test, showing the nature of fiber yielding due to the magnetic force. All fibers were initially inclined as those on far right.
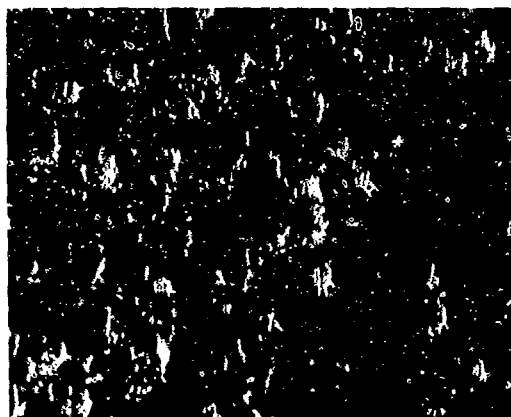
(a)
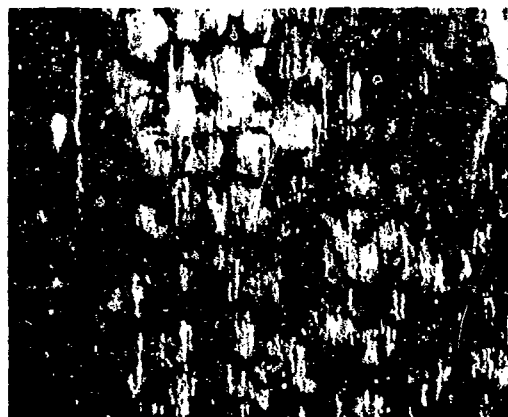
(b)
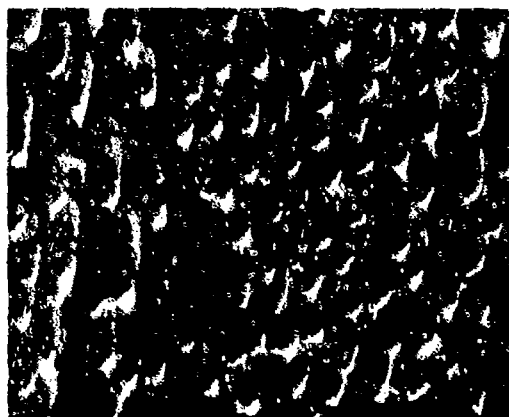
(c)

Fig. 6. Photomicrographs of copper fiber brush contact surface (the direction of slip ring motion is downward; fiber diameter, 150 μm): (a), (b) brushes worn by a sequence of 19 shots; (c) brush refurbished by sanding.

relatively cleaner leading edges with more material build-up near their trailing edges. This suggests that some of the adhering copper particles are transported from neighboring wires. Figure 6(b) shows the worst worn brush of the set. In the photograph, several places are seen where the build-up of copper covers the tips of four or five adjacent wires.

The highest speed shots were made at $15\,600$ rev min^{-1} (rim speed, 470 m s^{-1}; current, 60 kA). The brushes were inspected and refurbished after each such shot. The observed wear was similar to that described above but the area in which wear debris bridged adjacent fibers usually extended over a third of the axial width of the brush.

6. Discussion

The deformed fiber shape, for the brushes shown in Fig. 5, appears to be consistent with a magnetic-force-induced failure. In this case, the maximum bending stress occurs at a point $3/8$ of the fiber length from the slip ring end. However, the failure occurred at a somewhat lower current than expected. If it is assumed that all the wires in all 18 brushes carry equal current then, from eqn. (5), the calculated maximum stress for the $125\ \mu$m fiber is 140 MPa at 45 kA. For the shorter $150\ \mu$m fiber brush it is only 30 MPa. The yield strength for drawn copper wire is expected to be about 260 MPa, although the elastic limit would be less than this value. A transient thermal analysis has not yet been made to determine the fiber temperature rise due to frictional and electrical heating at the interface. Although the operating time is very brief, it is possible that some reduction in the copper fiber strength may result from annealing if a high temperature is attained.

A possible cause of this reduced capacity is the failure to collect current uniformly in all fibers. Figure 5 shows some unbent wires near the trailing edge of the brushes, which presumably did not participate in carrying the current. It is possible that those wires were simply not making contact because of misalignment at initial assembly. There are several possible additional causes for non-uniform fiber currents within a brush. First, there are slight irregularities in the wheel rim surface. If some fibers do not maintain contact as they move past the irregularities the remaining fibers are forced to carry more than their share of the current.

Unequal sharing of current may result from a decrease in the contact resistance with increased current. This is analogous to the selective action observed with graphite brushes where unequal current sharing is due to the negative temperature coefficient of resistance for that material. For a trailing-angle metal fiber brush, a reduction in contact resistance with increased current may occur because of the increased contact force resulting from the magnetic loading. The importance of this effect depends on the sensitivity of the contact resistance to force and the magnitude of that resistance in relation to the shunt resistance and other series resistance values.

148

Finally, variations in current density within the brush may result directly from circulating currents induced by small slip ring voltage gradients. Although not believed to be significant, they cannot be ruled out without further measurements.

Increasing the number of brushes increases the machine current at which the same degree of magnetic failure will occur. It was noted earlier, in eqn. (6), that the magnetic force per unit length on a fiber was proportional to current squared and inversely proportional to the number of fibers. Thus, if the brush complement is increased from 18 brushes with 4224 wires to 34 brushes with 3840 wires, it is predicted that the machine current required to produce this magnetic force will be increased from 45 to 60 kA.

As evidenced by Fig. 6, wear debris appears to be quite adherent to the fibers at the sliding interface. This may be due to the lack of an oxidizing atmosphere and the resulting high surface activity of the particles. It is speculated that, if it is allowed to continue, this cumulative build-up may reduce the capability of the individual fibers to follow independently the slip ring surface and could eventually destroy the usefulness of the brush as a high speed current collector.

7. Conclusions

With full complements of 34 of the stiffer copper fiber (150 μm in diameter) brushes for each flywheel, the pulse generator has been operated with a 60 kA output and a rubbing speed of 470 m s^{-1} without catastrophic magnetic failure. Satisfactory operation of these brushes depends on the maintenance of fiber flexibility. Within the permissible range of operating current, whose upper limit is determined by the strength of the material to withstand the magnetic force, brush lifetime is determined by the build-up of copper wear particles. The friction responsible for this wear is believed to be predominantly due to the magnetic force reaction load on the fiber tips. As a result, lifetime may be hundreds of shots at very low currents, falling to about twenty shots at 40 to 50 kA, and finally to one or two shots at 60 kA.

Acknowledgments

References

1 S. A. Nasar and H. H. Woodson, Storage and transfer of energy for pulsed-power applications. In *Proc. 6th Symp. on Engineering Problems of Fusion Research, San Diego, November 1975,* p. 316 (IEEE Publ. 75CH1097-5-NPS).

2 A. E. Robson, R. E. Lanham, W. H. Lupton, T. J. O'Connell, P. J. Turchi and W. L. Warnick, An inductive energy storage system based on a self-excited homopolar generator. In *Proc. 6th Symp. on Engineering Problems of Fusion Research, San Diego, November 1975*, p. 298 (IEEE Publ. 75CH1097-5-NPS).

3 I. R. McNab, Pulsed high power brush research, *IEEE Trans. Compon., Hybrids Manuf. Technol.*, *1* (1) (1978) 30 - 35.

4 R. A. Marshall and R. M. Slepian, Pulsed high-power brush research. Part III: Experiments at 15.5 MA/m^2 and 277 m/s, *IEEE Trans. Compon., Hybrids Manuf. Technol.*, *2* (1) (1979) 100 - 107.

5 I. R. McNab and G. A. Wilkin, Carbon fiber brushes for superconducting machines, *Electron. Power*, *18* (January 1972) 8 - 10.

6 P. Reichner, Metallic brushes for extreme high current applications, *IEEE Trans. Compon., Hybrids Manuf. Technol.*, *3* (1) (1980) 21 - 26.

7 P. Reichner, High current tests of metal fiber brushes, *IEEE Trans. Compon., Hybrids Manuf. Technol.*, *4* (1) (1981) 2 - 4.

SOLID BRUSH SYSTEM EVALUATION FOR PULSED HIGH CURRENT APPLICATIONS*

O. S. TAYLOR and W. F. HANNAN

Electrotechnology Department, Westinghouse Research and Development Center, Pittsburgh, PA 15235 (U.S.A.)

(Received November 5, 1981)

Summary

In this paper a solid brush current collection system used in a 15 MJ, 1.5 MA, homopolar pulse generator is described. A theoretical and experimental evaluation of the brush performance is made based on current, sliding velocity and pulse time. The evaluation utilizes the brush-to-rotor interface temperature as an indication of the solid brush system performance.

1. Introduction

A solid brush system was designed for a homopolar pulse generator machine to be used in an electromagnetic launcher test facility [1]. The pulse generator requires a current collection system capable of operating at extreme current and speed conditions for short periods of time. Most pulse generators use solid brushes of high metal metal–graphite composition to meet these severe needs [2]. The problem in solid brush current collection design for the pulse current applications is to establish limits for current density and sliding velocity at a given current pulse time. The design limits used in this particular configuration are 12 000 A in^{-2} (18.6 MA m^{-2}) peak current density and 236 m s^{-1} sliding velocity at a current pulse time of 200 ms. These limits were established as a result of an extrapolation of previous work [3] at 11 000 A in^{-2} current density, 277 m s^{-1} sliding velocity and 70 ms pulse time.

To substantiate these designs, and to evaluate new applications under alternative design conditions, a predictive contact performance model was needed. A thermal model of the brush system was developed since the contact temperature is an indication of the brush performance. The thermal model was used to predict the transient temperature of the sliding contact

---

between the brush and the rotor. The performance predictions were evaluated by comparison with data recorded in laboratory experiments on prototypic hardware.

2. Solid brush system design

The design parameters of the pulse generator are listed in Table 1. The rotor tip velocity is limited by the capabilities of the solid brush system. The collector magnetic flux density values shown are the result of a great deal of design effort to minimize these values. The magnetic field components coupled with the high brush currents result in brush forces that must be kept to acceptable values for reasonable mechanical loads applied to the brush. The radial magnetic field is particularly important due to the resulting voltage generated across the collector region when the rotor is turning. This voltage produces circulating currents in the brush system.

The current collection system specifications are shown in Table 2. This brush system is modular for ease of assembly and maintenance. A part module used in laboratory testing is shown in Fig. 1. This brush module has three rows of eleven brushes per row, whereas a full module for the homopolar pulse generator has six rows of ten brushes per row. The full brush module also has two pneumatic loading pistons instead of one as shown for the part module in Fig. 1. Otherwise the critical geometries of the full module and the test part module brush systems are identical.

Inside the brush holder module, the brushes are held by a metal bracket from which each brush is independently sprung. This metal bracket is rigidly attached to the piston in the pneumatic cylinder. The brushes are arranged in an egg-crate fashion and current is transferred from the brushes to the holder through silver-plated Be–Cu finger contacts. A row of six finger contacts is located along each 0.5 in side of the brush. The fingers are nestled inside the holder and contact the brushes as close to the rotor as possible to minimize the brush current path.

TABLE 1

Pulse generator parameters

Current	1.5×10^6 A
Rotor diameter	25.1 in (0.64 m)
Rotor tip speed	44000 ft min^{-1} (225 m s^{-1})
Collector magnetic flux density	
Radial	0.02 T
Axial	0.11 T
Circumferential	0.92 T
Number of pulses	1000
Current pulse time	200 ms

TABLE 2

Current collection system specifications

Brush current density	12 000 A in^{-2} (19 MA m^{-2})
Brush size	0.12 in thick × 0.5 in wide × 1.75 in long
	(3.2 mm × 12.7 mm × 44.5 mm)
Brushes per module	60 (33 per part module for test program)
Brush actuation	Pneumatic load–spring return
Brush pressure	20 lbf in^{-2} (138 kPa)
Brush atmosphere	Water humidified helium
Brush material	Cu–graphite
Rotor material	Copper-plated aluminum
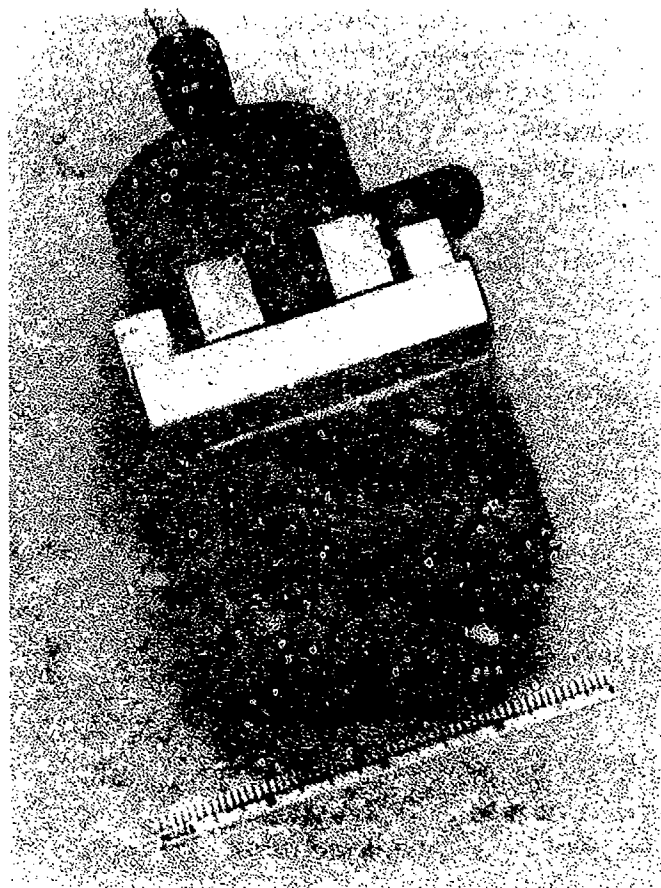
Fig. 1. Experimental brush module.

3. Test apparatus

A laboratory test facility was constructed to test the current collection arrangement. The brush holders were mounted in a test rig where current and speed were supplied externally. A variable-speed drive motor was used to drive the test rotor by a flat belt arrangement to the desired sliding speeds.

The current was supplied by a homopolar generator rated at 6 V and 20 000 A that was driven by a variable-speed drive motor.

The electrical circuit was made up of four main components which were the test brush system, the homopolar generator, a fuse and a coil. Prior to each test, the electrical circuit was complete except for the brushes which were retracted from the rotor. When the brush system was actuated, the brushes contacted the test rotor and current began to flow from the homopolar generator. The homopolar generator acted as a constant voltage source due to the large rotating inertia of the drive train. A 30 μH coil was designed and built for the circuit to give the proper current–time profile. The fuse was included in the circuit to limit the flow of current to the desired time.

The brushes were actuated by pneumatic piston–cylinder assemblies that were mounted atop the brush holders. The cylinders were connected to a manifold, valve and accumulator arrangement. For operation, the accumulator was filled to the proper pressure with the test gas. Then the valve (solenoid) that connected the accumulator to the manifold was opened, and the manifold and cylinders became pressurized, resulting in the design brush contact pressure.

4. Theory

The temperature at the brush–rotor interface is dependent on the heat generated at the interface, the heat conducted away from the interface and the heat transformed into internal energy. Consider the heat generated uniformly over the brush interface. The real contact between the brush and the rotor moves from front to back on the brush face approximately 20 times during the 200 ms pulse time due to rotor eccentricity effects [4], thereby distributing the heat uniformly.

The heat balance between the brush and the rotor is

$$q_B + q_R = Q_T \tag{1}$$

where q_B (W) is the heat rate into the brush, q_R (W) is the heat rate into the rotor and Q_T (W) is the generated heat rate at the interface.

Subscripts B and R will be used to designate the brush and rotor respectively. Assuming equal brush and rotor temperatures at the interface, the ratio of brush to rotor heat is [5]

$$\frac{q_B}{q_R} = \frac{A_B K_B}{A_R K_R} \left(\frac{\alpha_R}{\alpha_B}\right)^{1/2} \tag{2}$$

where K (W m^{-1} °C^{-1}) is the thermal conductivity, A (m^2) is the area and α (m^2 s^{-1}) is the thermal diffusivity.

For a uniformly distributed heat rate generated at a plane in a semi-infinite body, the temperature at the plane is [5]

$$T = \frac{1}{A\rho C(\pi\alpha)^{1/2}2} \int_0^\tau \frac{q(t)\,dt}{(\tau-t)^{1/2}} \tag{3}$$

where T (°C) is the temperature at the interface, ρ (kg m^{-3}) is the density, C (J kg^{-1} °C^{-1}) is the specific heat, $q(t)$ (W) is the heat rate, t (s) is the time (variable) and τ (s) is the time limit.

Equation (3) can be rewritten with the proper subscripts and combined with eqns. (1) and (2) to yield

$$T = \left[\rho_B C_B A_B (\pi\alpha_B)^{1/2}\left\{1 + \frac{A_R K_R}{A_B K_B}\left(\frac{\alpha_B}{\alpha_R}\right)^{1/2}\right\}\right]^{-1} \int_0^\tau \frac{Q_T(t)\,dt}{(\tau-t)^{1/2}} \tag{4}$$

The temperature at the interface is a constant, dependent on material properties and geometry, times an integral containing the total heat rate as a function of time.

The total heat rate at the interface is made up of two components:

$$Q_T = Q_L + Q_F \tag{5}$$

where $Q_L = I^2 R_c$ (W) is the contact current loss and Q_F (W) is the contact frictional loss.

The contact current loss is

$$Q_L = I^2 R_c \tag{6}$$

where R_c (Ω) is the total contact resistance, I (A) is the contact current, $R_c = r_c/N$, r_c (Ω) is the contact resistance per brush and N is the number of brushes.

The contact current is made up of two components:

$$I = I_L + I_c \tag{7}$$

where I_L (A) is the load current and I_c (A) is the circulating current.

The load current is determined by the overall system and is given as an input to the current collection system design. The circulating current, resulting from brushes located in a radial magnetic field, must be calculated. The circulating current is

$$I_c = \frac{NB_r lV}{2(r_c + r_s)} \tag{8}$$

where B_r (T) is the uniform radial magnetic field in the collector region, l (m) is the axial length of the collector region from center-line to center-line of end brushes, r_s (Ω) is the shunt resistance of a brush, i.e. the resistance from the brush to the holder, and V (m s^{-1}) is the rotor sliding velocity.

The circulating current calculated from eqn. (8) is used for determining the maximum contact temperature. The circulating current will be maximum at one end of the collector. For our calculation purpose, the circulating current is assumed uniform across the collector at its maximum value. The

average brush temperatures will occur in the center brush row and can be found by setting $I_c = 0$. The maximum temperature will be in the end brush row and can be found by calculating I_c and including it in the analysis.

The value of the rotor sliding velocity V is similar to the load current I_L, since both are determined by the overall system and are given as input to the current collection system design.

The contact frictional loss is

$$Q_F = \mu P_B A_B V \tag{9}$$

where μ is the brush-to-rotor friction coefficient and P_B (N m^{-2}) is the brush pressure.

The integral in eqn. (4) can now be evaluated over the time period of interest for any rotor sliding velocity and load current as functions of time. The above equations were programmed on a computer and a numerical integration was employed for the various current and velocity profiles.

5. Test results

Thermocouples were embedded in several brushes at distances of 0.06 in (1.5 mm) and 0.25 in (6.4 mm) from the rotor surface. The brush test system was then operated and the temperatures recorded. The predicted temperatures were compared with the measured values to determine the accuracy of the program. The instrumentation was unable to measure temperatures during a current test, so that tests to compare the predicted with the measured temperature values could only be made with contact frictional heat as input.

The results of the tests are shown in Fig. 2. The variable conditions of the tests were as follows: number of brushes used, 33 and 66; brush pressure, 20 and 30 lbf in^{-2} (138 and 207 kPa); sliding velocities, 113 and 225 m s^{-1}. The actual data plots shown in Fig. 2 are representative of the numerous tests performed at the conditions listed and were chosen due to close agreement with the average results. The data for each of the conditions shown in Fig. 2 were averaged at time intervals of 1 and 3 s. The spread of the data is indicated as a vertical line, the average is a point on the line and the number of tests is indicated below the line. A computer prediction based on a coefficient of friction of 0.3 is also plotted on the graphs.

Typical test results at operating conditions of current and sliding velocity are shown in Fig. 3. The results in Fig. 3(a) represent the standard design operating conditions listed in Tables 1 and 2. The current reached in this test was 25 000 A which represents the brush design current density of 12 000 A in^{-2} (18.6 MA m^{-2}). The current pulse time was approximately 200 ms and the sliding velocity was 225 m s^{-1}; these values duplicate the design conditions. The voltage drop was measured from the positive-polarity brush holder to the negative-polarity brush holder and included both of the brush-to-rotor
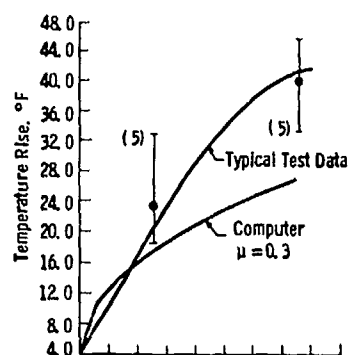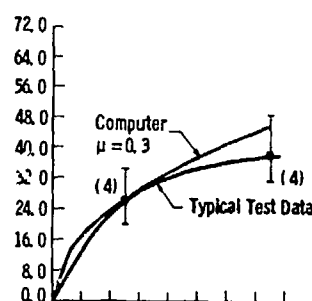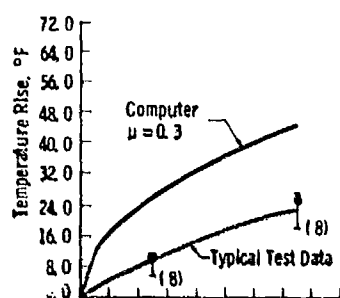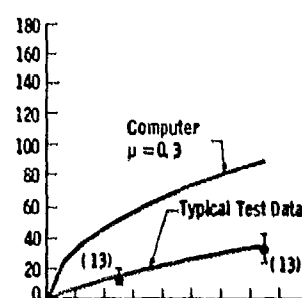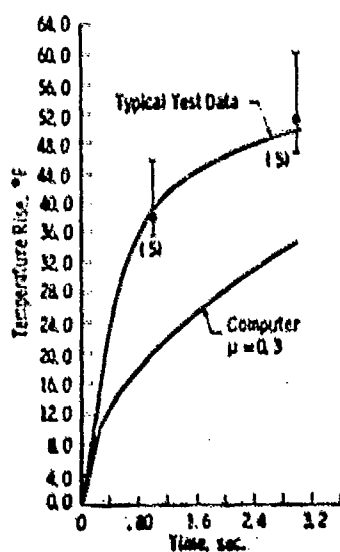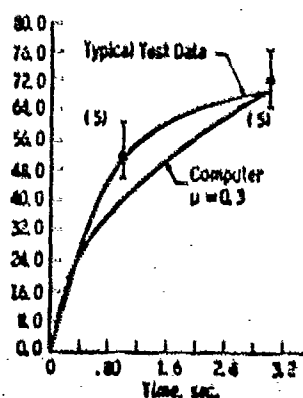
Fig. 2. Test data comparison with computer program prediction at constant friction coefficient $\mu = 0.3$: (a) $N = 33$, $P_B = 20\,\text{lbf in}^{-2}$ (138 kPa), $V = 113\,\text{m s}^{-1}$; (b) $N = 33$, $P_B = 20\,\text{lbf in}^{-2}$ (138 kPa), $V = 225\,\text{m s}^{-1}$; (c) $N = 66$, $P_B = 20\,\text{lbf in}^{-2}$ (138 kPa), $V = 113\,\text{m s}^{-1}$; (d) $N = 66$, $P_B = 20\,\text{lbf in}^{-2}$ (138 kPa), $V = 225\,\text{m s}^{-1}$; (e) $N = 33$, $P_B = 30\,\text{lbf in}^{-2}$ (207 kPa), $V = 113\,\text{m s}^{-1}$; (f) $N = 33$, $P_B = 30\,\text{lbf in}^{-2}$ (207 kPa), $V = 225\,\text{m s}^{-1}$.
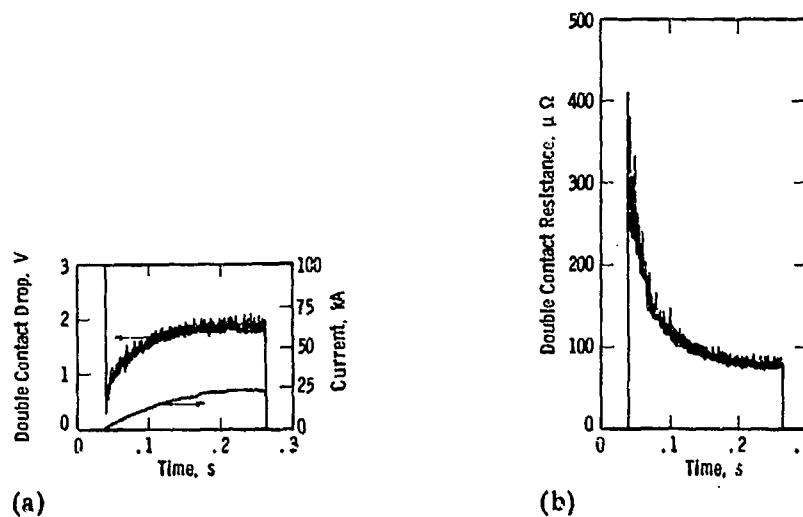
Fig. 3. Test results at design operating conditions.

voltage drops as well as voltage drops within each holder. Current level was measured by voltage measurement using a calibrated length of bus bar. The results in Fig. 3(b) represent the brush resistance obtained through dividing the voltage in Fig. 3(a) by the corresponding current. The total resistance at the end of the pulse was approximately 8×10^{-4} Ω. This translates into a half-module resistance of 40 $\mu\Omega$, and a resistance per brush of approximately 1 mΩ, which agrees with previous tests at shorter pulse times [3].

The maximum sliding velocity attained was 225 m s^{-1}, which is limited by the test rig. The maximum current level, representing a brush current density of 14 400 A in^{-2} (22.3 MA m^{-2}), was 30 000 A, which is limited by the circuit resistance and the voltage capability of the current source. The maximum pulse time was 500 ms, which is limited by the finger contacts due to a temperature rise in the fingers that would cause the material strength to fade if allowed to rise higher. Based on an $I^2 t$ evaluation, these maximum conditions represent a brush current density of 23 000 A in^{-2} at a pulse time of 200 ms and a sliding velocity of 225 m s^{-1}.

6. Discussion

For the data shown in Fig. 2, the closest correlations between actual data and computer predictions were in Figs. 2(b) and 2(f). The common parameters were 225 m s^{-1} sliding velocity and 33 brushes. In contrast, the worst correlations were in Figs. 2(c) and 2(d) where the common parameters were a brush pressure of 20 lbf in^{-2} and 66 brushes. It appears that the number of brushes has an effect on the correlation. According to the model, the effect of the number of brushes at or near these conditions is essentially the same as that of increasing the heat input by means such as increasing the brush pressure or speed. The brushes were concentrated in one location on the

rotor periphery. It might at first be thought that the trailing brush should be significantly hotter than the leading brush and that more brushes would accentuate this effect. Calculations show that the trailing brush is hotter, but the difference is insignificant relative to the total temperature rise. Several brushes located in the same track were instrumented with thermocouples, and no significant differences were found in the recorded temperatures; this agrees with the model.

It is believed that the results of Figs. 2(e) and 2(f), where the brush contact pressure was 30 lbf in^{-2}, were the most realistic results. The confidence in the results of Figs. 2(e) and 2(f) is due primarily to the ability of the brush to follow the rotor. At the higher brush loads, the effects due to brush side friction or pneumatic cylinder friction are less significant. In addition, the manifold pressure varied from test to test by as much as 2 lbf in^{-2}. A larger number of tests in addition to higher test pressure would help reduce these effects.

Other tests revealed that the minimum allowable brush pressure for non-arcing operation was 16 lbf in^{-2}. The incentive for operation at the lower brush pressures was lower wear and less frictional heat input. The wear was not significant for the laboratory tests. However, when operating conditions are pushed to higher values, the wear could become significant.

The value of the friction coefficient used for the computer predictions in Fig. 2 was based on an average of all of the data taken. This average value of the friction coefficient was 0.3 which seems reasonable for high metal metal–graphite brushes. The shapes of the curves of actual data in Fig. 2 are different from the shapes of the computer predictions. If a variable coefficient of friction is assumed, the curve shapes agree more closely. To decide how the variable coefficient of friction should be explained, we would have to determine the fundamental cause of the variation. That is, does the coefficient change due to temperature rise which would change the surface properties, or change due to strain rate effects tied directly to velocity. In any case, this is certainly an area worth pursuing in future investigations that deal with pulse applications at high power densities.

The graphs shown in Fig. 4 represent the condition for a full-scale 15 MJ, 1.5 MA, homopolar pulse generator [1]. Figure 4(a) shows the machine current and rotor velocity as a function of time. Figure 4(b) shows the predicted brush-to-rotor interface temperature rise with and without the radial magnetic field. The appropriate input data for the computer prediction are found in Table 3. The maximum temperature rise occurs near the end of the current pulse. This maximum predicted temperature rise is 229 °F at zero radial magnetic field and 270 °F at the design 0.02 T radial magnetic field. The magnetic field effects are more clearly shown in Table 4. One can see that the circulating currents due to magnetic fields can cause significant temperature rises.

No quantitative data were taken for the wear of the brushes during the pulse current test program. However, no significant wear was observed by eye during the program. The temperature rise predicted for the laboratory
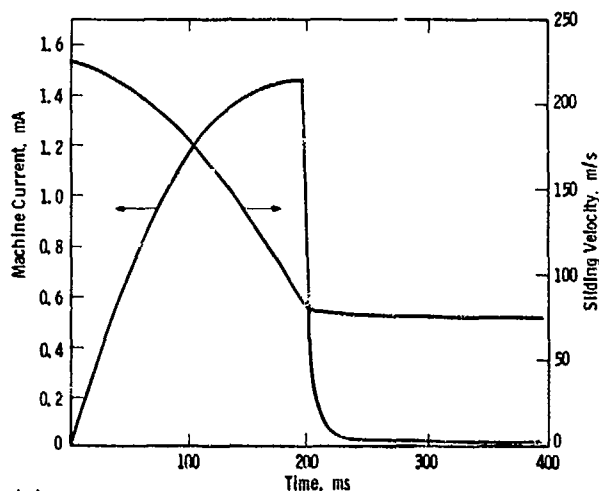
(a)
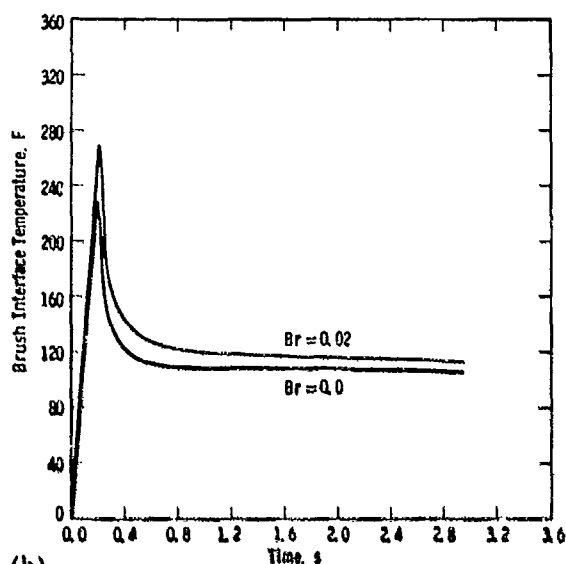
(b)

Fig. 4. Temperature predictions for design speed and current conditions in a machine environment.

current pulse test condition shown in Fig. 3 is 42 °F. This is low in comparison with the predicted values for the full-scale application. This also points out that seemingly adequate laboratory tests at design input conditions do not necessarily indicate the true performance. However, we do not anticipate an unacceptable wear rate at the full-scale conditions even though the interface temperature is higher. Laboratory tests on continuously operating brushes show acceptable wear rates at brush bulk temperatures in this range. The importance of the evaluation is to determine whether the expected temperature rise is near reasonable limits. Since the maximum predicted temperature rise is close to acceptable steady state limits, the wear rate will be similar to that predicted by the steady state limits at the same temperature rise.

TABLE 3

Computer input data for predictions found in Fig. 4

ρ_B = 374 lb ft^{-3} (6000 kg m^{-3}), brush density

C_B = 0.095 B.t.u. lb^{-1} °F^{-1} (397 J kg^{-1} °C^{-1}), brush specific heat

α_B = 2.77 ft^2 h^{-1}(7.1 × 10^{-5} m^2 s^{-1}), brush diffusivity

A_B = 112.5 in^2 (0.073 m^2), total brush area

K_B = 98.3 B.t.u. h^{-1} ft^{-1} °F^{-1} (170 W m^{-1} °C^{-1}), brush thermal conductivity

α_R = 1.6 ft^2 h^{-1}(4.1 × 10^{-5} m^2 s^{-1}), rotor diffusivity

A_R = 327 in^2 (0.21 m^2), rotor area swept by brushes

K_R = 60 B.t.u. h^{-1} ft^{-1} °F^{-1} (104 W m^{-1} °C^{-1}), rotor thermal conductivity

r_c = 1.0 × 10^{-3} Ω, contact resistance per brush

r_s = 3.0 × 10^{-4} Ω, shunt resistance per brush

N = 1800, number of brushes per machine end

n = 6, number of brush rows per machine end

μ = 0.3, brush-to-rotor coefficient of friction

P_B = 20 lbf in^{-2} (138 kPa), brush pressure

B_r = 0.02 T, collector region radial magnetic flux

l = 3.75 in (95 mm), axial length of collector region from center line to center line of end brushes

---

TABLE 4

Brush-to-rotor maximum interface temperature

Radial magnetic field B_r (T)	Temperature rise ΔT (°F (°C))
0	229 (127)
0.01	248 (138)
0.05	347 (193)
0.10	515 (286)
0.50	4150 (2306)

The pulse times investigated were up to 5 s. Predictions using pulse times above this value are questionable due to the thermal model limitations. The model assumes an infinite brush length rather than a finite length. For short periods of time (approximately 3 - 5 s for typical brush materials and geometries), the interface temperature predicted by the finite length model is virtually identical to the infinite length model. At higher pulse times, the temperature rise is greater than the present model predicts.

7. Conclusions

The thermal model outlined is a convenient method for analyzing solid brush systems for homopolar pulse generators. The analysis allows one to

establish realistic values for the relationship between current, sliding velocity and pulse time. The circulating currents induced in the solid brush systems in high power density pulse generators can cause a significant temperature rise at the brush-to-rotor interface.

An additional benefit from this test program was the verification of the ability of the current collection system to serve as a make switch to initiate the discharge of the homopolar generator.

Acknowledgments

References

1 D. W. Deis and I. R. McNab, A laboratory demonstration electromagnetic launcher, in *Proc. Electromugnetic Guns and Launchers Conf., San Diego, CA, November 4, 1980*, in *Proc. IEEE*, to be published.

2 I. R. McNab, Pulsed high power brush research, *Proc. Holm Conf. on Electrical Contacts, Illinois Institute of Technology, Chicago, IL, November 1 - 3, 1977*, Illinois Institute of Technology, Chicago, IL, pp. 105 - 114.

3 R. A. Marshall, P. Reichner and R. M. Slepian, Current collection systems for pulse power homopolar machines, *Proc. 7th Symp. on Engineering Problems of Fusion Research, Knoxville, TN, October 25 - 28, 1977, IEEE Publ. 77CH1267-4-NPS, 1977*, pp. 434 - 438.

4 P. Reichner, Brush contact on eccentric slip rings, *IEEE Trans. Power Appar. Syst., 100* (1) (1981) 281 - 287.

5 H. S. Carslaw and J. C. Jaeger, *Conduction of Heat in Solids*, Clarendon, Oxford, 2nd edn., 1959, pp. 75, 76.

CONTACT PHENOMENA AT HYPERVELOCITIES*

JOHN P. BARBER and DAVID P. BAUER

IAP Research, Dayton, OH 45459 (U.S.A.)

(Received December 1, 1981)

Summary

The phenomena which control contact between solids are understood in terms of the interaction of microscopic surface asperities. At low sliding speeds these asperities interact in a quasi-steady manner and the interaction is primarily mechanical. At very high sliding velocities the asperities impact and inertial forces dominate the interaction. Asperity impact can be prevented by the development of a fluid interlayer. The few observations which have been made on sliding at hypervelocities indicate that asperity impact does occur and that transition to a fluid interlayer can occur at velocities below which impact phenomena dominate or at velocities above the impact threshold. The transition velocity depends primarily on material properties.

1. Introduction

There is a growing interest in sliding and contact phenomena at extremely high velocities. Sliding at several kilometers per second is encountered in conventional guns, electric guns and rocket sleds. The behavior of contacts at these velocities is particularly important in electric guns [1, 2], while frictional losses and catastrophic wear mechanisms are of continuing concern in guns [3] and rocket sleds [4].

Hypervelocity is commonly used to denote the regime of velocity in which the predominant forces of interaction are inertial. The velocity at which inertial stresses dominate depends on the material under investigation and the mechanism by which interaction occurs. For most solids, velocities in excess of 1 km s^{-1} usually produce important shock and inertial loading effects. Contact phenomena can occur during sliding at hypervelocity which do not occur at lower velocities. In this paper we examine the effect of some of these phenomena on contact behavior.

---

2. Low and high speed sliding

Contact phenomena at low (less than 30 m s^{-1}) and high (less than 300 m s^{-1}) speeds have been studied extensively. Contact at these velocities is understood in terms of the interference of microscopic surface asperities [5]. When two solids are brought together, actual physical contact occurs at only a small number of discrete contact points. The normal load between the two solids is borne by these discrete areas. The number and size of the contact points increase with increasing applied load.

Adhesion between two bodies in contact occurs at the contact spots. The bodies become "welded" together at the contact spots. Tangential motion of one body with respect to the other must deform or shear material in the contact spot. A frictional force arises because of the ability of the contact spots to resist this deformation. Wear results from material fracture due to excessive straining in the contact spot region.

The effects of increasing sliding velocity on these basic contact phenomena have been extensively studied by Bowden and coworkers [6, 7]. The same basic contact phenomena occur at high velocities. The normal load is carried by interfering asperities and the frictional force arises from shearing of the resulting contact spots. During contact spot shearing, energy is dissipated in the deformation zone. At low speeds this dissipated energy is removed from the deformation zone by thermal conduction into the substrate (the bulk of the contacting bodies). The material in the deformation zone therefore remains in thermal equilibrium at a temperature close to that of the substrate. As the sliding velocity increases, the rate of energy dissipation in the deformation zone exceeds the conduction rate out of the deformation zone. The deformation zone temperature therefore rises. The rising temperature results in thermal softening of the material and reduced resistance to deformation. Therefore, as the sliding velocity increases, the frictional force and coefficient of friction are observed to decrease very markedly. This effect is illustrated in Fig. 1.

If velocity is further increased, the temperature of the entire surface of the slider may reach the melting point. The interface is then a liquid film and further asperity contact is prevented. The interface will behave as a hydrodynamic bearing. Viscoshearing of the liquid film dissipates energy which results in intense heating of the slider surface. This heating results in surface melting. Surface recession occurs, providing an influx of melted material from the slider surface which is equal to the material efflux from the interface due to slider motion and a steady state hydrodynamic interface is established. This behavior was observed by Bowden and coworkers [6, 7] for a variety of materials and material combinations.

The development of a hydrodynamic fluid layer obviously depends on the material properties of the slider, the sliding velocity, the normal load and perhaps the geometry of the slider. Under some circumstances, therefore, asperity contact will continue to occur to very high velocities.
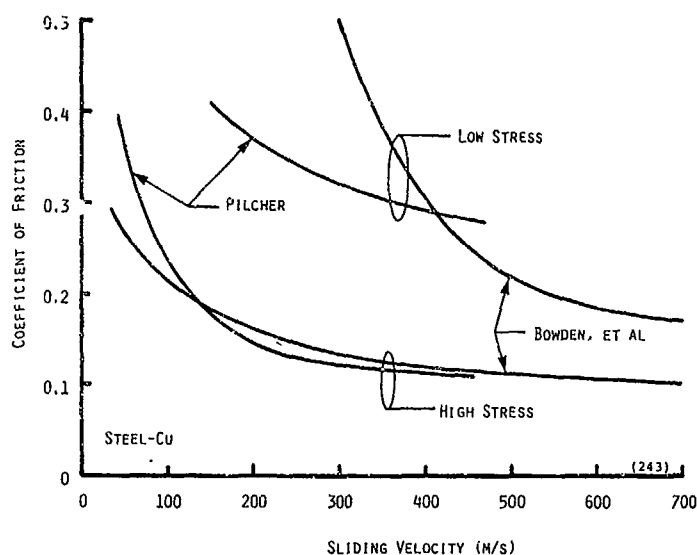
Fig. 1. The coefficient of friction for copper on steel. (Data from Bowden and Persson [7] and Pilcher and Wineholt [3].)

3. Hypervelocity contact effects

If a fluid interface is developed then sliding at hypervelocities will be primarily characterized by shearing of the fluid interface zone. As the sliding velocity increases, the velocity gradients in the interface will increase. The frictional force and the energy deposition in the interface will therefore both increase. Surface recession, slider wear and interface temperature will also increase. At some velocity it is probable that the temperature of the interface region becomes so high that the interface material is vaporized, with a resultant drop in viscosity and frictional force.

If a liquid interface is not established, then asperity contact will continue to occur at very high velocities. The asperities, however, can no longer come into contact in a steady or quasi-steady mechanical mode. Asperities will impact, generating shock stresses. In general the impact of the asperities will be oblique. The impact stress is then related to the impact velocity, the angle of impact and the density and shock speed of the materials involved [8]. The hypervelocity sliding threshold velocity is the velocity at which the impact-induced stress is equal to the ultimate strength of the material. For a symmetrical asperity contact (*i.e.* both asperities of the same material) the threshold velocity may be readily calculated. Threshold velocity is shown in Fig. 2 as a function of impact angle and material type. The threshold velocity is obviously very sensitive to materials and to the impact angle. For impact angles near 90° (normal impacts), the threshold velocity is relatively low. As the impact angle declines the threshold velocity increases.

Asperity impact will be a discrete, localized and violent event. This localized rapid release in energy resembles a microscopic explosion and would be expected to produce a small crater in the surface of the material.
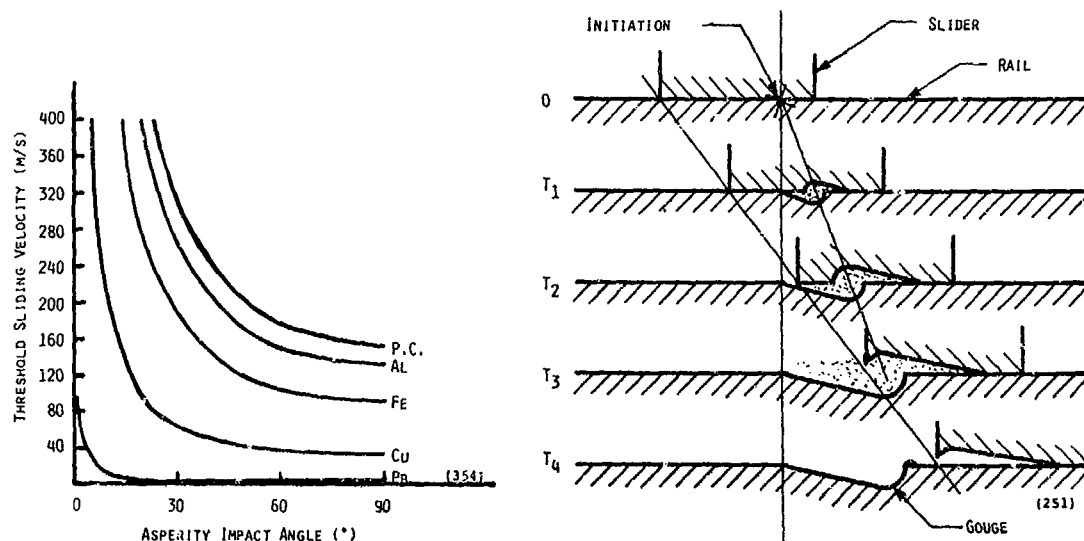
Fig. 2. The threshold sliding velocity *vs.* impact angle for several materials.

Fig. 3. The process of asperity impact and gouge formation.

The center of mass of this explosion will travel at approximately one-half of the slider velocity. Due to the relative motion of the slider, a tear-shaped crater results rather than a simple hemispherical shape, as illustrated in Fig. 3. Such tear-shaped craters or gouges have been observed [4].

During the asperity impact event the high stresses developed in the asperity region support the normal load between the surfaces while the tangential components of this stress (due to oblique impact) result in the frictional force.

The temperature of the entire slider surface at the interface will be raised by the asperity impact process. Impacts will occur randomly over the entire surface and the surface temperature may reach the melting point of the material. If the energy dissipation at the interface is adequate, sufficient molten material will enter the interface to establish a liquid layer. Further asperity contact is prevented (or at least greatly reduced) and the frequency of cratering or gouging would be expected to decline. The interface would behave as a hydrodynamic bearing as described previously.

4. Hypervelocity sliding observations

There are very few quantitative or qualitative observations of sliding phenomena at hypervelocities. The most complete set of data is that generated by Bowden and coworkers [6, 7] and extends only to the threshold of hypervelocity sliding for most of the materials investigated. The development of a fluid dynamic layer was clearly demonstrated for certain materials (tin, lead, bismuth) but not for others (copper, steel). There is some evidence

of the impact of asperities (gross surface damage); however, the experiments were not well suited to the observation of this phenomenon.

Graff and Dettloff [4] conducted excellent experiments to investigate the hypervelocity gouging phenomena observed on rocket sled rails. Their gouging observations are perhaps the strongest evidence of asperity impact available. The rocket sled data showed that gouging did not occur below a threshold velocity of approximately 1600 m s^{-1} on steel rails. Above the threshold velocity the frequency of gouging appeared to increase with velocity, as expected. In their laboratory experiments, similar general characteristics for a wide variety of materials were observed. In general they concluded that a minimum sliding velocity and a minimum normal load were both required to initiate gouging. The shape of the gouges was exactly as expected from the process illustrated in Fig. 3.

The electric rail gun at the Australian National University [1] was used to conduct many experiments on sliding metal contacts at hypervelocities. These experiments were characterized by high velocities (up to 2.5 km s^{-1}), high normal loads and high current densities (greater than 100 kA cm^{-2}). Most of the experiments were conducted with copper sliders on copper rails.

Smooth damage-free sliding was observed to occur up to a velocity of about 300 m s^{-1}. Above about 300 m s^{-1} gouging of the rails was found to occur. The gouges were randomly located on the surface of the rail. As the velocity increased, both the size and number of gouges appeared to increase, up to a velocity of about 900 m s^{-1}. Above 900 m s^{-1}, the frequency of gouging appeared to decline and a sudden transition to arcing at the contact occurred at about 1100 m s^{-1}. The contact voltage drop between the slider and rail was measured and the results are illustrated in Fig. 4. Contact
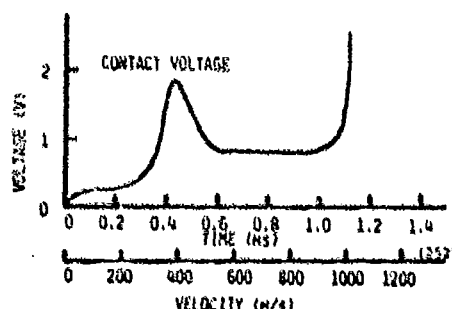
Fig. 4. Contact voltage drop for metal armature accelerated in the Australian National University rail gun.

voltage remained low (typically 0.5 V per side of the armature) with occasional excursions at velocities below 1100 m s^{-1}. At a velocity of 1100 m s^{-1}, the transition to arcing produced a rapid increase in contact voltage to several tens of volts. Similar results were obtained for many experiments with different current densities, different accelerations and different normal loads.

The onset of gouging at a velocity of 300 m s^{-1} is consistent with the asperity impact results illustrated in Fig. 2. By 300 m s^{-1} all but the most

oblique of impacts (less than $5°$) will produce stresses at or above the ultimate strength of copper. As the velocity increases, the energy dissipated in each collision grows and the gouges tend to become larger. The electrical contact obtained during the gouging process appears to be very good as illustrated by the very low measured contact voltage drop. By 900 m s^{-1} the interface is apparently becoming filled with fluid material. The development of a fluid layer decreases asperity impact and decreases gouging. By 1100 m s^{-1} a fully developed fluid layer is established. The electrical resistivity of this layer is, however, very high and it cannot stably support the very high current densities which were passed through it. As a result, the liquid interlayer was immediately vaporized and ionized by the high current. The resulting interface vapor and rapid surface recession prevented any further asperity contact and no further gouges were observed.

5. Conclusions

The phenomena which occur in hypervelocity sliding contacts can be quite different from those which occur at lower velocities. Quasi-steady mechanical contact of asperities cannot occur in most materials above a few hundred meters per second. At these velocities the asperities impact. Impact-generated stresses are well in excess of the ultimate strength of the material. The localized energy release involved in the asperity collision results in the formation of gouges. Asperity impact can be prevented by the development of a hydrodynamic fluid interlayer. Shear deformation in adhering asperities generates localized intense heating with associated melting. For some materials this fluid interlayer can develop at relatively low velocities. For other materials insufficient energy is released in shear deformation to produce large-scale surface melting. In these materials, asperity impact will occur and gouges will be formed. The asperity impact process may itself be sufficiently energetic to produce a fluid interlayer which will in turn prevent further asperity impact and result in smooth hydrodynamic sliding.

Much remains to be done to quantify the description of these processes. Further analysis and much better instrumentation of experiments are required before the processes of hypervelocity contact will be fully understood.

References

1 J. P. Barber, The acceleration of macroparticles in a hypervelocity electromagnetic accelerator, *Ph.D. Thesis*, The Australian National University, 1972.
2 I. R. McNab, D. W. Deis, V. R. Doshi, D. A. Fikse, H. R. Howland, W. F. Hughes, G. A. Kemeny, P. Reichner, O. S. Taylor, F. J. Young, J. P. Barber, D. P. Bauer, H. F. Swift and S. J. Bless, DC electromagnetic launcher development: phase I, *Rep. 79-9B2-EMACK-R7*, November 16, 1979 (Westinghouse Research and Development Center).
3 J. O. Pilcher II and E. M. Wincholt, Analysis of the friction behavior at high sliding velocities and pressures for gilding metal, annealed iron, copper and projectile steel, *ORL Rep. R 1955*, January 1977 (Ballistic Research Laboratories).

4 K. F. Graff and B. B. Dettloff, The gouging phenomenon between metal surfaces at very high sliding speeds, *Wear, 14* (1969) 87 - 97.

5 R. Holm, *Electric Contacts Theory and Application,* Springer, New York, 4th edn., 1967.

6 F. P. Bowden and E. H. Freitag, The friction of solids at very high speeds: I, metal on metal; II, metal on diamond, *Proc. R. Soc. London, Ser. A, 248* (1958) 350 - 367.

7 F. P. Bowden and P. A. Persson, Deformation, heating and melting of solids in high-speed friction, *Proc. R. Soc. London, Ser. A, 260* (1961) 433 - 458.

8 J. S. Rinehart, *Stress Transients in Solids,* HyperDynamicS, Santa Fe, NM, 1975.

DIFFUSION SKIN EFFECTS IN ULTRAHIGH VELOCITY LAMINATED CURRENT COLLECTORS*

W. F. HUGHES

Department of Mechanical Engineering, Carnegie–Mellon University, Pittsburgh, PA 15213 (U.S.A.)

F. J. YOUNG

Frontier Timber Company, EMF Division, State College, PA 16801 (U.S.A.)

(Received November 5, 1981)

Summary

Transient and steady state effects of diffusion and transport are analyzed in a high velocity current collector. The current is assumed to flow through the stationary conductor into the trailing edge of the collector.

The general two-dimensional magnetic transport equation is solved both for transient motion with an arbitrarily specified velocity and for constant velocity. The current distribution and the magnetic field in the feeding conductor and the laminated collector are found analytically for steady motion and numerically for transient motion.

At low velocity the diffusion skin effect dominates, allowing the current to diffuse into the collector. As the velocity increases, the velocity transport effect becomes dominant and tends to concentrate the current in the trailing edge of the collector.

1. Introduction

The performance of ultrahigh velocity current collectors was considered by Barber and Marshall [1] in connection with electromagnetic launcher experiments. The configuration, shown in Fig. 1, consists of a collector moving between two parallel rails which form a continuous circuit for a large current which may be varied with time. The studies of ref. 1, and subsequent unpublished work by the present authors, were based on the assumption of quasi-steady state operation and approximate mathematical techniques. As a result, it was concluded that a laminated collector, consisting of several

---
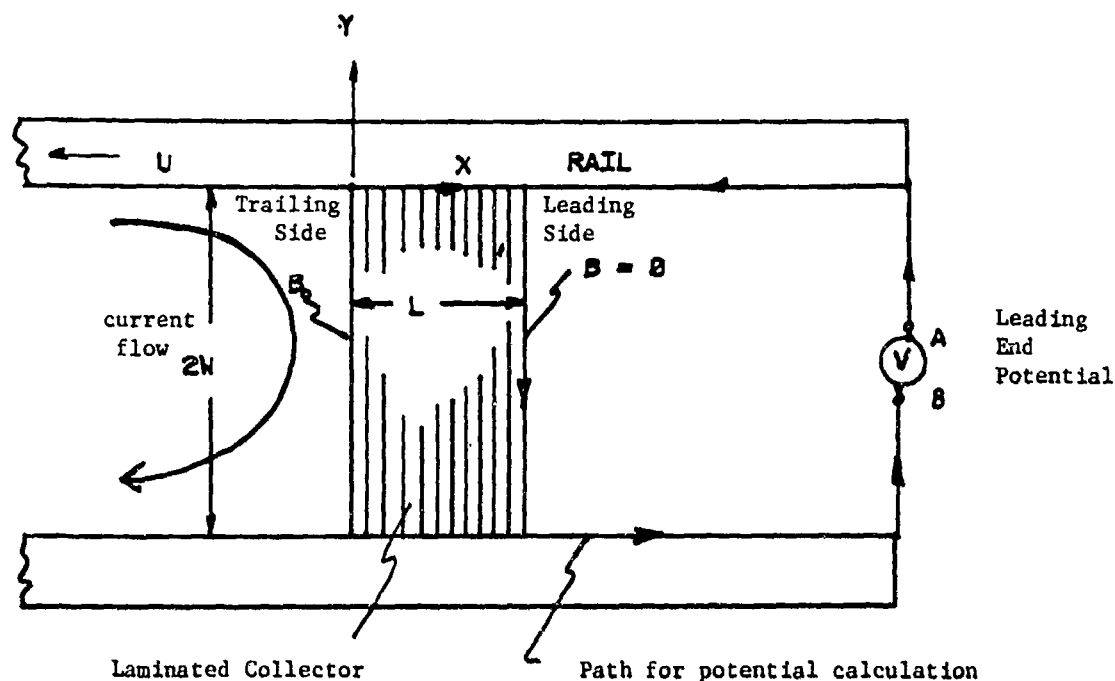
Fig. 1. The collector–rail configuration.

stacked leaves (the plane of each leaf being perpendicular to the direction of motion), would yield better performance than a solid current collector.

The main criterion of performance here is the uniformity of current distribution in the collector. Because of the high velocity of the collector relative to the rails, the current tends to pass through a narrow constriction at the trailing corner of the rail–collector interface. A primary objective in collector design is to achieve a more uniform current distribution throughout the collector and to prevent the high current densities and consequent local heating at these corners. A laminated design is considerably more effective in this regard than a solid current collector.

In these prior studies it was assumed that the velocity was constant so that in an actual accelerating collector the analyses were essentially quasi-steady. That is, the transient effects were entirely neglected, which is equivalent to neglecting (from a circuit point of view) the inductive effects in the collector compared with the resistive effects. *A priori* it is not clear that this is a valid procedure, and a complete study of the transient effects has therefore been undertaken and is reported here.

A numerical solution to the transient behavior, and an exact analytical solution to the steady state behavior of the infinitely laminated collector, is now presented. In the transient analysis, account may be taken of the actual velocity–time variation, of any arbitrary grading in the electrical conductivity of the leaves and of variation in conductivity with time due to heating or to material change.

The transient analysis considers both the time diffusion of current and magnetic field into the collector and the transport due to velocity. This

diffusion is countered by the velocity transport effect (which alone is considered in the quasi-steady analysis). When the velocity is low, diffusion dominates, but as the velocity increases, transport dominates. Consequently, the magnetic field begins to diffuse into the collector and, as the velocity increases, the magnetic field may begin to move back out toward the trailing side as the transport effect begins to dominate. The magnetic field and current profiles then will be given accurately by the quasi-steady analysis.

It will be seen that the transient effects are important only at low velocities and that the exact solution for quasi-steady operation gives quite an accurate representation of the instantaneous performance.

2. Mathematical formulation

Figure 1 shows the physical arrangement of the rails and the collector. The configuration is assumed to be two-dimensional so that the total current (per unit depth into the paper) I_0 is related to the magnetic field B_0 between the rails as $B_0 = \mu_0 I_0$. I_0 will be, in general, a specified function of time. We discuss the rail and the laminated collector separately.

2.1. The rail
In the rail, the magnetic transport equation is

$$\frac{\partial B}{\partial t} = \eta_r \nabla^2 B + \nabla \times (V \times B) \tag{1}$$

where η_r is the magnetic diffusivity given by $1/\sigma_r \mu_0$. In the frame of reference (attached to the collector) shown in Fig. 1, the velocity V of the rail is given by $V = -u\hat{x}$. We denote the negative z component of B as B. Then eqn. (1) becomes

$$\frac{\partial B}{\partial t} = \eta_r \left(\frac{\partial^2 B}{\partial x^2} + \frac{\partial^2 B}{\partial y^2} \right) + u \frac{\partial B}{\partial x} \tag{2}$$

Now $\partial^2 B/\partial x^2$ may be neglected compared with $\partial^2 B/\partial y^2$. If the skin depth is of order δ in the y direction, it will be shown later than $\delta \ll l$ so that $\partial^2 B/\partial x^2$ is of order B/l^2 and $\partial^2 B/\partial y^2$ is of order B/δ^2. This assumption is valid except very close to start-up where any error should have little effect over most of the time of interest.

The term $\partial B/\partial t - u\partial B/\partial x$ represents the eulerian derivative in the frame of reference indicated, which is at rest with respect to the collector. This is then precisely the time derivative with respect to an observer at rest on the rail. With respect to a frame of reference attached to the rails, eqn. (2) is

$$\frac{\partial B}{\partial \theta} = \eta_r \frac{\partial^2 B}{\partial y^2} \tag{3}$$

This is a one-dimensional diffusion equation for diffusion into the rail at any fixed position on the rail. If we assume that u is nearly constant over the time l/u of traverse of the armature, then θ and x may be related as

$$\theta = \frac{l-x}{u} \tag{4}$$

Equation (3) may be solved for $B(\theta, y)$ and transformed using eqn. (4) into $B(x, y)$ for the region of rail $0 < x < l$ in the frame of reference of the armature. For the rail region $x < 0$ (between the muzzle and the armature) eqn. (3) is still valid but the transformation from $B(\theta, y)$ to $B(x, y)$ must be carried out carefully since relationship (4) is no longer valid. The procedure is relatively simple and will be discussed later.

The boundary conditions on B are

$$
\begin{array}{llll}
B = B_0(t) & x = 0 & \text{on the trailing side of the collector and} \\
& & \text{on the inside surface of the rails} & (5) \\
B = 0 & x = l & \text{on the leading side of the collector}
\end{array}
$$

At the rail–collector interface $y = 0$, $0 < x < l$, B is continuous and the interfacial value is denoted as B_i which will be a function of time as well as of the x location.

Equation (3) may now be solved as a one-dimensional diffusion problem with input with time θ given by B_i. In other words, an observer riding with the rail beginning at the leading side of the collector will pass across the collector to the trailing side while seeing B_i as an input along the surface $y = 0$. We assume that $B_i(x)$ does not change during this traverse which occurs in time l/u.

The solution to eqn. (3) may be written in terms of a unit step function response using Duhamel's theorem as

$$B(\theta, y) = \int_0^\theta B_i{}'(\theta - \tau)\, B_u(\tau, y)\, d\tau \tag{6}$$

where B_u is the response to a unit step input. Since the skin depth δ is much less than the rail thickness h ($\delta \ll h$), the domain of diffusion in the y direction is effectively infinite. Hence

$$B_u(\tau, y) = \text{erfc}\left\{\frac{y}{2(\eta_r \tau)^{1/2}}\right\} \tag{7}$$

Of particular interest is the expression

$$\left(\frac{\partial B}{\partial y}\right)_{y=0}$$

evaluated in the rail. This expression will be useful for current density evaluation from Ampère's law $J = \nabla \times H$. Since the functional forms are continuous we can write

$$\left(\frac{\partial B}{\partial y}\right)_{y=0} = \int_0^\theta B'(\theta-\tau)\left\{\frac{\partial}{\partial y}B_u(\tau,y)\right\}_{y=0} d\tau \tag{8}$$

Further,

$$\left(\frac{\partial}{\partial y}\left[\text{erfc}\left\{\frac{y}{2(\eta_r\tau)^{1/2}}\right\}\right]\right)_{y=0} = -\frac{1}{(\pi\eta_r\tau)^{1/2}} \tag{9}$$

so that

$$\left(\frac{\partial B}{\partial y}\right)_{y=0} = -\int_0^\theta B'(\theta-\tau)\frac{1}{(\pi\eta_r\tau)^{1/2}} d\tau \tag{10}$$

Now at the interface between the rail and the collector the tangential electric field E_x is continuous. From Ohm's law $E_x = J_x/\sigma$ we have

$$\left(\frac{J_x}{\sigma_r}\right)_{y=0 \text{ rail}} = \left(\frac{J_x}{\sigma}\right)_{y=0 \text{ armature}} \tag{11}$$

where σ is the conductivity of the collector and may be a function of position x and of time if heating effects are considered. From Ampère's law,

$$\mu_0 J_x = \frac{\partial B_z}{\partial y} = -\frac{\partial B}{\partial y} \tag{12}$$

so that

$$(\mu_0 J_x)_{y=0 \text{ rail}} = \int_0^\theta B'(\theta-\tau)\frac{1}{(\pi\eta_r\tau)^{1/2}} d\tau \tag{13}$$

We now consider the collector where the above expression will be used to effect a solution.

2.2. The collector

The collector consists of a stack of infinitesimally thin leaves as shown in Fig. 2. The conductivity may be thought of as anisotropic, with a value in the y direction (which may depend on x) and a zero value in the x direction since the leaves are assumed to be insulated from each other. Hence we may use a field theory approach with an anisotropic conductivity or a circuit approach with a conductivity σ along a leaf. The approaches are equivalent and will yield the same results.

Let us consider a circuit approach. Referring to Fig. 2, a line integral may be formed about the circuit ABCDEFA. The e.m.f. around the loop must equal the voltage IR drop. Hence

$$\oint E\cdot dl = -\int_A \frac{\partial B_z}{\partial t} dA = \int_A \frac{\partial B}{\partial t} dA \tag{14}$$

Fig. 2. Path of integration for the collector equation.

By Ohm's law $J = \sigma E$ the integral becomes

$$\left(\frac{J_y}{\sigma}\,2w\right)_{x+\Delta x} - \left(\frac{J_y}{\sigma}\,2w\right)_{x} - \frac{2J_x}{\sigma_r}\,\Delta x - \frac{\partial B}{\partial t}\,2w\,\Delta x = 0 \tag{15}$$

From the expression for J_x in eqn. (12), and from $J_y = (1/\mu_0)\partial B/\partial x$, we have

$$\frac{\partial}{\partial x}\left(\frac{J_y}{\sigma}\right) = \frac{J_x}{w\sigma_r} + \frac{\partial B}{\partial t}$$

$$\frac{\partial}{\partial x}\left(\frac{1}{\sigma}\,\frac{\partial B}{\partial x}\right) = -\frac{1}{w\sigma_r}\left(\frac{\partial B}{\partial y}\right)_{y=0\ \text{rail}} + \mu_0\frac{\partial B}{\partial t} \tag{16}$$

And finally, using eqn. (13)

$$\frac{\partial}{\partial x}\left(\frac{1}{\sigma}\,\frac{\partial B}{\partial x}\right) = \frac{1}{w\sigma_r}\int_0^\theta B'(\theta-\tau)\,\frac{1}{(\pi\eta_r\tau)^{1/2}}\,d\tau + \mu_0\frac{\partial B}{\partial t} \tag{17}$$

which is the integrodifferential equation for $B(x)$ in the collector. Note that the subscript i has been dropped on $B'(\theta-\tau)$ since the interfacial value is the same as in the collector where B is only a function of x.

It is convenient to transform the integral back to x from θ. B' becomes $(-1/u)\partial B/\partial x$ and we introduce the variable $x' = x + u\tau$. Equation (17) becomes

$$\frac{\partial}{\partial x}\left(\frac{1}{\sigma}\,\frac{\partial B}{\partial x}\right) = -\frac{1}{w\sigma_r}\int_x^l\frac{\partial B}{\partial x}(x')\,\frac{dx'}{\{(x'-x)\pi\eta_r/u\}^{1/2}} + \mu\frac{\partial B}{\partial t} \tag{18}$$

It may be noted that $B(\theta - \tau)$ is meant to be evaluated with time as the independent variable. The value of time would be $(l - x)/u - \tau$. This is equivalent to using x' as an independent variable with value $x + u\tau$. In other words, if an observer riding on the rail begins at the leading side of the collector, he will travel a distance $l - x - u\tau$ in time $(l - x)/u - \tau$. This motion places him at position $x + u\tau$ in the frame of reference of the collector.

It is convenient to normalize this equation. We define the following dimensionless variables and parameters:

$$x^* = x/l$$

$$B^* = B/B_0(t = 0)$$

$$\sigma^* = \sigma/\sigma_0$$

where σ_0 is the conductivity of the armature at $x = 0$, $t = 0$ (initial value for the trailing leaf);

$$t^* = t/\mu_0 l^2 \sigma_0$$

$$\alpha = \frac{l}{w}\,\frac{\sigma_0}{\sigma_r}\left(\frac{ul}{\pi\eta_r}\right)^{1/2}$$

where u is a specified function of time. Equation (18) then takes the form

$$\frac{\partial}{\partial x^*}\left(\frac{1}{\sigma^*}\frac{\partial B^*}{\partial x^*}\right) = -\alpha\int_{x^*}^{1}\frac{\partial B^*(x'^*)}{\partial x'^*}\,\frac{dx'^*}{(x'^* - x^*)^{1/2}} + \frac{\partial B^*}{\partial t^*} \tag{19}$$

with boundary and initial conditions given as

$$B^*(x^* = 0, t^*) = B_0^*(t^*)$$

$$B^*(x^* = 1, t^*) = 0$$

$$B^*(x^*, t^* = 0) = 0$$

and $\sigma^*(x^*, t^*)$ and $\alpha(t^*)$ are to be specified. This equation is to be solved for $B^*(x^*, t^*)$, which is the magnetic field profile in the collector. Once B^* is found, the current distribution may be evaluated and B^* in the rail may be determined for $0 < x < l$.

Before proceeding to the general solution of the above equation, which must be implemented numerically, the quasi-steady case for which an analytical solution may be found will be discussed.

3. Quasi-steady state operation with uniform conductivity

If σ^* is assumed to be constant and the unsteady term $\partial B^*/\partial t$ is neglected, an exact analytical solution to eqn. (19) may be effected. We can now obtain an exact solution to this problem of the multileaved laminated

collector. The solution will be a function of only one parameter α, which depends on the velocity u.

We begin with eqn. (19) with the unsteady term neglected and the conductivity uniform so that $\sigma^* = 1$:

$$\frac{\mathrm{d}^2B^*}{\mathrm{d}x^{*2}} = \alpha\int_1^{x^*}\frac{\mathrm{d}B^*(x'^*)}{\mathrm{d}x'^*}\frac{\mathrm{d}x'^*}{(x'^* - x^*)^{1/2}} \tag{20}$$

The equation may be simplified by the following transformation. Let

$$v = 1 - x^*$$
$$v' = 1 - x'^* \tag{21}$$

The primes merely indicate dummy variables of integration. Then

$$\frac{\mathrm{d}^2B^*}{\mathrm{d}v^2} = \alpha\int_0^v\frac{\mathrm{d}B^*}{\mathrm{d}v'}\frac{\mathrm{d}v'}{(v - v')^{1/2}} \tag{22}$$

Equation (22) is an integrodifferential equation with the following boundary conditions:

$$v = 0\ (x^* = 1) \qquad\qquad B^* = 0$$
$$v = 1\ (x^* = 0) \qquad\qquad B^* = 1 \tag{23}$$

This equation is a Volterra integral equation of the second kind with a convolution-type kernel. A solution for $B^*(x^*)$ may be carried out as follows.

By using the convolution theorem we can take the Laplace transform of eqn. (22). The convolution of two functions $F_1(t)$ and $F_2(t)$ is defined as

$$F_1(t)*F_2(t) = \int_0^t F_1(t - \tau)F_2(\tau)\,\mathrm{d}\tau \tag{24}$$

and

$$f_1(s)f_2(s) = \mathcal{L}\{F_1(t)*F_2(t)\} \tag{25}$$

and here F_2 is actually $\mathrm{d}B^*/\mathrm{d}v'$. Hence $f_2(s)$ is the Laplace transform of the derivative. Carrying out the operation and using the condition $B^*(v = 0) = 0$ we have

$$s^2f(s) - B'^*(v = 0^+) = \alpha\left[\{sf(s)\}\left(\frac{\pi}{s}\right)^{1/2}\right] \tag{26}$$

where B^* is a function of v, so that

$$f(s) = \frac{B'^*(v = 0^+)}{s^2 - \alpha\pi^{1/2}s^{1/2}} \tag{27}$$

The inverse of this transformed equation is not immediately obtainable. It may be effected, however, by expanding the expression for $f(s)$ in a series

of negative powers in s, essentially a Laurent series about $s = 0$. The result of the expansion is

$$\frac{f(s)}{B'^*(v = 0^+)} = \sum_{n=0}^{\infty} \frac{A^{2n}}{s^{3n+2}} + \sum_{n=0}^{\infty} \frac{A^{2n+1}}{s^{\{6(n+1)+1\}/2}} \quad (28)$$

where A is $\alpha\pi^{1/2}$.

Now the inverse transform may be taken term by term to give

$$\frac{B^*(v)}{B'^*(v = 0^+)} = \sum_{n=0}^{\infty} \frac{A^{2n}v^{3n+1}}{(3n+1)!} + \sum_{n=0}^{\infty} \frac{A^{2n+1}2^{3(n+1)}v^{3(n+1)-1/2}}{\pi^{1/2} \times 1 \times 3 \times 5 \times \ldots \times \{6(n+1)-1\}} \quad (29)$$

The denominator in the second series is meant to be the product of $\pi^{1/2}$ and all odd integers from unity up to and including the number $6(n + 1) - 1$.

Now the constant $B'^*(v = 0^+)$ may be evaluated. $B^*(v = 1) = B^*(x^* = 0) = 1$ so that eqn. (29) becomes

$$B'^*(v = 0^+) = \left[\sum_{n=0}^{\infty} \frac{A^{2n}}{(3n+1)!} + \sum_{n=0}^{\infty} \frac{A^{2n+1}2^{3(n+1)}}{\pi^{1/2} \times 1 \times 3 \times 5 \times \ldots \times \{6(n+1)-1\}} \right]^{-1} \quad (30)$$

Then the final expression for $B^*(x^*)$ from eqn. (29) is found by transforming back to the variable x^* and using eqn. (30):

$$B^*(x^*)$$
$$= \left(\sum_{n=0}^{\infty} \frac{A^{2n}(1-x^*)^{3n+1}}{(3n+1)!} + \sum_{n=0}^{\infty} \frac{A^{2n+1}2^{3(n+1)}(1-x^*)^{3(n+1)-1/2}}{\pi^{1/2} \times 1 \times 3 \times 5 \times \ldots \times \{6(n+1)-1\}} \right) \times$$
$$\times \left(\sum_{n=0}^{\infty} \frac{A^{2n}}{(3n+1)!} + \sum_{n=0}^{\infty} \frac{A^{2n+1}2^{3(n+1)}}{\pi^{1/2} \times 1 \times 3 \times 5 \times \ldots \times \{6(n+1)-1\}} \right)^{-1} \quad (31)$$

This is the expression for $B^*(x^*)$ through the collector. It is interesting to note that the normalized magnetic induction profile is a function of only one parameter α. This profile is shown in Fig. 3.

3.1. The current distribution and Joule heating rate in the collector

The current flux J_y in the collector may be found from $J_y = (1/\mu_0)\partial B/\partial x$ by differentiating eqn. (31). A normalized current density J_y^* defined as

$$J_y^* = \frac{J_y \mu_0 l}{B_0}$$

may be found simply as

$$J_y^* = \frac{\partial B^*}{\partial x^*} \quad (32)$$
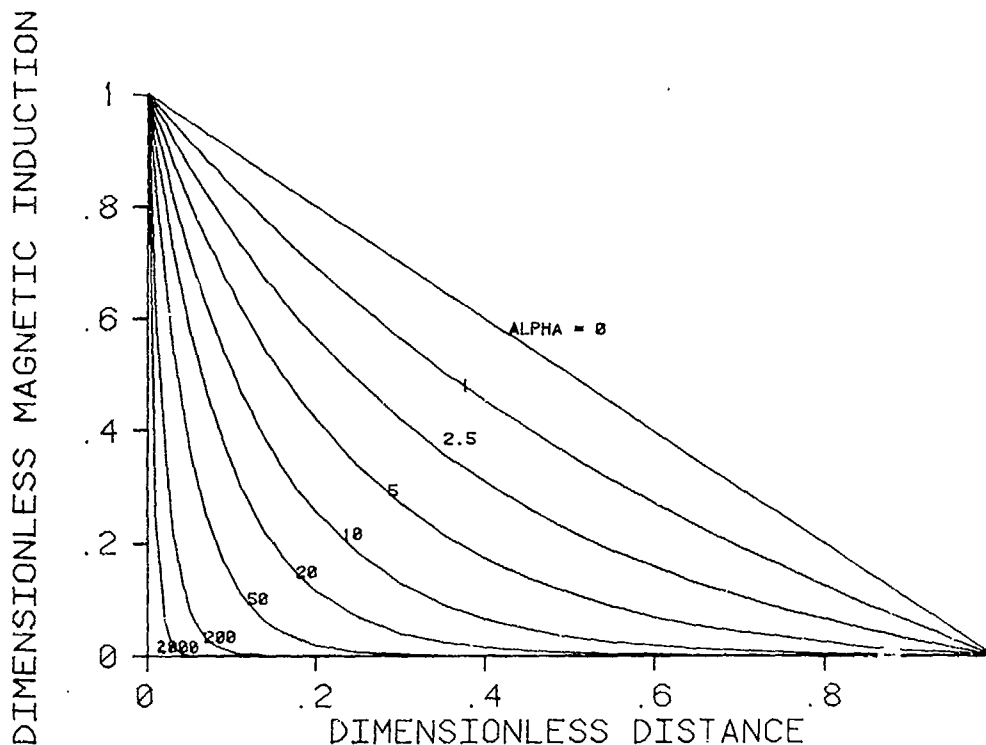
Fig. 3. The magnetic field profile through the collector for quasi-steady state operation with uniform conductivity.

From the expression for $B^*(x^*)$ we find

$$J_y^* = \left(-\sum_{n=0}^{\infty} \frac{A^{2n}(1-x^*)^{3n}}{(3n)!} - \sum_{n=0}^{\infty} \frac{A^{2n+1}2^{3n+2}(1-x^*)^{3(n+1)-3/2}}{\pi^{1/2} \times 1 \times 3 \times 5 \times \dots \times \{6(n+1)-3\}}\right) \times$$

$$\times \left(\sum_{n=0}^{\infty} \frac{A^{2n}}{(3n+1)!} + \sum_{n=0}^{\infty} \frac{A^{2n+1}2^{3(n+1)}}{\pi^{1/2} \times 1 \times 3 \times 5 \times \dots \times \{6(n+1)-1\}}\right)^{-1} \quad (33)$$

This profile depends only on α and is shown in Fig. 4. Of course, $J_x = 0$ in the armature since it is laminated.

The Joule heat rate density in the armature may be found numerically by simply forming J_y^2/σ after J_y is calculated.

In terms of J_y^*, a normalized Joule heat rate density may be defined. We define it as

$$\frac{J_y^{*2}}{\sigma^*} = \frac{J_y^2}{\sigma} \frac{\sigma_0 \mu_0^2 l^2}{B_0^2} \quad (34)$$

This normalized Joule heat rate distribution with x^* then depends only on one parameter α and the $\sigma^*(x^*)$ profile. For the situation being considered here with constant σ (i.e. $\sigma^* = 1$), the normalized Joule heat profile with x^* depends only on α.
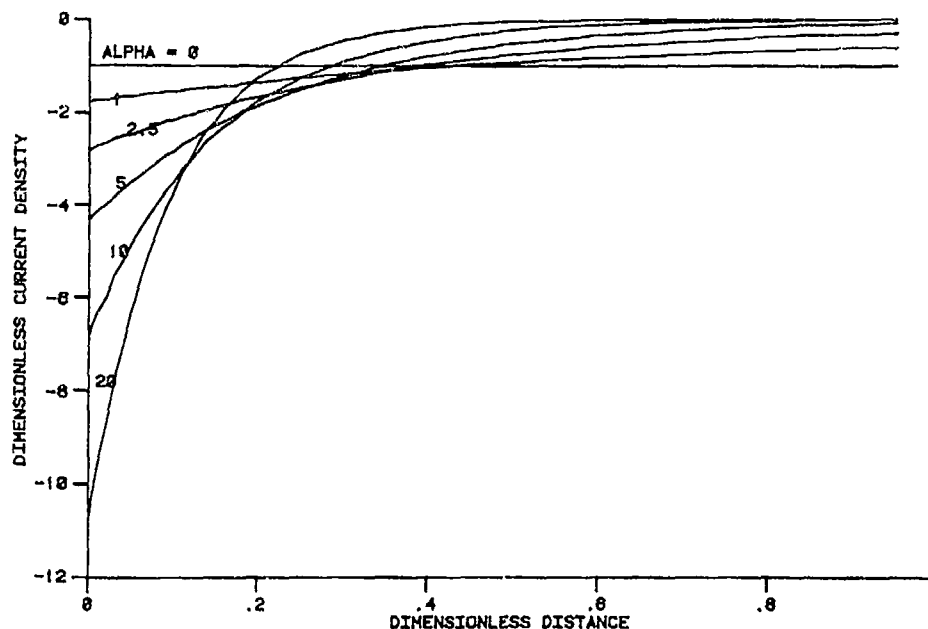
Fig. 4. Normalized current density in the collector for quasi-steady state operation with uniform collector conductivity.

3.2. The current distribution and Joule heating rate in the rail

It is not practical to find the general field distribution in the rail adjacent to the collector. The analysis becomes rather unwieldly.

We can, however, calculate the current densities in the rail just at the rail–collector interface. J_y is continuous across the interface and expression (33) is valid just inside the rail at $y = 0^+$. J_x just inside the rail at $y = 0^+$ may be found from eqn. (16) and the above expression for J_y^* (eqn. (33)). From eqn. (16)

$$(J_x)_{y=0^+} = w\sigma_x \frac{\mathrm{d}}{\mathrm{d}x}\left(\frac{J_y}{\sigma}\right) \tag{35}$$

Defining a normalized J_x as before

$$(J_x^*)_{y=0^+} = (J_x)_{y=0^+} \frac{\mu_0 l}{B_0} \tag{36}$$

we have

$$(J_x^*)_{y=0^+} = \frac{\sigma_x w}{\sigma_0 l} \frac{\mathrm{d}}{\mathrm{d}x^*}\left(\frac{J_y^*}{\sigma^*}\right)$$

The term $\sigma_x w/\sigma_0 l$ is a dimensionless conductivity ratio which we denote as C. Then

$$(J_x^*)_{y=0^+} = C\frac{\mathrm{d}}{\mathrm{d}x^*}\left(\frac{J_x^*}{\sigma^*}\right) \tag{37}$$

182

For the problem considered here, $\sigma^* = 1$ so that $(J_x{}^*)_{y=0^+}$ may be found immediately by differentiating eqn. (33). We obtain $J_x{}^*/C$ in the rail at $y = 0^+$:

$$\frac{(J_x{}^*)_{y=0^+}}{C}$$

$$= \left(\sum_{n=0}^{\infty} \frac{A^{2n}(1-x^*)^{3n-1}}{(3n-1)!} + \sum_{n=0}^{\infty} \frac{A^{2n+1}2^{3n+1}(1-x^*)^{3(n+1)-5/2}}{\pi^{1/2} \times 1 \times 3 \times 5 \times \ldots \times \{6(n+1)-5\}} \right) \times$$

$$\times \left(\sum_{n=0}^{\infty} \frac{A^{2n}}{(3n+1)!} + \sum_{n=0}^{\infty} \frac{A^{2n+1}2^{3(n+1)}}{\pi^{1/2} \times 1 \times 3 \times 5 \times \ldots \times \{6(n+1)-1\}} \right)^{-1} \quad (38)$$

which depends only on α.

Again, the Joule heating rate density in the rail along the rail–collector interface may be obtained by calculating

$$\frac{J_x{}^2 + J_y{}^2}{\sigma_r}$$

after $J_x{}^*$ and $J_y{}^*$ are found from the above expressions.

A normalized Joule heat rate density JH^* may be found in the rail as follows in terms of the actual Joule heat rate:

$$JH = \frac{J_x{}^2 + J_y{}^2}{\sigma_r}$$

$$JH^*_{y=0^+ \text{ rail}} = J_x{}^{*2} + J_y{}^{*2} = JH\sigma_r \left(\frac{\mu_0 l}{B_0}\right)^2 = \frac{J_x{}^2 + J_y{}^2}{\sigma_r} \sigma_r \left(\frac{\mu_0 l}{B_0}\right)^2 \quad (39)$$

This normalized Joule heat rate density is then a function of two dimensionless parameters α and C.

4. Transient analysis

The complete transient analysis requires a solution to eqn. (19) with an arbitrary input of velocity u and magnetic field B_0, with time and of the conductivity σ with position x and time. That is, the functions $B_0{}^*(t^*)$, $\sigma^*(x^*, t^*)$ and $\alpha(t^*)$ must be specified. An analytical solution to this equation is not feasible and a numerical solution must be implemented. If this solution were incorporated as part of a simulation code, the $B_0{}^*$, σ^* and α functions would be obtained as part of the complete solutions. From a practical point of view, the solution is effected by a finite difference technique and values of $B_0{}^*$, σ^* and α would be updated at each time step. The normalized conductivity σ^* can be, in general, a function of position and time due to heating effects in the collector and/or conductivity grading.

For simplicity, we assume in what follows that $\sigma^* = 1$; this means that the conductivity of the collector is assumed to be uniform and constant in time.

Referring to eqn. (19), the integral on the right-hand side has a singularity at $x^{*\prime} = x^*$ and involves the derivative $\partial B^*/\partial x^*$. The derivative may be removed by integrating by parts, and the singularity removed by performing an analytical integration (using the trapezoidal rule) over the first spatial interval Δx. That is, the function $B^*(x^*)$ is assumed to be linear between x^* and $x^* + \Delta x^*$. The result of these operations is

$$\frac{\partial B^*}{\partial t^*} = \frac{\partial^2 B^*}{\partial x^{*2}} - \frac{\alpha}{(\Delta x^*)^{1/2}} \{(2B^*)_x - (B^*)_{x+\Delta x}\} + \frac{\alpha}{2} \int_{x^*+\Delta x^*}^{1} \frac{B^* \, dx^{*\prime}}{(x^{*\prime} - x^*)^{3/2}}$$

(40)

This equation may be put into finite difference form for numerical integration (we use j as the time index and i for the spatial index):

$$B_{i,j+1}^* = B_{i,j}^* + \frac{\Delta t^*}{(\Delta x^*)^2}(B_{i+1,j}^* + B_{i-1,j}^* - 2B_{i,j}^*) -$$

$$- \frac{(\Delta t^*)\alpha}{(\Delta x^*)^{1/2}}(2B_{i,j}^* - B_{i+1,j}^*) + \frac{(\Delta t^*)\alpha}{2(\Delta x^*)^{1/2}} \sum_{k=i+1}^{P} \frac{B_{k,j}}{(k-i)^{3/2}}$$

(41)

where P is the number of spatial intervals. This equation can be put into the following form, which is convenient for programming:

$$B_{i,j+1}^* = \{\lambda + \alpha\lambda(\Delta x^*)^{3/2}\}B_{i+1,j}^* - \lambda B_{i-1,j}^* +$$

$$+ \{1 - 2\lambda - 2\alpha\lambda(\Delta x)^{3/2}\}B_{i,j}^* + \frac{\alpha\lambda(\Delta x^*)^{3/2}}{2} \sum_{k=i+1}^{P} \frac{B_{k,j}^*}{(k-i)^{3/2}}$$

(42)

where $\lambda = \Delta t^*/(\Delta x^*)^2$. For convergence, λ must be kept below a critical value. For a pure diffusion equation with no integral on the right-hand side, the classical maximum value of λ is 0.5 but here we use λ of the order of 0.25 since an exact convergence criterion is not established.

5. The leading side inter-rail potential

The leading end potential (the voltage between the inside of the rails at the leading end) may be found by calculating the e.m.f. minus the IR drop around any arbitrary loop of rail–collector–rail. For convenience, we take a path along the inside of the rails and down the leading leaf of the collector as shown in Fig. 1. The magnetic flux through this loop is zero in our two-dimensional approximation and Faraday's law then gives a zero value for the e.m.f. around the loop. Explicitly, the potential V is given by

$$V_{BA} = -\int_A \frac{\partial B}{\partial t} \cdot dA + \oint_C v \times B \cdot dl - \int_A^B E' \cdot dl$$

(43)

where the area A is that instantaneously enclosed by the loop. This is the potential at point B with respect to point A. Since $B = 0$ in the loop and $B = 0$ along the muzzle leaf, the first two terms which represent the induced e.m.f. are zero. It should be emphasized that the loop could be taken down the rail further and through any arbitrary leaf of the collector. Then the e.m.f. would not be zero but the IR drop given by $\int_A^B E' \cdot dl$ would be different so that the value of V would be the same. Here, the total electric field E' in the conductor is the same as that seen by an observer at rest on the collector or on the rails at the muzzle, since $v \times B$ in the armature is normal to the direction of the local electric field. Hence we have by Ohm's law $J = \sigma E' = \sigma E$

$$V_{BA} = -\int_A^B E \cdot dl = -\int_A^B \frac{J}{\sigma_m} \cdot dl = J_y \frac{2w}{\sigma_m} \tag{44}$$

where σ_m is the instantaneous leading leaf conductivity. Defining a dimensionless current $J_y{}^*$, we have from $J = \nabla \times H$

$$J_y{}^* = \left(\frac{J_y \mu_0 l}{B_0}\right)_{t=0} = \frac{\partial B^*}{\partial x^*} \tag{45}$$

and we define a dimensionless terminal potential

$$V_{AB}{}^* = \frac{V_{AB} \mu_0 l \sigma_m}{(2w B_0)_{t=0}} = -\frac{\partial B^*}{\partial x^*} \tag{46}$$

where we have used the potential of point A with respect to point B (i.e. $V_{AB}{}^* = -V_{BA}{}^*$) for convenience, since $\partial B^*/\partial x^*$ will generally be a negative number. In general, σ_m may change with time and this must be considered if the actual voltage $V_{AB}{}^*$ is to be found at any particular time.

Once $B^*(x^*, t^*)$ is found it is a simple matter to differentiate the function, which must be done numerically, to find $V_{AB}{}^*$.

6. Discussion of results

For steady state operation with uniform conductivity throughout the collector an exact solution has been effected. The profiles of the normalized magnetic induction are shown in Fig. 3 and again they are a function of only one parameter α.

Figure 4 shows the normalized current density $J_y{}^*$ in the collector as a function of α. This curve follows directly from Fig. 3. This current density is negative because the flow is in the negative y direction. The Joule heat rate density may be obtained simply by squaring the current density and is not shown here. Its calculation in the collector and the rail have been discussed in the text.

Complete solutions including transient effects are illustrated by Figs. 5 and 6, which show typical magnetic induction profiles as a function of time.
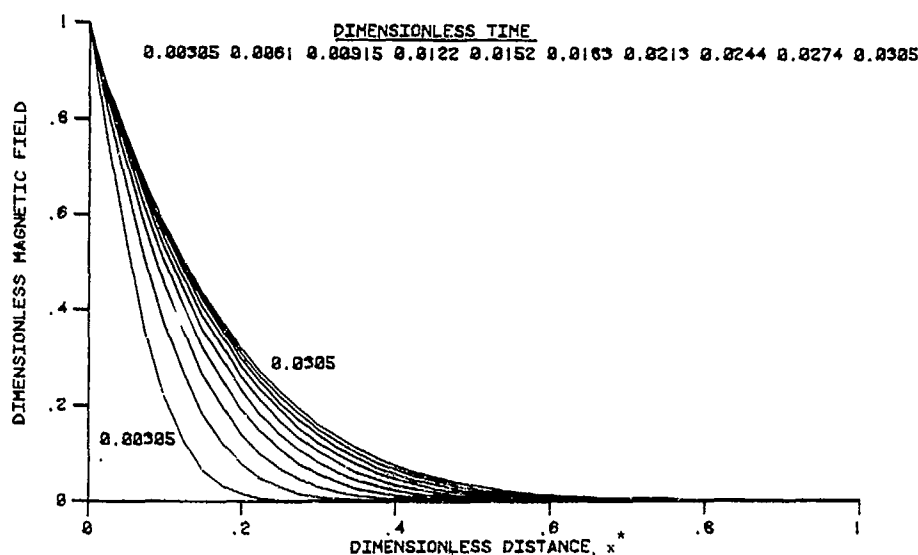
Fig. 5. Plot of magnetic field vs. position for various values of time.
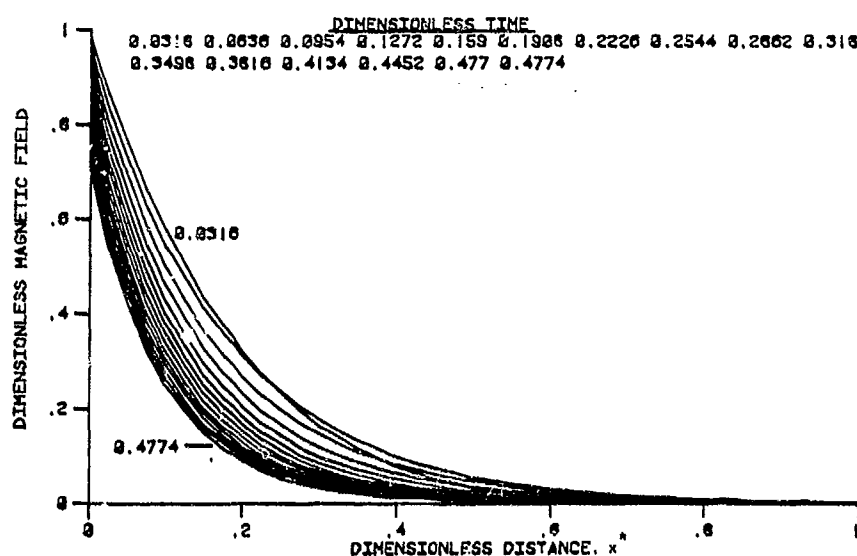
Fig. 6. Plot of magnetic field vs. position for various values of time.

We use a velocity that rises linearly from zero to 3000 m s^{-1} over a dimensionless time of 0.4774. This corresponds to a real time of 3.0 ms with $l = 0.01$ m, $w = 0.02$ m and $\sigma_0 = \sigma_r = 5 \times 10^7$ Ω^{-1} m^{-1}. The dimensionless conductivity $\sigma^{\circ} = 1$ is held constant and uniform throughout the armature. The current is ramped linearly down from its initial value to 0.7 of that value in the same time. Hence $B_0^*(t^*)$ ramps downward from unity to 0.7 in that time. The ramping is quite evident in Fig. 6.

Initially, pure diffusion dominates and the magnetic field diffuses into the armature before B_0^* decreases very much. This is evident in Fig. 5, which shows the behavior for small time. When the dimensionless time has reached

186

approximately 0.03, the field has reached its greatest diffusion depth. At that time the velocity is about 190 m s^{-1} and the velocity skin effect becomes dominant.

Referring to Fig. 6 we see that as the velocity increases, the fields are forced down on the trailing side, but continue to diffuse at a low level toward the leading side. Figure 7 shows this onset of the velocity dominance. Eventually the velocity does begin to reduce the fields even at the leading side.

Any simulation of the entire system would require a simultaneous solution of the present finite difference equation and the system equation
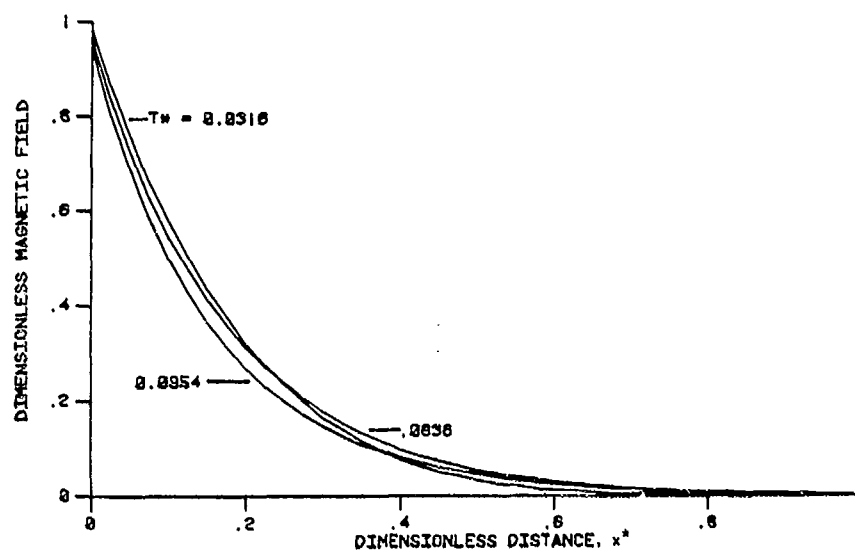
Fig. 7. Plot of magnetic field vs. position for various values of time.
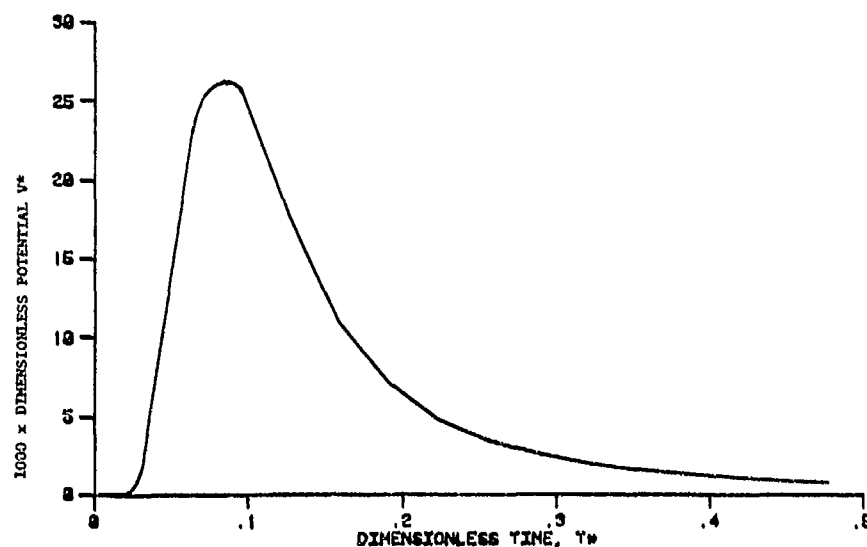
Fig. 8. Plot of dimensionless leading end potential as a function of time.

for current and velocity. Temperature effects could also be included, and the consequent conductivity changes could be taken into account.

The leading end voltage for the example case discussed above is shown in Fig. 8. When the dimensionless time is about 0.8, the voltage reaches a peak. Then the velocity effects begin to become dominant even at the leading end, forcing even the small fields at the leading side back toward the trailing side.

Acknowledgments

Reference

1 J. P. Barber, R. A. Marshall and P. Muttik, Projectile and current behavior in the ANU rail gun, *Proc. 25th Meet. of the Aeroballistics Range Assoc., Canberra, October 1, 1974,* Australian Government Publication, Canberra.

EXPERIMENTAL DETERMINATION OF THE CONTACT FRICTION FOR AN ELECTROMAGNETICALLY ACCELERATED ARMATURE*

D. P. ROSS and G. L. FERRENTINO

Westinghouse Research and Development Center, Pittsburgh, PA 15235 (U.S.A.)

F. J. YOUNG

Frontier Timber Company, EMF Division, State College, PA 16801 (U.S.A.)

(Received November 5, 1981)

Summary

The friction forces on the contacts of the sliding armature in an electromagnetic launcher represent significant energy losses affecting the overall performance of these systems. Friction produces unwanted heating at the contact–rail interface which leads to accelerated wear and chemical erosion of the contacts. Eventually, the armature material at the interface will soften and melt followed by rapid evaporation due to arcing. To prevent this mode of failure, the contact force must be gauged accordingly; the compliance must account for not only changes in barrel width due to rail unevenness but changes in contact length due to wear. Usually for successful operation at high current densities (greater than 1 GA m^{-2}) armatures with multiple contacts are employed to circumvent this dilemma.

An extensive experimental program at Westinghouse Research and Development Center supported by the Defense Advanced Research Projects Agency was instituted to define the limitations of high speed high current contacts for electromagnetically accelerated armatures. One facet of this work, the determination of friction and contact forces for a simple plate-type armature, is presented in this paper.

1. Introduction

The friction or drag force on the contacts of a simple armature constructed from laminated copper plates is calculated from data obtained during recent tests conducted at Westinghouse's experimental launcher

---

facility (ELF-I). The ELF-I electromagnetic launcher is a single-shot device consisting of a 36 kJ capacitor bank and pulse conditioning circuitry capable of producing 120 kA peak currents [1]. This pulse-forming network is directly coupled to the breech of a short (1 m) linear rail launcher. Peak magnetic pressure developed in the launch tube is of the order of 10 MPa which corresponds to a magnetic field of 50 kOe. The peak magnetic pressure is well below the elastic limit for copper [2]; therefore non-linear magnetic diffusion effects that occur at the yield point are insignificant in this system. In addition, the mechanical structure of a properly designed projectile armature can be described by elastic beam theory. Hence, closed-form solutions are attainable for the contact force as a function of the elastic bending strength and the electromagnetic pressure.

In ELF experiments two types of armatures were tested: (1) the multifiber brush which consists of bundled copper wires 0.13 mm in diameter (Fig. 1); (2) the trailing leaf chevron (TLC) which is formed by V-shaped slotted copper plates (Fig. 2). The multifiber armatures operate at sliding velocities of 500 m s^{-1} and peak current densities of 3 G $_A$ m^{-2} without any significant damage to the rails. Unfortunately the multifiber armature is difficult to analyze mechanically; thus it does not easily yield vital information concerning friction and wear and their relationship to the magnetic accelerating force as do other types of armatures. To understand fully the contact force and compliance requirements for the multifiber armature, a detailed evaluation of the transient current distribution in the brush is necessary. The solution to this problem is intractable and is not pursued. Instead, the less complicated TLC is chosen for the calculation of friction and contact forces.

The mechanical analysis of the TLC assumes that only elastic deformations occur during acceleration. A complete set of formulae expressing the
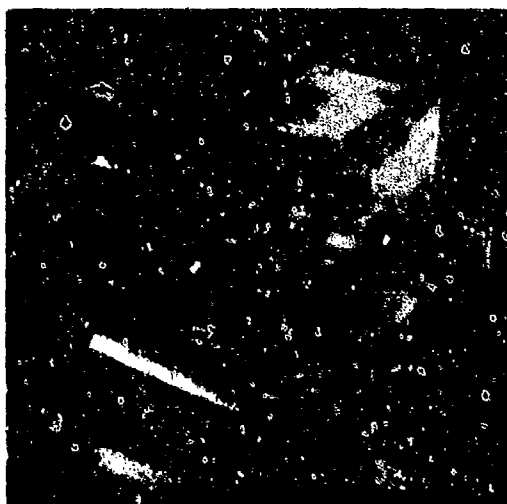
Fig. 1. A multifiber armature attached to a Lexan payload.
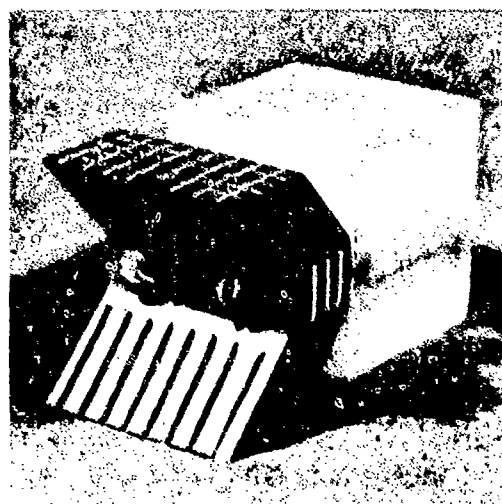
Fig. 2. A TLC similar to the one used in shot 38.

relationship between force and compliance for the TLC (the compliance being the amount of leaf tip deflection) is derived in Appendix A. Figures A2 and A3 are graphical representations of the contact force and the maximum bending moment for one of the finger contacts on a trailing chevron armature. By comparison of the two figures it can be seen that a cant angle θ of about $45°$ is optimum for producing sufficient contact force for armature currents over a range from 0 to 100 kA and, at the same time, minimizing bending moments along the leaf. The maximum bending moment is limited by the yield strength of the material. If this limit is exceeded a plastic hinge is formed and the leaf collapses. This collapse mode of failure is illustrated in the flash X-ray photograph of Fig. 3.

The analysis to follow concerns itself with shot 38. Shot 38 is a typical launch of a TLC with a capacitor charge of 3600 V (equivalent to about 18.7 kJ). The peak current in this experiment is about 62.5 kA. The armature leaves consist of a three-layer lamination of copper plates 0.3 mm thick nested one on top of the other and soldered in the center. The laminated structure provides a larger number of contact spots at the rail and the necessary strength along the canted portion of the leaf to prevent electromechanical collapse. The cant angle is $45°$ and the compliance is 0.08 mm.

2. Experimental diagnostics

The accuracy of the data analysis technique used in Section 3 to resolve contact friction depends on the level of sophistication of the diagnostics used to measure and record the data. Thus a brief discussion of the experimental diagnostics at the ELF-I facility is appropriate.
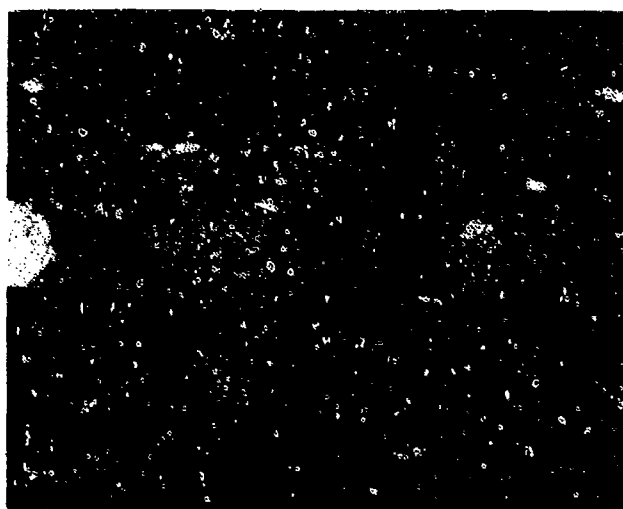
Fig 3. Two radiographs showing the condition of the armature before current is commutated in the breech and afterwards. The high electromagnetic pressure generated by the current causes the leaves to buckle.

The accelerating current is measured by two Rogowski coils located near the breech of the barrel. The output dI/dt of one of the coils is recorded directly. The other coil output is integrated and then recorded to give current directly.

The breech and muzzle voltages are measured by probes attached directly to the rails. Because of potentially high common mode voltages, these voltage probes are isolated from recording instrumentation with standard analog optical couplers.

In-bore velocity is measured indirectly by magnetic flux coils located along the barrel. The flux coils are oriented to detect the passage of the armature, thus providing displacement *versus* time data. Velocities outside the barrel are estimated by laser "fences" placed down-range from the muzzle.

Finally, a flash X-ray system allows in-bore photography of the projectile at three different locations. This system can be triggered by the flux coil output or the laser fences.

The signals from these transducers are recorded with digital transient recorders that are interfaced to a mainframe computer to facilitate data storage and processing. The details of this data acquisition and processing system are found elsewhere [3].

3. Calculation of the friction force

The friction force F_f is calculated by using the measured displacement data and accelerating current for shot 38. The contact force F_n is determined by the closed-form solutions in Appendix A and the calculated F_f. Finally, the coefficient of friction is deduced based on the previous results.

Before the friction force can be determined the projectile acceleration is calculated from displacement *versus* time data. The displacement data (19 points) are fitted with a sixth-order polynomial curve and are illustrated in Fig. 4. The velocity and acceleration profiles, Figs. 5 and 6 respectively, are calculated by finding the first and second derivatives of the polynomial. The acceleration profile is truncated at both ends since the greatest uncertainty in the polynomial fit occurs at these points. From Fig. 5 the 5.282 projectile of shot 38 attains an exit velocity of 242 m s^{-1} after traveling 1.0 m.

The projectile acceleration is related to the electromagnetic accelerating force and the friction force by Newton's equation

$$\frac{1}{2}L'I^2 - F_f = Ma \tag{1}$$

where L' is the barrel inductance per unit length and M is the total projectile mass (armature and payload mass). The value of L', 481 nH m^{-1}, was measured with a calibrated LCR meter at 400 Hz. Equation (1) was solved for F_f using the measured accelerating current (Fig. 7), L' and Ma. The force of friction is plotted as a function of velocity in Fig. 8. As expected, the
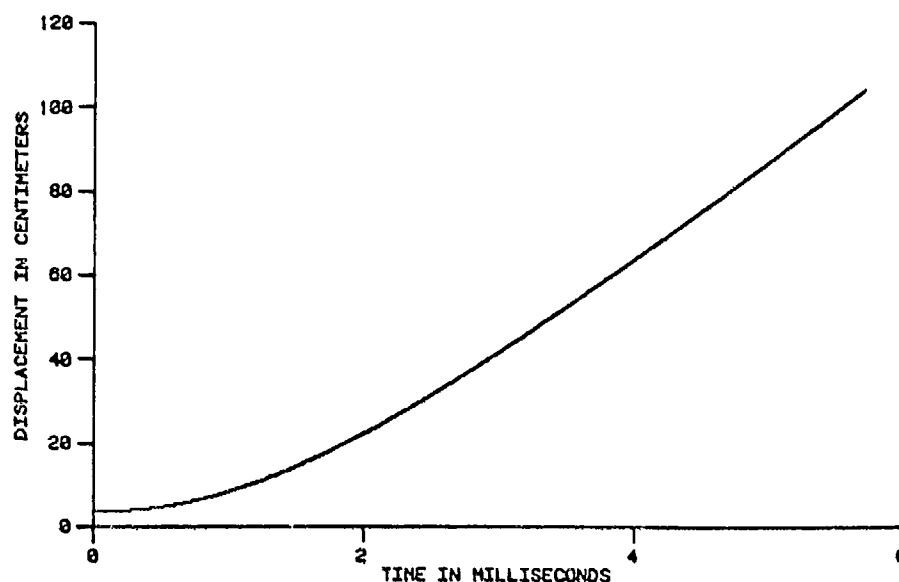
Fig. 4. Sixth-order polynomial curve fit of the displacement data for shot 38.
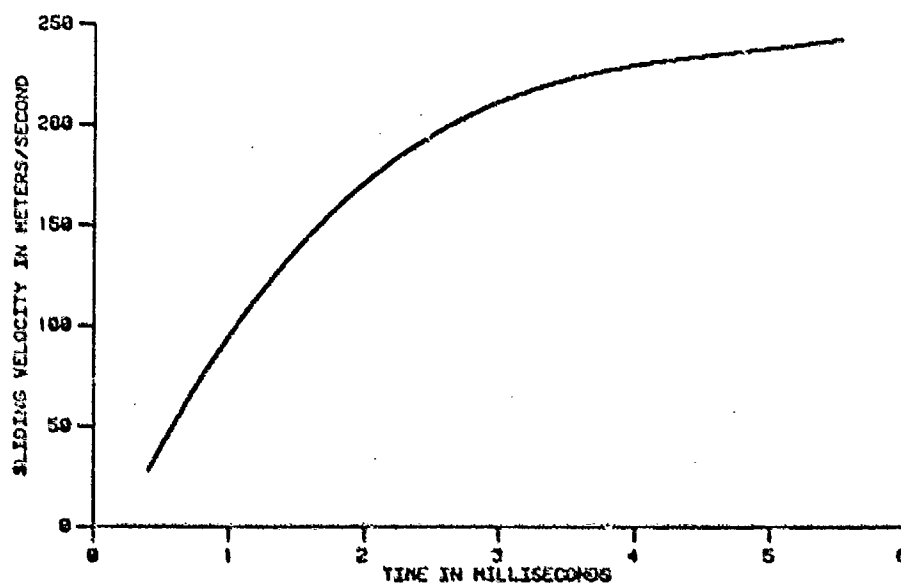
Fig. 5. Velocity–time history for shot 38.

friction force is a monotonically decreasing function of velocity. The only assumption made in this calculation is that L' is constant. A more detailed calculation where L' changes due to the transient diffusion of currents in the rails is possible.

Now that the force of friction is known the contact force is resolved with eqn. (A3). After substituting F_t/F_n for μ, eqn. (A3) becomes

$$F_n = \frac{3l(P - ma \sin \theta)}{8 \cos \theta} + \frac{3EI\delta}{l^3 \cos^2\theta} - \frac{F_t \tan \theta}{n_T} \qquad (2)$$

194
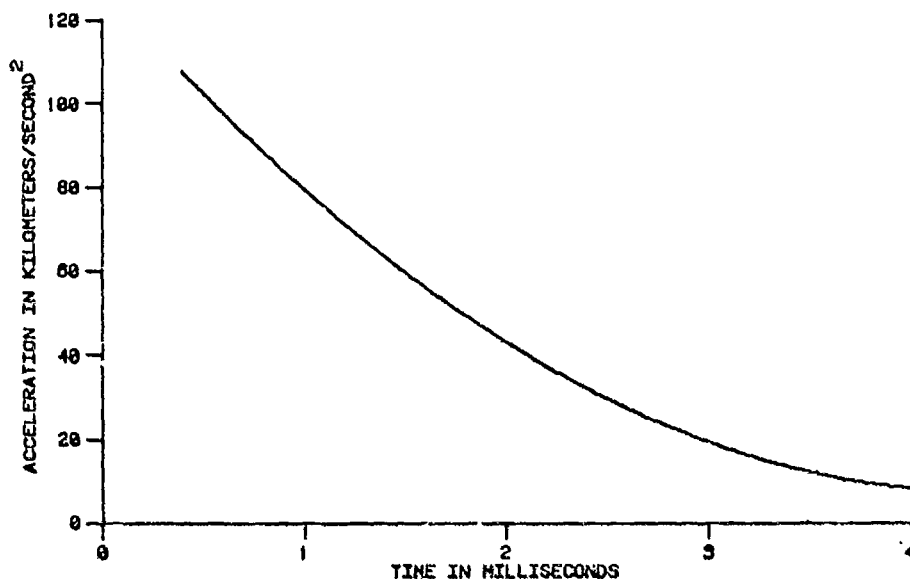
Fig. 6. The acceleration profile for shot 38 calculated from the displacement data.
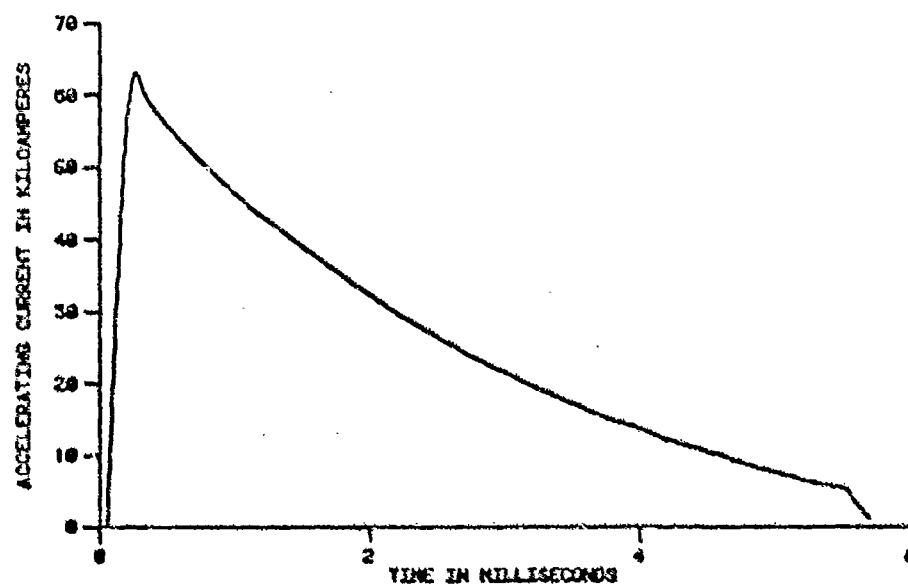
Fig. 7. Measured accelerating current for shot 38 as a function of time.

All of the variables on the right-hand side of eqn. (2) are either known constants or functions of time. There are two assumptions made in the calculation of F_n: (1) the current is uniformly distributed within the armature; (2) the compliance δ remains constant over the length of the launch tube. The first assumption is justifiable if the transient skin depth is greater than the total armature thickness (about 1.0 mm). For copper the diffusion time corresponding to a skin depth of 1.0 mm is about 500 μs.

Changes in δ are due either to wear of the leaf tips or to variations in the width between the rails. Both of these effects require prior knowledge of
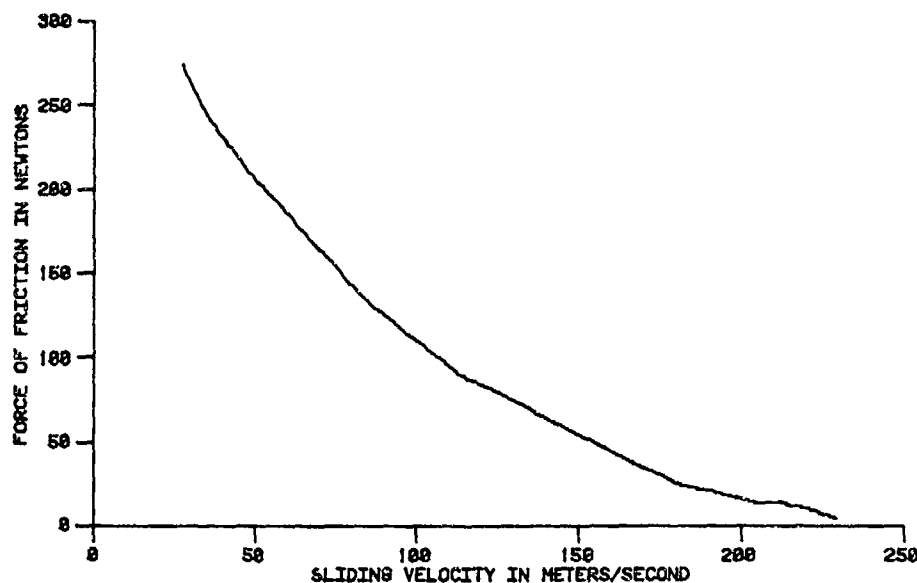
Fig. 8. Dynamic contact friction force as a function of velocity calculated from eqn. (4).

the contact force; therefore the second assumption is necessary in this first iteration. Furthermore, the initial leaf tip deflection is chosen so that the elastic bending term in eqn. (2) is small compared with the distributed electromagnetic force P_i during most of the launch.

The total contact force and the total friction force at the contacts are illustrated in Fig. 9 as functions of time. The coefficient of friction is calculated from the data given by these curves and is plotted as a function of velocity in Fig. 10. The initial values for the coefficient of friction (0.40 -
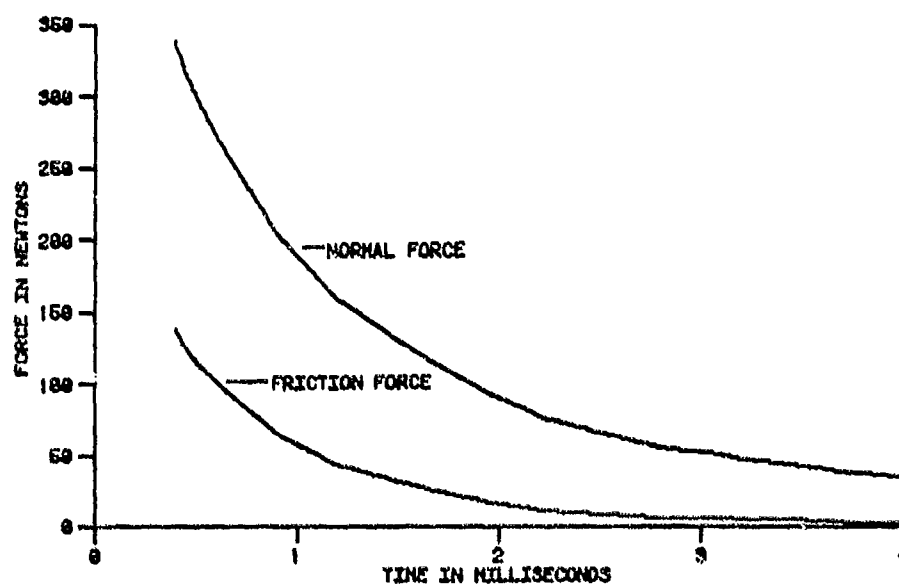
Fig. 9. Total contact force and total friction force at the contacts as functions of time for the armature in shot 38.
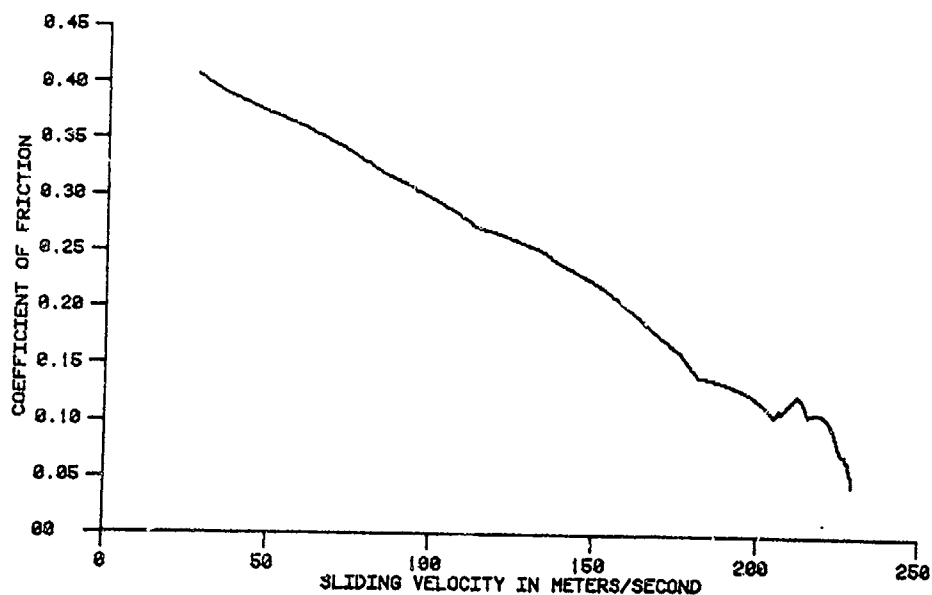
Fig. 10. Coefficient of friction plotted as a function of velocity for copper contacts.

0.29) agree with earlier findings [4]. Agreement beyond 100 m s^{-1} would probably be better if changes in δ due to wear or rail asperities were included in the calculation of F_n. Since wear is directly proportional to the normal force [5] we would expect that the wear rate is greatest during the first 20 cm of travel.

The value of F_n beyond this point is probably too high taking into account the series of voltage flashes that occur on the muzzle voltage trace (Fig. 11) starting at about 3.5 ms. A calculation of the muzzle voltage
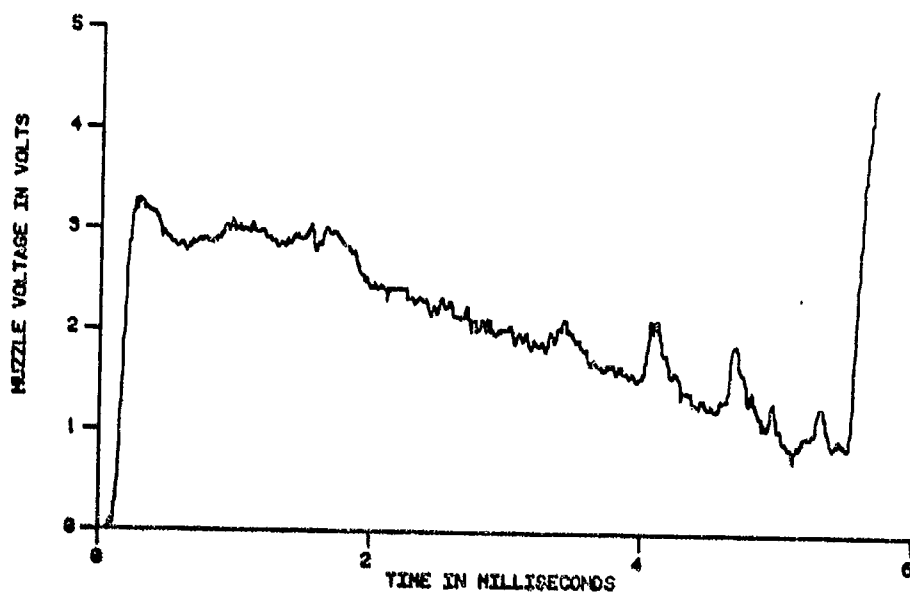
Fig. 11. Muzzle voltage $IR_{armature} + 2V_{contact}$ for shot 38. The jagged peaks that occur at about 3.5 ms are due to arcing.

$IR_{armature} + 2V_{contact}$ from F_n, including temperature effects, will be presented elsewhere.

4. Conclusions

The technique presented to calculate the dynamic friction force produced encouraging results. The analysis depends largely on the accuracy with which the acceleration is determined. A random error of $\pm 5\,\mu s$ introduced in the displacement data changes the acceleration profile by as much as 10%. Direct measurement of the in-bore velocity with a laser interferometer would dramatically increase the accuracy of the calculation.

Calculation of the contact force, however, is limited to armatures composed of simple mechanical structures. Otherwise, for more complicated designs such as the multifiber armature the analysis becomes exceedingly difficult.

The friction coefficients calculated for velocities greater than 100 m s^{-1} are low probably for two reasons. First, in the calculation of the Lorentz force $L'I^2/2$, L' is assumed to be a constant. Barrel inductance measurements indicate that L' increases as frequency decreases. Thus the friction forces calculated toward the end of the current pulse should be adjusted to account for this effect. Secondly, the contact force calculation does not account for changes in contact length due to wear. A more detailed calculation including both of these effects should be the subject of future work.

Acknowledgment

References

1 D. W. Deis and D. P. Ross, Experimental launcher facility — ELF-I: design and operation, *Conf. on Electromagnetic Guns and Launchers, San Diego, CA, November 4, 1980*.

2 H. Knoepfel, *Pulsed High Magnetic Fields*. Elsevier, New York, 1970, Chap. 1.

3 G. L. Ferrentino and D. P. Ross, Electromagnetic accelerator data acquisition and processing system, *Proc. Int. Congr. on Instrumentation in Aerospace Simulation Facilities, Dayton, OH, September 30, 1981*.

4 R. S. Montgomery, Friction and wear at high sliding speeds, *Wear, 36* (1976) 275 - 298.

5 R. Holm, *Electric Contacts*, Springer, New York, 1976, pp. 230 - 233.

6 I. R. McNab, J. P. Barber *et al.*, DC electromagnetic launcher development: phase I, *ARRADCOM Contract. Rep. ARLCD-CR-80009*, 1980 (Army Armament Research and Development Command).

Appendix A

Force–compliance relationships for the trailing leaf chevron armature

Consider the single control beam segment of the trailing leaf chevron (TLC) armature illustrated in Fig. A1. The beam segment is assumed to be cantilevered from the end fixed to the launch package payload and simply supported at the rail. The loadings on the beam segment and the resulting reaction forces at the supports shown in the free-body diagram are the following: P, the electromagnetic force per unit length; F_n, the contact or normal force; ma, the distributed inertial loading on the leaf; $F_F = \mu F_n$, the friction force at the contact–rail interface; F_{ay} and F_{ax}, reaction forces at the cantilevered end; M_A, the moment at the cantilevered end.

Considering now the static equilibrium of this free body, we have the general case of a system of forces in one plane. For such a system there are three equations of equilibrium:

$$\Sigma X_i = 0 \qquad \Sigma Y_i = 0 \qquad \Sigma M_i = 0 \tag{A1}$$

These equations, however, are insufficient to determine more than three unknowns; hence the beam segment is statically indeterminate. If the elastic limit of the leaf material is not exceeded and the deflection of the leaf tips (compliance δ) is kept small, then the moment curvature equation given by

$$\frac{d^2 y}{dx^2} = \frac{M(x)}{EI} \tag{A2}$$

where E is Young's modulus and I is the cross-sectional moment of inertia, is applicable with the appropriate boundary conditions at the supported ends to solve eqn. (A1) [6].

The boundary conditions in this case are
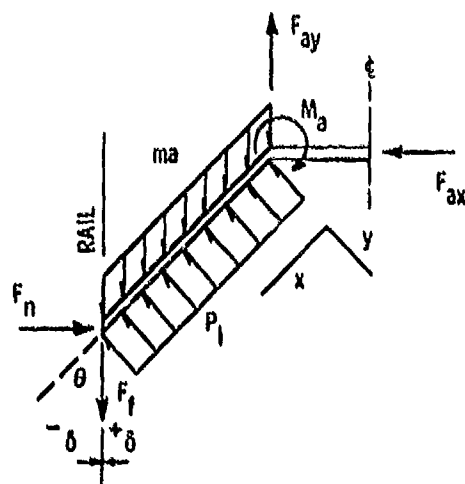
Fig. A1. Free-body diagram for a single leaf of a TLC armature.

$$y = 0 \text{ at } x = 0$$

$$\frac{dy}{dx} = 0 \text{ at } x = 0$$

$$y = \frac{\delta}{\cos \theta} \text{ at } x = l$$

where the x–y coordinate system has its origin at the cantilevered end with the x axis aligned parallel to the beam segment. Using these boundary conditions together with eqns. (A1) and (A2) the reaction forces and moments of Fig. A1 are determined:

$$F_n = \frac{3l(P - ma \sin \theta)}{8(\cos \theta + \mu \sin \theta)} + \frac{3EI\delta}{(1 + \mu \tan \theta)l^3 \cos^2\theta} \tag{A3}$$

$$F_{ax} = Pl \cos \theta - F_n \tag{A4}$$

$$F_{ay} = \mu F_n + mal - Wl \sin \theta \tag{A5}$$

$$M_A = \frac{l^2}{8} (P - ma \sin \theta) - \frac{3EI\delta}{l^2 \cos \theta} \tag{A6}$$
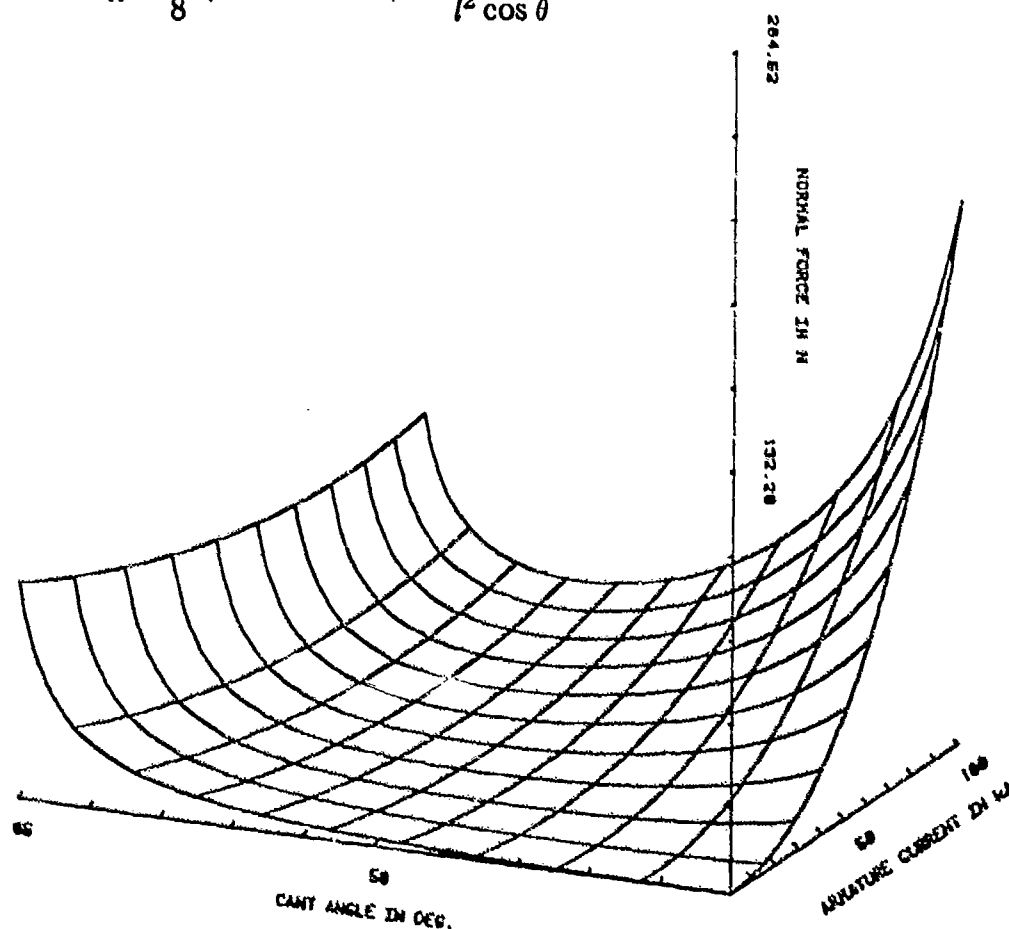
Fig. A2. Three-dimensional view of the normal or contact force as a function of the cant angle θ and the total armature current I for the TLC.

200

The normal force given by eqn. (A3) is plotted as a function of the cant angle θ and total armature current in Fig. A2. Also, the maximum bending moment obtained by differentiating a more general form of eqn. (A6) is plotted as a function of the cant angle θ and total armature current in Fig. A3. The compliance δ is the same in both calculations.
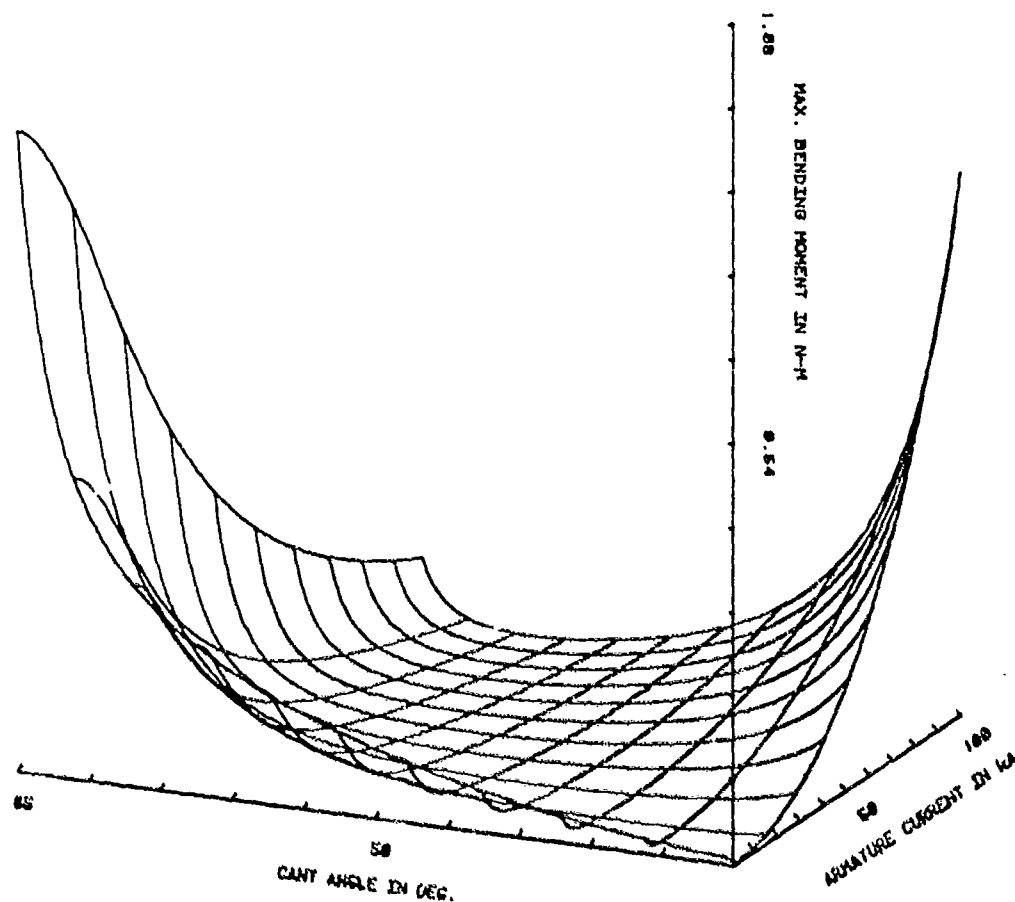
Fig. A3. Three-dimensional view of the maximum bending moment on the leaves of a TLC armature as a function of cant angle θ and total armature current I.

U.K. MINISTRY OF DEFENCE CURRENT COLLECTION PROGRAMME FOR SUPERCONDUCTING HOMOPOLAR MOTORS*

TREVOR C. BARTRAM

International Research and Development Company Limited, Newcastle-upon-Tyne, NE6 2YD (Gt. Britain)

(Received November 5, 1981)

Summary

A programme which at the time of writing was beginning to yield preliminary results is described in this paper. The objectives of the programme and the test plan are outlined. The experimental facilities which have been purpose designed and constructed are described. A summary of the results obtained up to the time of writing, albeit at an early stage in the test schedule, is presented.

1. Introduction

The U.K. Ministry of Defence is presently sponsoring a Research Programme on superconducting homopolar motors, the largest proportion of which is being undertaken by International Research and Development Co. Ltd., Newcastle-upon-Tyne. An important aspect of the programme in early phases is current collection. The machines require a direct current transfer system from several pairs of continuous slip rings, the electrical circuit being a series one such that all slip rings transfer the armature current of the motor. A high current density system allows motor sizes to be reduced, or more power to be produced in a given frame size, but also gives the option of fewer brushes in cases in which the previous advantage is not fully utilized. The duty cycle for a proposed application (ship propulsion) is such that maximum speed and current density apply for less than 5% of the operational time. The target performance for achievement during phase I of the programme is given in Table 1.

The wear target for brushes is calculated to give convenient brush life to match major overhaul periods for the vessel. The loss target does not represent the limit for machine design but is consistent with the efficiency requirements for the motors.

TABLE 1

Current density (peak)	100 A cm^{-2}	
Brush wear	10^{-11} dimensionless units	Average values
Slip ring wear	10^{-12} dimensionless units	over a duty cycle
Losses	0.4 W A^{-1}	at 100 A cm^{-2}

2. Experimental facilities

Two types of rig are employed, each being purpose designed as part of the programme. The first type of rig is described as a screening rig and 20 have been constructed. It is an aim of phase I of the programme to achieve the target conditions on this type of rig. The second type of rig is more representative of the conditions in a motor and two such rigs are being constructed during phase I, the intention being to fit the favoured materials from the screening programme for further evaluation in phase II.

A schematic diagram of a screening rig is shown in Fig. 1. The slip ring is liquid cooled and has separate tracks on which the input and output brushes run. The brushgear is supported from the top plate which is located from bearings on the rotor. The top plate is prevented from rotating by a rigidly mounted transducer for frictional torque measurement. The rig is
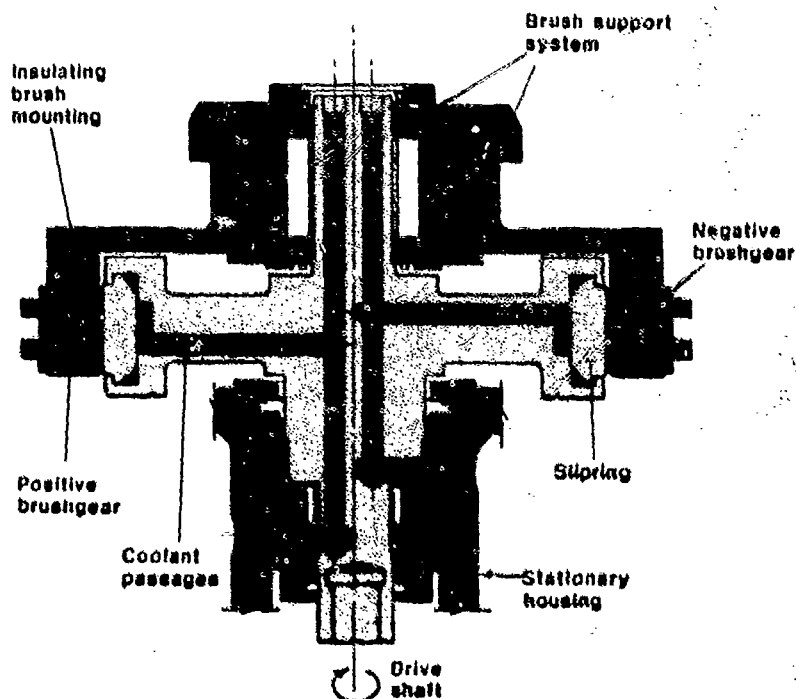
Fig. 1. Brush–slip ring screening rig.
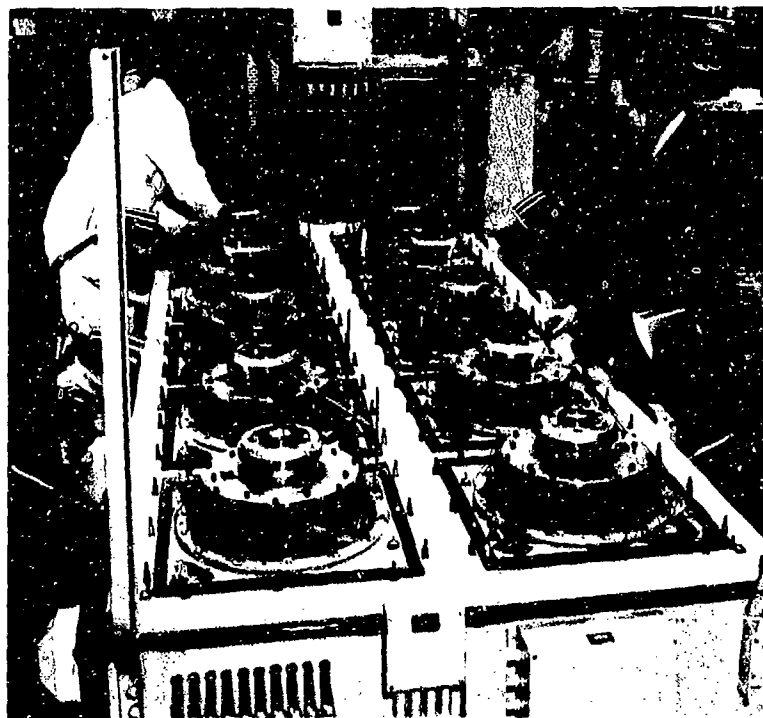
Fig. 2. Screening rig test stand.

mounted with its axis vertical and is driven by an induction motor. A range of motors is available giving slip ring speeds of 40, 20 and 13.3 m s^{-1}. 14 brushes of each polarity may be fitted; each brush is 2 cm^2 in area. Brush pressure is provided from a range of constant-force springs. The screening rigs are arranged on two test stands (Fig. 2), each having ten test positions. They are electrically in series with shorting straps for non-operational locations. Each test stand has its own d.c. power supply. Each rig has a gas-tight enclosure.

Instrumentation is in the form of a computer-controlled data logger sampling any transducer once every 10 s. Mean, high, low and variance parameters are calculated at the same frequency. An hourly record of these values is stored on disk and the derived parameters reset for calculation over the next hour. The computer also calculates derived parameters such as losses and friction coefficients for display purposes. Each rig has instrumentation for the following parameters: positive voltage drop; negative voltage drop; frictional torque; brush temperatures (four brushes); coolant inlet temperature; coolant temperature rise; enclosure temperature. The common services are instrumented as follows: total current (rigs in series); total gas flow (rigs in parallel); gas humidity. Any rig may be selected for connection to the following instrumentation: brush current sharing (tail voltage drop); gas composition (gas chromatograph); slip ring surface temperature. Brush wear is measured weekly (i.e. about every 150 running hours) and slip ring wear occasionally (i.e. at a frequency not yet established).

3. Test programme and results

The first test stand for ten rigs became operational in March 1981 with testing commencing in April 1981. The second test stand became operational in September 1981. The initial list for evaluation is given in Table 2.

TABLE 2

Slip ring materials[a]	Brush							Cover gases[b]	Speeds (m s^{-1})	Brush pressures (N cm^{-2})
	Materials	Composition (%)								
		Cu	C	Pb	Sn	Ag				
Cu–0.7%Cr–0.1%Mg	CM	81	8	11	—	—		N$_2$	13.3	1.9
OFHC 99.95% Cu	CM1S	82	12	2	4	—		Ar	20	2.3[c]
Cu–0.07%Ag	CM2	82	18	—	—	—		Air	40[c]	3.8
PD135 (0.4% Cr; 0.4% Cd)	CM3H	75	25	—	—	—		CO$_2$[c]		
Ag plated	CM5H	40	60	—	—	—				
Cu–4%Ni	DM4A	45	55	—	—	—				
Cu–10%Ni	SM3	—	55	—	—	45				
Cu–Cr–Zr										

[a] Slip rings are plain initially, but grooving is included in the planned programme.
[b] The gases are humidified (dew point, 10 - 15 °C).
[c] Initial test conditions.

The tests are, at the time of writing, in their early stages and are being carried out at 25 A cm^{-2}. No conclusions may be drawn because of the limited test data but rankings determined from the results so far are presented in Tables 3 and 4.

TABLE 3

Order of merit for slip rings (independent of brush grade)

Friction coefficient		Positive voltage drop		Negative voltage drop
Cu–0.7%Cr–0.1%Mg	} Equal	OFHC	} Equal	OFHC
PD135		Cu–0.07%Ag		Cu–0.07%Ag
Cu–0.07%Ag	} Equal	Cu–0.7%Cr–0.1%Mg		Cu–0.7%Cr–0.1%Mg
OFHC		PD135		PD135

Attention is being given to current sharing between brushes, and relationships between this factor and other conditions are being sought. Table 5 shows a relationship between the current per brush and the wear for the combination of OFHC copper and CM grade brush run for over 90 h for the positive polarity. The table is in descending order of current carried. The mean current density is again 25 A cm^{-2}. This combination shows a wear rate, for this test, outside the target for the wear rate.

TABLE 4

Order of merit for brushes (independent of slip ring type)

Wear	Friction coefficient		Positive voltage drop		Negative voltage drop
CM1S	CM		CM1S		CM
CM	CM2	Equal	CM	Equal	CM1S
CM2	CM3H		CM2		CM2
CM3H	CM1S		CM3H		CM3H

TABLE 5

Brush number	Current (%)	Wear (mm)
23	15	0.66
27	14	0.55
19	13	0.66
1	11	0.56
7	9	0.48
13	9	0.53
17	8	—
25	8	0.29
9	6	0.59
15	4	0.22
21	1.5	0.00
3	0	0.02
5	0	0.06
11	0	0.00
Average	7.14	0.39

$(\times 10^{-11}$ dimensionless units)

TABLE 6

Slip ring	Cu–0.7%Cr–0.1%Mg	Cu–0.7%Cr–0.1%Mg	PD135	Cu–0.07%Ag	OFHC	Ideal
Brush	CM1S	CM	CM	CM1S	CM	
Polarity	+	+	+	–	+	
Smallest number of brushes taking the following amounts of current						
25%	2.7	1.0	1.5	2.5	1.6	3.5
50%	5.6	3.2	3.1	5.3	3.7	7.0
75%	8.9	6.5	5.3	8.7	6.1	10.5
Positive brush wear ranking (this test)	2	4	3	1	5	

206

Many combinations do not show trends as marked as this result although brushes showing poor current sharing may also be categorized as having a high wear rate. This is illustrated by Table 6 in which the current sharing parameters were recorded over an 8 h period. The wear data are from a 150 h run.

4. Conclusions

The test programme is not sufficiently far advanced to allow conclusions to be drawn.

Acknowledgments

WEAR-INDUCED PROFILES OF BRUSHES ON ECCENTRIC ROTORS*

P. REICHNER

Westinghouse Research and Development Center, Pittsburgh, PA 15235 (U.S.A.)

(Received November 5, 1981)

Summary

Brushes in electrical machines are worn to a profile that is modified by rotor eccentricity. As a result, conventional values of applied contact force produce only fractional contact of the nominal interface area. The local contact position shifts as the rotor turns, to include the entire brush face in the wear process. The steady state profile is determined by two requirements: that the wear per cycle is equal for all points on the brush face and that the brush face is tangential to the rotor surface at the point of contact. These conditions are applied to two examples in the calculation of wear-induced brush profiles.

1. Introduction

In many electrical machines, high current must be transferred from rotating to stationary members to complete the electrical circuit. Brushes, which are blocks of graphite or metal–graphite mixtures, are generally used to provide this current transfer capability. They are more easily replaced than the rotor surface on which they slide and, therefore, are designed to wear at a much faster rate. The performance of the current collection system depends on many factors including materials, environment, contact pressure and dynamic stability. Rotor eccentricity, for example, can reduce the brush effectiveness because of the inertial modification of the contact force and also by causing a modified brush wear pattern [1]. The eccentricity produces a radius of curvature of the brush face which is greater than that of the rotor. This tends to concentrate the current transfer within a reduced area of the apparent contact face, and this region changes location with different angular positions of the rotor. The size of the contact zone depends on the elastic deformation which occurs in the brush and rotor at the contact point.

___

Previous estimates of contact width were based on the assumption of a circular brush-wear profile [2]. However, the true profile is induced, by wear phenomena and geometric constraints, to produce a uniform progression of the wear face under steady state conditions. For each rotation, the wear increment in the direction of the brush feed axis will be the same for every point. This is accomplished through the adjustment of contact pressure and time of contact at each point. The analytical technique for determination of the brush profile will be illustrated for two cases of rotor eccentricity. The first example is that of an axially applied brush on the face of a disc which rotates about an axis that is at an angle to the axis of symmetry (Fig. 1). The second is that of a brush applied to the periphery of a circular rotor which rotates about an axis which is parallel to, but offset from, the axis of symmetry. It will be assumed that the brush is constrained to prevent rotation, that no mechanical instabilities occur and that the rotor wear is negligible.
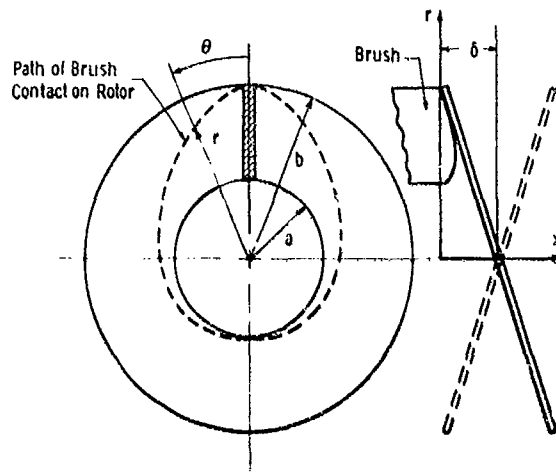
Fig. 1. Axial slip ring eccentricity model.

2. Axial slip ring

In the case of an ideal axial-face slip ring without geometric eccentricity, the brush face will nominally contact the ring continuously at all radial positions. However, the varying sliding velocity will induce a contact pressure distribution that results in a uniform wear rate over the brush face [3]. With ring angular eccentricity, as shown in Fig. 1, the brush contact will be concentrated and will shift along the brush face from outer to inner edge and back as the ring is rotated. At the steady state, the wear rate must be equal for all points, over an integral number of revolutions, so that the brush profile remains the same. This profile may be predicted for the simple mode of eccentricity (shown in Fig. 1), in which the geometric axis of the ring is at an angle to the axis of rotation. The inner and outer extremes of the brush contact are at radii a and b respectively, and the angle of eccentric-

ity is defined by the half-run-out amplitude δ at the radius b. The following simplifying assumptions are made for the analysis.

(a) Circumferential line contact occurs between the brush and the slip ring (for a narrow brush in the tangential direction).

(b) The wear per revolution is the same for each radial position in the brush.

(c) The wear rate at each position is proportional to the sliding velocity.

(d) The brush face is tangential to the slip ring at the contact location.

The time of contact for a brush element of radial height Δr will vary with its radial position such that the total sliding distance, and therefore the wear volume, will have the same value independent of position. At the outer region, where the sliding velocity is greater, the radially inward shift in the position of contact will be faster to accomplish this. However, since neither the brush nor the ring particles have any radial velocity component, there is no radial sliding and no wear is caused by the radial shift in the contact point. Only the tangential velocity and sliding distance on the rotor contribute to the wear process. For a circumferential brush thickness z, the element wear volume is

$$W = KFs$$

$$zl\,\Delta r = KFr\,\Delta\theta \tag{1}$$

where l is the wear depth (at any position) for a half-revolution (because of symmetry, only a half-revolution need be analyzed), F is the brush contact force, s is the circumferential sliding distance during the contact period for the height Δr and $\Delta\theta$ is the angle of slip ring rotation for the period. The element height Δr has been assumed to be small in comparison with the radius.

In the limit, as Δr approaches zero, eqn. (1) may be written

$$\frac{dr}{r} = \frac{KF}{zl}\,d\theta \tag{2}$$

The solution of eqn. (2), with $r = b$ at $\theta = 0$, is

$$\ln\left(\frac{r}{b}\right) = \frac{KF}{zl}\theta \tag{3}$$

Symmetry dictates that $r = a$ at $\theta = \pi$, so that eqn. (3) may be used to determine the half-cycle wear depth:

$$l = \frac{\pi KF}{z\,\ln(a/b)} \tag{4}$$

With this expression, eqn. (3) becomes

$$\ln\left(\frac{r}{b}\right) = \frac{\theta}{\pi}\,\ln\left(\frac{a}{b}\right) \tag{5}$$

which defines the contact path along the slip ring face for uniform wear depth.

210

The brush contour may now be found from the requirement that the brush and ring surfaces are tangential at the point of contact. Only a single value of the slope (tangent angle) of the ring exists at any given angular position, and it is defined in terms of the maximum slope δ/b as

$$\frac{dx}{dr} = -\frac{\delta}{b} \cos\theta \tag{6}$$

where the negative sign is due to the selection of the coordinate axes in Fig. 1.

If θ, as found from eqn. (5), is used eqn. (6) may be written as

$$d\left(\frac{x}{\delta}\right) = -\cos\left\{\frac{\pi \ln(r/b)}{\ln(a/b)}\right\} d\left(\frac{r}{b}\right)$$

or

$$dX = -\cos(A \ln R)\, dR \tag{7a}$$

where

$$X = \frac{x}{\delta} \qquad A = \frac{\pi}{\ln(a/b)} \qquad R = \frac{r}{b} \tag{7b}$$

The solution of eqn. (7a) was found to be

$$X = -\frac{R\{\cos(A \ln R) + A \sin(A \ln R)\}}{1 + A^2} + B \tag{8}$$

If we select $X = 0$ at $R = 1$, the integration constant is found to be

$$B = \frac{1}{1 + A^2}$$

and with this value, eqn. (8) becomes

$$X = \frac{1 - R\{\cos(A \ln R) + A \sin(A \ln R)\}}{1 + A^2} \tag{9}$$

Equations (9) and (7b) define the steady state shape of the brush face in terms of the radial span and the eccentricity magnitude. The profile is seen to be independent of the material wear coefficient and brush load. Figure 2 shows the relative profiles (exaggerated) for various values of brush radius ratio.

The maximum value of X is found from eqn. (7a) to occur when $\cos(A \ln R) = 0$, for which $R = (a/b)^{1/2}$. The maximum value then becomes

$$X = \frac{1 - A(a/b)^{1/2}}{1 + A^2} \tag{10}$$

although an even greater separation will occur at the outer edge of the brush when the inner edge is in contact with the rotor. This maximum separation is the sum of the rotor angle effect and the height of the brush inner edge as determined from eqn. (9). Noting that $x = X\delta$,
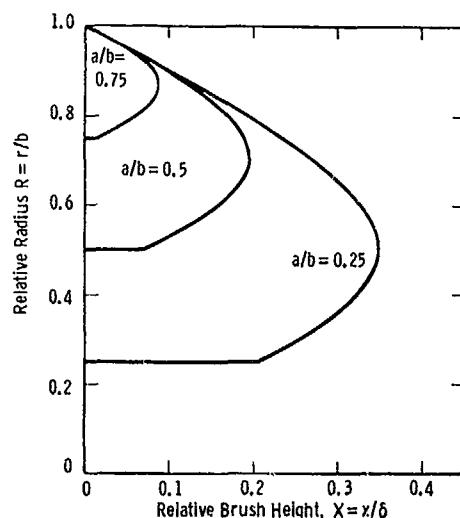
Fig. 2. Brush profiles caused by axial rotor face eccentricity.

$$\frac{g}{\delta} = 1 - \frac{a}{b} + \frac{1 + a/b}{1 + A^2} \tag{11}$$

3. Radial eccentricity

As a second example of the computation of wear-induced profiles, consider a circular slip ring which is rotating about an axis that is displaced by an amount ϵ from its center of geometric symmetry (Fig. 3). A brush with negligible inertia is held in continuous contact with the ring with free radial movement but with constraint to prevent any other motion. Line contact is again assumed in order to avoid the complication of the pressure distribution along the area of contact which would result from elastic deformation of the two components. The angle ϕ of the tangent to the surfaces at the contact point is seen in Fig. 3 to be defined by

$$\sin \phi = (x - \epsilon \sin \theta)/R \tag{12}$$

where x is the horizontal distance from the brush axis to the point of contact, R is the rotor radius and θ is the angle of rotation.

The mode of contact between a brush and an eccentric rotor has been described earlier [2]. The contact point sweeps back and forth along the brush face, completing one full cycle for each rotor revolution. The contact shifts from the brush center to an edge, or back, in 90° of rotation. The brush and ring surfaces are tangential at their point of contact. Since there are two points on the rotor which contact each point on the brush, these two points must have the same tangent angle ϕ. It is seen from eqn. (12) that the tangent angle is symmetrical about the angle $\theta = 90°$, which must therefore correspond to contact at the edge of the brush. It can be seen that

212
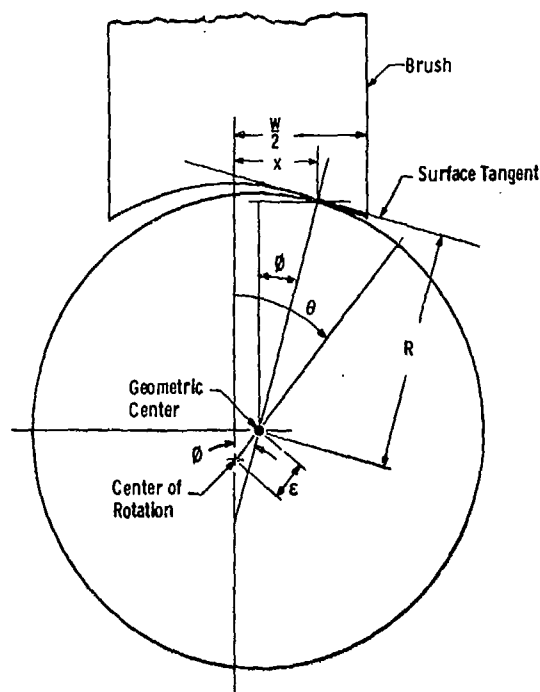
Fig. 3. Slip ring with offset center of rotation.

at that point, because of the finite brush thickness, the total sliding distance for the first quarter-revolution,

$$S = R(\theta - \phi) \tag{13}$$

is less than one-quarter of the rotor circumference. During the next 90° of rotation, the sliding distance is greater so that, at $\theta = 180°$, the total sliding distance is one-half of the rotor circumference.

For the small element Δx of the brush face, the corresponding sliding distance will be

$$\Delta S = R(\Delta\theta - \Delta\phi) \tag{14}$$

Since $\Delta\phi$ will be equal in magnitude, but of opposite sign, for that element during the first and second contact traversals of a half-revolution, the average value of eqn. (14) will be simply

$$\Delta S = R \, \Delta\theta \tag{15}$$

For the element of brush width Δx located at position x, the wear volume W during a single pass of the contact point will be

$$W = z \, \Delta x \, l \tag{16}$$

where z is the transverse brush width and l is the wear depth (reduction in brush length) per half-cycle. The wear volume may also be expressed in terms of the general wear expression as

$$W = KN \, \Delta S \tag{17}$$

where K is the wear coefficient, N is the force normal to the sliding surface and ΔS is the travel distance of the brush along the slip ring surface while the contact point is within the element Δx.

If F is the contact force applied to the brush along its axial direction, and with a contact friction coefficient μ, the force normal to the contact surface can be found:

$$N = \frac{F}{\cos\phi - \mu \sin\phi} \tag{18}$$

Equations (15) - (18) may be combined to show that

$$z \, \Delta x \, l = \frac{KFR \, \Delta\phi}{\cos\phi - \mu \sin\phi}$$

or, as Δx approaches zero,

$$dx = \frac{KFR \, d\theta}{zl(\cos\phi - \mu \sin\phi)} \tag{19}$$

Equations (12) and (19) may be used to define the brush face curvature. It should be noted that the friction force tends to reduce the normal force on the leading half of the brush and to increase the normal force along the trailing half. This would require that, for equal wear rate, there would be some asymmetry and the leading brush half would be in contact with slightly more than half the full periphery. However, in most cases the tangent angle ϕ is small, and a reasonable approximation to eqn. (19) is

$$dx = \frac{KFR \, d\theta}{zl} \tag{20}$$

Integration of eqn. (20) with the specification that $x = 0$ at $\theta = 0$ yields

$$\theta = \frac{zlx}{KFR} \tag{21}$$

Also, since $\theta = \pi/2$ corresponds to contact at the brush edge (at $x = w/2$), the average wear depth per half-cycle is found from eqn. (21) to be

$$l = \frac{KF\pi R}{zw} \tag{22}$$

Substitution of eqn. (22) into eqn. (21) yields

$$\theta = \frac{\pi x}{w} \tag{23}$$

Noting that for small angles the tangent dy/dx is approximately equal to the sine, substitution of eqn. (23) into eqn. (12) yields

$$\frac{dy}{dx} = \frac{X - \varepsilon \sin(\pi x/w)}{R} \tag{24}$$

214

As expressed in eqn. (24), y is the vertical coordinate and would be positive downward in Fig. 3. Integration of eqn. (24), with $y = 0$ at $x = 0$, gives the analytical expression for the shape of the brush face

$$y = \frac{x^2}{2R} - \left(\frac{w\epsilon}{\pi R}\right)\left\{1 - \cos\left(\frac{\pi x}{w}\right)\right\} \tag{25}$$

For small values of dy/dx, the radius of curvature at any point on the brush face is found by differentiation of eqn. (25) to be approximately

$$\rho \approx \frac{1}{d^2y/dx^2}$$

$$= \frac{R}{1 - (\epsilon\pi/w)\cos(\pi x/w)} \tag{26}$$

It is seen from eqn. (26) that the radius of curvature of the brush matches that of the rotor at the edges ($x = w/2$), and increases to a maximum value at the center ($x = 0$):

$$\rho = \frac{R}{1 - \epsilon\pi/w} \tag{27}$$

The maximum gap at a brush edge will depend on the location of the contact point (*i.e.* the angle of rotation). For the symmetrical case with contact at the brush center, the approximate equation for the rotor surface relative to the contact point is, for small values of x/R,

$$y = \frac{x^2}{2R} \tag{28}$$

where y is measured as positive downward in Fig. 3. In this rotor position, if elastic deformation is not considered, the maximum gap g between the rotor and the edge of the brush is determined by subtracting eqn. (28) from eqn. (25) and setting $x = w/2$:

$$g = \frac{w\epsilon}{\pi R} \tag{29}$$

With a 90° rotation and contact at the brush edge, the maximum gap occurs at the opposite edge. This may be found through translation of the rotor coordinates (eqn. (28)) by an amount ϵ in the x direction, and by an amount in the y direction which will provide a coincident point with the brush at $x = w/2$. Subtraction of the brush curve (eqn. (25)) from that for the displaced rotor gives the gap equation for small eccentricity:

$$\Delta y = \frac{\epsilon}{R}\left\{\frac{w}{2} - x - \frac{w}{\pi}\cos\left(\frac{\pi x}{w}\right)\right\} \tag{30}$$

The maximum gap is then found at $x = -w/2$ as

$$g = \frac{w\epsilon}{R} \tag{31}$$

which is greater by the factor π than that for the symmetrical condition.

4. Discussion

The separation of points on the brush face from the rotor will be small for most practical values of rotor eccentricity. The order of magnitude that may be expected is illustrated by the following example of a brush running on the periphery of an eccentric rotor: brush thickness (circumferential), 2.5 cm (1 in); rotor diameter, 25 cm (10 in); radial eccentricity, 25 μm (1×10^{-3} in) (50 μm FIR). For the symmetrical condition of contact at the brush center-line, as found from eqn. (29), the gap at the brush edges would be only 1.6 μm (64 μin). When the rotor contacts at a brush edge, the opposite edge will have a separation from the rotor of about 5.0 μm (200 μin), as indicated by eqn. (31).

In the case of a brush which contacts the axial face of a rotor, for small brush coverage (i.e. for small $(b - a)/b$), the values for the maximum gap as determined from eqns. (10) and (11) will be quite similar to those found above, for the same dimensional assumptions. (Radial brush width is substituted for circumferential thickness, axial eccentricity for radial eccentricity and outer diameter b for rotor diameter.)

Holm and Holm [4] presented a method which defines the brush force required to close an interface gap. They related the width of the contact area, as determined from elastic contact theory, to the (symmetrical) gap which existed at the edges of the contact region prior to loading. The common expression for the width h of the contact zone for a cylinder against a cylindrical socket is [5]

$$h^2 = 4.66p\left(\frac{R_1 R_2}{R_1 - R_2}\right)\left(\frac{1}{E_1} + \frac{1}{E_2}\right) \tag{32}$$

when expressed in terms of the radii R_1 and R_2 of the two surfaces, and with the assumption that Poisson's ratio is 0.3 for each of the contacting materials. E is the elastic modulus and p the applied contact force per unit length along the cylinder axis. The approximation given in eqn. (28) is used to define each of the two surfaces so that the initial gap is

$$y_2 - y_1 = \frac{x^2}{2} \frac{R_1 - R_2}{R_1 R_2} \tag{33}$$

In accordance with eqn. (32), application of the force p results in elimination of the original gap within the positions $x = \pm h/2$. Therefore, substitution of the value $h^2/4$ as determined from eqn. (32) for the value x^2 in eqn. (33) gives the relationship between applied force and the maximum gap that it will close:

216

$$(y_2 - y_1)_{max} = 0.58p\left(\frac{1}{E_1} + \frac{1}{E_2}\right)$$

(34)

It should be noted that the expression is independent of the radius, for the small contact width assumption, and should apply as well to contact between surfaces of varying brush radius, as found in eqn. (30).

The effect of brush and rotor elasticity on the contact width may now be determined for the above example, with the following additional assumptions for a high metal content Ag–graphite brush on a copper rotor: brush elastic modulus, 17.2 GPa (2.5×10^6 lbf in^{-2}); rotor elastic modulus, 1.17×10^5 MPa (17×10^6 lbf in^{-2}); contact force, 2.5 kN m^{-1} (15 lbf in^{-1}) for a 2.5 cm (1 in) brush width. For these conditions, the gap which can be closed, as determined from eqn. (34), would be only 0.1 μm (4 μin).

The corresponding contact width $2x$ may be found from the general equation of the gap for the brush on the eccentric rotor. For the symmetrical position this is found by subtraction of eqn. (25) from eqn. (28):

$$\Delta y = \frac{w\epsilon}{\pi R}\left\{1 - \cos\left(\frac{\pi x}{w}\right)\right\}$$

$$\frac{2x}{w} = \frac{2}{\pi}\cos^{-1}\left\{1 - \left(\frac{\Delta y}{g}\right)\right\}$$

(35)

where g is the edge gap as determined from eqn. (29) and Δy is the closed gap found from eqn. (34). For the example, the contact width is only 23% of the brush width or 0.57 cm (0.23 in). It should be noted that the pressure at the edge of this contact width would be zero and it would reach a peak value at the center. It is expected, therefore, that the current flow would be further concentrated near the center of the contact zone where a greater area of contacting asperities may be expected.

In a recent paper [6], the worn profile of a slider was described for uniform motion relative to a plane semi-infinite base (without eccentricity). In this case, the worn slider shape matches the shape of the elastically deformed base that results from a uniform contact pressure. The uniform pressure satisfies the requirement of uniform steady state slider wear. From elastic theory, and from the results of that paper, the maximum deviation of the worn brush profile from a plane surface may be calculated. For a short transverse depth, equal depth for the slider and the base and a frictionless contact, the slider edges are worn back symmetrically from the center of the face by an amount

$$\delta = 0.441qL/E$$

(36)

where q is the applied contact pressure, L is the slider length in the direction of motion and E is the elastic modulus of the base material. For an infinite depth of both rider and base as described in ref. 6, and with Poisson's ratio equal to 0.3, this becomes

$$\delta = 0.401qL/E$$

(37)

If a friction coefficient of 0.5 is used, the contact shape becomes asymmetrical with the maximum worn height from the trailing edge to a point forward of the center of

$$\delta = 0.545qL/E \qquad (38)$$

In the case of electrical brushes, even for high current applications, the contact pressure is quite low. For the conditions assumed in the example above, for a 2.5 cm (1 in) brush on a copper rotor at the relatively high pressure of $q = 100$ kPa (15 lbf in^{-2}), the wear height determined from eqn. (38) is only 0.012 μm (0.48 μin). This is small in comparison with the possible effect of practical rotor eccentricities as found above.

5. Conclusions

The worn shape of a brush on an eccentric rotor may be computed on the basis of two requirements.
(1) The wear per cycle is equal for all points on the brush face.
(2) The brush face is tangent to the rotor surface at the point of contact.
The resulting radius of curvature varies with position on the brush face but is always equal to, or larger than, that of the rotor and results in a separation along much of the nominal brush–rotor interface. Although this gap is small, normal values of the brush contact force are not sufficient to close it fully through elastic deformation.

Acknowledgment

References

1 O. S. Taylor and P. Reichner, Mechanical load aspects of high current brush system design, *IEEE Trans. Components. Hybrids Manuf. Technol.*, 1 (1979) 95 - 99.
2 P. Reichner, Brush contact on eccentric sliprings, *IEEE Trans., Power Appar. Syst.*, 100 (1) (1981) 281 - 287.
3 P. Reichner, Pressure–wear theory for sliding electrical contacts, *IEEE Trans. Components, Hybrids Manuf. Technol.*, 1 (1981) 45 - 51.
4 R. Holm and E. Holm, *Electric Contacts*, Springer, New York, 4th edn., 1967.
5 R. J. Roark, *Formulas for Stress and Strain*, McGraw-Hill, New York, 3rd edn., 1954.
6 J. Dundurs and M. Comninou, Shape of a worn slider, *Wear*, 62 (1980) 419 - 424.

HIGH CURRENT BRUSHES
VIII: EFFECT OF ELECTRICAL LOAD*

J. L. JOHNSON and J. SCHREURS

Westinghouse Research and Development Center, Pittsburgh, PA 15235 (U.S.A.)

(Received December 1, 1981)

Summary

Performance data are presented from controlled experiments with Ag–graphite brushes sliding on copper slip rings in a continuous-operating mode over a wide range of electrical loads (0.8 - 8 MA m^{-2}) in a humidified CO_2 environment. The observed contact resistance, friction and wear characteristics are explained on the basis in part of past and recent contact models and in part of thermophysical property data acquired for the specific Ag–graphite brush material (mass fraction of silver in graphite, 0.75). The phenomenon of electromigration of silver is invoked to explain observed consistent asymmetry in contact resistance between anode and cathode brushes. Direct evidence in support of the models and observed brush performance is offered from results of detailed contact surface morphology and structure analyses.

1. Introduction

Previous studies at Westinghouse showed that a marked increase in lifetime can be achieved when carbon and metal–graphite solid brushes are operated in inert gas atmospheres rather than in air [1 - 3]. More recent experiments were conducted at much higher current densities. Using commercially available graphite brushes, containing a 0.6 - 0.8 mass fraction of silver, combined with high strength high conductivity copper alloy slip rings, the current density state-of-the-art practice was extended to at least 0.8 MA m^{-2} [4]. Excellent performance was achieved with the metal–graphite brushes operating in gas atmospheres of CO_2, SF_6, N_2, helium and argon in the presence of constant water partial pressure (600 Pa) and under a dry CO_2 atmosphere in the presence of n-paraffinic hydrocarbon vapors (n-heptane to n-hexadecane: 1300 - 0.2 Pa) as vapor additives [5].

Analysis of the performance (resistance, friction and wear) of Ag-graphite brushes (mass fraction of silver, 0.75) indicated that the total resistance (average 230 $\mu\Omega$ per brush) was dominated by constriction effects, with three contact spots effectively present at the contact interface [6]. The film contribution to the total resistance was small, the thin film resistivity being less than 10^{-12} Ω m^2. The measured friction (0.18) was in close agreement with calculated values based on (1) individual friction coefficients for graphite and silver and the area fractions of each in the composite brush, (2) brush material hardness and quoted boundary lubrication shear strength values and (3) shearing of thin water films. Wear was well into the microwear regime (4 mm^3 Mm^{-1}) when the brushes were electrically and mechanically loaded to 0.8 MA m^{-2} and 80 kN m^{-2} respectively.

Using diagnostic techniques of optical microscopy, scanning electron microscopy (SEM) and Auger electron spectroscopy (AES), two types of film have been found on copper rings which slide against monolithic Ag-graphite brushes in a humidified CO_2 atmosphere [7, 8]. The first was an extremely "thin" film consisting of an adsorbed water layer (1.5 - 3.0 nm thick). It is believed that this water film separates the brush from the slip ring in areas where elastic contact is made, while providing a low shear resistance. Under certain conditions (e.g. if the load becomes high enough), the water film may break down, so that a microscopic brush–ring weld can form, thereby permitting material transfer (and subsequent wear) by adhesion. Thus, the second type of film results from occasional welds formed between the silver in the brush and the copper in the slip ring followed by the rupture of a weaker interface in the brush material. The "thick film" deposited on the copper slip ring is a composite of individual lumps of material, whose thickness (0.5 - 150 μm) varies from location to location. This thick film is a highly conducting metallic extension of the slip ring surface as a result of the excellent metallurgical bonding (welding) of the transferred silver to the underlying copper. Thin films adsorbed on the surface of the thick film (silver and graphite) control the contact friction and wear by inhibiting metal-to-metal weld formation but allowing efficient electron conduction, presumably by tunneling.

Extensive multibrush testing at higher current densities was accomplished with a homopolar generator [9]. The performance of 92 brushes (46 in parallel per polarity) was evaluated at electrical loads up to 9500 A (1.6 MA m^{-2}) and a slip ring speed of 42 m s^{-1}. At the maximum load conditions, the anode and cathode brush interface contact voltage drops were 0.17 V and 0.09 V respectively, with a typical wear rate (anode brush) of 2.2 mm^3 Mm^{-1}. This wear rate is about one-sixth of that for diesel electric locomotive motor brushes, which operate at similar peripheral speeds but with less than one-tenth the electrical load.

The results of investigations of the steady state performance of monolithic Ag-graphite brushes on copper slip rings with electrical loads significantly greater than 1.6 MA m^{-2} (up to 8 MA m^{-2}) are reported in this paper.

2. Test conditions and results

2.1. Apparatus and definition of polarity

The apparatus used for the tests is fully described in an earlier paper [4]. The test conditions are summarized in Table 1. During each test the following responses were monitored: contact electrical resistance; frictional power loss for the brush–ring system; brush bulk temperature. Brush wear was calculated from brush length measurements.

TABLE 1

Test conditions

Slip ring speed	12.7 m s^{-1} (ring diameter, 8.3 × 10^{-2} m)
Slip ring material	Cu (Ag bearing)
Slip ring surface	Helical groove
Brush composition	0.75 mass fraction Ag in graphite
Brush face area	10^{-4} m^2
Brush angle	15° trailing
Brush force	11.5 N
Brush current	78 · 800 A d.c.
Gas atmosphere	CO_2
Humidity dew point	20 °C
Brush holder temperature	75 °C (nominal)
Number of brushes	One anode and one cathode (separate track operation)
Test duration	24 h for each test, or less if dusting wear occurred

The following nomenclature has been used in the discussion of polarity effects: electrons enter the brush (leave the slip ring) at the anode brush; the track where electrons leave the slip ring will be called the cathode track. The anode brush slides on the cathode track.

2.2. Contact resistance

In Fig. 1, the contact resistance is plotted against current density (based on the total brush face area). A current density of 1.0 MA m^{-2} represents a total current of 100 A in the brushes used for the experiments.

The contact resistances presented here were obtained from potential probes embedded in the brushes approximately 1.6 mm from the sliding surface and therefore include the constriction resistance but exclude the brush body resistance.

The contact resistance varied considerably for a given brush polarity and current density. The values plotted are time averages, and the arrows and bars indicate the range of individual measured values. The resistance values measured at the anode brush were consistently higher than those at the cathode brush (typically by a factor of 2 below 4 MA m^{-2}). The band of observed data for the anode brush is wider than the band for the cathode brush. Within each band, the resistance increases, a maximum is reached and the resistance then decreases when the current density is further increased.
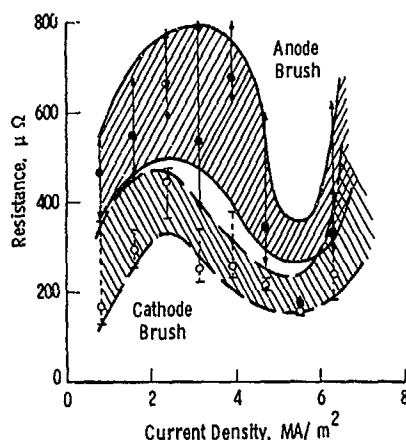
Fig. 1. Electrical contact resistance of 0.75 Ag–graphite brushes in humidified CO_2 (brush face area, 10^{-4} m^2).
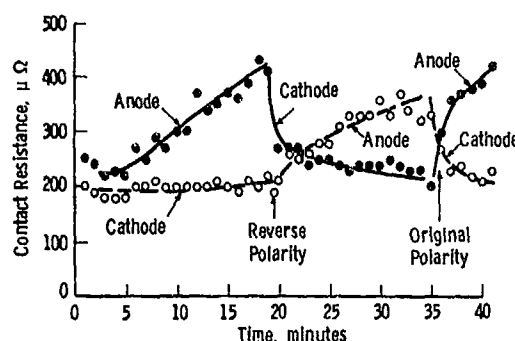
Fig. 2. Electrical current polarity–time effects on the contact resistance of 0.75 Ag–graphite brushes sliding on a copper slip ring (peripheral speed, 2.8 m s^{-1}; electrical load, 0.8 MA m^{-2}; mechanical load, 100 kN m^{-2}; CO_2 gas environment; dew point, 0 °C; initial brush faces generated without electrical load): ●, brush 1; ○, brush 2.

In this current density range, the contact resistance always remains well within values quoted by Holm [10] for "clean" metal–metal and metal–graphite static contact pairs having comparable mechanical loads. At some current density (greater than 6 MA m^{-2}), dusting wear occurs and the resistance rises rapidly.

2.3. Polarity effect

Figure 2 illustrates the changes in contact resistance with time for a fixed current density and speed. The brush faces were run in without electrical load; time zero represents the current switch-on. The contact resistance at the cathode brush remained virtually constant but the contact resistance at the anode brush increased with time. (An equilibrium value was reached but is not shown in Fig. 2; equilibrium values are reported in Fig. 1.)

When the polarity was reversed, the new cathode resistance initially dropped rapidly and then decreased more slowly to a value close to that of the original cathode resistance. At the new anode, the contact resistance rose slowly, similar to the rise observed at the original anode brush. When the original polarity was restored, the original contact resistance value was restored, after some time. The time scale for these changes ranged from 5 to 20 min.

2.4. Friction and wear

In Fig. 3 the average friction coefficient for both brushes is plotted against current density. Typical brush bulk temperatures are indicated at the top of the plot; water cooling of the brush holders helped to limit these temperatures. However, despite this, brush temperature increased to 200 °C
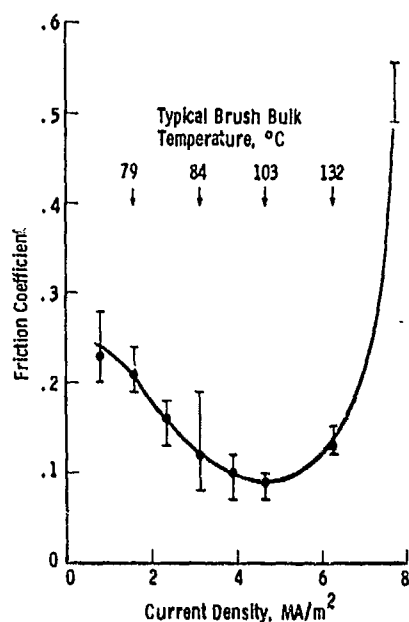
Fig. 3. Average friction coefficient of anode and cathode 0.75Ag–graphite brushes in humidified CO_2 (copper slip ring).
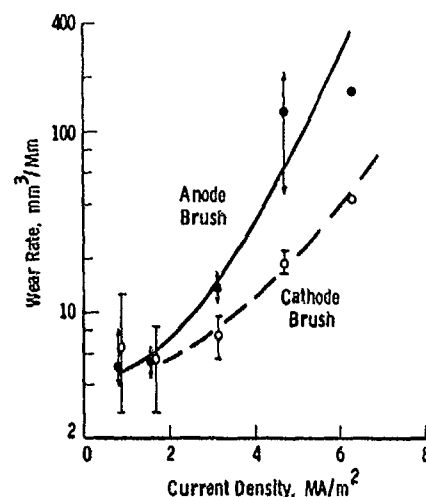
Fig. 4. Wear performance of 0.75Ag–graphite brushes in humidified CO_2.

within seconds when dusting wear occurred (at current densities greater than 6 MA m^{-2}).

As the current density increased, the friction coefficient decreased. Near the onset of dusting wear, the friction coefficient increased slightly. When dusting wear occurred, a dramatic increase in friction was observed.

The measured wear rate is plotted against current density in Fig. 4. The wear rate increased monotonically as the current density was increased with the anode brush wearing faster than the cathode brush at current densities exceeding 2 MA m^{-2}.

2.5. Power losses

The combined electrical and mechanical interface losses for each brush are plotted against current density in Fig. 5. It was assumed that the mechanical losses are divided equally for both brushes.

The total power dissipated at each brush–slip ring interface rises monotonically with current density. The electrical losses dominate the mechanical losses except at the very lowest current densities (less than 1 MA m^{-2}), where they are about equal.

3. Materials characterization

3.1. Bulk physical properties

The bulk electrical resistivity and contact hardness were measured for 0.75Ag–graphite brushes at various temperatures. In Fig. 6, full circles
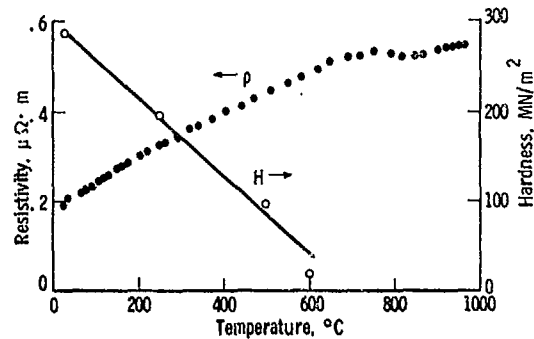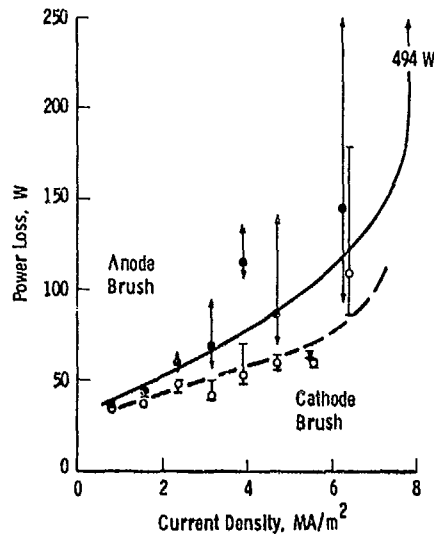
Fig. 5. Contact interface power loss of 0.75Ag–graphite brushes in humidified CO_2.

Fig. 6. Effect of temperature on electrical resistivity (●) and contact hardness (○) of 0.75Ag–graphite (hardness measured with a ball 6.4 mm in diameter under a load of 147 N).

represent resistivity values measured between 22 and 960 °C (the melting point of silver). The open circles represent hardness values, which were measured using a 6.4 mm (0.25 in) diameter ball and a 147 N (15 kgf) load.

The electrical resistivity was measured by a standard four-terminal potential–current technique. The resistivity of the compound brush increased by a factor of 3 over the temperature range of interest from about 12 times that of pure silver at 22 °C.

Hardness values were measured in air up to 600 °C, at which temperature the carbon at the brush surfaces oxidized. The hardness values decreased with temperature and the dependence was linear, at least up to 500 °C.

3.2. Brush contact faces

A 0.75Ag–graphite brush should have a 0.36 area fraction of silver on a polished face since the volume fraction is equal to the area fraction for a random two-dimensional section. In all the brushes analyzed after the tests, contact faces were found to be considerably enriched in silver. Table 2 gives the area fractions of silver observed on the cathode and anode brush faces. The area fraction of silver was consistently higher in the cathode brush than in the anode brush for the same current density.

Scanning electron microscopy revealed that wear marks (polishing lines) were continuous across the brush face for low current densities, being visible in the silver and graphite phases (Fig. 7(a)). Brushes run at higher current densities (greater than 6 MA m^{-2}) showed wear lines only in the silver phase (Fig. 7(b)). This indicates that the silver constituted almost 100% of the contact area and that the graphite was recessed.

TABLE 2

Area fractions of silver in brush contact faces following
high current tests

Current density	Ag area fraction	
$(MA\ m^{-2})$	Anode brush	Cathode brush
0.75	0.43	0.51
1.56	0.43	0.53
3.12	0.58	0.60
6.24	0.55	0.66
7.75 (dusted)	0.66	0.72
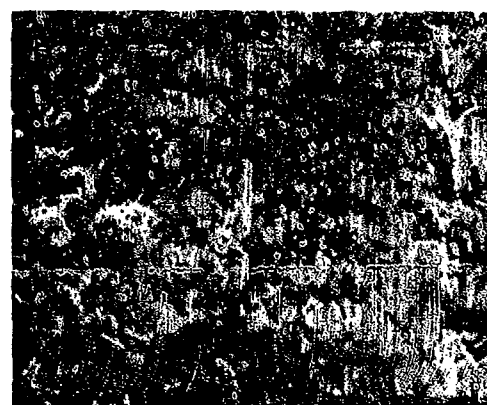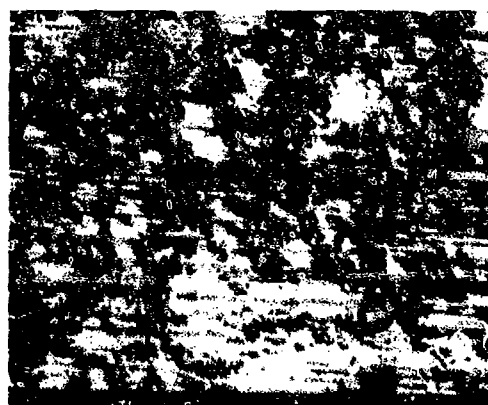
(a)   (b)

Fig. 7. Electron micrographs of brush faces for two current densities: (a) cathode (top) and anode (bottom) run at 0.78 MA m^{-2}; (b) cathode (top) and anode (bottom) run at 6.24 MA m^{-2}.

3.3. Slip ring tracks

Two sets of tracks were analyzed by AES. Details of the technique and difficulties associated with the technique when applied to slip ring tracks were explained in an earlier paper [7].

Low current density (1.6 MA m^{-2}) operation produced anode tracks that were different in composition from the cathode tracks. The anode tracks (tracks under the cathode brush) were richer in silver than the cathode tracks and the cathode tracks (tracks under the anode brush) were richer in carbon. These differences disappeared after about 10 nm of material was removed by argon sputtering. These differences were observed at five different locations in each track. In tracks produced at 6 MA m^{-2}, the differences noted were less pronounced but the average of seven areas showed that the anode track was, again, richer in silver than the cathode track (Table 3).

TABLE 3

Average element composition[a] of slip ring track surfaces at different current densities

Element	1.6 MA m^{-2}		6.2 MA m^{-2}	
	Cathode	Anode	Cathode	Anode
Cl	32	40	10	16
S	—	—	4	6
C	109	117	89	95
Ag	26	53	46	61
O	39	53	43	35
Cu	63	93	54	42
Number of samples	5	6	7	7

[a]The element composition is proportional to the atomic per cent.

SEM also revealed some differences between cathode and anode tracks. Again, the differences were much more pronounced at low current densities. The low current density cathode track (running under the anode brush) was smooth and homogeneous; all analyses (visual, AES and SEM) indicated that it consisted of an Ag–Cu alloy. In contrast, the low current density anode track consisted of pure silver islands deposited on a copper background (Fig. 8(a)).

In the higher current density tracks, the same trend existed but the differences were less pronounced. The cathode track was as smooth and homogeneous as in the low current test; the anode track was much smoother than in the low current test but some islands could still be seen.

4. Discussion

4.1. Contact resistance

Characteristic of the (Ag–graphite brush)–(Cu ring) combination is that the electrical contact resistance varies within limits, maintaining a semblance of equilibrium (see Fig. 1). Above a critically high load current density (7 MA m^{-2}), however, an abrupt transition or irreversible instability in the
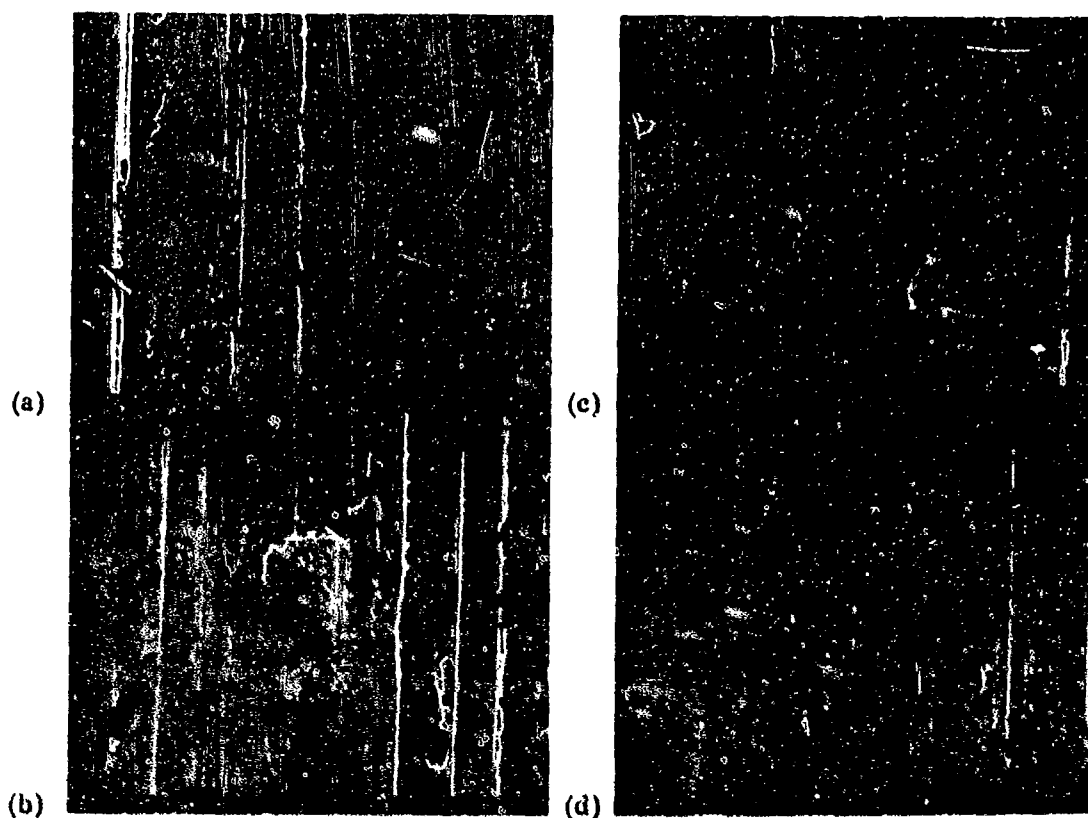
Fig. 8. Electron micrographs of slip ring surface inside ((a), (b)) and outside ((c), (d)) the sliding tracks: (a) cathode track (under anode brush) with silver and copper present at all locations; (b) anode track (under cathode brush) with a silver deposit in the center of the photograph (silver track at right); high magnification (c) and low magnification (d) photographs of original slip ring surface (the dark stains in (c) are carbon deposits formed when the electron beam interacts with the adsorbed layers on the copper surface).

brush operating performance occurs. An explanation for the overall contact resistance behavior is based on a contact resistance model, supertemperature calculations and the phenomenon of self-healing [11].

4.1.1. Contact resistance model
A model expression for the total contact resistance [6] is

$$R = 0.4(\rho_b + \rho_s)\left(\frac{\xi H}{nF}\right)^{0.5} + \sigma_f \frac{\xi H}{F} \tag{1}$$

where ρ_b and ρ_s are the brush and slip ring electrical resistivities, n is the number of contact spots, ξ relates the average indentation pressure in the range from beginning of plastic deformation to the "contact" hardness H, F is the applied brush force and σ_f is the surface film resistivity. A contact spot ellipticity of 3 is assumed. A further assumption is that the contact spots are

sufficiently far separated that interaction effects may be neglected [12]. Surface details revealed by our microanalytical technique show that the Ag–graphite brush faces were worked in the plastic deformation regime, which justifies the exponent (0.5) used in the constriction resistance term.

4.1.2. Temperature–load current effects

The influence of temperature on contact resistance was estimated by expressing ρ_b and H (see Fig. 6) as functions of temperature t in eqn. (1). For this estimate the film resistance term and the slip ring resistivity were deleted. Previous evaluations revealed that the effects of these terms on contact resistance as applied here are of small consequence [6 - 8]. A value of unity was selected for n and ξ. Evidence for n approaching unity has recently been suggested from observations of "thermal mounding" in Cu–graphite brushes subjected to high current (1200 A) pulses [13]. As the brush material becomes less hard with increasing temperature the factor ξ will also approach unity, since the average indentation pressure will approach that of the contact hardness H. Using $F = 11.5$ N,

$$R = (5.93 \times 10^{-11}t + 2.23 \times 10^{-8})(-4.3 \times 10^{5}t + 3.0 \times 10^{8})^{0.5} \ \Omega \qquad (2)$$

The calculated results of R as a function of t are shown in Table 4. Brush temperatures selected are the averages of the maximum supertemperatures [14] calculated for both anode and cathode brushes, based on contact resistance and friction data and concomitant load current densities. First we see that the contact resistance increases with temperature, reaches a maximum value, then decreases with higher temperature. The experimental results reveal that similar changes in R also occurred with increasing current density (see Fig. 1). These changes depend on the increasing electrical resistivity and decreasing hardness *versus* temperature properties of the brush material, in compliance with expression (1). Electrical resistivity controls the sliding contact resistance in the lower current density (temperature) range. Values of the surface temperature greater than 315 °C will cause the contact resistance to decrease (self-heal). In this range, the contact area increases because hardness of the brush material has been reduced.

TABLE 4

Calculated contact resistance *versus* current density for Ag–graphite brushes

Brush temperature[a] (°C)	Contact resistance (μΩ)	Current density (MA m^{-2})
155	481	1.6
279	521	3.1
315	526	4.7
614	362	6.2

[a] Average supertemperature in anode and cathode brushes.

Finally, the onset of high contact resistance, high friction drag and high wear is attributed to the attainment of a critically high current (approximately 7 MA m^{-2}) wherein the contact heating load is greater than the contact's cooling capacity. At this point an irreversible thermally induced instability occurs [15, 16]. Temperatures approaching the melting point of silver, gross physical deformations in the true contact surface, and excessive wear, are barriers to satisfactory achievement of even short-term continuous running performance. Controlled brush performance is restored to normal, however, on reduction in the load current to below the critical value.

4.2. Polarity effect

The polarity effect noted here for Ag–graphite brushes operating in humidified CO_2 is not observed when graphite brushes are used in the same environment. The effect is observed when Ag–graphite brushes are operated in other non-air environments.

Any explanation of the polarity effect must account for (a) the higher contact resistance at the anode brush, (b) the polarity reversal data (see Fig. 2), (c) the difference in silver area fractions on the brush faces and (d) the fact that the brush faces of both anode and cathode have silver area fractions that are significantly higher than those expected from the silver volume fractions in the bulk. The explanation that we propose invokes the phenomenon of electromigration, but further experiments are needed to account for all of the present observations.

Ho and Huntington [17] described the electromigration effect that occurs in silver bars at high current densities and high temperatures. They observed silver ion migration at rates of up to 20 μm day^{-1} under current densities of 100 MA m^{-2} at temperatures of 700 - 900 °C. The silver ions migrate in the direction of the electron flow (towards the anode).

The migration rates are proportional to current density and they depend on temperature as the diffusion rates do. Current densities in the small, real contact areas of the Ag–graphite brushes here are 10 - 100 times higher than the highest current densities tested by Ho and Huntington.

In sliding contact applications, the wear rate determines whether electromigration has an effect or not. If the linear wear rate is much higher than the electromigration rate, electromigration will have a negligible effect. We have calculated the electromigration rate of silver in the anode brush (about 200 μm day^{-1}) when it wears at a rate of 9 mm^3 Mm^{-1} (about 100 μm day^{-1}). If this holds true, the silver will migrate away from the brush face (into the brush). This would explain the consistently observed higher area fraction of silver in the cathode brush face (Table 2) and the differences in contact resistance between anode and cathode brushes (Figs. 1 and 2).

4.3. Friction and wear

The friction coefficient of graphite–graphite and graphite–metal contact pairs sliding in air, with or without electrical loads, has been noted by others

to decrease with increasing contact temperature [18]. This was shown for contact temperatures (bulk temperature plus supertemperature) in the range to at least 200 °C. We observe here a similar trend in the friction coefficient of Ag–graphite brushes which are contacting copper rings in a humidified CO_2 environment, but as a function of increasing current density. As in ref. 18, we note that the brush bulk temperature also increased (see Fig. 3). The corresponding interface temperatures (supertemperatures) are undoubtedly higher. As previously discussed in Section 4.1, interface temperatures significantly greater than 200 °C were probably attained. The impact of temperature on gas and vapor adsorption to metal and graphite sliding contact surfaces undoubtedly controls the friction and wear characteristics [19 - 23].

It was previously shown that the wear debris consist of a much finer powder than the original starting materials (10 - 14 μm [8]). Typical wear debris particles have dimensions in the range 0.3 - 2 μm. Although particles larger than about 2 μm constitute the majority of the volume, they represent only a small fraction of the number of wear particles. Wear apparently proceeds by a physical fragmentation process. On average, such fragments are much smaller than the typical contact spot area of 0.1 - 0.3 mm. Possibly the burden of dissipating concentrated bursts of high energy within the true contact spot zones encourages such physical wear of the contact surface. Mild wear occurs as bonds between graphite–graphite crystallites and graphite–Ag particles are weakened, for example, by thermally induced expansion stresses. If true, wear should be expected to increase with increasing current loading because of increased interface power loss and concomitant increased temperature. Our experimental results show that the composite Ag–graphite brush volume wear rate increased directly with the electrical current load.

Finally, with further increases in the interface temperature with increasing current density, dissociation of chemisorbed surface films occurs at rates greater than they are formed [24]. This leads to greatly increased contact adhesive forces and to even higher friction and wear, as revealed by the experimental results. Wear of this magnitude is commonly referred to as severe wear or "dusting" because of the dust-like clouds of wear debris originating at the interface.

The high temperature which triggers the abrupt transition from low to high friction and mild to severe (dusting) wear is attributed to exceeding a critical contact load current [25]. Just beyond the critically high current, the rate of heat produced in the true contact area exceeds the rate at which heat is lost. Then, the contact temperature continues to rise, unless the load current is reduced below the critical value. Our results suggest that the critical current for each Ag–graphite brush, as applied here, is near 625 A. Some extension of the critical load current is possible by increasing the brush mechanical load force. Experimental results, not presented here, show this to be true. The penalty, however, is higher brush wear.

5. Conclusions

(1) Low contact resistance (200 - 800 $\mu\Omega$) was achieved with Ag-graphite brushes (mass fraction of silver, 0.75; load, 11.5 N) operating in a humidified CO_2 atmosphere and loaded with currents in the range 80 - 800 A (0.8 - 8 MA m^{-2}).

(2) A maximum in the contact resistance–current density curve was ascribed to the concomitant thermally induced rising electrical resistivity and falling hardness characteristics of the brush material.

(3) Reduction in the friction coefficient with increasing electrical load (temperature) was attributed to "activated adsorption" of vapor films on the contact interface graphite–metal constituents.

(4) An increasing mild wear–current load characteristic was attributed to thermally accelerated microfragmentation of graphite. Increasing physical stresses with increasing electrical load weakens the graphite–graphite and graphite–metal bonds, leading to increasing wear rates.

(5) Abrupt transitions from mild to severe wear and low to high friction were observed at a current load near 624 A. These onsets were envisioned to occur as the heating rate of the true contact area becomes higher than the cooling rate, leading to thermal runaway.

(6) Electromigration was postulated as the mechanism which causes consistently lower contact resistance at the cathode brush interface. Mass transport of silver away from the anode brush face (into the brush) would lead to a higher contact resistance at the anode brush.

(7) Electromigration alone cannot explain all the observations associated with the polarity effect. Further study of this effect is needed.

Acknowledgments

References

1 R. M. Baker and G. W. Hewitt, Contact drop and wear of sliding contacts, *AIEE Trans.*, 56 (January 1937) 123 - 128.
2 J. L. Johnson and L. E. Moberly, Brush life and commutation in atmospheres of air, SF_6 and CO_2. In *Proc. Conf. on Electrical Contacts, 1967*, Illinois Institute of Technology, Chicago, IL, 1967, pp. 109 - 116.

232

3 J. L. Johnson and J. L. McKinney, Electrical power brushes for dry inert-gas atmospheres. In *Proc. Conf. on Electrical Contacts, 1970*, Illinois Institute of Technology, Chicago, IL, 1970, pp. 155 - 162.

4 J. L. Johnson and L. E. Moberly, High-current brushes. Part I: effect of brush and ring materials, *IEEE Trans. Compon., Hybrids Manuf. Technol., 1* (1) (1978) 36 - 40.

5 P. K. Lee and J. L. Johnson, High-current brushes. Part II: effects of gases and hydrocarbon vapors, *IEEE Trans. Compon., Hybrids Manuf. Technol., 1* (1) (1978) 40 - 45.

6 I. R. McNab and J. L. Johnson, High-current brushes. Part III: performance evaluation for sintered silver–graphite grades, *IEEE Trans. Compon., Hybrids Manuf. Technol., 2* (1) (1979) 84 - 89.

7 J. Schreurs, J. L. Johnson and I. R. McNab, High-current brushes. Part VI: evaluation of slip ring surface films, *IEEE Trans. Compon., Hybrids Manuf. Technol., 3* (1) (1980) 83 - 88.

8 J. Schreurs, J. L. Johnson and I. R. McNab, Characterization of thick films formed on slip rings during high current density operation, *IEEE Trans. Compon., Hybrids Manuf. Technol., 4* (1) (1981) 30 - 35.

9 J. L. Johnson and O. S. Taylor, High-current brushes. Part IV: machine environment tests, *IEEE Trans. Compon., Hybrids Manuf. Technol., 3* (1) (1980) 31 - 36.

10 R. Holm, *Electric Contacts*, Springer, New York, 1967, pp. 1 - 11, 32 - 37, 41, 124 - 126, 232, 234.

11 J. B. P. Williamson, The self-healing effect: its implications in the accelerated testing of connectors, *10th Int. Conf. on Electrical Contact Phenomena, Hungarian Institute of Electrical Engineering, Budapest, August 1980*.

12 J. A. Greenwood, Constriction resistance and the real area of contact, *Br. J. Appl. Phys., 17* (1966) 1621 - 1632.

13 R. A. Marshall, The mechanism of current transfer in high current sliding contacts, *Wear, 37* (1976) 233 - 240.

14 E. I. Shobert II, *Carbon Brushes — The Physics and Chemistry of Sliding Contacts*, Chemical Publishing Co., New York, 1965, pp. 138 - 152.

15 F. P. Bowden and J. B. P. Williamson, Electrical conduction in solids. I: influence of the passage of current on the contact between solids, *Proc. R. Soc. London, Ser. A, 246* (1958) 1 - 31.

16 R. A. Burton, Thermal deformation in frictionally heated contact, *Wear, 59* (1980) 1 - 20.

17 P. S. Ho and H. B. Huntington, Electromigration and void observation in silver, *J. Phys. Chem. Solids, 27* (1966) 1319 - 1329.

18 E. Holm, Specific friction force in a graphite brush contact as a function of the temperature in the contact spots, *J. Appl. Phys., 33* (1) (1962) 156 - 163.

19 B. M. Derman and B. V. Kantorovich, Rate of adsorption and evaporation of moisture from carbon particles, *Nov. Metody Szhiganiya Top. Vapr. Teor. Goreniya*, (1965) 131 - 136 (in Russian); *Chem. Abstr., 64* (1966) no. 13966b.

20 F. M. Lang and H. Goenvec, Adsorption and desorption of water by carbons, *C.R. Acad. Sci., Ser. C, 262* (June 1966) 1820 - 1823.

21 F. M. Lang and Y. Lafargue, Different states of the water–carbon system: case of porous graphite, *C.R. Acad. Sci., Ser. C, 266* (February 1968) 485 - 488.

22 P. Magne, R. Sauvageot and X. Duval, Formation of a graphite–water surface complex relation with oxidation reaction, *Carbon, 11* (1973) 485 - 495.

23 D. O. Hayward and B. M. W. Trapnell, *Chemisorption*, Butterworths, Washington, DC, 1964, pp. 80 - 86.

24 J. K. Lancaster, Instabilities in the frictional behavior of carbons and graphites, *Wear, 34* (1975) 275 - 290.

25 J. A. Greenwood and J. B. P. Williamson, Electrical conduction in solids. II: theory of temperature-dependent conductors, *Proc. R. Soc. London, Ser. A, 246* (1958) 13 - 31.

DAMPING CHARACTERISTICS OF SOLID BRUSH CURRENT COLLECTION SYSTEMS*

C. A. BRONIAREK

Mechanical Engineering Department, Tuskegee Institute, AL 36088 (U.S.A.)

(Received November 20, 1981)

Summary

The damping characteristics of a current collection system were examined. The following three categories of damping were selected: (1) damping in the brush material due to rheological properties of the brush material (called internal friction); (2) damping in the interface between the brush and the holder or between the brush and the rotor (called interface damping); (3) fluidic damping, or viscous damping, due to interaction with the ambient fluid, such as air, vapor etc.

The theoretical analysis of several types of mechanisms and models is postulated. The experimental tests for measurements of the damping parameters are suggested.

The analytical methods of calculation of the equivalent of damping constants to be used in the standard stability analysis are presented.

---

1. Introduction

Some dynamic mechanical characteristics of a current collection system such as damping and elastic properties are examined here. The three categories of damping selected are as follows: (1) internal damping in the brush material (rheological damping); (2) external damping in the interface between the brush and the holder and between the brush and the rotor (collector or commutator); (3) external damping due to the brush interaction with the ambient fluid (air, other gases, vapor–gas mixtures etc.).

The most suitable rheological models for rate-dependent and rate-independent friction are postulated. The damping energy dissipation in each of these models was calculated. The methods of experimental identification of each model are presented in graphical and analytical forms. The methods of calculation of the equivalent damping coefficients from the hysteretic loops, as well as from the bandwidth of the resonant peak at the half-power location, are presented in detail.

---

*Paper presented at the Advanced Current Collection Conference, Chicago, IL, U.S.A., September 23 - 25, 1981.

234

Recommendations are made concerning the applied load cycling for experimental measurements of the internal damping hysteretic loop and the interface damping energy dissipation.

For the interface damping energy dissipation, the load cycling must be within the compressive load zones only. For the internal damping energy dissipation measurements, the load cycling must vary from the tensile load zone through the symmetric load variation to the compressive non-symmetrical loads.

The brush material and the brush interface with the brush-holder or with the rotor do not behave in a perfectly elastic manner even at very low stresses [1]. Inelasticity is always present under all types of brush loading, although extremely precise measurements are necessary to detect it. In all types of brush loading, the materials or interfaces that dissipate energy under cyclic loads display one phenomenon in common; the cyclic load–deformation (F–X) curve of Fig. 1 is not a single-valued function but forms a hysteretic loop. Since energy is absorbed by a brush material and interface under cyclic load, the unloading branch of the loop must lie below the loading branch as shown in Fig. 2. The area (shaded) between these two branches is proportional to the energy absorbed.

(a)   (b)
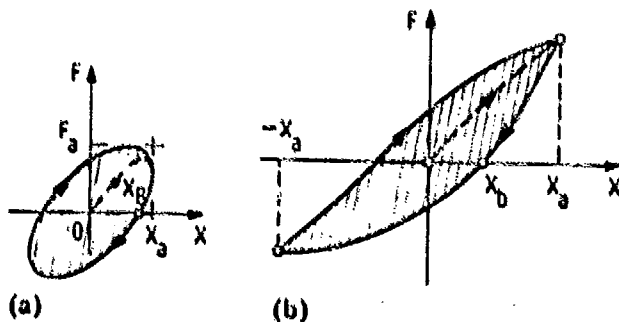
Fig. 1. Typical hysteretic loops for linear and non-linear materials under sinusoidal reversed loading: (a) symmetric elliptical loop for linear material under rate-dependent loading; (b) symmetric hysteretic loop for a non-linear material under rate-independent loading. The shaded area represents the energy loss per cycle.
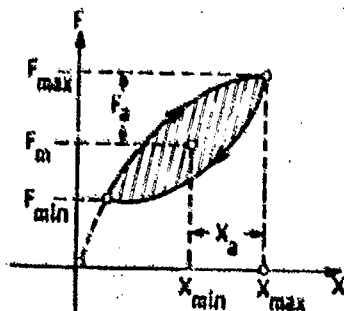
Fig. 2. Typical non-symmetric hysteretic loop for a non-linear material under non-symmetrical and rate-independent loading. The shaded area represents the energy loss D per cycle.

Rate-independent material and rheological models of the interfaces display hysteretic loops which have sharp corners at the extreme points such as those shown in Figs. 1(b) and 2. These hysteretic loops are concerned with the unidirectional (or half-) sinusoidal loading.

For a Voigt model (Fig. 3(b)), the inelastic strain is completely recoverable. For the Maxwell model (see Fig. 3(a)), the inelastic strain is non-recoverable.
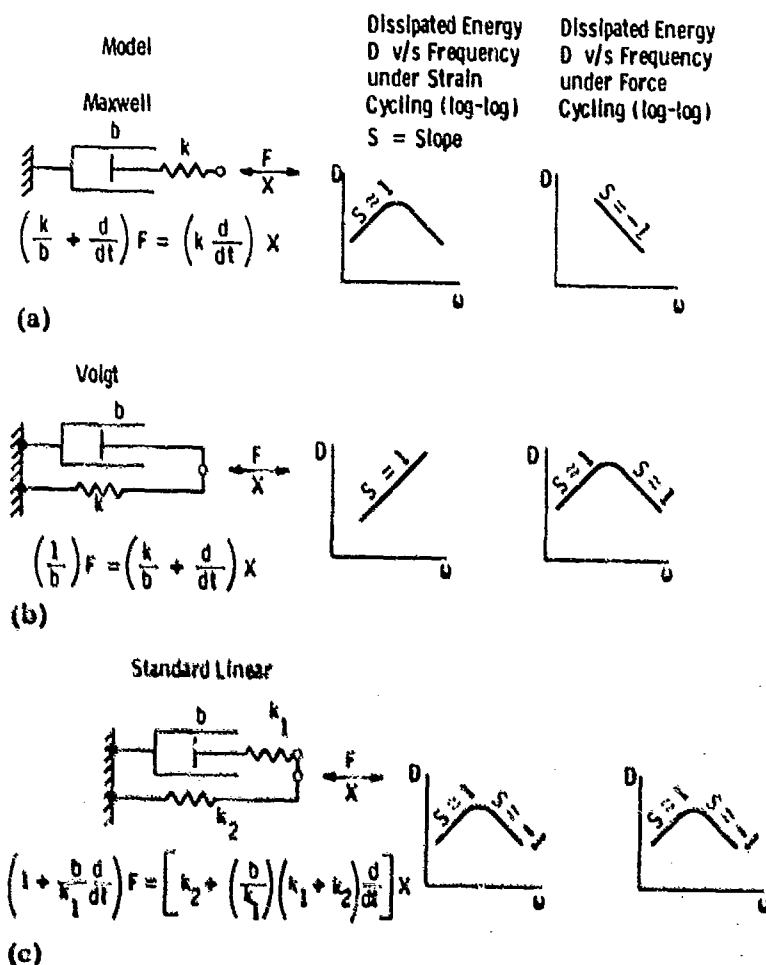
Fig. 3. The simplest rheological models and the nature of the dissipated damping energy vs. frequency plots which can be used to identify the model experimentally (S is the slope).

If the brush system is subjected to a unidirectional sinusoidal load which is only partially released (leaving a residual force F_{min}), recovery can then occur, as shown in Fig. 4(a), along the line 2–5.

The energy dissipation from the vibrating brush is caused by various mechanical interactions between particles of the brush material and between the brush–brush-holder–rotor system. The presence of a granular brush material (near debris) at the interface may significantly contribute to the energy dissipation [2, 3].
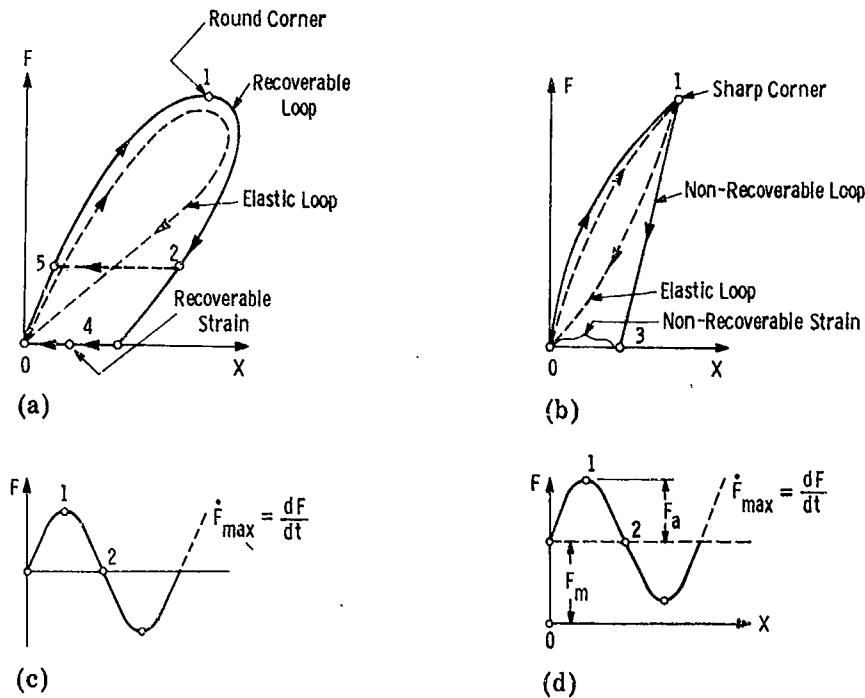
Fig. 4. Types of (a) rate-dependent and (b) rate-independent hysteretic loops; types of (c) reversed sine wave ($F = F_a \sin(\omega t)$) and (d) non-reversed sine wave ($F = F_m + F_a \sin(\omega t)$). The load is unidirectional as at the brush–brush-holder interface.

2. Damping nomenclature and background

2.1. Linear viscosity

Linear viscous damping leads to an elliptical hysteretic loop such as shown in Figs. 1 and 2. The force–displacement relation of a linear visco-elastic material can be represented by the differential equation known as a constitutive equation:

$$\left(a_0 + a_1 \frac{\partial}{\partial t} + a_2 \frac{\partial^2}{\partial t^2} + \ldots + a_n \frac{\partial^n}{\partial t^n} \right) F$$

$$= \left(b_0 + b_1 \frac{\partial}{\partial t} + b_2 \frac{\partial^2}{\partial t^2} + \ldots + b_n \frac{\partial^n}{\partial t^n} \right) x \tag{1}$$

where a_i and b_i ($i = 1 - n$) are material constants. In general, derivatives of all orders are required for real materials. However, in many engineering applications, a finite number of terms provide a good approximation. The term "viscous damping" is usually associated with the damping force expressed in terms of velocity as

viscous damping force = constant X velocity

or in terms of b and $\dot{x} = dx/dt$ as

$$F_{vd} = b \frac{dx}{dt} \tag{2}$$

where b is the damping constant and x is the displacement.

The fluidic damping force other than the viscous force is a non-linear function of the velocity, *i.e.*

$$F_d = f(\dot{x}) \tag{3}$$

The viscoelastic or inelastic properties of the brush material or of the brush interface can be represented by the combinations of the dashpots and spring as shown in Fig. 3.

The constitutive equation for a single spring unit of spring constant k is

$$F = kX \tag{4}$$

By comparison of eqn. (4) with eqn. (1), we observe that

$$a_0 = 1 \qquad b_0 = k$$

The other coefficients

$$a_1 = a_2 = \ldots = a_n = 0$$
$$b_1 = b_2 = \ldots = b_n = 0$$

Similarly, for a dashpot, the force–velocity relationship given by eqn. (2) can be written as

$$F_{vd} = b \frac{dX}{dt} \tag{5}$$

The coefficients in eqn. (1) for a dashpot damping force (see eqn. (5)) are

$$a_0 = 1 \qquad b_0 = 0 \qquad d_1 = b$$

These constitute the "standard linear model".

Figure 3 shows the models, the corresponding constitutive equations and the shape of the dissipated energy plots *versus* vibration frequencies on logarithmic scales.

In the experimental testing of the brush, a distinction must be made between conditions that lead to a constant amplitude of displacement X (irrespective of the resultant force behavior) and conditions that produce a constant amplitude of force F (irrespective of the displacement). The logarithmic plots for a damping energy D *versus* frequency under both displacement cycling and force cycling conditions are shown in Fig. 3, second and third columns.

The experimental damping energy D *versus* frequency ω plot is compared with the plots in Fig. 3 to determine the appropriate model.

2.2. Damping energy

The most general definition of the damping energy absorbed per cycle is

$$D = \oint F \, dX \tag{6}$$

238

where F and X are the force and the displacement respectively as given by the constitutive equation (eqn. (1)) and illustrated in Figs. 1, 2 and 4. The value of the integral for one complete cycle is proportional to the area within the hysteretic loop.

The damping energy dissipation calculations are shown in ref. 1.

2.3. Damping categories in the brush system: rate-dependent damping; rate-independent damping

This paper is concerned with energy loss and damping in the brush system. Three categories of damping are identified as follows: (1) damping in the brush material due to rheological properties of the brush material (called internal damping); (2) damping in the interface due to sliding friction and the contact damping; (3) fluidic damping due to interaction with the ambient fluid (gas, air, vapor etc.).

The energy loss per cycle of the harmonic motion is the basis for calculation of the "equivalent viscous damping coefficient". The experimental near-resonant vibration response of the brush can be used for calculation of the linear viscous damping coefficient b from the frequency bandwidth $\Delta\omega$ at the "half-power" response amplitude [4].

The energy loss per cycle for the vibrating brush can be determined from the experimental hysteretic loop. The series of experiments on the hysteretic loops in the interface damping is recommended. Since the behavior of the brush material is not very well known, the interface hysteretic loop must be determined under various load conditions. They are as follows: symmetric, non-symmetric compressive and non-symmetric tensile loading (Figs. 1 and 2).

In line with the classification of inelastic strain, the various types of damping encountered in the brush material and the brush–brush-holder interface may generally be classified under two major types [4]: (1) rate-dependent damping, type R (Fig. 1(a)); (2) rate-independent damping, type S (Fig. 1(b)).

The energy dissipated under both types of damping may be amplitude dependent; however, type R damping also depends on the rate $\dot{F} = dF/dt$ of loading. Type S damping is independent of loading rate or of frequency ω.

The rheological equations or force–displacement laws for type R damping generally involve time derivatives of force and displacement, whereas for type S damping such derivatives are not applicable.

2.4. Linearization of non-linear hysteretic loops and the equivalent damping values

It is convenient in the dynamic approximate analysis to linearize the non-linear hysteretic loop by replacing it with ellipses that produce equivalent effects. The linearization and calculation of an equivalent damping value are presented in ref. 1.

Fig. 5. Solid brush system model. The local coordinate system x, y is fixed to the brush. The basic coordinate system X, Y is fixed in space (S_0, constant brush load; T, brush thickness; $L_3 = L_0 - L_1$; $L_4 = L - L_0 - L_2$; $L_5 = L - L_0$). (See ref. 5.)

2.5. Calculation of the reaction force at the brush interface B_1 in Fig. 5

The brush configuration is shown in Fig. 5 (which is an excerpt from ref. 5). In order to calculate the static normal reaction force F_{0x1}, the moment balance equation about point B_{02} is used as follows:

$$\sum M_{B02} = S_0 \frac{T}{2} - N_0 \left(\frac{T}{2} \cos \alpha_0 - L_2 \sin \alpha_0 \right) +$$

$$+ \mu_v N_0 \Delta - F_{0x1}(L - L_1 - L_2)$$

$$= 0 \tag{7}$$

where

$$\Delta = \frac{T}{2}\sin\alpha_0 + L_2\cos\alpha_0$$

is the overhang of the brush. The other symbols used in eqns. (7) are defined in ref. 5.

$$N_0 = \frac{S_0}{\cos\alpha_0 - \mu_v\sin\alpha_0} \qquad (8)$$

Substituting eqn. (8) into eqn. (7) gives

$$S_0\frac{T}{2} - \frac{S_0}{\cos\alpha_0 - \mu_v\sin\alpha_0}\left(\frac{T}{2}\cos\alpha_0 - L_2\sin\alpha_0\right) +$$

$$+ \frac{\mu_v\Delta S_0}{\cos\alpha_0 - \mu_v\sin\alpha_0}$$

$$= F_{0x1} \times (L - L_1 - L_2) \qquad (9)$$

Multiplying both sides of eqn. (9) by $(\cos\alpha_0 - \mu_v\sin\alpha_0)$ and solving for F_{0x1} gives

$$F_{0x1} = \frac{S_0}{(L-L_1)\cos\alpha_0/\{\Delta - (T/2)\sin\alpha_0\} - 1}\frac{\sin\alpha_0 + \mu_v\cos\alpha_0}{\cos\alpha_0 - \mu_v\sin\alpha_0} \qquad (10)$$
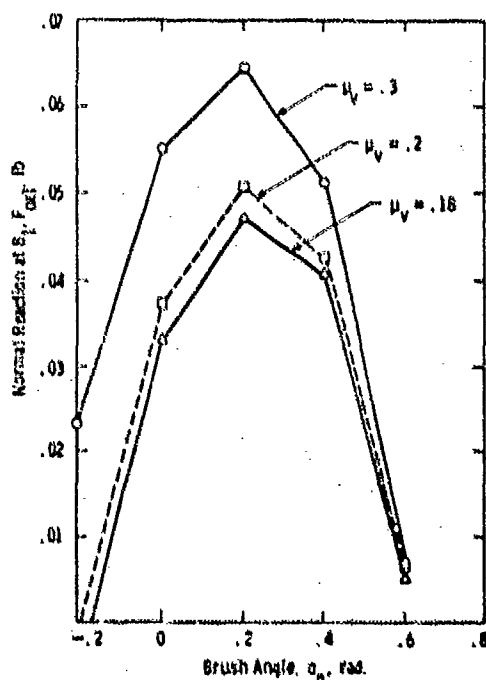

Fig. 6. Effect of the brush angle α_0 and the friction coefficient μ on the normal reaction at B_1 in Fig. 5.

For the radial brush, $\alpha_0 = 0$, and eqn. (10) gives the following value for the normal reaction at B_1:

$$(F_{0x1})_{\alpha_0=0} = S_0 \frac{L_2}{L - L_1 - L_2} \mu_v \tag{11}$$

The results of calculations of the normal reaction at B_1 for various brush angles α_0 and friction coefficients $\mu_v = 0.18$, 0.2 and 0.3 are shown in Fig. 6.

It should be noticed that the reaction F_{0x1} at B_1 becomes a maximum for the brush angle $\alpha = 0.2$.

3. Conclusions

(1) The damping in the current collection systems was identified as being caused by the brush material internal friction (hysteretic damping), by friction at the interface between the brush and the holder and between the brush and the rotor, and by the external fluidic forces.

(2) The internal friction mechanism can be represented in terms of the combination of the dashpots, springs and slides (or shoes). The values of each of the elements can be determined experimentally.

(3) The interface friction in the tangential direction is essentially the Coulomb type of friction with the friction force changing sign between the positive and the negative directions. The normal friction force is the compressive force only, with values oscillating between maximum and minimum compression.

(4) The fluidic damping of the brush mechanism is a velocity-dependent phenomenon such as in the typical viscous friction [6].

(5) Each of the three categories of friction can be modelled in terms of a linear viscous damping with an equivalent damping constant. These constants are expected to be applicable in the current collection mechanical stability analysis.

(6) At an assumed vibration amplitude of 0.001 in, the equivalent damping constant at location B_1 (Fig. 5) obtained using standard values is $b_{y1} = 0.0062$ lbf s in^{-1} [5].

4. Recommendations

(1) A forced response analysis of the solid brush system is required to obtain vibration amplitudes and modes that can be used to determine damping coefficients.

(2) Dynamic material property tests are required to determine the shape of the contact force–deflection curve and the corresponding damping energy associated with the hysteresis.

(3) Friction force–sliding velocity tests are required to determine the equivalent damping coefficients for Coulomb friction at the interface.

242

Acknowledgments

References

1 B. J. Lazan, *Damping of Materials and Members in Structural Mechanics*, Pergamon, Oxford, 1968.
2 A. V. Grin, Internal friction at the grain boundaries in aluminum, *Phys. Met. Metallogr. (Engl. Transl.)*, 9 (4) (1960) 124 - 126.
3 G. M. Leak and G. W. Miles, Grain boundary damping. II. Iron interstitial alloys, *Proc. Phys. Soc., London*, 78 (December 1961) 1529 - 1542.
4 W. T. Thompson, *Vibration Theory and Applications*, Prentice-Hall, New York, 1965.
5 C. A. Broniarek and O. S. Taylor, Mechanical stability of solid brush current collection systems, *IEEE Power Apparatus and Systems Summer Meet., Minneapolis, MN, July 13 - 18, 1980*, Paper 80 SM 504-1.
6 A. M. Freudenthal, *The Inelastic Behavior of Engineering Materials and Structures*, Wiley, New York, 1950.

CALCULATION OF THE CONDUCTIVITY OF MOULDED POWDER PRODUCTS FOR CONTACT MATERIALS*

A. I. SVIRIDYONOK, N. K. MYSHKIN and V. V. MESHKOV

Institute of Mechanics of Metal–Polymer Systems, Byelorussian Academy of Sciences, Gomel, B.S.S.R. (U.S.S.R.)

(Received December 4, 1981)

Summary

A method for calculating the electrical conductivity of moulded powder products for contact materials, using the assumption that the particles have uniform size and that their shape is close to spherical, is suggested. The heterogeneity of the pressure distribution through the moulded layer as a result of interparticle friction forces has been taken into account. Methods of modelling moulded layers of different porosity with regularly repeated elemental conduction cells have been used.

The experimental results are in closer agreement with values calculated using the authors' expression than values obtained from other expressions.

1. Introduction

The problem of making highly reliable sliding electrical contacts has been given growing attention recently [1 - 4]. An important aspect of the problem is the development of novel contact materials, possessing a set of given properties, based on a metallic matrix. Successful solution of the problem depends largely on the possibility of monitoring and controlling the properties of such materials during sintering by applying an electric current.

In a number of papers, methods are described for calculating the conductivity of a dispersed system using the size of its components and their physical properties [5]. The papers deal with both a macroscopic approach based on the principle of generalized conductivity and a microscopic approach based on modelling of the elemental cell. The generalized approach to the solution of the problem has been described elsewhere [6]. However, it should be noted that, even for two-phase systems, considerable discrepancies exist between the contact conductivity predicted theoretically and that found experimentally. In addition, in various practical applications the

___

heterogeneity of the pressure distribution through the bulk powder should be taken into account, since it leads to changes in its conducting properties.

2. Calculation

In the present paper the contact conductivity of a powder system containing homogeneous metallic particles under pressure is calculated and compared with experiment.

In the calculation the assumption was made that the powder particles have a shape close to spheres of the same diameter, and their mutual arrangement is similar through the whole volume. The powder systems were tested over a pressure range at which the contact spot stress neither caused distortion of the particle shape beyond the contact zone nor its fracture.

It is well known that powders poured freely possess high porosity, corresponding to loose packing of the particles in bulk. An applied pressure forces relative displacement of the particles, increases the number of contacts between them and decreases the pore volume. As examples of "loose" and "dense" packings (with the latter, the pore volume can decrease only by destruction of the particles) are cubic packing ($c = 6; P = 47\%$) and tetrahedral packing ($c = 12; P = 25\%$) respectively.

The contact conductivity of a dispersed system depends on both the number of contacts between particles and the area of an individual contact. In particular, when two spheres of the same radius of the same material are in contact, the sphere conductivity including the contact resistance will be defined from Laplace's equation as follows [1]:

$$\sigma_{1,2\,k} = \pi \left\{ \rho \left(\frac{1}{a} - \frac{1}{2R_0} \right) \right\}^{-1} \tag{1}$$

A most important parameter determining the contact conductivity is the radius of the contact spot which, in turn, depends on the contact pressure. The latter is not the same through the whole volume since there are friction forces between the particles and the contacts have angles to the normal. For powder systems under loading an exponential variation in pressure with height is accepted as being in good agreement with the experimental data [7]. For example, for a cylindrical component of diameter D and height H the pressure varies across the height as follows:

$$p_z = p_{\max} \exp\left(-4f\xi \frac{H-z}{D} \right) \tag{2}$$

In this connection the area of the contact spots will be different for particles in different layers through the component thickness and the contact conductivities of those particles would consequently also change. With loose and dense packing the equivalent scheme of the contact conductivity would consist of repeated cells formed by elemental contact conductivities.

245

Assuming that the pressure over the horizontal plane of each layer to be the same and the equipotential planes are vertically perpendicular to the axis, the contact conductivities can be neglected within the horizontal plane; this simplifies the calculation by reducing it to a set of parallel columns of element conductivities σ_k connected in series. Here the total conductivity would be expressed as

$$\sigma_\Sigma = m_{1,2} K_{\alpha_{1,2}} \sum_1^{n_{1,2}} \frac{1}{\sigma_k}$$
$$\approx m_{1,2} K_{\alpha_{1,2}} \int_0^H \frac{dz}{\sigma_{1,2}(z)} \tag{3}$$

The area of a contact spot can be defined by the number of particles in each layer, the number of contacts between them, the angles of slope of the contact normals to the vertical axis, the interparticle friction forces and the appearance of deformations over the contact. With dense packing, when more than one pair of opposite current-carrying contacts is found per single particle, the exact solution must allow for the mutual influence of the neighbouring contact pairs. However, when the radii of contact spots are small compared with the distances between them (which is observed within the pressure range of the systems under discussion here) the mutual influence can be neglected.

With plastic deformation, when the normal stresses on the contact equal the yield point, the function for the spot radius can be written according to eqn. (2) [8] as

$$a_k = \left[\left\{ N_{k_0} \exp\left(-4f\xi \frac{H-z}{D}\right) \right\} \{\pi c\sigma_s m K_\alpha (\cos\varphi + f\cos\tau)\}^{-1} \right]^{1/2} \tag{4}$$

With elastic deformation, which may be the prevailing case for loose packing under low loads, the function can be written using the known hertzian relationships:

$$a_k = 1.818 \left[\left\{ N_{k_0} \exp\left(-4f\xi \frac{H-z}{D}\right)(1-\mu^2)R_0 \right\} \times \right.$$
$$\left. \times \{EmK_\alpha(\cos\varphi + f\cos\tau)\}^{-1} \right]^{1/3} \tag{5}$$

Substituting eqns. (4) and (5) into eqn. (1) and integrating along the moulded component height, we obtain relationships for the calculation of the generalized contact conductivity [9] (indices 1 and 2 denote cubic and tetrahedral packings respectively; one prime (') and two primes (") denote elastic and plastic contact deformations respectively):

$$\sigma_{\Sigma_1}' = K_\alpha \sigma_0 \left[\frac{0.36}{f\xi} \left(\frac{EK_m}{N_{0_1}D}\right)^{1/3} \left\{ \exp\left(2f\xi\frac{H_1}{D}\right) - 1 \right\} - \frac{4H_1}{\pi^2 D^2} \right]^{-1} \tag{6}$$

$$\sigma_{\Sigma_1}{}'' = K_\alpha \sigma_0 \left[\frac{1}{\pi f \xi} \left(\frac{H_B K_m}{N_{0_1}} \right)^{1/2} \left\{ \exp\left(2f\xi \frac{H_1}{D} \right) - 1 \right\} - \frac{4H_1}{\pi^2 D^2} \right]^{-1} \tag{7}$$

$$\sigma_{\Sigma_2}{}'' = K_\alpha \sigma_0 \left[\frac{2.13}{\pi f \xi} \left(\frac{H_B K_m}{N_{0_2}} \right)^{1/2} \left\{ \exp\left(2f\xi \frac{H_2}{D} \right) - 1 \right\} - \frac{2.4H_2}{\pi^2 D^2} \right]^{-1} \tag{8}$$

3. Results and discussion

Analysis of the expressions obtained shows that, with the assumptions made, a predominant influence on the contact conductivity of metal powders are the physicomechanical properties of the particle material that determine the contact spot area and the geometric dimensions of the whole system. The particle shape does not influence the total conductivity directly, and in this connection it is possible to use the equations for particles of non-spherical shape if differences in the maximum dimensions are not large along the coordinate axes. The particle size is also not a determining factor when the condition $a \ll R_0$ is satisfied, which is in agreement with conclusions from other work [6].

The values of the friction coefficient f between particles and the ratio ξ of lateral thrust associated with f and with the particle arrangement are nearly equal for a wide group of metal powders [7, 8]. In particular, the product $f\xi = 0.45$ can be used with adequate accuracy.

The calculated dependences for the conductivity of powders having arbitrary porosity can be easily obtained from expressions (6) - (8) in a similar manner.

The correlation between the model and the analytical expressions (eqns. (6) - (8)) and the properties of metal powders was tested for spherical and near-spherical silver and copper particles of diameter 50 - 60 μm.

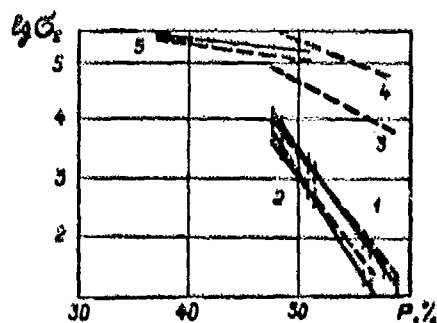Fig. 1. Dependence of experimental (———) and calculated (— — —) values of the generalized contact conductivity on powder system porosity: according to eqns. (6) - (8) for powders of silver (curves 1) and copper (curves 2); according to expressions of Riman-Weber (curve 3) and Sigalova (curve 4); according to experimental data from ref. 10 for iron powder using the present authors' equation (curves 5).

The contact conductivity of the moulded powder systems was measured in a quartz tube using a semiautomatic d.c. potentiometer by a four-probe technique. The statistical processing of the results obtained and the analytical approximation of the experimental dependences were carried out according to standard subprograms employing a minicomputer.

Figure 1 shows the results of experimental measurement of the conductivity and the calculated values. For comparison, the results for the conductivity calculated employing Riman-Weber's and Sigalova's expressions [5] are given, together with the experimental data, taken from another work [10], on the conductivity of moulded iron powder; close to these is a curve describing the conductivity calculated using the present authors' expressions.

4. Conclusions

The present calculations satisfactorily describe the behaviour of powder systems, and the results give the nearest fit to the experimental data for a wide pressure range.

The dependences obtained can be used to describe contact processes for contact materials fabricated from powders, to monitor the material quality during manufacture and to calculate the conductivity.

Further analyses are required for metal powders to account for heterogeneity in the pressure distribution over the plane normal to the axis of load application, as well as the consideration of the conductivity of powders containing functional fillers.

Nomenclature

a	radius of a contact spot
c	coordination number
D	diameter of the moulded system
E	Young's modulus
f	coefficient of interparticle friction
H	height of the moulded system
H_B	Brinell hardness
K_m	coefficient dependent on the orientation of the particles and the interparticle friction
K_α	number of conducting contact pairs
m	number of columns
n	number of layers
N	load
p	pressure
P	porosity
R_0	particle radius
z	direction of load application
α	angle between normals to opposing conjugate contact spots
μ	Poisson's ratio
ξ	coefficient of lateral thrust

248

ρ	specific resistance
σ	conductivity
σ_s	yield point of the metal
τ	$90° - \varphi$, axis of load application
φ	angle between the normal to the contact area and the direction z of load application

References

1 R. Holm, *Electrical Contacts*, Springer, Berlin, 1958.
2 *Proc. 25th Holm Conf. on Electrical Contacts, Chicago, IL, September 10 - 12, 1979,* Illinois Institute of Technology, Chicago, 1979.
3 P. S. Lifshits, *Sliding Contact in Electrical Machines*, Energia, Moscow, 1974.
4 I. R. McNab, Recent advances in electrical current collection, *Wear, 59* (1) (1980) 259 - 276.
5 L. L. Vasiliev and Yu. Eu. Fraiman, *Thermophysical Properties of Poor Heat Conductors,* Nauka i Tekhnika, Minsk, 1967.
6 V. A. Boroulia and Yu. A. Buevich, On network conductivity of grain systems, *Inzh.-Fiz. Zh., 32* (2) (1977) 275 - 283.
7 W. D. Jones, *Fundamental Principles of Powder Metallurgy*, Arnold, London, 1960.
8 G. M. Zhdanovich, *Theory of Metal Powder Compression*, Metallurgia, Moscow, 1969.
9 N. K. Myshkin and V. V. Meshkov, On contact conductivity of moulded powder systems, *Inzh.-Fiz. Zh., 39* (2) (1980) 353 - 354.
10 I. D. Radomyselskii and Eu. V. Rymorov, Compressibility and electric resistance of metal powders and their blends at low pressures of cold compression, *Poroshk. Metall.*, (11) (1976) 8 - 11.

POLAR EFFECTS WITHIN THE SLIDING CONTACT OF METAL-CONTAINING BRUSHES*

V. A. BELYI, V. V. KONCHITS and V. G. SAVKIN

Institute of Mechanics of Metal–Polymer Systems, Byelorussian Academy of Sciences, Gomel, B.S.S.R. (U.S.S.R.)

(Received December 1, 1981)

Summary

The major factors which determine the voltage drop inequality under heteropolar metal-containing brushes operated with copper collectors or slip rings were studied. It was shown that polar effects are connected with the transfer of part of the electric current through transferred brush material on the collector surface and with the semiconductor properties of the collector film developed under such conditions. The relation between the contact voltage drop for the anode-polarized (ΔU_+) and cathode-polarized (ΔU_-) brushes is determined by the type of the collector film formed. With intact cuprous oxide layers beneath the transferred material layer, the relationship $\Delta U_- > \Delta U_+$ is satisfied; with destroyed cuprous oxide layers the relationship has the opposite sign. For the range of electric loads found in electric machines, the metal-containing brushes form collector films with "gaps" within the protoxide layers beneath the transferred layer, which explains the observed inequality $\Delta U_+ > \Delta U_-$. With the brushes operated along individual paths on slip rings, an increase in the brush material in the collector film under the anode-polarized brush, and a decrease under the cathode-polarized brush, contributes to the occurrence of the inequality $\Delta U_+ > \Delta U_-$. An equivalent model of the brush contact is suggested to account for the peculiarity of the current flow under heteropolar brushes.

1. Introduction

It is known [1 - 3] that during the contact of a brush and collector (slip ring) the magnitudes of the contact voltage drop may differ for anodic (ΔU_+) and cathodic (ΔU_-) brushes, sometimes by a factor of 2 or 3. As a rule, the relationship is $\Delta U_+ > \Delta U_-$ for metal-containing brushes; for carbon

brushes, containing no metal, this relationship has the opposite sign. This polarity difference creates difficulties, both when considering the brush properties in the commutation expression and when developing new brush materials having required performance characteristics.

Most often the expression $\Delta U_- > \Delta U_+$ is explained by the assumption that current is transferred in the contact zone by electrical breakdown (fritting) of the insulating cuprous oxide (Cu_2O) layers on the microasperities of the collector surface. Several workers [1 - 4] have suggested that the thickness of the Cu_2O layer formed under the cathodic brush is higher than that under the anodic brush, thereby leading to the observed polar differences. Other workers [2, 5] believe that the main cause of the inequality between ΔU_+ and ΔU_- relates to the semiconductive properties of the Cu_2O of the collector film at the Cu_2O–Cu interface with the cathode-polarized brush. According to several authors [1 - 5] the brush contact can only give the relationship $\Delta U_- > \Delta U_+$ and therefore cannot explain the polar effects observed with metal-containing brushes. In this connection Baker [6] suggested that owing to oxide films found on metal-containing (Cu–graphite) brush surfaces, a complicated system of insulating layers develops, leading to the relationship $\Delta U_+ > \Delta U_-$. Later such a hypothesis was suggested by others [2, 7]. However, there is no convincing evidence of the importance of oxide films on the brush surfaces. On the contrary, according to Karasev et al. [7], the Cu–graphite brushes, which show polar differences when operated on a copper collector, have no such differences when operated on a silver collector. It is not clear why, in the latter case, the oxide films on the copper particles of the brush surface do not have insulating layers and do not affect the contact voltage.

In the present work we try to establish the major factors which cause the inequality in the contact voltage drop under metal-containing heteropolar brushes operated on copper collectors.

2. Experimental details

Polar effects are most clearly manifested with brushes containing metals in proportions of 40 - 60 wt.% [2, 3]. Batch-produced Cu–graphite brushes (MGS-7), as well as metal–polymer brushes [8, 9] based on copper (MP-7M) and silver (MP-7S) foil, containing the above quantity of metallic components were therefore chosen for these investigations. Colloidal copper for the MP-7M brushes and colloidal silver for the MP-7S brushes were used as the current-conducting fillers in the adhesive which joins the foil layers.

Brushes of 2.5 mm × 4 mm × 6 mm were tested on slip rings made of electrolytic copper (diameter $\phi = 40$ mm; $R_a = 0.25$ μm) at a specific pressure of 50 kPa, a sliding speed of 1.5 m s^{-1} and current densities from 0 to 30 A cm^{-2}. The current–voltage characteristics for heteropolar brushes were measured with a two-coordinate potentiometer over a 1 - 3 s period. Variations in the contact characteristics with time when brush polarities were

changed were recorded by a multichannel fast response potentiometer. The surfaces of the contacting components were studied with a feeler whose design [10] was based on an electromechanical profilograph–profilometer that allowed simultaneous recording of the electroconductivity and micro-geometry characteristics of the tested surfaces. A gold needle with a maximum radius of curvature of 50 μm was used as the feeler at the load of 2×10^{-4} N. The electrophysical properties of the tested surfaces were evaluated by the current–voltage characteristics as measured during sliding and by the feeler on typical patches in the static case.

3. Results and discussion

3.1. The operation of brushes along a single track

For all tested materials rubbed along a single path (which is typical of brush–collector contacts) the relationship $\Delta U_+ > \Delta U_-$ was satisfied (Fig. 1) over the range of current densities found in electric machines. It is clear that the non-oxidizing silver-containing brushes (MP-7S) exhibited the same polar differences as the oxidized copper-containing brushes. A similar effect was described elsewhere [3] for Ag–graphite brushes. Therefore, the inequality $\Delta U_+ > \Delta U_-$ inherent in sliding contact of the metal-containing brushes cannot be explained by the oxide films found on the brush surface. An explanation should be sought which relates to the properties of the films formed by the metal-containing brushes on the copper counterface.

To find the reasons for polar effects, the influence of polarity on the resistivity of the major conduction channels in the brush contact has been investigated. During sliding, the brush makes mechanical contacts with both the layer of transferred brush material and microasperities on the collector surface free of transferred material (Fig. 2(a)). In the latter case contact
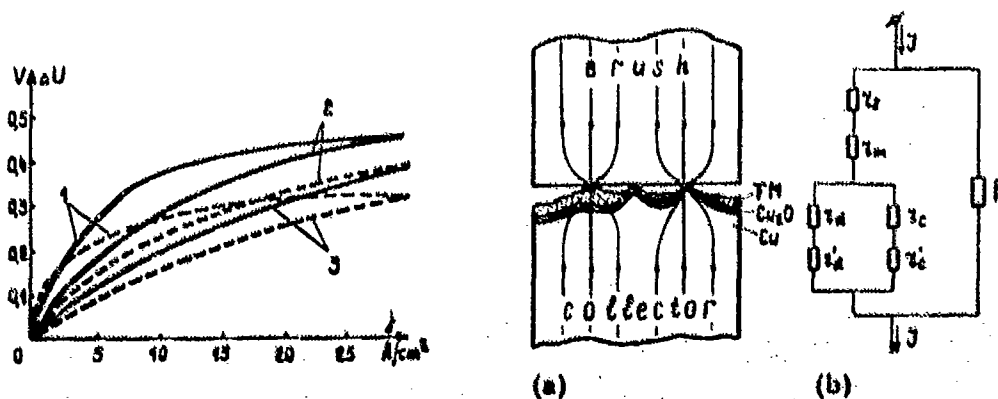

Fig. 1. Current–voltage characteristics of brushes MGS-7 (curves 1), MP-7M (curves 2) and MP-7S (curves 3) brushes running on common tracks: ——, anode-polarized brushes; – – –, cathode-polarized brushes.

Fig. 2. (a) A model (TM, transferred material) and (b) an equivalent schematic of simulation of brush–copper collector contact.

252

patches of the following types may occur [1, 11]: α-spots, which consist of a physical contact between the brush surface and molten copper; a-spots, which occur during the contact of the brush and solid copper; b-spots, which appear to involve physical contact of the brush and Cu_2O. In the theories of Holm and coworkers [1, 3, 12], α-spots and a-spots, which are formed as the result of oxide film fritting, are generally responsible for the current transfer across the brush contact, while the current that passes through b-spots may be neglected, owing to the high electrical resistance. It has been shown in refs. 13 and 14 that, under certain conditions, an essential part of the current transfer may occur through the transferred layer. Here, the current passes across the areas with an intact Cu_2O layer beneath the transferred layer (at low current loads) or across "gaps" formed within the protoxide film beneath the transferred layer as the result of electrical and mechanical effects. Therefore, the electric current with the brush contact may be transferred along two parallel branches: across α-spots or a-spots and across the transferred layer. For the sake of simplicity, the conduction across α-spots or a-spots will be called a-type conduction, that across the areas with destroyed Cu_2O layers on which physical contacts occur between the copper and the transferred layer will be called c-type conduction and that across the areas with an intact Cu_2O layer under the transferred layer will be called d-type conduction.

The conduction of the a-spots as a function of the current direction was tested on a device that allowed monitoring of the current transfer across individual contact patches. With the gold feeler on the collector film areas not covered with the brush material, current–voltage characteristics were obtained that were characterized by the presence of a high initial resistivity (greater than 10^6 Ω) and fritting of the protoxide film at a certain voltage (Fig. 3(a)). After fritting (i.e. when α-spots or a-spots were formed), the polarity change in the feeler did not lead to a variation in the contact voltage drop ΔU_k. Similar results were obtained when the gold feeler was replaced
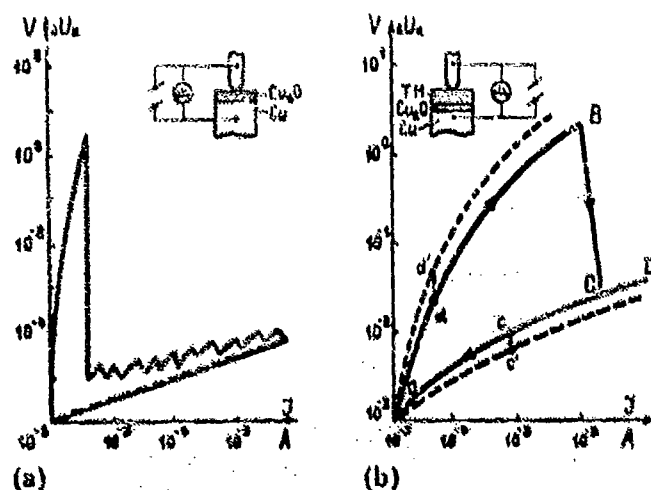

(a)   (b)

Fig. 3. Current–voltage characteristics obtained with a feeler on collector film patches with (a) weak and (b) continuous layers of transferred brush material.

by a feeler made of copper or electrographite. Thus, under static conditions the conduction of a-spots formed during the contact of any patches of the metal-containing brushes and collector microasperities did not depend on the current direction. During brush sliding, a-spots are formed continuously owing to oxidation of the contact patches. The amount of the additional contact resistivity occurring with the formation of a-spots due to local excessive strain on the contact patches is determined by the oxide film thickness [1, 3]. Here, the anode-induced polarization of the contact element favours its oxidation, while cathode-induced polarization prevents that process. Since, for a metal-containing brush–collector pair, the metal components are present in both contact surfaces, it is almost impossible to evaluate the influence of the polarity on the resistance. The problem was studied experimentally for the conditions of the brush sliding against a "fresh" surface of the copper counterface free of the brush material, *i.e.* when the current transfers primarily by means of a-type conduction. Cylindrical samples ($\phi = 1$ mm) made of the tested brush material were rubbed with the butt end against a flat copper sample ($v = 1 \ \mu m \ s^{-1}$; $j = 10 \ A \ cm^{-2}$; $p = 50$ kPa). The original copper samples were tested together with those oxidized in air ($T = 373$ K; $\tau = 7.2$ ks). It was found that, irrespective of the counterface state, the current direction did not significantly influence the value of the contact voltage drop. Thus, without transferred brush material on the collector (ring) surface, there were no major differences between ΔU_+ and ΔU_- for the sliding contact of the metal-containing brushes.

The peculiarities of electric current transfer across the collector film patches covered with a layer of the transferred brush material are shown in Fig. 3(b)). The line OBCD depicts the current–voltage characteristics obtained for the collector films formed by the de-energized brush MGS-7; the feeler was anode polarized. A sharp drop in ΔU_k at point B indicates fritting of the Cu_2O layer below the transferred material. After repeated recording of the current–voltage characteristics on the given portion (line OCD), no more fritting was observed. The polarity change of the feeler from "+" to "–" at the voltage below that of fritting (*e.g.* point d on the OB branch) leads to a step increase in ΔU_k (from d to d'). A similar change in the feeler polarity with fritting (point c on the OCD branch) gives an opposite picture; ΔU_k falls in jumps (from point c to c'). Correspondingly, current–voltage characteristics taken with the cathode-polarized feeler (broken lines) before fritting lie above (and those after fritting lie below) the characteristics obtained with the anode-polarized feeler. For the collector films formed by the energized brush MGS-7, except that described above, current–voltage characteristics were also obtained without fritting (they resemble Fig. 3(b), curve OCD). In this case, irrespective of the voltage applied, the contact voltage drop ΔU_k with the feeler polarity "+" is higher than with the polarity "–". Characteristics of this type, indicating the presence of gaps in the protoxide film beneath the transferred material, are most characteristic of the collector films formed by the metal–polymer brushes, MP-7M and MP-7S.

Thus, the polar effects in the sliding contact of the metal-containing brushes may occur across the layer of transferred material in the collector film. Here, the presence of an intact Cu_2O film under the transferred material contributes to the relationship $\Delta U_- > \Delta U_+$; with a disrupted oxide film, the sign of the inequality changes to its opposite. The results obtained allow a representation of the sliding contact of metal-containing brushes by an equivalent model (Fig. 2(b)) that clarifies the reasons of the polar differences. The electric current flows through two parallel branches, namely across a-spots or α-spots with resistivity R and across the transferred material layer in the collector film. In the latter case, resistivities r_s and r_m exist within the coupling regions and the layer of transferred brush material respectively. Depending on the collector film structure, the current may then flow across the Cu_2O layers with resistivity r_d or across gaps within the protoxide films with resistivity r_c. At the Cu_2O–Cu or transferred material–Cu interfaces non-linear resistivities r_d' and r_c' which depend on the brush polarity exist. The additional resistivity r_d' acts at the current direction from the collector to brush (cathode-polarized brush) and the resistivity r_c' acts at the opposite current direction. When the collector film is a uniform structure beneath the heteropolar brushes (with brushes running along the common track), the relationship between ΔU_+ and ΔU_- is determined by the prevailing type of conduction across the transferred material. At low current densities when the Cu_2O layer beneath the transferred material is intact (d-type conduction prevails) under the cathode-polarized brush, an additional resistivity acts so that ΔU_- exceeds ΔU_+ (Fig. 1, curves 1). An increase in the current load leads to the fritting of the protoxide film: c-type conduction then prevails, introducing, as a result, an additional resistivity r_c' under the non-polarized brush, so that the relationship between ΔU_+ and ΔU_- changes. Metal–polymer silver-containing brushes, irrespective of the operating regime, form a collector film in which no continuous Cu_2O layer is formed under the transferred layer [15, 16]. Since c-type conduction prevails in this case, the inequality $\Delta U_+ > \Delta U_-$ at any current density is satisfied (Fig. 1, curves 3).

The relationship $\Delta U_+ > \Delta U_-$ found for metal-containing brushes implies that under operating conditions characteristic of the sliding contact of electric machines, the transfer of a large current portion across the contact is provided by c-type conduction. At any instant the absolute value of the difference between ΔU_+ and ΔU_- depends on the operating regime of the contact couple and the properties of the brush material. The electrophysical properties of the brush material determine the coefficient of rectification of the semiconducting layer at the interface between the transferred material and the copper; the structure of the collector film depends on its adhesiveness and corrosion resistance [15, 16].

3.2. Operation of brushes along individual tracks

Polar differences in the tested brushes show themselves more distinctly when the brushes are operated on individual sliding tracks (which is charac-

teristic of brush–slip ring contacts), rather than on a common path (Fig. 4(a)). Other aspects have been described previously [1 - 3, 17]. The anode-polarized brushes form deep dark films on the counterface containing a considerable quantity of transferred brush material. On the contrary, under the cathode-polarized brush the brush tends to clean the counterface of foreign particles (as compared with zero current flow operation).

Our studies showed that the electroconductive properties of the sliding tracks and the mechanism of the current flow also differ under heteropolar brushes. When the feeler moves along the path on a cathode-polarized brush, a quick alternation of the contacting and non-contacting patches takes place (Fig. 5), indicating the fritting of the oxide films and the absence of a transfer layer between the feeler and the ring [15]. The appearance of the contact voltage drop ΔU_k recorded from the path of the anode-polarized brush indicates current transfer from the feeler to the ring across a layer of transferred brush material and that gaps formed in the Cu_2O film under the transferred material [15].

Several experiments were carried out to estimate the effect of the ring working surface on the electric characteristics of the contact (Fig. 4(b) - 4(d)). For the brush operated continuously under a given regime along an individual path, current–voltage characteristics were taken in a short period of time (5 - 10 s) with the opposite current direction. It is seen from Fig. 4 that distinctive polar differences exist irrespective of the operating regime, and hence track condition, before the characteristics were measured.

Since during the measurement of characteristics, the track surface condition could not change significantly, this again shows the semiconducting properties of the surface films on the copper counterface. In contrast, the comparison of Fig. 4, curves 3, and Fig. 4, curves 5, obtained for a homopolar (positive, for instance) MGS-7 brush shows that for the same brush the
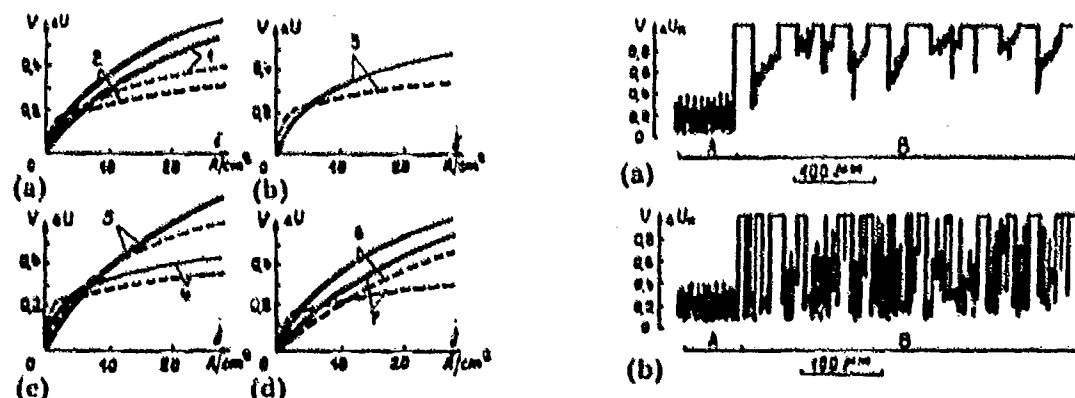
Fig. 4. (a) Current–voltage characteristics of MP-7M brushes running along common (curves 1) and individual (curves 2) tracks; (b) - (d) current–voltage characteristics of MGS-7 (curves 3 - 5) and MP-7M (curves 6, 7) brushes after long term operation at $j = 0$ A cm^{-2} (curves 3), $j = +20$ A cm^{-2} (curves 5, 6) and $j = -20$ A cm^{-2} (curves 4, 7) ($\tau = 108$ ks; $p = 50$ kPa; $v = 1.5$ m s^{-1}): ———, anode-polarized brush; – – –, cathode-polarized brush.

Fig. 5. Transient voltage drop ΔU_k with gold feeler travel along the track of (a) anode-polarized and (b) cathode-polarized MGS-7 brushes (source e.m.f., 1 V; A, free portion of the ring; B, friction track).

current–voltage characteristics are higher when more wear debris is found on the ring surface. The maximum amount of transferred material on the ring was observed after brush operation at $j = +20$ A cm^{-2}; the minimum amount was found at $j = -20$ A cm^{-2}. For MP-7M brushes, an increase in the transferred material quantity led to an increase in the transient voltage drop (Fig. 4, curves 6, 7).

A characteristic feature was the difference in the shape of current–voltage characteristics taken after the operation of cathode-polarized and anode-polarized brushes. The characteristics of the brushes operated as a cathode have a distinctive "knee" over the range of low current densities (from 2 to 5 A cm^{-2}). In many cases the characteristics taken after the same brushes were operated as an anode showed no knees.

The influence of the ring working surface condition is clearly manifested during the simultaneous recording of the electrical and frictional characteristics of the brush contact after changing polarity (Fig. 6). The sharp variations in ΔU_{k} when the polarity is changed are associated with the rectifier properties of the surface film on the ring (according to Section 3.1). It is clear that the sharp jump in ΔU_{k} as the brush polarity changes from "−" to "+" is smaller than for the reverse change. The foregoing shows that the rectifier properties of the films on a copper counterface become greater as the current passing across the transferred brush material increases. Consequently, under the steady regime of the cathode-polarized brush operation, the current flows mainly across the patches of direct contact of the brush and ring; from the anode-polarized brush the current is transferred to the ring with the help of the intermediate layer of transferred material. The present statement agrees with the mode of variation in the coefficient f of friction (Fig. 6). A rapid decrease or increase in f after the polarity changes implies that either formation or removal of the brush material film with weaker shear resistance takes place, depending on the polarity. When the brush polarity changes from "+" to "−", for example, the value of the transient voltage drop, which is similar to that characteristic of the cathode-
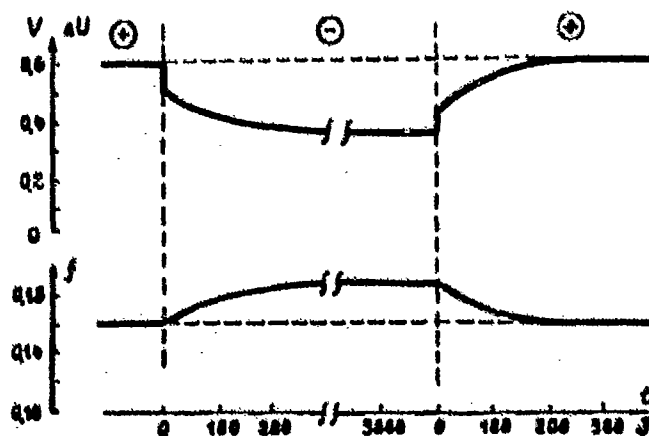

Fig. 6. Variation in the transient voltage drop ΔU and the friction coefficient f with the polarity change for an MGS brush ($j = 20$ A cm^{-2}).

polarized brush, is reached after a few minutes (Fig. 6). However, the appearance of the sliding track did not undergo clear changes (the steady state sliding track for the cathode-polarized brush was formed over several hours). This implies that with polarity change the transfer (removal) of brush material takes place, first of all, from the ring surface microasperities in direct contact with the brush surface.

The experimental data obtained imply different mechanisms for the current flow under heteropolar brushes. For a cathode-polarized brush the major mechanism is the current transfer by fritting of the oxide films on the patches of physical contact of the brush and ring surfaces. The contact between the anode-polarized brush and ring is mainly realized across the intermediate layer of the transferred brush material. It is seen from Figs. 4 and 6 that at current loads applied in current-collecting assemblies of electric machines (from 5 to 30 A cm^{-2}) the differences described for the track conditions and the mechanism of current flow increase the contact voltage drop beneath the anode-polarized brush and decrease that beneath the cathode-polarized brush. As a result, the relationship $\Delta U_+ > \Delta U_-$ related to metal-containing brushes is more strongly manifested on the slip rings than on the collector.

4. Conclusions

The difference in the values of the contact voltage drop beneath metal-containing brushes sliding along a common track on the collector is caused by the rectifier properties of the collector film that show themselves during electric current flow across the transferred brush material layer on the collector surface. The relationship between the transient voltage drop under the anode-polarized and cathode-polarized brushes is determined by the nature of the collector film formed. When an intact Cu_2O layer is found under the transferred material layer, the relationship $\Delta U_- > \Delta U_+$ is satisfied; for a destroyed protoxide layer, the opposite inequality holds. Under operating conditions typical of the sliding contact in electric machines, the metal-containing brushes form a collector layer with gaps in the protoxide layer beneath the transferred layer, which explains the observed inequality $\Delta U_+ > \Delta U_-$.

As well as the rectifier effect, when metal-containing brushes run on individual tracks on a slip ring an additional factor exists which favours the inequality $\Delta U_+ > \Delta U_-$, as a result of the differences in the condition of the tracks and the mechanism of current transfer under heteropolar brushes. These differences are caused by the influence of polarity on the transfer process in a brush contact which increases the amount of the transferred brush material on the track under the anode-polarized brush and decreases that under the cathode-polarized brush.

258

References

1 R. Holm, *Electric Contacts*, Springer, Göttingen, 1967.
2 V. I. Nellin, On polar properties of electric brushes, *Proc. Tomsk Electromech. Inst. Transp. Eng.*, *24* (1967) 88 - 108.
3 E. I. Shobert, *Carbon Brushes*, Chemical Publishing Co., New York, 1965.
4 W. Davies, The sliding contact of graphite and copper, *Proc. Inst. Electr. Eng., Part C*, *105* (7) (1958) 203 - 211.
5 F. Shroter, The contact resistance of sliding contacts, *Eng. Dig. (London)*, *16* (10) (1955) 468 - 471.
6 R. M. Baker, Sliding contacts electrical characteristics, *Electr. Eng.*, *55* (1) (1936) 94 - 100.
7 M. F. Karasev, V. I. Kozlov, L. V. Lozhkin and M. F. Khlystov, An analysis of current–voltage characteristics of electric brushes of different polarities by a schematic of brush contact modelling, *Proc. Omsk Inst. Railw. Transp. Eng.*, *122* (2) (1971) 54 - 58.
8 V. A. Belyi, F. G. Ivannikov, V. M. Kenko, E. A. Lodochnikov, V. G. Savkin and A. I. Sviridyonok, Contact brush, *U.S. Patent 4,000,439*, 1976.
9 V. A. Belyi, A. I. Sviridyonok and V. G. Savkin, New metal–polymer materials for electric brushes, in *Abstracts All-Union Meet. on the Ways of Improving the Quality and Reliability of Electric Contacts*, Leningrad, 1978, pp. 62 - 63.
10 V. V. Konchits, V. V. Meshkov and V. G. Savkin, A device for observing surface layers of electroconductive materials, *Izv. Akad. Nauk B.S.S.R., Ser. Fiz.-Tekh. Nauk*, (1) (1977) 125.
11 A. E. Stebbens, Review of theories of the brush interface, in *Proc. 1st Carbon Brush Conf.*, Morganite Carbon Ltd., London, 1961, pp. 1 - 5.
12 E. Holm, Dependence of the conduction mechanism on polarity in stationary and sliding contact, when high-resistivity films are present in the contact, *IEEE Trans. Power Appar. Syst.*, *84* (5) (1965) 65 - 75.
13 A. I. Sviridyonok, V. G. Savkin and V. V. Konchits, The influence of collector film composition on the mechanism of current passage across electric sliding contact, in *The Mechanics and Physics of Contact Interaction*, Kalinin State University, Kalinin, 1978, pp. 113 - 120 (Inter-Institutions Collection of Papers).
14 V. V. Konchits and V. G. Savkin, On influence of collector film properties on the characteristics of brush–collector contact, in *Abstracts All-Union Meet. on the Ways of Improving the Quality and Reliability of Electric Contacts*, Leningrad, 1978, pp. 63 - 64.
15 V. A. Belyi, V. V. Konchits, V. V. Meshkov, V. G. Savkin and A. I. Sviridyonok, The influence of electric brush materials on collector brush properties, *Elektrotekhnika*, (12) (1977) 43 - 46.
16 V. A. Belyi and V. G. Savkin, Peculiarities of formation and properties of metal–polymer sliding electrical contact, *Wear*, *47* (1978) 329 - 337.
17 N. S. Lifshits, *The Sliding Contact of Electric Machines*, Energia, Moscow, 1974.

NOTES ON CONTRIBUTORS

Nancy Allen: graduated with high honours in physics and mathematics from Mount Holyoke College in 1979. She is currently an engineer in the High Current Systems Section of the Westinghouse Research and Development Center. Her work has primarily been in the area of fundamental research on contact interfaces.

J. R. Barber: (for biographic note see *Wear, 59* (1980) 289).

Trevor C. Bartram: was born in Hull, Yorkshire, in 1946. After receiving a grammar school education he was employed in 1964 as a student apprentice with the Yorkshire Electricity Board, whose sponsorship at the University of Bradford led to the Degree of Bachelor of Technology in electrical and electronic engineering. In 1968 he undertook postgraduate research at the University of Bradford in the field of power system stability, concentrating on the computer modelling of turbogenerators under transient conditions. He joined International Research and Development Company Limited in 1969 working on motor control systems and thyristor rectifier equipment in support of the company's programme on superconducting d.c. homopolar motors. Having held the post of Group Leader, Electrical Systems, from 1972, he was appointed Head of the Electrical Engineering Department in 1977.

V. A. Belyi: (for biographic note see *Wear, 25* (1973) 399).

Lionel Boyer: was born in 1946 and obtained his Docteur ès-Sciences Degree from the University of Paris VI in 1979. He has worked on magnetic instability problems encountered with hard superconductors and also on superconducting machinery. For a few years, while continuing research on superconducting motors, an important part of his activities has been connected with studies on multifilamentary sliding brushes.

Czeslaw A. Broniarek: was born in Warsaw in 1927. He received his B.S. in mechanical engineering and M.S. in engineering science from Warsaw Technical University in 1949 and 1951 respectively and his Ph.D. from the Polish Academy of Sciences in Warsaw in 1966. From 1966 to 1967 he was an Independent Scientist at the Polish Academy of Sciences. From 1967 to 1974 he was at various Polish and U.S. institutes and in 1974 he was nominated adjunct professor at Rensselaer Polytechnic Institute. From 1974 to 1979 he worked at Westinghouse Research and Development Center, Pittsburgh, PA. In 1980 he joined the faculty of Tuskegee Institute, Tuskegee, AL, where he is presently a professor and Head of the Mechanical Engineering Department. He is the author of over 30 publications including two books. At present he is a consultant to the Westinghouse Research and Development Center in Pittsburgh. He is a principal investigator of the research on the hypervelocity impact sponsored by the U.S. Army Research Center. He is a member of the ASME and ASEE.

R. A. Burton: (for biographic note see *Wear, 19* (1972) 368).

Jean-Pierre Chabrerie: was born in 1941 and obtained his Engineer Degree from the Ecole Spéciale de Mécanique et d'Electricité and his Docteur ès-Sciences Degree from the University of Paris VI in 1973. He has principally worked in the following fields: superconducting homopolar machines, magnetohydrodynamic flows and sliding electrical contact phenomena (with both liquid metal and multifilamentary brushes). He is now maître de recherche at the French National Research Centre and head of the Electro-

technics team at the Laboratoire de Génie Electrique de Paris. He is a professor at the Ecole Supérieure d'Electricité et Ecole Centrale de Paris.

V. B. Doshi: received his Bachelor of Mechanical Engineering from Jadavpur University, India, in 1959, his M.S. degree in mechanical engineering from the Illinois Institute of Technology in 1961 and his M.S. degree in industrial engineering from the New York University in 1966. He has previously held positions at the Curtiss Wright Corporation and the Louis Allis Co. In previously held positions he has contributed to the development of gas turbine and Wankel engine components at Curtiss Wright and of eddy current clutches, variable speed drives and large a.c. motors at Louis Allis. Since joining the Westinghouse Research and Development Center in 1974, he has performed conceptual and detail design and analysis of advanced electric machines. He has also been responsible for the design and development of composite structures for the Trident Launch Tube, the MX missiles and the high preload rotor banding for advanced electrical machines. He is presently a senior engineer in the Electrotechnology Department at the Westinghouse Research and Development Center.

R. M. Garrett: was born in 1955. He obtained his B.S. (Eng.) from Harvey Mudd College in 1977. He joined the Westinghouse Research and Development Center where his work included data acquisition systems, electric machine development, and minicomputer-based graphics systems. He is currently employed by Brown Boveri Control Systems and engaged in graduate studies in electrical engineering at the University of Pittsburgh.

W. F. Hannan III: received his B.S.M.E. and M.S.M.E. degrees from Carnegie–Mellon University in 1973 and 1978. From 1973 to 1980, he worked with Carrier Corporation in the design and product development of integrally geared centrifugal air compressors. He joined Westinghouse in 1980 and he has been assigned various projects concerning the mechanical aspects of electrical devices.

William F. Hughes: is Professor of Mechanical Engineering at Carnegie–Mellon University in Pittsburgh, PA, and a consultant to Westinghouse Research Laboratories. He was educated at Carnegie Institute of Technology and has held research appointments at Cambridge University, Argonne National Laboratory and the University of Sydney. His active research interests are in magnetohydrodynamics, electrodynamics and friction and lubrication.

G. T. Hummert: was born in Pittsburgh, PA, in 1938. After obtaining his B.S. in electrical engineering from Carnegie–Mellon University in 1960, he worked first for McDonnell-Douglas and then for Hercules, Inc., as an instrumentation engineer. In 1968 he obtained his Ph.D. from Carnegie–Mellon University, where his thesis topic was photoionization. Since joining the Westinghouse Research Center in 1968 he has worked in a wide variety of technical areas including high voltage instrumentation and test systems, minicomputer programming and real-time control applications, hybrid computer simulations, electromagnetic analysis and magnetofluidynamics. Presently he is manager of the Electromagnetics Group, and his responsibilities include development of interactive computer graphic systems for electromagnetic analysis.

Bing-Hwai Hwang: obtained a B.S. degree in mechanical engineering in 1976 from the National Tsing Hua University in Hsinchu, Taiwan. He joined the Department of Chemical Engineering and Materials Science of Syracuse University in 1979 and received his M.S. in solid state science and technology in 1981.

J. L. Johnson: is an advisory engineer at the Westinghouse Research and Development Center, Pittsburgh, PA. He has worked for 31 years with Westinghouse and is the author of 24 papers in the field of electrical contacts, covering a wide range of applications. He is a licensed Professional Engineer and holds membership in the IEEE and two honorary societies.

William H. Lupton: is a research physicist in the Plasma Physics Division of the Naval Research Laboratory. While at that laboratory, he has been involved in the development of pulsed power systems for applications to controlled fusion and particle accelerators. Recently his interests have been related to the use of inductive and inertial energy storage for large energy pulse generators.

Alfred Marcus: received his B.E.E. from New York University in 1953 and his Master of Science in Management from Case Western Reserve University in 1971. He joined Safety Electrical Equipment Corporation, Wallingford, CT, a division of Stone–Platt Industries, in May 1979 as Chief Engineer of Rotating Equipment. He has been involved in the design, development, research and marketing of d.c. machines since graduating. He is the author of papers on ultrahigh temperature motors, linear motors and d.c. drives for electric vehicles. He is a member of IEEE, Eta Kappa Nu and Tau Beta Pi.

J. T. McLane: graduated in 1951 from Lafayette College with a B.S. degree in physics. Since then he has studied at the University of Maryland and the Catholic University of America. He has been working in the field of current collectors for the past two years. Before then he worked in the fields of electronics, photometry, colorimetry, spectroscopy, ergonomics and mechanical controls manufacturing.

I. R. McNab: received his B.Sc. in physics from Leeds University in 1960 and a Ph.D. in applied sciences from the University of Reading in 1974. Since 1975 he has been with the Westinghouse Research and Development Center in Pittsburgh, where he is manager of the Electrodynamics Section. His research activities have included sliding current transfer, magnetofluidynamics, electromagnetic launchers and plasma physics, and he holds patents in several of these areas. Dr. McNab is a Fellow of the Institute of Physics (Gt. Britain) and a Member of the Institution of Electrical Engineers (Gt. Britain).

E. Rabinowicz: (for biographic note see *Wear*, 7 (1964) 220).

Philip Reichner: received his Bachelor of Mechanical Engineering degree from the Polytechnic Institute of Brooklyn in 1954, his M.S. from the University of Pittsburgh in 1958 and his Ph.D. from Carnegie–Mellon University in 1974. He joined the Westinghouse Electric Corporation in 1954 where he has conducted research and development programs related to jet engines, refrigeration compressors, the NERVA nuclear rocket, medical devices and advanced electrical machinery. Recent programs include superconducting devices for energy storage and current collection systems using liquid metals or advanced solid brushes. He is presently a Fellow Engineer at the Westinghouse Research and Development Center.

Jacques Saint-Michel: was born in 1949 and obtained his Engineer degree in 1972 from Ecole Centrale des Arts et Manufactures, Paris. After having studied Josephson junctions for volt metrology, he is now interested in electrical machines including high performance brushes for current collection (homopolar machines) and commutation (high voltage homopolar machines and special heteropolar machines).

V. G. Savkin: (for biographic note see *Wear*, 25 (1973) 400).

J. Schreurs: received his ir. degree in metallurgical engineering from the University of Leuven, Belgium, and his Ph.D. in materials science from Northwestern University. He is now on the staff of the physical metallurgy group at the Westinghouse Research and Development Center. His fields of interest include surface spectroscopy, microcharacterization of materials and diffraction techniques with emphasis on the applications to electrical contact materials for sliding contacts and non-sliding contacts.

Bhoj Singh: obtained his Ph.D. degree in physics from Keele University, Gt. Britain, in 1971. He was a lecturer in physics at the University of Jodhpur in India before working

as a postdoctoral research fellow in the Department of Chemical Engineering and Materials Science, Syracuse University, Syracuse, NY. He is the author of 18 papers in the area of electrical conduction and gaseous adsorption on thin films. At present his research problems involve the surface physics of electrical contact phenomena.

B. R. G. Swinnerton: was born in 1940. He obtained his H.N.C. in physics in 1962, served a technical apprenticeship with English Electric Company and worked for five years in the Research Laboratories. He joined Morganite Electrical Carbon in 1968 as a sales engineer, became overseas marketing engineer in 1973, project manager in 1975, technical sales manager in 1976 and business manager in 1979.

O. S. Taylor: received his B.S.M.E. in 1969 from Pennsylvania State University. From 1969 to 1974 he worked with Carrier Corporation in the design and development of centrifugal compressors. Since 1974 he has worked with Westinghouse Research and Development in the area of current collection for advanced electrical machines. His current research interests are the thermal and mechanical aspects of high current density current collection.

Richard W. Vook: obtained his Ph.D. degree in physics from the University of Illinois, Urbana, in 1957. From 1957 to 1961 he worked as a staff physicist for the IBM Research Laboratory in Poughkeepsie and Yorktown Heights, NY. In 1961 he joined the Franklin Institute Research Laboratory, Philadelphia, PA, as a senior research physicist. He joined Syracuse University, Syracuse, NY, as an associate professor of metallurgy in 1965. He is currently a professor of materials science. He has also held short temporary summer positions at the General Electric Company, Bell Aircraft Company, the Naval Research Laboratory, Lockheed Aircraft Corporation and the University of California Lawrence Livermore National Laboratory. His research interests lie in the areas of surface physics and chemistry of electrical contact phenomena, epitaxial growth of thin films Auger electron spectroscopy, electron microscopy and X-ray and electron diffraction. He has published over 85 research papers in these and related fields.

J. B. P. Williamson: was educated at Cambridge University. For the past thirty years he has been engaged in surface physics research, particularly in the areas of surface texture and of electrical contacts. He is a Fellow of the Institution of Mechanical Engineers, of the Institute of Physics, of the Institution of Electrical Engineers and of the Institute of Welding. He has received the Jacquard Medal for Contributions to Surface Physics and the Holm Award for Achievement in Electric Contacts. He has served on the Council of the Welding Institute, and is a past Chairman of the International Committee for Electrical Contact Phenomena. After spending six years as a section head in the Tube Investments Research Laboratories, he joined the Burndy Corporation in the U.S.A. in 1962 as Director of Research. He is now President of Williamson Interface Ltd., Malvern, a company specializing in consulting on mechanical and electrical surface phenomena.

Frederick J. Young: received his B.S., M.S. and Ph.D. degrees from the Carnegie Institute of Technology in Pittsburgh, PA. He is technical director of the EMF Division of the Frontier Timber Company, a corporation in the timber, oil and gas business. One of his interests is heavy current electromagnetic phenomena.

Ji Gao Zhang: is a visiting scientist in materials science at Syracuse University on leave from the Peking Institute of Posts and Telecommunications where he is a lecturer in the area of packaging design of electronic systems. His research interests include the reliability and design of electronic connectors and most recently the friction, lubrication and wear of electrical contacts using modern surface science techniques. He has published 15 papers in these areas and was co-editor of a textbook entitled *Electronic Packaging Design*.